The Need for Accurate Pre-processing and Data Integration for the Application of Hyperspectral Imaging in Mineral Exploration

Von der Fakultät für Geowissenschaften, Geotechnik und Bergbau

der Technischen Universität Bergakademie Freiberg

genehmigte

DISSERTATION

zur Erlangung des akademischen Grades

Doktor der Naturwissenschaften

Dr. rer. nat.,

vorgelegt von Sandra Lorenz, M. Sc.

geboren am 13. Mai 1991 in Zwickau

Gutachter: Prof. Dr. Jens Gutzmer, Technische Universität Bergakademie Freiberg
Prof. Dr. Jocelyn Chanussot, Grenoble Institute of Technology
Prof. Dr. Bethany L. Ehlmann, California Institute of Technology

Tag der Verleihung: 24.10.2019

Versicherung

Hiermit versichere ich, dass ich die vorliegende Arbeit ohne unzulässige Hilfe Dritter und ohne Benutzung anderer als der angegebenen Hilfsmittel angefertigt habe; die aus fremden Quellen direkt oder indirekt übernommenen Gedanken sind als solche kenntlich gemacht.
Bei der Auswahl und Auswertung des Materials sowie bei der Herstellung des Manuskripts habe ich Unterstützungsleistungen ausschließlich durch die angegebenen Co-Autoren erhalten.
Weitere Personen waren an der Abfassung der vorliegenden Arbeit nicht beteiligt. Die Hilfe eines Promotionsberaters habe ich nicht in Anspruch genommen. Weitere Personen haben von mir keine geldwerten Leistungen für Arbeiten erhalten, die nicht als solche kenntlich gemacht worden sind.
Die Arbeit wurde bisher weder im Inland noch im Ausland in gleicher oder ähnlicher Form einer anderen Prüfungsbehörde vorgelegt.

Freiberg, den 02.04.2019

Sandra Lorenz

Abstract

Hyperspectral imaging (HSI) is one of the key technologies in current non-invasive material analysis. Recent developments in sensor design and computer technology allow the acquisition and processing of high spectral and spatial resolution datasets. In contrast to active spectroscopic approaches such as X-ray fluorescence or laser-induced breakdown spectroscopy, passive hyperspectral reflectance measurements in the visible and infrared parts of the electromagnetic spectrum are considered rapid, non-destructive, and safe. Compared to true color or multi-spectral imagery, a much larger range and even small compositional changes of substances can be differentiated and analyzed. Applications of hyperspectral reflectance imaging can be found in a wide range of scientific and industrial fields, especially when physically inaccessible or sensitive samples and processes need to be analyzed. In geosciences, this method offers a possibility to obtain spatially continuous compositional information of samples, outcrops, or regions that might be otherwise inaccessible or too large, dangerous, or environmentally valuable for a traditional exploration at reasonable expenditure. Depending on the spectral range and resolution of the deployed sensor, HSI can provide information about the distribution of rock-forming and alteration minerals, specific chemical compounds and ions. Traditional operational applications comprise space-, airborne, and lab-scale measurements with a usually (near-)nadir viewing angle. The diversity of available sensors, in particular the ongoing miniaturization, enables their usage from a wide range of distances and viewing angles on a large variety of platforms. Many recent approaches focus on the application of hyperspectral sensors in an intermediate to close sensor-target distance (one to several hundred meters) between airborne and lab-scale, usually implying exceptional acquisition parameters. These comprise unusual viewing angles as for the imaging of vertical targets, specific geometric and radiometric distortions associated with the deployment of small moving platforms such as unmanned aerial systems (UAS), or extreme size and complexity of data created by large imaging campaigns. Accurate geometric and radiometric data corrections using established methods is often not possible. Another important challenge results from the overall variety of spatial scales, sensors, and viewing angles, which often impedes a combined interpretation of datasets, such as in a 2D geographic information system (GIS). Recent studies mostly referred to work with at least partly uncorrected data that is not able to set the results in a meaningful spatial context.

These major unsolved challenges of hyperspectral imaging in mineral exploration initiated the motivation for this work. The core aim is the development of tools that bridge data acquisition and interpretation, by providing full image processing workflows from the acquisition of raw data in the field or lab, to fully corrected, validated and spatially registered at-target reflectance datasets, which are valuable for subsequent spectral analysis, image classification, or fusion in different operational environments at multiple scales. I focus on promising emerging HSI approaches, i.e.: (1) the use of lightweight UAS platforms, (2) mapping of inaccessible vertical outcrops, sometimes at up to several kilometers distance, (3) multi-sensor integration for versatile sample analysis in the near-field or lab-scale, and (4) the combination of reflectance HSI with other spectroscopic methods such as photoluminescence (PL) spectroscopy for the characterization of valuable elements in low-grade ores. In each topic, the state of the art is analyzed, tailored workflows are developed to meet key challenges and the potential of the resulting dataset is showcased on prominent mineral exploration related examples. Combined in a Python toolbox, the developed workflows aim to be versatile in regard to utilized sensors and desired applications.

Acknowledgements

This dissertation was written as part of my work as a research associate at the Helmholtz Institute Freiberg for Resource Technology, Helmholtz-Zentrum Dresden-Rossendorf (HZDR-HIF). In this context, I would like to thank the Helmholtz Association for granting me financial support and hosting me during this time.

My special thanks go to my supervisors Prof. Dr. Jens Gutzmer and Dr. Richard Gloaguen. Your outstanding support, guidance and trust allowed me to create this work under excellent conditions. I am deeply grateful for your inspiration and advice that opened up new fields of research for me.

I would like to thank all my colleagues at HZDR-HIF, especially the whole Division of Exploration, for their tremendous support in any occasion and during the whole time of my studies. I am grateful for the friendly and inspiring atmosphere you all created, the fruitful discussions and constructive remarks. Many thanks also go to the administration and technical staff for their years of cooperation.

Finally, my sincere thanks got to my family and loved ones, who have supported me throughout my educational and academic career in every possible way. Without your love and understanding, this work would not have been possible in this form.

Table of Contents

List of Abbreviations

AA	*Average Accuracy*
ALF	*Airborne Laser-induced Fluorescence*
AMD	*Acidic Mine Drainage*
BRDF	*Bidirectional Reflectance Distribution Function*
BSE	*Backscattered Electrons*
CAPEX	*Capital Expenditures*
DC	*Dark Current*
DN	*Digital Number*
DEM	*Digital Elevation Model*
DSM	*Digital Surface Model*
ELC	*Empirical Line Calibration*
EMPA	*Electron Microprobe Analysis*
FLANN	*Fast Library for Approximate Nearest Neighbors*
FOV	*Field of View*
FIR	*Far Infrared*
FTIR	*Fourier-Transform Infrared Spectrometry*
FWHM	*Full Width at Half Maximum*
GCP	*Ground Control Point*
GIS	*Geographic Information System*
GPS	*Global Positioning System*
HREE	*Heavy Rare Earth Element(s)*
HS	*Hyperspectral*
HSI	*Hyperspectral Imaging/Image*
IDW	*Inverse Distance Weighting*
IMA	*International Mineralogical Association*
IMU	*Inertial Measurement Unit*
IPB	*Iberian Pyrite Belt*
Lat/Lon	*Latitude/Longitude*
LED	*Light-Emitting Diode*
LIBS	*Laser-Induced Breakdown Spectroscopy*
LiDAR	*Light Detection and Ranging*
LOD	*Limit of Detection*
LREE	*Light Rare Earth Element(s)*
LWIR	*Long-Wave Infrared*
MB	*Megabyte*
MEPHySTo	*Mineral Exploration Python Hyperspectral Toolbox*
MLA	*Mineral Liberation Analysis*
MNF	*Minimum Noise Fraction*
MP	*Megapixel*
MVS	*MultiView Stereo*
MVT	*Mississippi Valley-Type*
MWIR	*Mid-Wave Infrared*
MWL	*Minimum Wavelength*
NA	*Not Available*
NDVI	*Normalized Difference Vegetation Index*
NIR	*Near Infrared*
OA	*Overall Accuracy*
ORB	*Oriented FAST and Rotated Brief*
OTVCA	*Orthogonal Total Variation Component Analysis*
PL	*Photoluminescence*
PSR	*Portable Spectroradiometer*
PTFE	*Polytetrafluoroethylene*
PVC	*Polyvinyl Chloride*
RANSAC	*Random Sample Consensus*
RBF	*Radial Basis Function*
REE	*Rare Earth Element(s)*
RGB	*Red-Green-Blue*
SCS	*Sun-Canopy-Sensor*
SEM	*Scanning Electron Microscope*
SfM	*Structure from Motion*
SIFT	*Scale-Invariant Feature Transform*
SNR	*Signal-to-Noise Ratio*
SVM	*Support Vector Machine*
SWIR	*Short-Wave Infrared*
TES	*Temperature-Emissivity-Separation*
TRLS	*Time-Resolved Luminescence Spectroscopy*
TLS	*Terrestrial Laser-Scanning*
TOA	*Top of Atmosphere*
TV	*Total Variation*
UAS	*Unmanned Aerial System*
UV	*Ultraviolet*
VIS	*Visible*
VMS	*Volcanogenic Massive Sulfide*
VNIR	*Visible and Near Infrared*
(p)XRF	*(portable) X-ray fluorescence*

List of Important Symbols

AZ	*Solar azimuth*
D	*Transmittance*
E	*Irradiance*
IL	*Illumination factor*
L	*Radiance*
R	*Reflectance / Reflectivity*
SZ	*Solar zenith angle*
T	*Temperature*
c	*Speed of light*
h	*Planck constant*
i	*Incidence angle with respect to surface normal*
k	*Extinction coefficient*
k_B	*Boltzmann constant*
n	*Refractive index*
o	*Terrain aspect (azimuth)*
s	*Terrain slope*
t	*Temporal axis*
x, y, z	*Spatial axes in a 3D space*
ε	*Emissivity*
λ	*Wavelength*

List of Figures

List of Tables

Motivation and Outline of the Thesis

Hyperspectral (HS) sensors currently undergo a rapid development in terms of size, performance, spectral range, and overall data quality. Innovative operational technologies open up new scales, viewing angles, and application fields. Simultaneously, recent image processing developments led to the optimization of machine learning algorithms for big data and real-time processing.

In the application sector, however, conventional or even outdated approaches remain the methods of choice. The reasons mainly originate from a general lack of awareness as well as the perceived impracticability of novel methods for the end user. The establishment of novel workflows is complicated by challenges not yet tackled in terms of adequate data pre-processing or the integration of multi-source image data in a common spatial context.

The emphasis of this work is to develop and provide tools and workflows that are able to address these challenges. The methods should provide versatile solutions for different sensors types, wavelength ranges, and sensor-target-distances, while still being robust and independent of the application sector. The developed tools were tested and validated on mineral exploration targets at different spatial scales such as natural outcrops, mines, drill-cores, and single mineral specimen. These targets feature a complexity in morphology, composition, and spectral properties. Simultaneously, the data acquisition is affected by a variety of geometric and radiometric effects in real field conditions. This makes mineral exploration objectives well-suited to demonstrate the performance of the developed workflows on demanding data sets. I address particular challenges of currently emerging HS operational principles and show the potential and importance of carefully corrected data sets for complex tasks in mineral exploration. Due to the diversity of subjects, each contribution is addressed in a separate chapter accompanied by a detailed introduction and method description. Chapters 2, 3, and 5 are formed by already published research articles that were reformatted to fit the style of the thesis. Chapter 4 forms the basis of another manuscript that is in preparation for publication.

Chapter 1 is an **introduction** on the physical processes important for the acquisition, correction, and interpretation of hyperspectral data. Additionally, it elaborates on the state of the art of sensors, workflows, and applications of hyperspectral imaging and reveals remaining challenges for different acquisition approaches.

Chapter 2 is devoted to **UAS- or drone-borne hyperspectral imagery**. As a new and promising technique for fast and precise data acquisition it delivers high-resolution hyperspectral data to a large variety of end-users. Drones can overcome the scale gap between field and air-borne remote sensing, thus providing high-resolution and multi-temporal data for a wide range of applications. However, complex geometric and radiometric effects impede their use for applications that require accurate and reliable spectral information such as in mineral mapping. A workflow for a proper and careful data pre-processing had to be developed and tested to enable the use of drone-borne HSI for advanced spectral analysis and mapping.

Chapter 3 addresses the various challenges of **terrestrial or ground-based hyperspectral imaging**. Despite its potential for the spectral analysis of any vertical or inaccessible target, adequate radiometric and geometric correction tools were missing. In particular, the extreme influence of atmospheric effects and relief-induced illumination differences remained an unmet challenge. Due to the small-angle view, these effects cannot be corrected by means of common correction tools for (near-)nadir satellite or airborne

data. New solutions for the georeferencing, visualization, and contextualization of hyperspectral image scans from different sensors, positions, angles, and distances were required.

Chapter 4 deals with the integration of **multi-sensor hyperspectral imagery for near-field sample scanning**. Despite the required sensor-specific geometric and radiometric corrections, this setup demands a fast and reliable technique for the co-registration and integration of large datasets with unique acquisition principles, spectral ranges, and spatial sampling distances. A successful fusion of high-resolution RGB (Red-Green-Blue), visible and near infrared (VNIR), shortwave infrared (SWIR), and longwave infrared (LWIR) image data multiplies the amount of materials detectable with a better accuracy and allows simultaneous queries of high-resolution spatial and spectral information over an extended spectral range.

Chapter 5 elaborates on the potential of **hyperspectral image sensors for near-field spectroscopy** and the **integration with photoluminescence spectroscopy** on the example of Rare Earth Element (REE) detection in natural minerals. Until now, both approaches have been proven to be capable of REE detection, but have never been compared or integrated in a combined characterization approach. A combination of the strengths of both methods has the potential to complement and cross-validate the individual findings and to be used in a broad range of applications along the entire value chain of raw materials, such as in exploration, mining, and recycling.

Chapter 6 is a conclusion on the outcomes of this work with a critical evaluation of their impact in a larger framework.

CHAPTER 1 INTRODUCTION TO HYPERSPECTRAL IMAGING

In the following, a summary of the most important processes for hyperspectral imaging is given, introducing crucial terms and relations important for data acquisition, correction, and interpretation.
This encompasses important physical spectroscopic processes within the observed material and wavelength range as well as sensor-specific and external influence factors during the acquisition. The state of the art on sensors, acquisition scales, and correction workflows are given to outline remaining challenges, of which several will be tackled in this thesis. This introduction is meant to serve as a general preface to the following chapters, which will then provide a deeper insight into the handling of each of the specific challenges.

1.1 The Spectrum: Physical Background on the Absorption and Emission of Light

Optical spectral analysis in general is the measurement of matter-light interactions as a function of their energy. More specifically, this encompasses any radiation that is emitted, reflected, or transmitted from the investigated target (Clark et al. 1999). The typical wavelength ranges analyzed in spectral imaging comprise Visible and Near-Infrared (VIS and NIR or VNIR), Short-Wave Infrared (SWIR), Mid-Wave Infrared (MWIR), and Long-Wave Infrared (LWIR), as depicted in **Figure 1-1**.

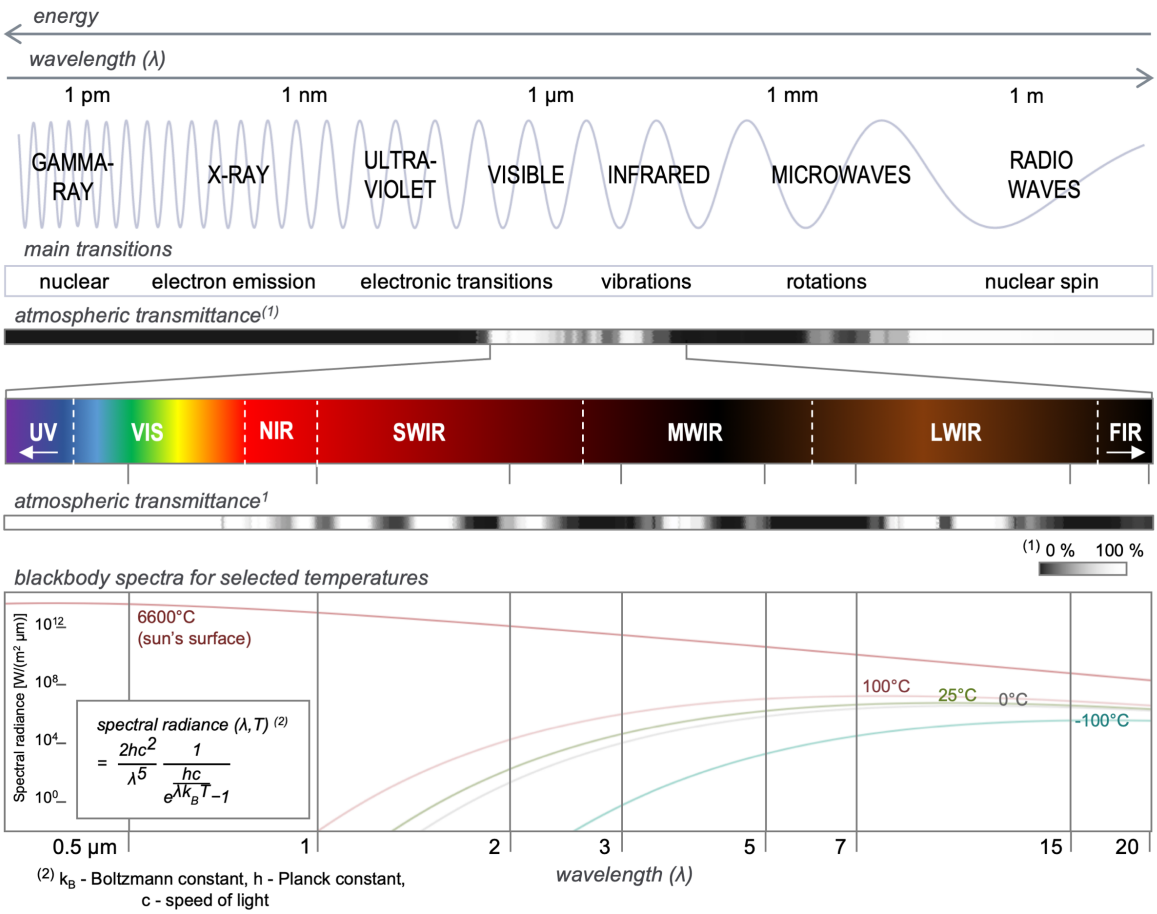

Figure 1-1. The electromagnetic spectrum: Important properties and relations for spectral imaging. (UV: Ultra-violet, FIR: Far Infrared).

The concept of quantized molecular energy is key to the understanding of any absorption and emission processes observed in spectral imaging. It states that the possible quantum states of individual atomic

species (atoms, ions, or molecules) are well-defined at a characteristic energy level. These states are characteristic for the particles' physical nature and the dynamic and energetic processes affecting them. An atomic species possesses different sets of energy levels, associated to electronic, vibrational, rotational, and translational processes as well as electron spins. Besides a low energy or ground state, each set can feature several high energy or excited states (**Figure 1-2**). An excited state is reached, when the center absorbs an amount of energy matching the state's energetic difference. Once excited, the transition back to a lower energy state usually happens spontaneously through the emission of energy with a frequency resembling the energy of the transition.

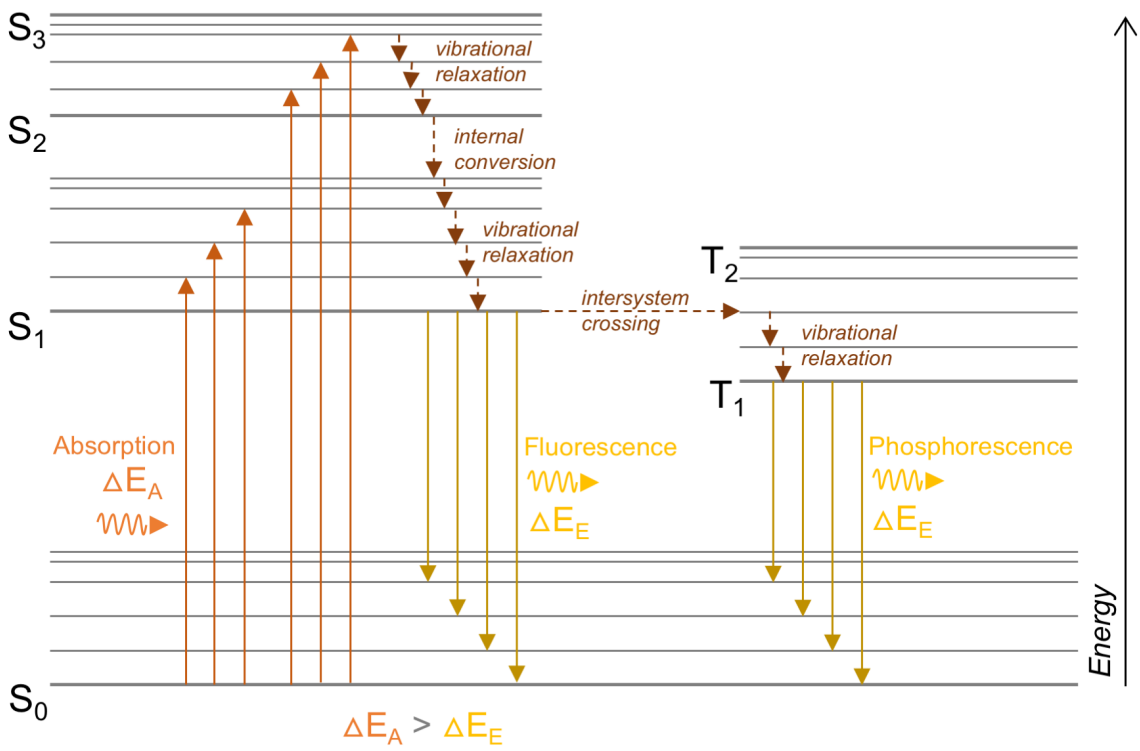

Figure 1-2. Energy diagram showing typical transitions between electronic states of a molecule. Illustrated are the main processes of absorption, fluorescence, and phosphorescence. S - single state, T - triplet state (based on Rhys-Williams 1981).

As the energy level differences vary depending on the type of the associated process, absorption and emission occur in different spectral ranges. Changes in rotational energy are observed in microwave down to UV, vibrational processes are mainly expressed in infrared to UV, and electronic energy transitions are characteristic to the visible and UV range (**Figure 1-1**). An optically active center is usually affected by several processes, resulting in characteristic absorption and emission features over the entire electromagnetic spectrum. In visible and infrared spectroscopy, observed absorption and emission effects mostly originate from atom or molecule vibrations and electronic transitions (Clark 1999).

Infrared-range photon energies are too small to excite electrons, instead atoms and groups in covalent bonds are excited to a range of **vibration motions** such as stretching and bending. Fundamental features at shorter wavelengths (4000–1450 cm^{-1} or 2.5–6.9 µm) are mostly broad and related to stretching vibrations of diatomic regions (group frequency region), while signatures in the so-called fingerprint region (1450–600 cm^{-1} or 6.9–16.7 µm) are a usually highly complex mixture of stretching and bending vibration effects. Weaker features occur at multiples of one fundamental absorption frequency and additions of several

fundamental absorption frequencies, referred to as overtones and combinations. Depending on the dominant scattering process, strong fundamental molecular vibrations are expressed not as absorption-related reflectance minima, but as strong and broad reflectance maxima (**Figure 1-3**). The manifestation of this so-called *Reststrahlen effect* is highly dependent on the dominance of surface over volume scattering. Important influencing parameters on the scattering type are grain size, porosity, and crystal order of the observed surface (Salisbury et al. 1987). When surface scattering is dominant, the Reststrahlen effect can be explained by taking the complex refractive index, $\underline{n}$, into account, consisting of a real part, n, and an imaginary part, k, whereby n and k represent the refractive index (or phase velocity) and the extinction (or attenuation) coefficient, respectively. After Fresnel's equations (Fresnel 1866), the reflectivity, R, of a plane at a normal incidence is defined by

$$R = \frac{(n-1)^2 + k^2}{(n+1)^2 + k^2} \tag{1-1}$$

An exemplary schematic illustration of the optical indices n and k, calculated reflectivity R, and an experimentally obtained reflectance spectrum of quartz is shown in **Figure 1-3**.

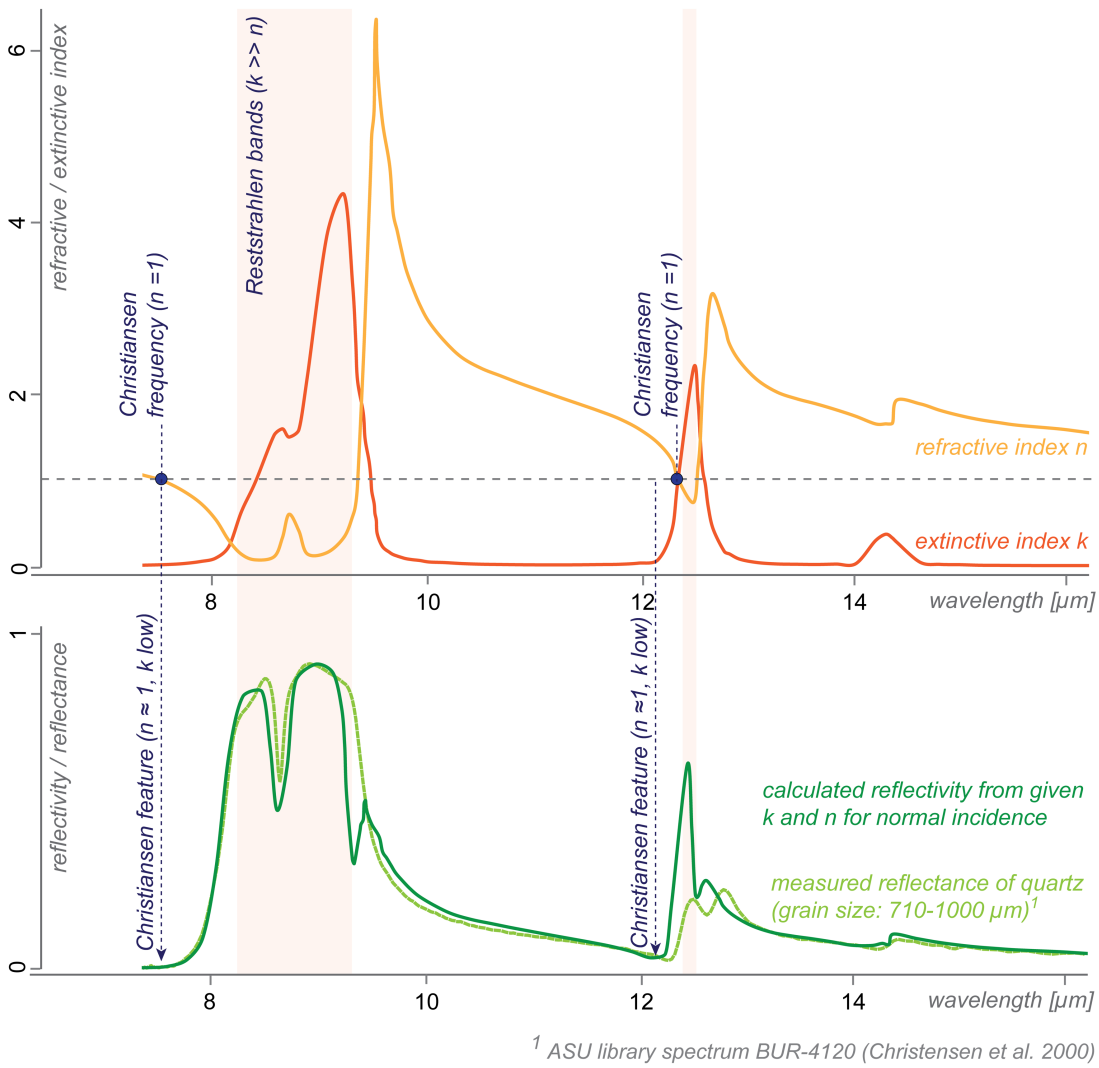

Figure 1-3. Optical parameters of α-quartz in the LWIR (data derived from Spitzer and Kleinman (1960), results for the ordinary ray and with plane polarized light) and position of respective Reststrahlen and Christiansen frequencies (**top**); resulting theoretical reflectivity for normal incidence and comparison to a real quartz reflectance spectrum (**bottom**).

It can be seen that a very strong absorption (equivalent to a high extinction coefficient, k, with $k >> n$) causes a high, specular reflectivity, R, i.e. most of the incoming radiation is hindered on entering the material. Instead, the radiation is reflected on the material's surface. These maxima in reflectance are also referred to as *Fresnel peaks*. At a slightly lower wavelength than the absorption, the *Christiansen wavelength* is situated. At this wavelength, the refractive index, n, of the material changes rapidly due to the nearby absorption wavelength and comes close to those of the surrounding medium ($n = 1$ for air), theoretically resulting in minimal scattering of incoming radiation. However, at the exact position of the Christiansen wavelength, the extinction coefficient is still significant. Slightly out of the Christiansen wavelength and therefore off from the absorption wavelength ($k << 1$), the photons can pass the material relatively unhindered, which is then observed as extremely low reflectance values (*Christiansen features*). The wavelength position of the Christiansen features has been proven to be highly characteristic for mineral composition (e.g., Logan et al. 1973, Salisbury & Walter 1989).

The excitation of **electronic transitions** requires higher excitation energies than thermal vibrations and can therefore be observed mainly in the visible, but also UV and SWIR range of the electromagnetic spectrum. The processes electronic transitions are related to are manifold:

Crystal field effects are associated to unfilled or partially filled shells of transition elements (such as Fe, Ni, Cr, and Co) located in a crystal field. The influence of the field causes a splitting of the transition elements electronic states, and thus a shift of the transition energy. The splitting and resulting absorbed or emitted energies are highly dependent on the crystal structure and therefore characteristic for the host mineral.

Charge transfer absorptions occur when electrons are transferred between two metal ions (intervalence charge transfer, e.g. Fe^{2+}-Fe^{3+}, Fe^{2+}-Ti^{4+}) or between a cation and oxygen (oxygen-metal charge transfer, e.g. Fe-O, Cr-O). Charge transfer absorptions are usually located in the UV and lower VIS and are much stronger than crystal field effects.

Band gap electronic transitions occur in materials featuring an energetic gap between conduction and valence band. Only electrons with energies exceeding the energetic gap between are absorbed, causing an absorption edge. At wavelengths above the edge and within the band gap, the material is theoretically transparent, whereas at lower wavelengths all incident radiation is absorbed. For silicates, the absorption edge is situated in the UV and the spectral signal in the VNIR remains unaffected. In sulfide minerals, the absorptions edge is located at much higher wavelengths, λ, from 350 nm for Sphalerite (ZnS) up to 3350 nm for Galena (PbS).

Color centers are caused by the incidence of ionizing radiation or an imperfect crystal (Hunt 1977). These imperfections may be lattice defects due to the presence of impurities (replaced ions), vacancies (missing ions), and interstitials (additional ions forced in between the lattice). Resulting modified ions and trapped electrons possess their own electronic states. Related absorptions appear as broad spectral features visible in the VNIR as a variety of distinct colors (e.g. the colors of irradiated apatite, topaz, or zircon).

Similar to vibrational processes, the energy absorbed by electronic processes in every case causes an excited energy state, from which the electron can relax. The respective spontaneous, discrete emission of light unrelated to thermal radiation is referred to as **luminescence**. Depending on the process triggering the excitation, multiple types of luminescence are distinguished, such as chemi-, electro-, and photoluminescence, which often can be further subdivided. Photoluminescence is referred to as fluorescence, if after photon absorption re-emitted photons are released rapidly (in the order of 10 to 1000 nanoseconds). Commonly, some of the initial excitation energy is dissipated before re-emission to internal energy transitions and relaxation processes. This leads to the emission of a photon with lower energy or longer wavelength than the exciting photon (**Figure 1-2**). The respective energy difference is defined as

“Stokes Shift” (Stokes 1852). The specific case of rapid re-emission at an equivalent wavelength is called resonance fluorescence. A slow emission, from milliseconds up to minutes or even hours, is known as phosphorescence (see **Figure 1-2**).

The returned luminescence intensity depends on a range of factors comprising the absorption cross-section of photons at the excitation wavelength as well as the concentration of the respective luminescence centers. Additional common influences are luminescence anisotropy, i.e. direction-specific response to the crystallographic structure of the material, or processes such as nonradiative return, in which the absorbed energy is used to heat the host lattice by the excitation of vibrations. Due to its resulting significantly lower intensity compared to absorption signatures, the contribution of luminescence is mostly neglected in spectral imaging analysis. However, as the intensity of luminescence is also directly proportional to the intensity of the incident radiation, respective experimental setups can be used to optimize the excitation of luminescence centers characteristic for many ions and minerals (Rhys-Williams 1981). A common approach to measure meaningful luminescence spectra is the excitation with a strong, monochromatic excitation source such as a laser or LED (Light-Emitting Diode) under dark lab conditions. A straight-forward realization is steady-state continuous-wave-laser spectroscopy, i.e. luminescence measurements under a constant excitation of the sample during the whole experiment duration. A short excitation pulse combined with time-resolved spectroscopy offers a more sophisticated, but complex approach, where materials with differing luminescence life-times and decay spectra can be distinguished. A pulsed light source offers the possibility of on-/off-measurements to retrieve a luminescence signal under ambient light. For all approaches, the target-specific choice of the used excitation wavelength is crucial and variations can be used to excite or avoid a response of specific luminescence centers. Under ideal conditions, luminescence analysis can reach sensitivities down to a detection limit of 10^{-12} moles, which highly exceeds the capabilities of absorption spectrometry that is barely able to reach 10^{-8} moles (Rhys-Williams 1981).

Thermal radiation and grey body emission are common effects to every object or surface with a temperature above 0 K, resulting in a constant emission of infrared radiation due to the thermal motions of its charged particles. At an assumed thermodynamic equilibrium, the emitted radiation behaves according to Planck’s law (Planck 1914). Idealizing the emitter to a blackbody, which absorbs every incident radiation at all wavelengths and emits solely thermal radiation, the emitted wavelength- and temperature-specific radiation are simplifiable by Planck’s function (see **Figure 1-1**). As a blackbody emits the highest possible radiation intensity at a given temperature, the emissivity, ε, of any real object can be defined as the ratio between its radiation observed to that of an assumed blackbody at the same temperature. According to Kirchhoff’s law, the corresponding reflectance, R, spectrum can be calculated by $R = 1 - \varepsilon$, provided that the transmittance of radiation through the investigated material is negligible (Kirchhoff 1860).

With increasing temperature, the intensity of the emitted radiation of any matter rises, while the wavelength, at which the maximum radiation intensity is observed, decreases. The radiance spectra of incandescent light sources, such as the sun or lightbulbs, often have their intensity maximum in the VIS, where radiation is visible to the human eye. For matter at temperatures commonly experienced on the earth’s surface, the maximum radiation intensity is situated within the invisible infrared range of the electromagnetic spectrum (**Figure 1-1**). This results in the interference of the matter’s thermal radiation with additional polychromatic light and complicates the interpretation of the observed radiance signature. In the SWIR range, thermal radiation has only a minor influence and is therefore mostly neglected. The MWIR range is equally influenced by both sources, making its interpretation extremely complicated and often limiting its usage in spectral imaging. The LWIR range is largely dominated by thermal radiation, making it the common range for thermal radiation analysis in remote sensing.

1.2 The Image: From Spectral to Hyperspectral

Independent of the observed wavelength range, investigated material, and the underlying spectroscopic processes, the format and visualization of any spectral dataset remains similar. All spectral datasets acquired by imaging spectroscopy in principle feature three dimensions with at least one, even indistinct, value defining the measured signal intensity along at least two spatial and one spectral axis. Depending on the type of data this basic model can be reduced or extended to different levels of spectral and spatial complexity (**Figure 1-4**).

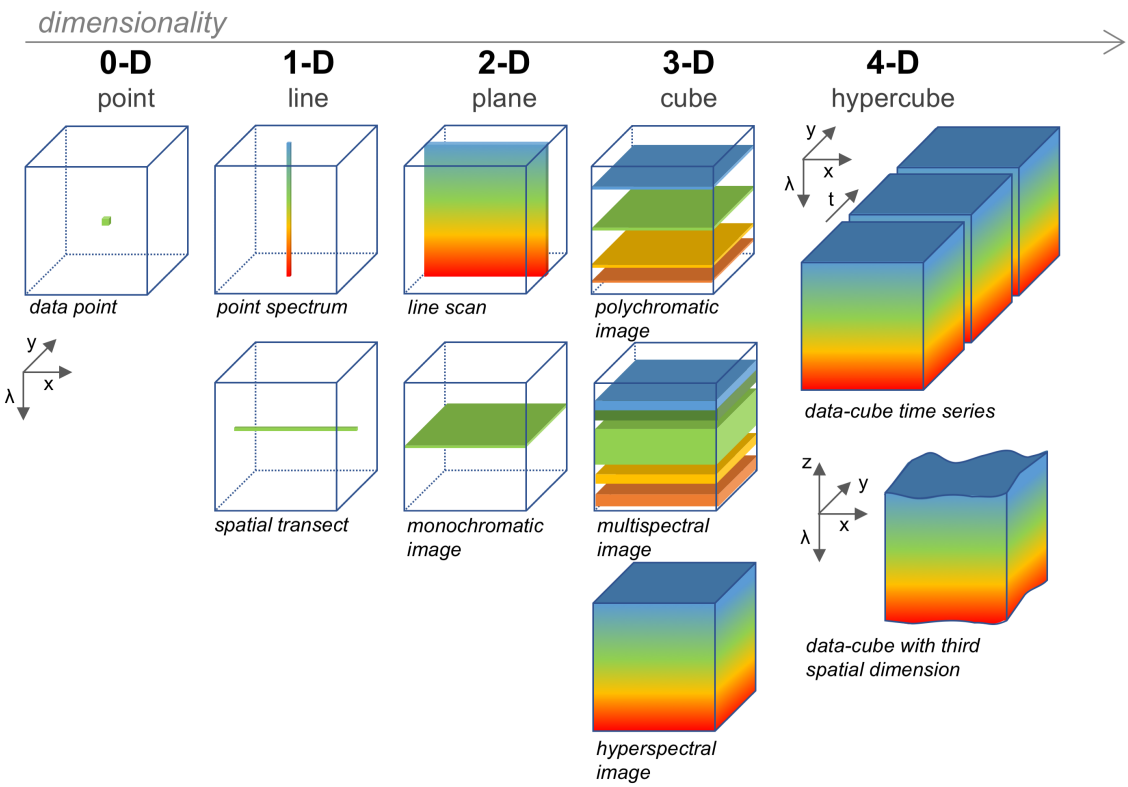

Figure 1-4. Schematic examples on different levels of dimensionality of spectral data with *x*, *y*, *z* being the spatial, λ the spectral, and *t* the temporal axes.

Within this framework, a hyperspectral image is defined as a three-dimensional data-cube with a large number of spectrally narrow, quasi-contiguous entries along the spectral axis. This provides the possibility to query a plottable spectral signature for each spatial position on a surface. The accompanying amount of information results in much larger data sizes compared to polychromatic or multispectral imagery. The acquisition of a hyperspectral dataset in a reasonable time is correspondingly more complicated. In theory, snapshot sensors enable the contemporaneous acquisition of one dataset at a time, but are still rarely used as this is often achieved by a decrease of either spectral or spatial resolution or signal-to-noise-ratio (SNR). Common sensors reduce the amount of simultaneously acquired data by sequential scanning of, e.g., one spatial pixel at a time (whisk broom or across track scanning), one spatial pixel line at a time (push broom or line scanning), or one spectral channel at a time (frame-based imaging). These approaches require either moving parts within the device or a movement of the whole sensor to acquire a complete data-cube. Due to the time offset between the individual recordings, additional movements of the sensor platform lead to image distortions and trigger the need for additional data pre-processing steps. According to their acquisition principles, whisk and push broom scans are dominantly in need for spatial alignments between the acquired

pixels or lines, while frame-based images may feature spatial offsets between spectral channels. Examples on current commercial hyperspectral sensors for each acquisition type are given in **Table 1-1**. Fast sensors that are less prone to generate distortion effects, such as snapshot or frame-based sensors, are deployed predominantly at smaller and less stable platforms such as unmanned aerial systems (UAS). Whisk and push broom scanners often provide spectrally higher quality data, but in general need more stable platforms with a higher payload to carry additional equipment for geometrical calibration, such as a global positioning system (GPS) and inertial measurement unit (IMU).

Table 1-1. Examples on current hyperspectral sensors and their specifications.

	Sensor name	**Platform**	**Spectral channels (ch) / FWHM (Full Width at Half Maximum)**	**Spatial image size / pixel size at typical operation distance**
Whisk broom	AVIRIS	Airborne	224 ch / 10 nm (VNIR/SWIR)	677 px / 1–20 m
	HyMap	Airborne	126 ch / 15-20 nm (VNIR/SWIR)	512 px / 2.5–5 m
Push broom	Hyperion EO-1	Satellite	220 ch / 10 nm (VNIR/SWIR)	250 px / 30 m
	Specim AisaFENIX	Airborne / Terrestrial	624 ch / 3.5 nm (VNIR), 12 nm (SWIR)	384 px / m–cm
	Specim FX10	UAS / Terrestrial	224 ch / 5.5 nm (VNIR)	1024 px / cm–mm
Frame-based	Senop (Rikola) Hyperspectral Imager	UAS / Terrestrial	50 ch (flight mode) / 10 nm (VNIR)	1010x648 px (flight mode) / cm–mm
Snapshot	Cubert FireflEYE PLUS	UAS / Terrestrial	125 ch / 8 nm (VNIR)	50x50 px /m–dm
	imec XIMEA SNt32	UAS / Terrestrial	32 ch / 10 nm (NIR)	256x256 px / cm

An overview on general data corrections required and sensor platforms available will be given in Sections 1.3 and 1.4, respectively. Sensor- and platform-specific details in terms of acquisition, correction and processing parameters will be discussed separately in the following chapters.

1.3 The Processing: Origin and Correction of Geometric and Radiometric Disturbances

1.3.1 Geometric Disturbances

Geometric disturbances encompass any effects that influence the spatial rightness of an image or dataset. Spatial rightness in this case is achieved if the spatial projection of any information delivered by the image/dataset matches its real location within a reference surface/space. The definition of the reference system is artificial, but allows to set different datasets into a spatial context and to describe the location of any image feature with unequivocal and universal coordinates. The compensation of any geometric distortion in conjunction with the geolocation of the dataset into a reference system is called orthorectification.

The origins of geometric disturbances in HS image data are manifold:

Sensor-specific, internal, or optical distortions occur due to the technical design and mechanical imperfections of the sensor itself. Common examples are one- and two-dimensional barrel (fish-eye) distortions or curvature effects at the slit of line-scanners due to diffraction. By careful determination of the individual device-specific distortion coefficients (radial and tangential) and internal camera parameters (focal length, skew and center coordinates), the distortions can be mapped and removed from the dataset.

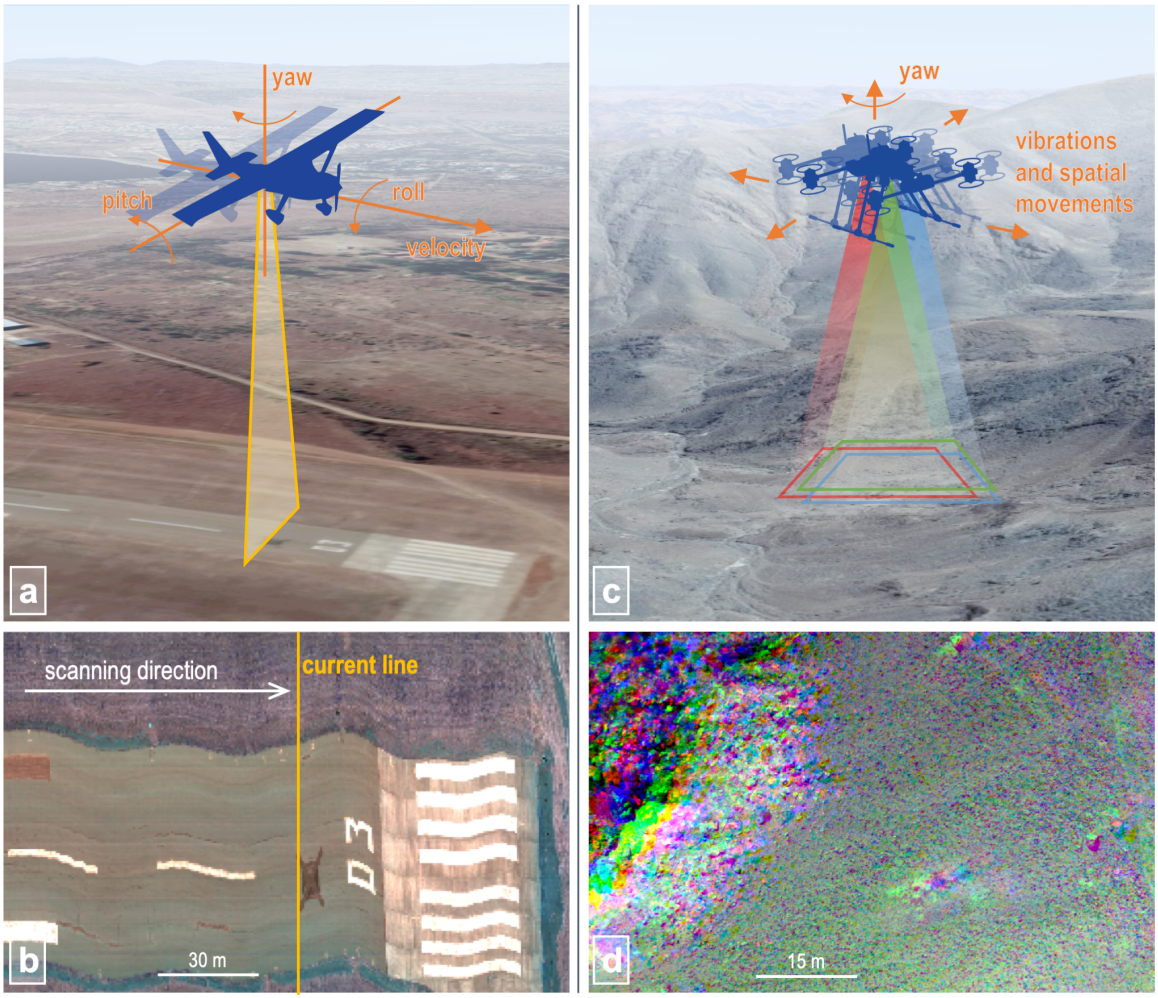

Figure 1-5. Schematic illustration of common geometric distortions due to sensor or platform movement, **left**: air-borne push broom scanning, **right**: drone-borne frame-based imaging. (**a**) characteristic movements of an unstabilized travelling aerial platform, (**b**) resulting line-wise distorted image of a push broom HSI, (**c**) characteristic movements of a hovering drone-borne gyro-stabilized platform, (**d**) resulting band-wise distorted image of a frame-based HSI.

The main **external distortions** originate from the **viewing angle** of the sensor, may it be stable during the acquisition of one or all datasets in a survey, or variable due to random and systematic movements of the platform. Stable off-nadir viewing angles can usually be corrected by perspective un-distortion of the image. Stable velocity of the sensor or platform can be used to calculate the appropriate aspect ratio of the resulting pixels. However, changing velocities are much harder to correct and require a logging during the acquisition for a satisfactory correction. The required parameters comprise any variability in **sensor or platform movement**, such as pitch, roll, yaw, skew, and changes in position and altitude (**Figure 1-5**). For whisk broom, push broom, and frame-based sensors this results in distortions between each acquired pixel, line, or spectral band, respectively (**Figure 1-5**). For snapshot sensors or at extreme movements, an additional blurring of the image may occur. The most common correction approach is the logging of the three-dimensional location, time, and angular position using an inertial measurement unit (IMU) and a geo-positioning system (GPS) attached or near to the sensor during the entire survey. After a careful boresight alignment, i.e. the correction of angular misalignment between the measurement axes of the single sensors, the recorded information can be used to separately orthorectify each distorted part of the image. For fast movements, such as for very small platforms, the approach does not apply, either because additional devices are not allowed by the limited payload of the platform or due to the limited accuracy and synchronicity of position, orientation, and HSI measurements. The cost factor also plays an important role for small surveys. For these reasons, alternative strategies need to be developed.

An additional effect specific for satellite data is the influence of the **rotation and curvature of the earth**. While negligible for lower-altitude data, it causes a common skew distortion effect in space-borne data, which can be easily corrected based on its systematic and predictable nature.

Topography can have a strong negative influence on the spatial correctness of a dataset. The amount of distortion is highly dependent on the topographical height differences within the scene as well as the altitude of the sensor. Especially with strong topographic effects, the number of required control points for an accurate orthorectification is manually not or hardly achievable. Alternative correction approaches encompass (1) automatic keypoint detection, matching, and respective warping of the dataset to an orthophoto with similar or higher spatial resolution, or (2) projection of the image on a high-resolution digital elevation model (DEM) using sensor position, angles, and altitude, as well as image specific parameters such as field-of-view (FOV). While approach (1) is independent from the exact knowledge of all acquisition parameters, approach (2) is robust to low information content or quality of the dataset (e.g., off-shore imaging, extremely noisy or cloud-covered images).

A combination of several external distortions - such as expressive topography in conjunction with low acquisition altitudes, strong sensor movements or high platform velocity - can complicate the distortion correction distinctly. For this reason, the use of a gyro-stabilized sensor or gimbal is highly advised for low-altitude airborne or drone-borne data, as they can help to reduce pitch and roll angular movement of the sensor during the acquisition, which eases the correction of the remaining effects.

1.3.2 Radiometric Disturbances

Radiometric effects disturb the spectroscopic information within the dataset, and comprise global, spatially-local, and/or spectrally-local deviations in the pixel values. Similar to geometric effects, their origin may be internal (sensor-related) or external (environment-related). A dataset corrected for any internal radiometric effects is usually referred to as at-sensor radiance. Correction for any external illumination effects results in TOA (top of atmosphere) reflectance, an additional atmospheric correction finally retrieves surface reflectance.

While irradiance, E, defines how much radiometric flux is received by a surface per unit area and is given in $W \cdot m^{-2}$ (or $W \cdot m^{-3}$ at wavelength dependency), the radiance, L, indicates how much radiometric flux is received or released from a surface per unit area and unit solid viewing angle. It is given in $W \cdot sr^{-1} \cdot m^{-2}$ (or $W \cdot sr^{-1} \cdot m^{-3}$ at wavelength dependency), and is in contrast to irradiance independent from the distance to the illumination source. Reflectance, R, as a ratio between the incident and reflected radiation, is unitless and usually given either in percent or as a factor between 0 and 1.

Important examples on **internal radiometric disturbances** comprise dark current, bad pixels, vignetting, smile, and keystone effects.

Dark current refers to the signal received by a photodetector in the absence of any incident external light. The measured electrons are generated due to the non-zero temperature of the sensor, leading to defects in the semiconductor band structure and a random noise pattern especially in low-signal images. This noise consists of a hardly correctable random or shot noise part and a rather fixed temperature- and pixel-specific pattern, which can be corrected by subtraction from the dataset. As dark current is a thermal effect, sensor cooling is highly advised to achieve stable and low-noise imagery.

Dead, stuck, and **hot pixels** (often summarized as "bad pixels") are sensor pixels that fail to return a meaningful signal, instead they provide permanently minimal (dead) or maximal (stuck) intensity or show anomalous values after sensor heating (hot). In the acquired image data, these pixels appear as definite one-dimensional lines along a spatial or spectral axis with zero, infinite, or anomalous values. Even if their information content is irrevocably lost, they can be eliminated by interpolation - for example from the spectrally and spatially closest image values (Kieffer 1996) - to avoid a further disturbance of the dataset in subsequent processing.

Similar to commercial RGB cameras, hyperspectral sensors utilizing a lens may be subject to **vignetting**, i.e. a radial loss in intensity towards the image edges. A correction requires knowledge on the optical pathway, and can be achieved by data-driven cross-track illumination correction or the application of a pixel- and wavelength-specific gain and offset matrix. The latter is used to correct for device-specific deviations in sensitivity between the pixels of the sensor array in general.

In push broom imagers, optical aberrations and misalignments of the sensor can lead to a concurrent spatially and spectrally curved distortion, known as **smile** (or frown) and **keystone effects**. In this context, smile refers to a shift of the center wavelength, keystone to a band-to-band-misregistration (e.g., Yokoya et al. 2010). Both effects are usually corrected using sensor-specific calibration values.

Depending on the acquisition circumstances, numerous **external radiometric effects** can influence the measured signal (**Figure 1-6**). The radiance of the illumination source defines the maximal achievable radiance (full reflection). For airborne, drone-borne, or outdoor terrestrial measurements, **illuminating irradiance** is usually a mixture between direct solar irradiance and diffuse sky irradiance resulting from the scattering of sunlight in the atmosphere. Changes in irradiance intensity or spectral shape during one or between several surveys result in global differences of measured at-sensor radiance, either within one or between several datasets. Depending on the sensor-target distance, different compensation approaches exist. For terrestrial and low altitude drone- and air-borne data, reference targets with known reflectance spectra and an orientation similar to the observed surface can be used to determine the current downwelling irradiance. The targets should be ideally featureless and of constant diffuse reflectance within the measured wavelength range. This may be white or grey polyvinyl chloride (PVC) plates in VNIR, high-purity polytetrafluoroethylene (PTFE) in the SWIR and brushed aluminum or coarse high-purity gold in the LWIR. If the reference targets are not visible within each acquired image or scan line, an on-board irradiance sensor can log any variances in irradiance intensity for later compensation. If no such sensor is available, a data-

driven bundle-block adjustment can be used to correct for overall illumination differences between overlapping images (Honkavaara et al. 2012). For space-borne and higher-altitude air-borne data the downwelling irradiance within one acquisition should be rather constant and can be estimated according to the current date and time, sensor-target distance, and assumed atmospheric composition.

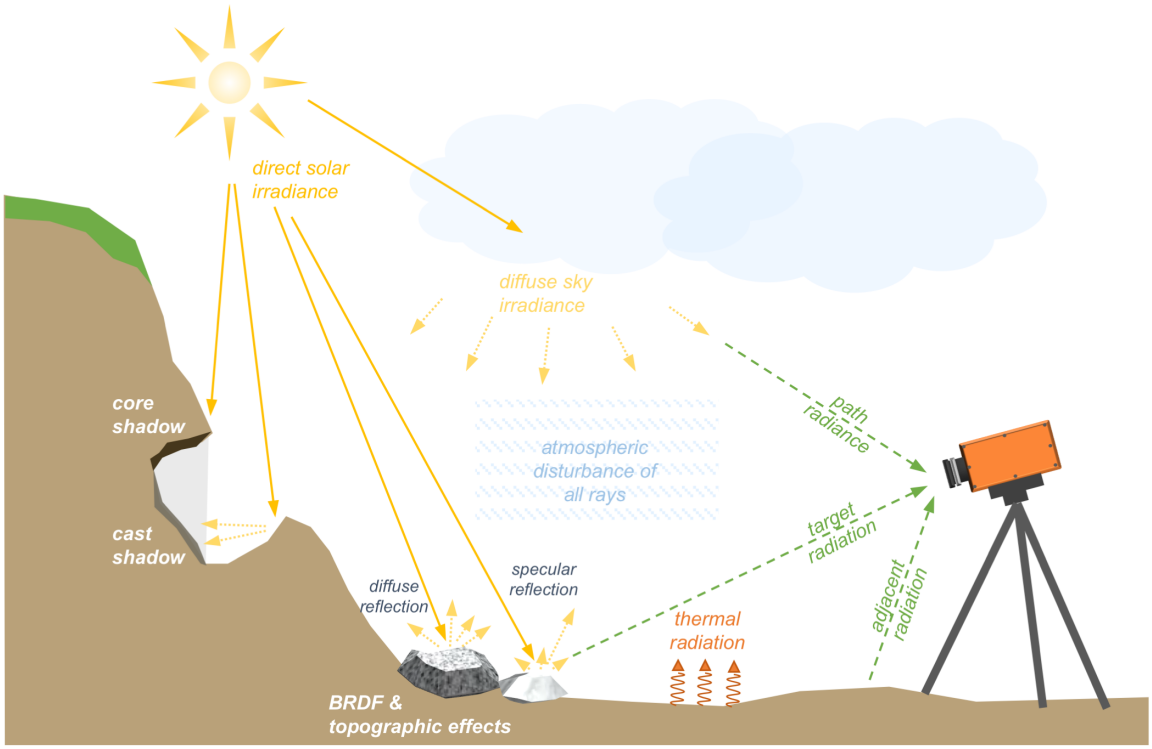

Figure 1-6. Paths of radiance and external radiometric disturbances in a hyperspectral field acquisition (based on the concept of Jensen 2007).

The reflected signal on a specific surface is dependent on a range of parameters and its behavior can be described by the **Bidirectional Reflectance Distribution Function** (BRDF, Nicodemus et al. 1977). It is defined as the ratio f_r between the differential scattered radiance, dL_r, in direction of the observing sensor and the differential incident irradiance, dE_i, with:

$$f_r(\lambda, \theta_i, \phi_i, \theta_r, \phi_r) = \frac{dL_r(\lambda, \theta_r, \phi_r)}{dE_i(\lambda, \theta_i, \phi_i)} = \frac{dL_r(\lambda, \theta_r, \phi_r)}{L_i(\lambda, \theta_i, \phi_i)\cos\theta_i \, d\omega_i} \,. \tag{1-2}$$

Here, λ shows the dependency of BRDF on the wavelength in spectral measurements. The terms (θ_i, ϕ_i) and (θ_r, ϕ_r) describe the azimuth and declination of irradiance and reflection, respectively. It can be seen that the incident irradiance, dE_i, is represented by the radiance, L_i, which is incident under the solid angle, $d\omega_i$, onto a surface. Hereby an incidence angle, θ_i, off the surface normal leads to a radiated surface area which is by $1/\cos\theta_i$ larger than at a normal angle incidence. By that the radiation intensity is reduced by the factor $\cos\theta_i$. In result, surfaces illuminated at an angle far from the surface normal appear darker than such with a near-normal illumination. Materials with an BRDF dependent from both ϕ_i and ϕ_r show an additional variation in radiance when the azimuth of the illumination is changed (the material is rotated). Such surfaces are referred to as anisotropic, in contrast to isotropic materials. Additionally, the BRDF is dividable in two main components, i.e. specular and diffuse reflection, and can be influenced not only by direct, but also concurrent ambient illumination.

An exhaustive experimental determination of BRDF is seldomly reasonable due to its high dimensionality as well as material and texture dependency. Instead, empirical and theoretical models can be used to approximate the material-specific effect of BRDF (e.g., Lambert 1760, Cook and Torrance 1981, Schlick 1994). In remote sensing, the assumption of a Lambertian behavior is common, which represents isotropic diffuse reflection (Teillet et al. 1982, Civco 1989). At image acquisition with large pixels, such as air- or spaceborne data, and areas with low topography this approach usually retrieves satisfactory results. Such, across-track brightness gradients in imagery of sensors with wide view angle can be corrected (Cross-Track Illumination Correction, Kennedy et al. 1997). However, in rugged terrain as well as over anisotropic surfaces such as forest or meadows, the Lambertian assumption can lead to strong overcorrection, especially at off-nadir viewing angles or at illumination at an angle far from the surface normal. A range of empirical non-Lambertian illumination/topographic correction methods has been developed, such as c-factor (Teillet et al. 1982), Sun-Canopy-Sensor (SCS, Gu and Gillespie 1998), or Minnaert (Minnaert 1941). The determined wavelength-specific empirical coefficients are retrieved by regression of pixel brightness and illumination angle. Despite the distinctly improved result for rugged terrain, these approaches lack performance in areas with high material variability, as in theory each material with different BRDF would require the calculation of a separate empirical coefficient. Data pre-classification and separate correction would be required to achieve a sufficient regression error.

None of the approaches are able to sufficiently correct for **shadows** yet. Usually, the affected pixels are determined using illumination angle (core shadow) and surrounding topography (cast shadow) and are masked out after. A compensation for shadows is practically almost impossible. Firstly, the signal intensity from shadowed areas commonly falls within the background noise level of the sensor and fails to contain any valuable information. Secondly, the retrieved signal is a specific mixture of reflection from different sources of diffuse irradiance (sky, trees, and neighboring topography). In illuminated pixels the contribution of these sources is mostly low enough to barely interfere the received signal. In shadowed pixels, they are the only light source and their single proportions of contribution are very specific and in no way estimable for each pixel.

Despite interactions on the surface of the target, every radiation path in the system is influenced by the **atmosphere**. Despite reflection and scattering at atmospheric particles that weaken the signal and produce diffuse sky irradiance, all travelling photons are subject to absorption by atmospheric gases and dust. Depending on the crossed thickness and composition of atmosphere the intensity and spectral shape of the atmospheric disturbances varies. For low flight altitudes, such as below a hundred meters, the influence of the atmosphere on the downwelling and reflected light is usually corrected using several reference ground targets (Empirical Line Calibration – ELC, Smith and Milton 1999). For higher altitudes, physics-based atmospheric compensation by modeling is common. Several tools exist to estimate the atmosphere's spectral contribution, usually combined with topographic illumination correction (e.g., ATCOR – Richter and Schläpfer 2018, FLAASH – Cooley et al. 2002). Such tools usually utilize lookup tables based on calculated radiative transfer models such as MODTRAN (Berk et al. 2014) or 6SV (Vermote et al. 1997). Several input parameters are required such as time, date, altitude, and location of the measurement, weather conditions and a high-resolution digital elevation model. It has been shown that these tools are also applicable for low-altitude UAS acquisitions (Schläpfer et al. 2018). For horizontal or small-angle measurements over long ranges, no appropriate methods existed at the beginning of this study.

The signal finally arriving at the sensor is composed not only of the radiance of the target (including all described disturbances), but also the **path radiance** of light scattered in the atmosphere without reaching the ground as well as light from surrounding surfaces scattered into the field of observation (**adjacency**

radiance). Every surface with a temperature above 0 K additionally emits **thermal radiation**, which interferes with the reflected signal. At common temperatures, this affects mainly the LWIR part of the electromagnetic spectrum. Only very hot surfaces (over several hundred degrees Celsius) such as lava flows can influence VNIR and SWIR measurements (see also Section 1.1). At substantial interference, a temperature-emissivity-separation (TES) is essential to retrieve the emissivity of the target, ε, and by that, its reflectance. The main step is the solution of the following equation, which describes at-sensor radiance, L, as:

$$L = [L_t\varepsilon + Dw(1-\varepsilon)]\tau_{atm} + L_{atm}(1-\tau_{atm}) \tag{1-3}$$

Required variables are the targets' thermal self-emission, L_t, the downwelling radiance onto the target, Dw, the atmospheric transmittance, τ_{atm}, and the thermal self-emission of all atmospheric components, L_{atm} (Gagnon et al. 2015). According to Planck's equation (Planck 1914), the self-emissions of target and atmosphere are a function of their thermodynamic temperatures. In a controlled environment, the equation can be simplified by controlling or neglecting specific contributions, for example defining the characteristics of the downwelling radiance by artificial illumination, adjusting the targets' self-emission by heating or cooling of the samples, or assuming $\tau_{atm} = 1$ in a lab environment.

At outdoor acquisitions, such simplifications can usually not be taken. A sensible approach utilizes two reference plates to retrieve the unknown variables. A diffuse reflector with low emissivity (usually a diffuse aluminum or gold surface) mirrors the atmospheric downwelling radiance. The second plate approximates a perfect absorber (black body), such that its at-sensor radiance is a nearly pure composition of its temperature-specific Planck function and the atmospheric transmittance between sensor and target. Both reference plates need to be set up in a similar orientation and sensor-distance to the observed target. Their emissivities and temperatures as well as the atmospheric temperature need to be known (e.g., Boubanga-Tombet et al. 2018).

1.4 The Scale: State of the Art on Multi-scale Hyperspectral Imaging

Hyperspectral imaging, regardless of the covered wavelength range or target, is currently deployed at a wide range of spatial dimensions ("scales"), ranging from satellites observing the Earth and other planets down to lab-scale sensing for small sample mineralogical analysis. New techniques such as UAS-borne imaging or terrestrial scanning of vertical targets allow to observe any target at a wide and contiguous range of scales (**Figure 1-7**). Despite basic similarities, each scale requires an adapted data processing scheme. While at some scales processing workflows are already advanced and well-deployed, others are still novel in industry and/or scientific community. Despite the possibilities, different scales are rarely integrated. The following section sheds light on the state of the art and the remaining challenges connected to each scale.

Figure 1-7. Schematic illustration of different spectral imaging platforms, scales, and acquisition principles. Common sensor-target distances are given for each.

1.4.1 Satellite (space-borne)

Spaceborne spectral imaging is a highly investigated and widely employed technique. A wide range of datasets is available online for free or at low cost, covering large parts of the Earth's surface and in addition often providing temporal resolution. This gives good prerequisites for numerous applications in geology, hydrology, ecology, and urban sciences, such as land cover, deforestation, and desertification analysis, lithological mapping and monitoring of glaciers and water systems (Transon et al. 2018).

On the one hand, the high costs and the effort to transport a sensor into space result in a sensor design that cannot be changed for several years and does not allow any subsequent customization by the individual user. On the other hand, it enables the establishment of fixed and mature data correction and processing routines. Whereas geometric correction parameters are usually retrievable from the data provider, the influence of topography and atmosphere is compensated with available digital elevation models and established atmospheric correction tools based on atmospheric models and user-defined parameters (see Section 1.3.2). A main part of recent developments focuses on the development of advanced classification and spectral unmixing algorithms as well as the handling of big data (Ghamisi et al 2017). Still, most users of space-borne spectral data need to restrict themselves to multispectral sensors. Till today, hyperspectral data is underrepresented in the space-borne scale not least because of a lack of available and appropriate sensors. To achieve contiguous spectra at acceptable data volumes, developers usually need to make sacrifices regarding spatial sampling to achieve sufficient spectral resolution, resulting in high ground sampling distances of most space-borne hyperspectral sensors (e.g., 250 m for NASA's MODIS sensor). Higher spatial resolutions were only achieved by few sensors such as the HS sensor aboard the Chinese space module Tiangong-1 (VNIR: 10 m, SWIR: 20 m) and the EO-1 Hyperion sensor (30 m). However, both platforms are out of operation today. Developers of new space-borne HSI need to face crucial challenges such as low SNR values due to the extreme influence of the atmosphere, high sensor costs and time-consuming processing of the retrieved large datasets. Nevertheless, a variety of hyperspectral space missions is in planning for the coming years, such as PRISMA (Italy) and HISUI (Japan) in 2019, or EnMAP (Germany) in 2020. In parallel, a range of tools is under development that aim to overcome the difficult correction and processing of the soon to be acquired data (e.g., van der Linden et al. 2015).

1.4.2 Manned Aircraft (airborne)

In the last decades, airborne surveys have been the most common way to acquire high-quality HSI, which has led to a strong development in acquisition workflows and correction tools. The variety of deployable HSI sensors is nearly unlimited, however, mostly confined to push broom scanners to utilize the fast and directed movement of the platform and to avoid blurring of the data. Common VNIR/SWIR sensors (among others) are HyMap (Integrated Spectronics, Sydney), AVIRIS (Jet Propulsion Laboratory, Pasadena), AisaFENIX (Spectral Imaging Ltd., Oulu), or HySpex ODIN-1024 (Norsk Elektro Optikk AS, Skedsmokorset). The most important LWIR sensors are the Hyper-Cam (Telops, Quebec) and AisaOWL (Spectral Imaging Ltd., Oulu).

Their spatial resolution and coverage are reasonable for a wide range of applications and can be adjusted by changing the flight altitude to fit the individual objective. However, extensive flight campaigns are usually costly, highly weather dependent, and require a not negligible amount of infrastructure and logistics. Multi-temporal measurements are accordingly time- and cost-consuming and sources for failures are manifold. In contrast to satellite surveys, prior knowledge of the approximate position of the target is crucial. At common flight altitudes (several hundred meters to kilometers), a radiometric correction with ground reference targets is not applicable and the geometric correction is complex due to the movements of

the platform. Therefore, data acquisition and respective corrections are often carried out by external companies. Properly corrected airborne HSI datasets can feature a high spatial and spectral resolution and coverage with significantly reduced noise in comparison to HS spaceborne data, not at least due to the possibility to fly any sensor regardless its weight. However, the costliness often denies small-budget stakeholders from targeted airborne surveys.

1.4.3 Unmanned Aircraft (drone-based)

One of the most promising application fields in the last decade arose from the deploying of hyperspectral imaging on unmanned aerial platforms or drones. Light-weight, cheap, customizable and usable by anyone and nearly anywhere, unmanned aerial systems (UAS) close the scale gap between air-borne and ground-based sampling and offer individual solutions for the respective application. Quick turnaround times and the high variability and customizability of platforms and sensors enable an aimed image surveying of inaccessible or complex targets. Depending on flight altitude and deployed HSI sensor, spatial sampling distances in the range of few centimeters can be reached while still offering a single image footprint of over one thousand square meters. With multi-image or push broom HSI surveys a sufficiently large area can be covered within 15 minutes. Current developments in UAS technology look to increase flight times, payload, and ease of operation. Concurrently, the market for small and light-weight HSI sensors is growing quickly. While sensors in the VNIR are well-represented and distributed by a variety of companies (e.g., Senop Rikola, Specim FX10, Cubert Firefly, imec XIMEA), the development of full-SWIR-sensors (up to 2500 nm) is just beginning. Today, only a few companies are able to offer SWIR push broom sensors with a mass below 3 kg (Headwall Inc., NEO HySpex, Corning).

Parallel to the technical development, the number of prospective users and application fields for drone-borne HSI rises fast. One of the main fields of interest encompasses the wide range of vegetation analysis, such as precision farming, forestry, plant species detection and health monitoring. Important, but less applied fields are hydrology, geology, and environmental monitoring. However, in recent publications containing drone-borne HS data corrections are applied rarely and the data interpretation is often not exploiting the potential of the dataset. Whereas many basic applications such as the calculation of vegetation indices on flat terrain are still possible with poorly corrected data, more advanced problems, such as spectral endmember analysis or lithological mapping in hilly terrain, rely crucially on the scientific rigor of the corrected dataset. Geometric and radiometric disturbances are often not trivial to handle and differ greatly from the effects known from satellite or air-borne data (compare Section 1.3). The influence of the atmospheric spectral component at low flight altitudes is usually small, while the differences in illumination caused by microtopography need to be strongly considered. So far, the novelty and diversity of UAS platforms and HS sensors has hindered the establishment of universal data processing routines as they exist for satellite and air-borne spectral data. Respective future development of universal open source workflows will be needed to ensure that not only developers, but all users of UAS imagery are able to obtain well-corrected data.

1.4.4 Terrestrial/Small-angle Scans

Especially geological targets, such as cliffs, vertical outcrops, or mine faces, tend to be hardly observable by common nadir or near-nadir imagery. This raised the need for a new approach of hyperspectral data acquisition at small angles. Usually this is achieved by horizontal or slightly tilted sensor mounting on a tripod or rotary stage (in case of a push broom sensor). Alternatively, any other sensor-bearing platform such as a car, boat, or low altitude UAS. Even if the acquisition is straight-forward and requires no additional

platform, the radiometric and geometric correction of the data is extremely complex. The main disturbances originate from strong topography-induced illumination differences, shadows and, in case of high-distance measurements, atmospheric effects. Due to the unusual viewing angle, none of the usual correction algorithms applies. So far, a few research groups have successfully used small-angle HSI, but neither of them applied a complete correction workflow (e.g., Greenberger et al. 2016, Sun et al. 2017, Boubanga-Tombet et al. 2018). Orthorectification, visualization and integration involve a lot of intricate processing steps. The common 2D Latitude/Longitude (Lat/Lon) image plot used for nadir data does not apply as vertical walls would lead to ambiguous 2D coordinates. The best solution so far was presented by Kurz et al. (2011) with the successful integration of HSI and LiDAR (Light Detection and Ranging) data by determining the external camera parameters using fixed control points. The method was applied for example by Denk et al. (2015) for visualization and contextualization of HS mapping results.

1.4.5 Lab-scale

Hyperspectral imaging at lab-scale or near-field (spatial sampling distances in the mm to sub-mm range) is a highly demanded topic in exploration, mining and processing industry, but also in the framework of most remote sensing studies regarding validation and detailed sample analysis. In geology and mining, samples of interest may encompass drill cores, hand specimen, rock chips, thick and thin sections or single mineral grains. The samples can show a number of possible surface appearances, from altered or fresh natural cleavages, over rough cuts, up to different stages of grinding and polishing. The required speed and accuracy of analysis can vary greatly depending on the application's desired outcome. Spectral imaging of rock material in mining and processing is usually highly automatized and simplified to produce only few classification criteria, for example to decide between waste rock and ore or between different ore grades. Since the focus lies on high throughput, the employed sensors need to be adequately highly specialized, robust and reduced to the essential task.

In exploration and lithological mapping, the amount and complexity of mineral phases to be distinguished is usually much higher and simple indices are no longer sufficient. Instead, the acquisition and careful analysis of full spectra is required. However, depending on the size of the project, large quantities of samples still have to be analyzed. A compromise between achieved detail and speed needs to be found, which is usually tackled using one or several fast push broom HS imagers with different spectral coverage in a fixed setup. To achieve a high spectral quality at a sufficient throughput, the spatial resolution is usually average (around 1–2 mm). The acquisition and processing of the data is often provided by external companies specialized in HS drill core scanning (e.g., TerraCore Geospectral Imaging, Corescan Pty Ltd). As a result, new developments on technical implementation and data evaluation are often not published. Integrated sensors covering more than one spectral range of an individual detector (e.g., VNIR for Si-based charge-coupled devices) are, as far as known, limited to the same manufacturer, FOV, and spatial resolution. The processed results of the acquired data are usually detailed mineral maps of case-relevant rock forming or alteration minerals. The maps may be based on spectral libraries, data-derived endmembers or on the analysis of depth and position of specific indicative absorption features.

A more detailed analysis is required for complex samples, for endmember validation of larger scanning surveys and whenever acquisition parameters need to be fulfilled that are not yet implemented in commercial scanning systems, such as sub-mm spatial resolution. Such experiments are commonly done in customized lab setups, with small sample numbers and a highly specialized processing. A modular approach that allows the integration of datasets of any source and specification at a speed that is sufficient for larger sample batches is currently not published.

References

Berk A, Conforti P, Kennett R, Perkins T, Hawes F, van den Bosch J. "MODTRAN6: a major upgrade of the MODTRAN radiative transfer code," In: Proceedings *of SPIE 9088: Algorithms and Technologies for Multispectral, Hyperspectral, and Ultraspectral Imagery XX*, 13 June **2014**, 90880H. DOI: 10.1117/12.2050433.

Boubanga-Tombet S, Huot A, Vitins I, Heuberger S, Veuve C, Eisele A, Hewson R, Guyot E, Marcotte F, Chamberland M. Thermal Infrared Hyperspectral Imaging for Mineralogy Mapping of a Mine Face. *Remote Sening* **2018**, 10, 1518. DOI: 10.3390/rs10101518

Civco DL. Topographic normalization of Landsat Thematic Mapper digital imagery. *Photogrammetric Engineering and Remote Sensing* **1989**, 55, 1303–1309.

Clark RN. Chapter 1: Spectroscopy of Rocks and Minerals, and Principles of Spectroscopy. *In*: Manual of Remote Sensing, 3, Remote Sensing for the Earth Sciences, (A.N. Rencz, ed.) John Wiley and Sons, New York, **1999**, 3–58.

Cook RL, Torrance KE. A reflectance model for computer graphics. *ACM SIGGRAPH Computer Graphics* **1981**, 15 (3), 307–316. DOI: 10.1145/965161.806819

Cooley T, Anderson GP, Felde GW, Hoke ML, Ratkowski AJ, Chetwynd JH, Gardner JA, Adler-Golden SM, Matthew MW, Berk A, Bernstein LS, Acharya PK, Miller D, Lewis P. FLAASH, a MODTRAN4-based atmospheric correction algorithm, its application and validation. In: *IEEE International Geoscience and Remote Sensing Symposium (IGARSS),* Toronto, Ontario, 24–28 June **2002**. DOI: 10.1109/IGARSS.2002.1026134

Denk M, Gläßer C, Kurz TH, Buckley SJ, Drissen P. Mapping of iron and steelwork by-products using close range hyperspectral imaging: A case study in Thuringia, Germany. *European Journal of Remote Sensing* **2015**, 48 (1), 489–509. DOI: 10.5721/EuJRS20154828

Fresnel AJ. Oeuvres completes d'Augustin Fresnel. **1866-1870**, 3 vols., Paris: Imprimerie Imperiale.

Gagnon MA, Tremblay P, Savary S, Duval M, Farley V, Lagueux P, Guyot É, Chamberland M. Airborne thermal infrared hyperspectral imaging for mineral mapping. In: *Proceedings of the International Workshop on Advanced Infrared Technology and Applications,* Pisa, Italy, 29 Sep–2 Oct **2015**, 29, 83–86.

Ghamisi P, Yokoya N, Li J, Liao W, Liu S, Plaza J, Rasti B, Plaza AJ. Advances in hyperspectral image and signal processing: a comprehensive overview of the state of the art. *IEEE Geoscience and Remote Sensing Magazine* **2017**, 5 (4), 37–78. DOI: 10.1109/MGRS.2017.2762087

Greenberger RN, Ehlmann BL, Jewell PW, Birgenheier LP, Green RO. Detection of organic-rich oil shales of the green river formation, Utah, with ground-based imaging spectroscopy. In: *8th Workshop on Hyperspectral Image and Signal Processing: Evolution in Remote Sensing (WHISPERS)*, Los Angeles, US, 21–24 Aug **2016**, 1–5. DOI: 10.1109/WHISPERS.2016.8071807

Gu D, Gillespie A. Topographic Normalization of Landsat TM Images of Forest Based on Subpixel Sun–Canopy–Sensor Geometry. *Remote Sensing of the Environment* **1998**, 64 (2), 166–175. DOI: 10.1016/s0034-4257(97)00177-6

Honkavara E, Hakala T, Saari H, Markelin L, Mäkynen J, Rosnell T. A process for radiometric correction of UAV image blocks. *Photogrammetrie, Fernerkundung, Geoinformation (PFG)* **2012**, 2, 115–127. DOI: 10.1127/1432-8364/2012/0106

Hunt GR. Spectral signatures of particulate minerals in the visible and near infrared. *Geophysics* **1977**, 42, 501–513. DOI: 10.1190/1.1440721

Jensen JR. Remote Sensing of the Environment: An Earth Resource Perspective. 2nd Edition, Pearson Prentice Hall, Upper Saddle River, **2007**.

Kennedy RE, Cohen WB, Takao G. Empirical methods to compensate for a view-angle-dependent brightness gradient in AVIRIS imagery. *Remote Sensing of the Environment* **1997**, 62 (3), 277–291. DOI: 10.1016/s0034-4257(97)00111-9

Kieffer HH. Detection and correction of bad pixels in hyperspectral sensors. In: *Proceedings of SPIE's 1996 International Symposium on Optical Science, Engineering, and Instrumentation*, Denver, US, 6 Nov **1996**, 2821, DOI: 10.1117/12.257162.

Kirchhoff G. Ueber das Verhältniss zwischen dem Emissionsvermögen und dem Absorptionsvermögen der Körper für Wärme and Licht". *Annalen der Physik und Chemie* **1860**, 109 (2), 275–301. DOI: 10.1002/andp.18601850205.

Kurz TH, Buckley SJ, Howell JA. Integration of Panoramic Hyperspectral Imaging with Terrestrial LIDAR Data. *The Photogrammetric Record* **2011**, 26 (134), 212–228. DOI: 10.1111/j.1477-9730.2011.00632.x

Lambert JH. Photometria, sive de Mensura et Gradibus Luminis, Colorum et Umbrae. Augsburg, Germany, **1760**.

Logan LM, Hunt GR, Salisbury JW, Balsamo SR. Compositional implications of Christiansen frequency maximums for infrared remote sensing applications. *Journal of Geophysical Research* **1973**, 78, 4983–5003. DOI: 10.1029/JB078i023p04983

Minnaert M. The reciprocity principle in lunar photometry. *The Astrophysical Journal* **1941**, 37, 978–986. DOI: 10.1086/144279

Nicodemus FE, Richmond JC, Hsia JJ, Ginsberg IW, Limperis T. Geometrical Considerations and Nomenclature for Reflectance. National Bureau of Standards report, Washington D.C., US, **1977**.

Planck M. The Theory of Heat Radiation. Masius M. (transl.) (2nd ed.), Dover Publications, Inc., New York, US, **1914**.

Rhys-Williams AT. An Introduction to Fluorescence Spectroscopy. PerkinElmer, Beaconsfield, UK, **1981**.

Richter R, Schläpfer D. Atmospheric / Topographic Correction for Satellite Imagery. DLR report DLR-IB 565-01/2018, Wessling, Germany, **2018**.

Salisbury JW, Walter LS, Vergo N. Mid-Infrared (2.1–25 mm) Spectra of Minerals: First Edition. *U.S. Geological Survey Open File Report* 87-263, **1987**. DOI: 10.3133/ofr87263

Salisbury JW, Walter LS. Thermal infrared (2.5 to 13.5 µm) spectroscopic remote sensing of igneous rock types on particulate planetary surfaces. *Journal of Geophysical Research* **1989**, 94, 9192–9202. DOI: 10.1029/jb094ib07p09192

Schläpfer D, Popp C, Richter R. Towards Atmospheric Compensation of Low Altitude High Spatial Resolution UAV Based Imagery. In: *9th Workshop on Hyperspectral Images and Signal Processing: Evolution in Remote Sensing (WHISPERS),* 23–26 Sept **2018**, Amsterdam, The Netherlands. DOI: 10.13140/RG.2.2.22919.24485

Schlick C. An inexpensive BRDF model for physically based rendering. *Computer Graphics Forum* **1994**, 13 (3), 233–246. DOI: 10.1111/1467-8659.1330233

Smith GM, Milton EJ. The use of the empirical line method to calibrate remotely sensed data to reflectance. *International Journal of Remote Sensing* **1999**, 20, 2653–2662. DOI: 10.1080/014311699211994

Stokes GG. On the change of refrangibility of light. *Philosophical Transactions of the Royal Society* **1852**, 142, 463–562. DOI: 10.1098/rstl.1852.0022

Sun L, Khan SD, Sarmiento S, Lakshmikantha MR, Zhou H. Ground-based hyperspectral imaging and terrestrial laser scanning for fracture characterization in the Mississippian Boone Formation. *International Journal of Applied Earth Observation and Geoinformation* **2017**, 63, 222–233. DOI: 10.1016/j.jag.2017.08.008

Teillet PM, Guindon B, Goodenough D. On the slope-aspect correction of multispectral scanner data. *Canadian Journal of Remote Sensing* **1982**, 8, 84–106. DOI: 10.1080/07038992.1982.10855028

Transon J, d'Andrimont R, Maugnard A, Defourny P. Survey of Hyperspectral Earth Observation Applications from Space in the Sentinel-2 Context. *Remote Sensing* **2018**, 10, 157. DOI: 10.3390/rs10020157

van der Linden S, Rabe A, Held M, Jakimow B, Leitão PJ, Okujeni A, Schwieder M, Suess S, Hostert P. The EnMAP-Box—A Toolbox and Application Programming Interface for EnMAP Data Processing. *Remote Sensing* **2015**, 7 (9), 11249–11266. DOI: 10.3390/rs70911249

Vermote EF, Tanré D, Deuzé JL, Herman M, Morcrette J-J. Second Simulation of the Satellite Signal in the Solar Spectrum, 6S: An Overview. *IEEE Transactions on Geoscience and Remote Sensing* **1997**, 35 (3), 675–686. DOI: 10.1109/36.581987

Yokoya N, Miyamura N, Iwasaki A. Preprocessing of hyperspectral imagery with consideration of smile and keystone properties. In: Proceedings of SPIE 7857: *Multispectral, Hyperspectral, and Ultraspectral Remote Sensing Technology, Techniques, and Applications III*, 78570B, 13 Nov **2010**, 78570B-9. DOI: 10.1117/12.870437

CHAPTER 2 THE NEED FOR ACCURATE GEOMETRIC AND RADIOMETRIC CORRECTIONS OF DRONE-BORNE HYPERSPECTRAL DATA FOR MINERAL EXPLORATION: MEPHYSTO—A TOOLBOX FOR PRE-PROCESSING DRONE-BORNE HYPERSPECTRAL DATA

Preface

The following chapter presents a new pre-processing toolbox that was developed for the difficult geometric and radiometric correction of hyperspectral drone-borne data. At the time of the study, hyperspectral drone-borne data was nearly exclusively used for environmental studies, precision agriculture, and vegetation mapping. Established preprocessing workflows were not existent, which impeded the analysis of spectrally complex targets such as in geological applications. Particular challenges are platform-induced geometric distortions and topography–induced illumination differences. The presented toolbox overcomes these effects and is shown to provide image data highly accurate in geometry, location, and spectral information. The chapter further demonstrates the advantages and possibilities of derived corrected drone-borne hyperspectral image data for geological applications such as mineral exploration and lithological mapping.
A prior version of the workflow was presented at the *2016 Workshop on Hyperspectral Images and Signal Processing: Evolution in Remote Sensing (WHISPERS)*[1] in Los Angeles, where it won a Best Paper Award. The full paper shown here was published in *Remote Sensing*[2], became the journals' cover story for January 2017 and its most downloaded paper in the year 2017. These achievements reflect both the recently increased popularity of light-weight Unmanned Aerial Systems and applicable hyperspectral sensors as well as the high demand in efficient and accurate solutions to overcome the challenges of drone-borne hyperspectral data.
The tools of the presented workflow were combined in the open-source Python toolbox MEPHySTo (Mineral Exploration Python Hyperspectral Toolbox), which has been continuously extended and improved since its creation. For example, the performance and speed of the used point matching workflows could be increased distinctly by the replacement of the keypoint detection algorithm SIFT (Scale-invariant feature transform) by ORB (Oriented FAST and Rotated Brief[3]). Today the toolbox comprises correction, processing and visualization tools for a wide range of HSI sensor types, platforms and applications.
The tools for drone-borne HSI correction established as in-house pre-processing routine and have been shared with scientists all over the world. A co-authored paper[4] showed the applicability of the corrected data for environmental studies, in this case by monitoring the influence of Acid Mine Drainage over time using drone-based iron mineral mapping.

---

[1] Jakob S, Zimmermann R, Gloaguen R. *8th Workshop on Hyperspectral Images and Signal Processing: Evolution in Remote Sensing (WHISPERS),* 21-24 Aug **2016**, Los Angeles, US.
[2] Jakob S, Zimmermann R, Gloaguen R. *Remote Sensing* ***2017***, 9, 88. DOI: 10.3390/rs9010088
[3] Rublee E, Rabaud V, Konolige K, Bradski G. *IEEE Int Conf Comput Vis* ***2011***, Barcelona, ES, 2564-2571. DOI: 10.1109/iccv.2011.6126544
[4] Jackisch R, Lorenz S, Zimmermann R, Möckel R, Gloaguen R. *Remote Sensing* ***2018***, 10 (3), 385. DOI: 10.3390/rs10030385

The Need for Accurate Geometric and Radiometric Corrections of Drone-Borne Hyperspectral Data for Mineral Exploration: MEPHySTo – A Toolbox for Pre-Processing Drone-Borne Hyperspectral Data[5]

Sandra Jakob, Robert Zimmermann, and Richard Gloaguen

Helmholtz-Zentrum Dresden-Rossendorf, Helmholtz Institute Freiberg for Resource Technology, Division "Exploration Technology", Chemnitzer Str. 40, 09599 Freiberg, Germany;
s.jakob@hzdr.de (S.J.); r.zimmermann@hzdr.de (R.Z.); r.gloaguen@hzdr.de (R.G.)

2.1 Abstract:

Drone-borne hyperspectral imaging is a new and promising technique for fast and precise acquisition, as well as delivery of high-resolution hyperspectral data to a large variety of end-users. Drones can overcome the scale gap between field and air-borne remote sensing, thus providing high-resolution and multi-temporal data. They are easy to use, flexible and deliver data within cm-scale resolution. So far, however, drone-borne imagery has prominently and successfully been almost solely used in precision agriculture and photogrammetry. Drone technology currently mainly relies on structure-from-motion photogrammetry, aerial photography and agricultural monitoring. Recently, a few hyperspectral sensors became available for drones, but complex geometric and radiometric effects complicate their use for geology-related studies. Using two examples, we first show that precise corrections are required for any geological mapping. We then present a processing toolbox for frame-based hyperspectral imaging systems adapted for the complex correction of drone-borne hyperspectral imagery. The toolbox performs sensor- and platform-specific geometric distortion corrections. Furthermore, a topographic correction step is implemented to correct for rough terrain surfaces. We recommend the c-factor-algorithm for geological applications. To our knowledge, we demonstrate for the first time the applicability of the corrected dataset for lithological mapping and mineral exploration.

Keywords: UAS; drone; hyperspectral; exploration; processing; structure-from-motion; point matching; Minas de Riotinto

2.2 Introduction

Hyperspectral sensors have become a key tool for a large range of applications in remote sensing and are now widely used in geology, mineral mapping and exploration (e.g., van der Meer et al. 2012, Laakso et al. 2015, Jakob et al. 2016, Zimmermann et al. 2016). During the last few years, lightweight hyperspectral imaging (HSI) sensors have been increasingly developed for use on unmanned aerial systems (UAS) (i.e., Cubert GmbH or Rikola Ltd.). These drone-borne sensors are able to close the gap between field- and air- or space-borne data and provide small-scale high-resolution hyperspectral imagery (Watts et al. 2012). The acquisition of image data with UAS is fast, easy, targeted, and without the need of extensive time- and cost-consuming planning. It is mostly independent of cloud cover conditions and is even applicable in barely accessible areas. The heavily decreased influence of the atmosphere obviates the need for the often difficult and complex atmospheric correction. Nevertheless, geometric and radiometric correction of drone-borne data is challenging mainly due to small, unpredictable platform shifts and the influence of the micro-topography. Thus, high resolution digital elevation models are required for correction. Common and

---

[5] Published: Jakob, S., Zimmermann, R., Gloaguen, R. *Remote Sensing* **2017**, 9, 88. DOI: 10.3390/rs9010088 (Author's post-print version)

established workflows for the pre-processing of aerial hyperspectral scanner data (e.g., Schläpfer and Richter 2002, Richter and Schläpfer 2002) are not or only partly applicable.

Sensors in the visible and near-infrared spectral range (VNIR) of the electromagnetic spectrum have been preferably used on UAS due to their low weight and size. In contrast, short wave infrared (SWIR) sensors exceed the payload capacity of most lightweight aerial platforms. Larger UAS with higher payload complicate the handling in remote areas and increase the difficulty to obtain flight permission by the local authorities in most countries.

The most prominent material absorption features in the VNIR spectral range originate from green vegetation, while only a few mineral groups, mainly iron oxides and some rare earth elements, show typical absorption features. Those mineralogical features can be quite shallow, and their truthful determination depends mainly on an accurate data correction. By contrast, the occurrence and health analysis of vegetation is easily determinable in the VNIR range even with a low spectral resolution (e.g., Hunt et al. 2010). This is a main reason why the development in drone-borne HSI has been mainly applied in and for agricultural and environmental monitoring (Aasen et al. 2015, Honkavaara et al. 2012, Laliberte et al. 2011, Lelong et al. 2008). Thus, the easy, fast, and reliable acquisition and in-time interpretation of drone-borne data increased the accuracy and abilities of precision agriculture. Numerous publications describe the assessment and processing of multispectral and hyperspectral drone-borne data in modern agriculture. They focus mainly on sensor calibration, photogrammetry, and illumination correction between single mosaic images (Aasen et al. 2015, Honkavaara et al. 2012, Johnson et al. 2003, Berni et al. 2009, Turner et al. 2012, Honkavaara et al. 2013). Georeferencing is commonly performed using ground control points (GCPs). However, Laliberte et al. (2011) presented a promising approach for an automated batch processing chain for multispectral drone-borne data including band alignment, orthorectification, and simple radiometric correction for the mapping of rangeland environments. Topographic correction, which is essential for geological targets, is not applied for the mostly flat, uniform, and smooth agricultural areas. An additional correction to reflectance and a high signal to noise ratio (SNR) are not necessary for most applications in precision agriculture and environmental research, as the commonly-used vegetation indexes can be determined even with low spectral resolution or high noise. Thus, correction algorithms used for vegetation monitoring are not applicable for geological targets. The great diversity of targets in terms of terrain, size, and spectral signatures demands a finer spectral resolution, a precise topographic correction and a higher SNR. As most of the minerals show no or weak absorption features in VNIR range, even subtle spectral differences can be important for interpretation and raise the need for a careful data processing.

The application of drone-borne data for geological issues therefore is extremely rare and mainly limited to UAS-based photogrammetry and 3D photogrammetry using RGB-sensors for structural geology (e.g., Micklethwaite et al. 2012, Westoby et al. 2012, Bemis et al. 2014) or landslide mapping (e.g., Niethammer et al. 2012). Beside RGB sensors, drone-borne thermal cameras have been used in a first attempt to observe the temperature of mud volcanoes (Amici et al. 2013). In 2014, Wu et al. presented a VNIR and SWIR drone-borne sensor for mineral mapping, but did not provide any drone-borne geological application yet. Until now, no published work known to us exists where hyperspectral drone-borne sensors have been successfully and provably used for geological applications.

In the following, we present an image pre-processing chain fitted for the challenging geometric and radiometric correction of drone-borne HSI data. It also contains automatic mosaicking and georeferencing algorithms enabling a fast and easy surveying of inaccessible areas, where the acquisition of GCPs would be impossible or time consuming. We further demonstrate the applicability of the resulting high resolution hyperspectral orthomosaics on real geological issues. This includes differentiation of spectral end-members

relating to different lithologies and the determination of the relative abundance of a certain mineralogical absorption feature.

2.3 Test Site

We first present a drone-borne example dataset originating from parts of the mining area of Minas de Riotinto in southern Spain (**Figure 2-1a**). This region hosts one of the giant massive sulfide deposits of the Iberian Pyrite Belt and has been extensively mined for copper and lower amounts of manganese, iron, and gold since the Bronze Age. The test site covers one of the gossanous ridges overlying a massive sulfide lens next to Riotinto River.

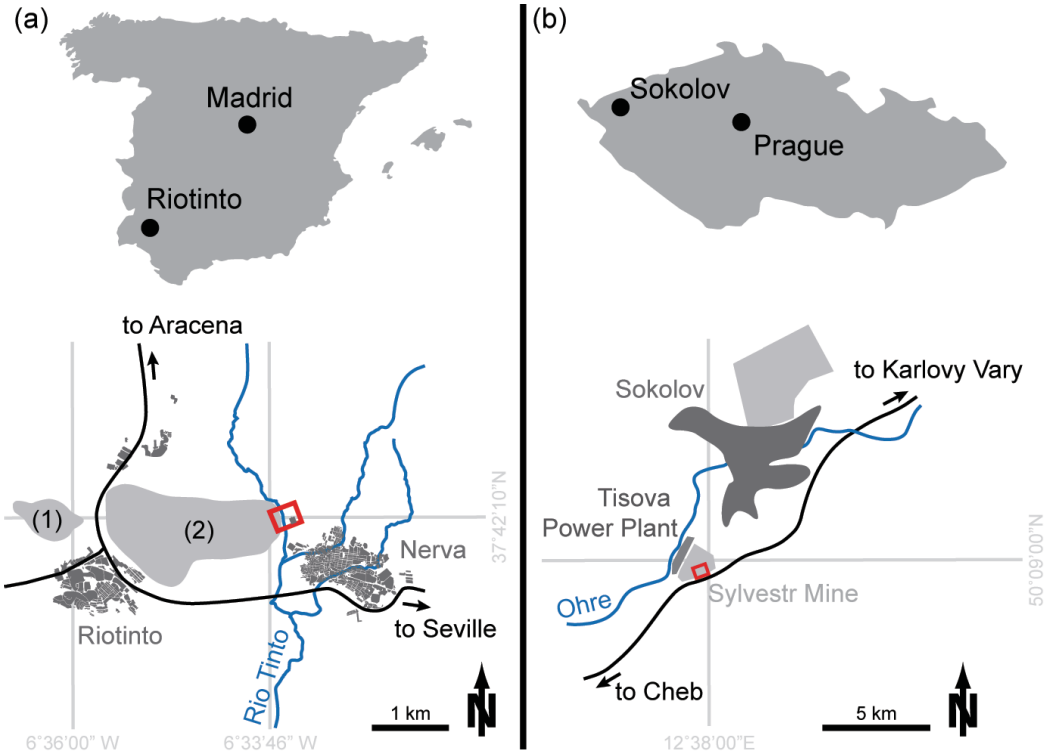

Figure 2-1. (a) Location of the first test site within Spain and the Riotinto mining area, with the open pit mines Corta Atalaya (1) and Cerro Colorado (2); **(b)** location of the second test site within the Czech Republic and the Sokolov area.

Within the test site, different iron-bearing facies occur, such as the gossan itself, massive sulfide, altered shale, and river sediments under the influence of acidic mine drainage (AMD) (Riaza et al. 2012).

The Iberian pyrite belt is hosted in a north-vergent fold and thrust belt of late Variscan age (Soriano and Casas 2002, Donaire et al. 2008) extending from east of Setubal/Portugal to north of Seville/Spain. A typical succession starts with a series of phyllites/quartzites, followed by slates, basalt sills, felsic volcanics (rhyolites and dacites) and Culm series (greywackes and slates) (Donaire et al. 2008). The stratabound, volcanogenic massive sulfide (VMS) lenses are hosted in felsic volcanics of Upper Devonian to Lower Carboniferous ages (Soriano and Casas 2002). Zones of chloritic and argillitic alteration (Saez and Donaire 2008) are associated with those lenses. Stockwork zones occur underneath the lenses in the vicinity of faults (Saez and Donaire 2008). A gossan usually forms in the cap-rock above. The deposit of Riotinto itself is located in a hinge of an E-W trending fold with the fold axis plunging towards E. The studied area of the gossan close to Nerva cemetery expresses the easternmost surface outcrop of the mineralized core zone. There, the highly folded, partly altered lower Culm series rock (slates) is overlain by gossan. Within the

Culm, a lens of pyrite-rich massive sulfide with associated argillitic alteration is exposed. Our primary geological target is to differentiate several geological endmembers that cannot be distinguished on an RGB orthophoto and to compare the image spectra to validation spectra measured in situ. We attempt to demonstrate that specific variations in the spectral information acquired by the HSI devices on UAS can be used to distinguish specific mineralogical associations. The proposed test site at Riotinto features a medium relief and was surveyed under nearly ideal illumination conditions.

We provide results from a second test site, the abandoned lignite mine of Sylvestr, which is located in the Eger Graben of the Czech Republic near the city of Sokolov (**Figure 2-1b**). It features a complex and steep relief to test the data processing algorithms under more extreme conditions. The area is surveyed under suboptimal illumination conditions, such as a low Sun-horizon angle. Within the mine, tertiary sediments of the Eger Graben and layers of lignite and petrified wood are exposed. The main lithostratigraphic units occurring in Sylvestr are the Nové Sedlo Formation and the Habartov member of the Sokolov Formation, both characterized by volcanic rocks and lignite-bearing sediments, comprising mainly tuffs, sands, and silty clays (Rojik 2004). Similar to surrounding active and closed mine and dump sites, the study area is largely affected by AMD, indicated by low to intermediate pH values and the presence of pyrite, lignite, jarosite, and goethite. This originates mainly in the presence of sulfur within the abundant lignite layers, as well as in hydrothermal deposits along the fault system bordering the basin (Kopackova 2014). After the stop of the mining activities, the pit was left open, and stream erosion incised deep canyon-like channels into the occurring sediments. This topographic variety combined with a sparse vegetation cover proposed Sylvester mine as the ideal test site for the topographic correction of drone-borne HSl data.

2.4 Data Acquisition

2.4.1 Aerial Platforms

The areas were studied by means of HSI techniques and structure-from-motion (SfM) photogrammetry. Each method requires specific preconditions for the aerial platform. While the frame-based HSI requires a stable platform at the time of image acquisition to allow a sufficient integration time, SfM requires a rapid platform in order to acquire numerous RGB pictures having sufficient overlap to compute a digital surface model (DSM).

In general, two types of aerial platforms or UAS are available: (1) fixed-wing systems with the advantage of long flight endurance and fast cruising speeds. So, large areas can be captured within one flight, but their disadvantage is a limited payload capacity. The greater the payload, the bigger is the wingspan. In this context, especially take-off and landing become thrilling with expensive and/or sensitive equipment on-board. Furthermore, a fast shutter speed is needed to get high quality image data. (2) Multi-copters have the disadvantage of limited range and flight time; however, they can carry heavier payloads. Due to their hovering capacities, they are more stable at the point of image acquisition, and also, landing is more controlled (especially important with expensive or sensitive payloads).

Based on the above listed arguments, two different platforms had been applied: (1) a sensefly ebee fixed-wing system with a Canon Powershot S110 RGB camera and maximum flight time of 50 min; (2) an Aibotix Aibot X6v2 hexacopter either equipped with a Rikola Hyperspectral Imager or a Nikon Coolpix A RGB camera. The Aibot has a maximum flight endurance of 15 min and a maximum payload of 2 kg.

Separate pre-defined flight plans were applied for each UAS to meet the requirements in terms of ground resolution, image acquisition time, and image overlap. Both systems store their flight logs internally (flight path and points of image acquisition), so a geo-location of the image data is possible afterwards.

2.4.2 Sensors

A frame-based hyperspectral camera (Rikola Hyperspectral Imager Rikola Ltd.) was used for data acquisition. Its low weight of just 720 g makes it perfectly suited for drone-borne surveys. The sensor provides snapshot images covering the VIS-NIR spectral range between 504 and 900 nm. In autonomous mode, up to 50 bands with a spectral resolution of >10 nm and spectral sampling of 1 nm can be acquired within one flight. The maximum image dimensions account for 1024x1011 px. However, the spatial resolution for flight images is 1011x648 px to enable the maximum number of spectral bands. The raw data are stored on a Compact Flash card in autonomous mode and later converted to radiance using the Rikola Hyperspectral Imager software provided by the manufacturer (Rikola Ltd. 2016).

SfM photogrammetry was flown with either a Canon Powershot S110 digital camera having a resolution of 12 MP (Megapixel, Spain) or a Nikon Coolpix A with 16-MP resolution (Czech Republic). They provide standard red, green, and blue band data that can be complemented by visual real color renderings. A correction for lens distortion was applied within the SfM process.

2.4.3 Flight-Site Setup

Local setup of the base station and final flight plan is always adjusted on-site due to local and meteorological conditions. Ensuring the maximum safety of the operation and a visual line of sight to the aerial system is the highest premise. The flight parameters of the presented study areas are listed in **Table 2-1**.

A total of six parallel flight lines were planned for photogrammetry in Test Site 1. Line spacing was set to have high overlap of the aerial photographs (85% horizontal and 70% vertical). The hyperspectral survey was performed as a single line profile perpendicular to the gossanous ridge.

Table 2-1. Flight setup for the surveys performed at Riotinto area / Spain (ES) and Sylvestr mine / Czech Republic (CZ). Flight altitude is given in meters above take-off location. Furthermore, note that the ground sampling distance is given for the respective flight altitude, but is varying due to topography.

		Hyperspectral Imaging	**Photogrammetry**
Riotinto / ES	UAS system	Aibotix Aibot X6v2	sensefly ebee
	Camera system	Rikola Hyperspectral Imager	Canon Powershot S110 RGB
	Flight altitude (above take-off)	50 m	118 m
	Ground sampling distance	3.25 cm/px	3.29 cm/px
	Flight time	3:42 min	6:50 min
	Number of pictures	10	50
	Area covered	0.3 ha	14.4 ha
Sylvestr / CZ	UAS system	Aibotix Aibot X6v2	Aibotix Aibot X6v2
	Camera system	Rikola Hyperspectral Imager	Nikon Coolpix A
	Flight altitude (above take-off)	50 m	60 m
	Ground sampling distance	3.25 cm/px	2.07 cm/px
	Flight time	8:20 min	10:58 min
	Number of pictures	20	190
	Area covered	0.7 ha	9.0 ha

Camera positions were set to have about 40% horizontal overlap. In total, 10 hyperspectral scenes were acquired. Three flexible PVC panels colored black, grey, and white with known spectra were put down underneath the flight line. These panels are used for calibration purposes in the later processing.

In Test Site 2, the photogrammetric survey was performed in seven parallel flight lines parallel to the direction of the main gully. Line spacing was set to 80% horizontal and 60% vertical overlap at a flight

altitude of 60 m. The hyperspectral survey was performed along a single line and follows the channel. The setup of hyperspectral data acquisition is similar to Test Site 1.

2.5 SfM Photogrammetry

The digital surface model was computed by using a standard structure-from-motion (SfM) algorithm implemented in the available commercial software Agisoft Photoscan. SfM (Turner et al. 2012, Westoby et al. 2012, Eltner et al. 2016) is a low-cost, user-friendly photogrammetric technique solving the equations for camera parameters and scene geometry using a highly redundant bundle adjustment. The SfM approach was pushed in the 1990s by the upcoming computer vision and the development of automatic feature-extraction and matching algorithms. A typical SfM workflow towards a final surface model consists of five steps (Westoby et al. 2012, Eltner et al. 2016, Snavely et al. 2006): (1) detection of characteristic image points (e.g., using SIFT) followed by automatic point matching using a homologous transformation (e.g., using Random Sample Consensus, RANSAC); (2) reconstruction of the image acquisition geometry and referencing of the intrinsic coordinate system to available reference points (either GPS or known camera locations) using a iterative bundle adjustment; (3) a dense point matching of the sparse cloud from image network geometry; (4) meshing of the dense point cloud; a digital surface model (DSM) can be obtained from this or the previous step; (5) calculating the textures from the images to compute the rectified orthomosaic.

2.6 Correction Steps for Drone-Based HSI

Drone-borne HSI data need a different and more complicated pre-processing chain as air- or space-borne HSI data due to the low acquisition height, difficult calculation and inconstant movement of the platform and, more importantly, the high influence of the micro-relief on illumination and viewing angle. Existing software for processing drone-borne data is often not applicable for hyperspectral images or does not address corrections needed for geological application. Many approaches are related to the use of RGB-images only and are not able to handle the size and especially the data format of hyperspectral imagery. Published approaches for the correction of drone-borne multi- or hyperspectral data are mainly limited to agricultural or environmental applications, assuming a flat topography. However, for geological application, surface geometry is a prominent and crucial factor to consider. Illumination angle changes caused by micro- and macro-relief can distort the spectral appearance of rocks and soils distinctly. This can lead to problematic misinterpretations, as the discrimination of rock or mineral phases is mainly based on subtle changes in the reflectance spectrum. Another important factor concerns the geolocation and orthorectification of the single images. Most available software assumes the use of an IMU, which records the exact position and orientation of the sensor during the acquisition for later correction. Unfortunately, the use of an IMU exceeds the payload of most light-weight UAS and is therefore not feasible. Another possibility is the manual georeferencing using GCPs, which, however, can be very time-consuming for larger UAS surveys. We therefore suggest to automate the geolocation and orthorectification process without the use of an IMU or GCPs. To meet the mentioned challenges, we combined new and known methods in a Python toolbox in a way to process drone-borne HSI data accurately, automatically and as lossless as possible. The processing steps are illustrated in **Figure 2-2** and are more precisely elaborated afterwards.

2.6.1 Dark Current Subtraction and Conversion to Radiance

A dark calibration is needed to determine the dark current (DC) of the camera's sensor. DC equals the noise the camera sensor adds to the signal when translating incoming radiation to digital numbers (DN). If the camera is triggered under completely light-free conditions, this noise becomes visible within the resulting

image and can be subtracted from the acquired raw image DN. As the shutter of the camera cannot be closed manually, we use a completely light-blocking plastic foil that is normally used for the transport of OSL (optically-stimulated luminescence) dating samples to prevent incidence light during the DC recording. The image DC subtraction is done with the Hyperspectral Imager software provided by Rikola Ltd. This software is also used to calibrate the image data for vignetting, as well as some camera specific values and to convert the raw DN to radiance.

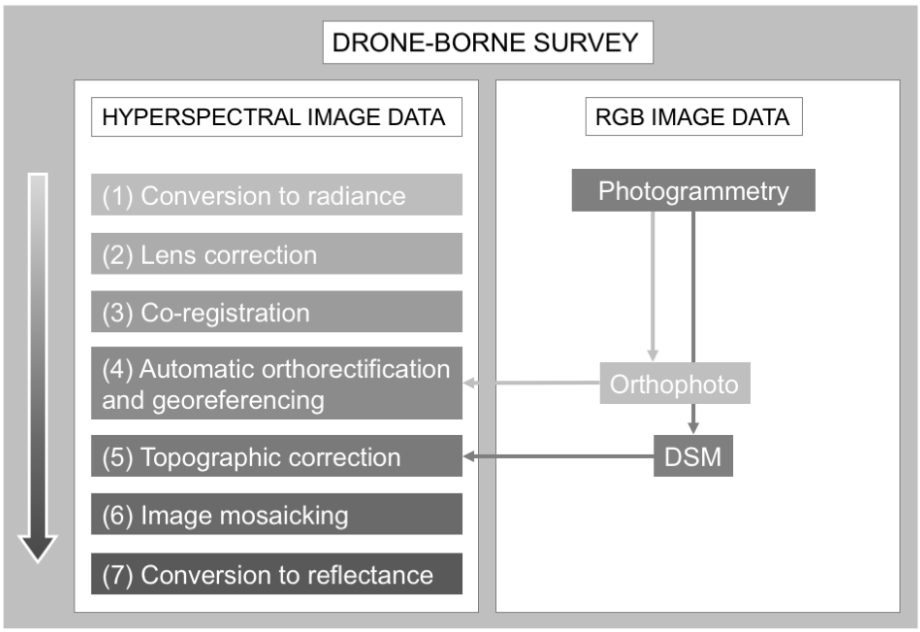

Figure 2-2. Flowchart of the processing steps.

2.6.2 Camera Distortion

Distortions caused by internal camera features relate mainly to radial and tangential distortions. Radial distortions are related to the shape of the lens and mostly become visible as a “barrel” or “fish-eye” effect. Tangential distortions can be caused by a non-parallel assembly of the lens in regard to the image plane. The lens distortion parameters of the Rikola hyperspectral camera were determined using Agisoft Lens, which uses a checkerboard pattern that is projected on a flat screen or printed out. The parameters are listed in **Table 2-2**. At least ten images need to be acquired from different angles and orientations. Using these images, the internal camera parameters, as well as the distortion coefficients can be calculated. The internal parameters can be expressed by the characteristic camera matrix, which includes focal length (fx and fy), skew, and center coordinates (cx and cy).

Table 2-2. Internal camera parameters and distortion coefficients of the Rikola hyperspectral camera for full and half image resolution.

Resolution	fx	fy	cx	cy	skew	k1	k2	k3	p1	p2
1011x1024	1587.36	1586.50	532.14	552.88	−0.3774	−0.3402	0.1560	0.0513	0.0003	0.0002
1011x648	1580.98	1580.41	537.10	369.76	−0.0535	−0.3141	−0.2665	2.4100	0.0003	0.0003

The distortion coefficient matrix comprises the radial distortion coefficients *k1*, *k2*, *k3* and the tangential distortion coefficients *p1* and *p2*. The Rikola Hyperspectral Imager shows a strong radial distortion, but a nearly negligible tangential distortion. The determined parameters are used to correct the lens distortion

using the OpenCV undistort function. Hereby, camera matrix and distortion coefficients are used to calculate the relation between the original and distorted camera pixel position. The resulting destination map is used in an inverse mapping algorithm to undistort the raw image (Bradski 2000).

2.6.3 Co-Registration

Single spectral bands of one image are acquired with a small temporal difference. Depending on the speed, movement, and vibrations of the aerial platform, this results in a spatial shift between the single bands of the HSI data cube. The correction of this mismatch is performed using an image-matching algorithm. We use the SIFT algorithm (Lowe 1999) for the detection of similar features within the several bands followed by the FLANN algorithm (Fast Library for Approximate Nearest Neighbors, Muja and Lowe 2009) for matching the detected points. The SIFT algorithm of Lowe (1999) aims to detect local feature vectors within an image, each invariant to image translation, rotation, and scaling and partially invariant to affine or 3D projection and illumination changes. The identification is conducted by a staged filtering approach, including extrema detection, keypoint localization, orientation assignment, and keypoint descriptor extraction. Due to its robustness to difficult geometric and radiometric conditions, SIFT is a popular tool, e.g., for image registration in photogrammetry, panorama stitching, and motion tracking (Lowe 1999). The FLANN matching algorithm library was presented by Muja and Lowe (2009). It contains a range of fast nearest neighbor matching algorithms for high dimensional features and large datasets and provides a routine, which automatically chooses the best method and parameters according to the input dataset.
From the point pairs detected with SIFT and FLANN, an affine transformation matrix, which considers translation, rotation, shift, and shear, is calculated and used to correct the mismatch between the single image bands with high precision. Additionally, a subsequent automatic cutting was implemented in order to remove the residual image borders, which originate from the relocation of single bands by the co-registration process.

2.6.4 Automatic Orthorectification and Georeferencing to the Orthophoto

Similar to the previous step, automatic orthorectification and georeferencing are based on point matching. The SIFT and FLANN algorithms are used to extract matching points between the dataset and a high resolution orthophoto created beforehand using SfM photogrammetry. The quality of the orthophoto regarding spatial resolution and location accuracy is hereby a crucial point to guarantee a successful matching. The matched points are now used to warp and orthorectify the original dataset to the right position. Depending on the level of distortion in the dataset, a polynomial or locally-adaptive transformation can be applied. Hereby, no additional information, such as rational polynomial coefficients or GCPs, is needed.

2.6.5 Topographic Correction

Topography can have a high influence on the local illumination within an image. The radiance of the same material varies if it is located on a slope oriented towards or away from the sunlight incidence. Thus, it is essential to correct for these effects to retrieve reliable data. We implemented and tested the most common topographic correction methods to aim for an optimal correction result. The methods comprise Lambertian, as well as non-Lambertian methods. For all methods, a digital surface model (DSM) is required, as well as the solar zenith and azimuth angle present at the acquisition time.
These parameters are needed to model the illumination, IL, conditions by:

$$\mathrm{IL} = \cos(\mathrm{i}) = \cos(\mathrm{s}) \cdot \cos(\mathrm{SZ}) + \sin(\mathrm{s}) \cdot \sin(\mathrm{SZ}) \cdot \cos(\mathrm{AZ} - \mathrm{o}) \tag{2-1}$$

with incidence angle *i*, terrain slope angle *s*, solar zenith angle *SZ*, solar azimuth angle *AZ* and terrain aspect angle *o*.

The calculated *IL* model is the basis for all implemented topographic correction methods. The cosine method is the most common Lambertian approach, which assumes that lower *IL* is related to higher corrected reflectance and regards the Sun zenith angle. It was introduced by Teillet et al. (1982) and is calculated as:

$$R_\mathrm{c} = R_\mathrm{o} \cdot \frac{\cos(\mathrm{SZ})}{\mathrm{IL}} \tag{2-2}$$

with R_c being corrected reflectance and R_o being original reflectance before topographic correction. As this approach has been seen to over-correct the image in areas with very low *IL*, Civco (1989) introduced the improved cosine method also considering average *IL* conditions with:

$$R_\mathrm{c} = R_\mathrm{o} \cdot \frac{R_\mathrm{o} \cdot (\mathrm{IL}_\mathrm{mean} - \mathrm{IL})}{\mathrm{IL}_\mathrm{mean}} \tag{2-3}$$

with IL_{mean} being the mean *IL* value of the whole study area. Another attempt to reduce the over-correction is the gamma method (Richter et al. 2009), which adds parameters for sensor view angle *v* on flat and inclined terrain with:

$$R_\mathrm{c} = R_\mathrm{o} \cdot \frac{\cos(\mathrm{SZ}) + \cos(v)}{\mathrm{IL} + \cos(90 - (v + s)} \tag{2-4}$$

The percent-method is a simple approach for topographic correction proposed in Tizado (2011). The amount of correction is calculated according to the percent of solar incidence on the Earth's surface, varying between no correction for direct Sun exhibition to infinite correction for a location in opposition to the solar incidence. Thus, the corrected reflectance is calculated by:

$$R_\mathrm{c} = \frac{R_\mathrm{o} \cdot 2}{\cos_i + 1} \tag{2-5}$$

The non-Lambertian Minnaert method is based on Minnaert (1941) and calculated by:

$$R_\mathrm{c} = R_\mathrm{o} \cdot \left(\frac{\cos(\mathrm{SZ})}{IL}\right)^k \tag{2-6}$$

where the Minnaert constant *k* is obtained by linear regression of $\ln(\mathrm{R}_o) = \ln(\mathrm{R}_c) - \mathrm{k} \cdot \ln(\mathrm{IL}/\cos(\mathrm{SZ}))$ for each wavelength band. The method was later supplemented for the inclusion of slope by Colby (1991) with:

$$R_\mathrm{c} = R_\mathrm{o} \cdot \cos(\mathrm{s}) \cdot \left(\frac{\cos(\mathrm{SZ})}{\mathrm{IL} \cdot \cos(\mathrm{s})}\right)^k \tag{2-7}$$

An empirical-statistical approach named c -factor was published by Teillet et al. (1982). It is determined by:

$$R_\mathrm{c} = R_\mathrm{o} \cdot \frac{\cos(SZ) + \mathrm{c}}{\mathrm{IL} + \mathrm{c}} \tag{2-8}$$

where *c* is *a/m* from the linear regression of $\mathrm{R_o} = \mathrm{a} + \mathrm{m} \cdot \mathrm{IL}$.

2.6.6 Mosaicking

The georeferenced and topographically-corrected images can now be easily combined into a hyperspectral image mosaic without further transformation. Alternatively, we also provide a tool for the automatic stitching of un-georeferenced images. The overlapping images of a survey are automatically mosaicked without the need of ground control points or any image position information. Again, we use an image matching algorithm based on SIFT and FLANN. This time, a homographic transformation matrix is calculated. In addition to the affine parameters, it also considers perspective distortions. Optional illumination correction between the several images can be applied. It uses matching points within the overlap of the images to calculate a regression function, which is afterwards applied to correct brightness differences caused by slightly changing illumination conditions during the acquisition of different images.

2.6.7 Radiometric Correction

After all geometric and illumination corrections are performed, the hyperspectral radiance image can be converted to reflectance. The influence of the atmosphere is nearly negligible due to the low acquisition altitude. Thus, no common atmospheric correction needs to be applied, as is done for space- or air-borne data. Instead, the empirical line method is recommended. It is a more direct approach using spectrally well-characterized ground reference targets. For that, we use 50x50 cm PVC panels in black, grey, and white. They feature relatively consistent and flat reflectance spectra in the VNIR spectral range, which were determined using a Spectral Evolution Portable Spectroradiometer PSR-3500 portable field spectrometer. Other targets, such as characteristic materials within the observed area, can be added by field spectrometer sampling as long as they can be individually resolved in the hyperspectral image. Within the empirical line correction, the reference spectra are compared to extracted image spectra of ground targets to estimate the correction factors for each band. The hyperspectral mosaic is converted to surface reflectance by applying those correction factors. After the conversion to reflectance, an optional spectral smoothing can be applied to remove remaining noise; for this, the Savitzky–Golay filter is recommended (Savitzky and Golay 1964).

2.7 Results

The toolbox presented above is able to perform a fast and reliable correction of the raw data. Every correction step is necessary and improves the dataset towards a useable solution. A reliable hypercube of a single image or a seamless mosaic is the result. Camera distortions were successfully eliminated using a simple lens correction algorithm. The result compared to the distorted image is shown in **Figure 2-3** with red lines added for better visibility. While a significant barrel distortion is obvious in the uncorrected image, it is completely removed after correction.

The lens corrected image is co-registered to remove the influence of platform shift afterwards. Co-registration is able to correct even high shifts with great accuracy even for bands within different wavelength ranges (**Figure 2-4a** and **b**). The subsequent residual edge cutting (**Figure 2-4c**) worked well and prepared the single images for subsequent seamless mosaicking. The preprocessed images were georeferenced and orthorectified before mosaicking. The automatic processing happens with high accuracy despite the differing imaging distances caused by overflying the gossanous ridge. For very low topography, a polynomial transformation is reasonable, for more difficult terrain, a finer adaption to the topography is achieved using a locally-adaptive linear interpolation grid. The automatic georeferencing tool worked well for the orthorectification of single images using polynomial, as well as locally-adaptive transformation.

However, the registration of images with the adaptive transformation method shows a distinctly increased fit accuracy compared to the polynomial fitting at the cost of a higher processing time.

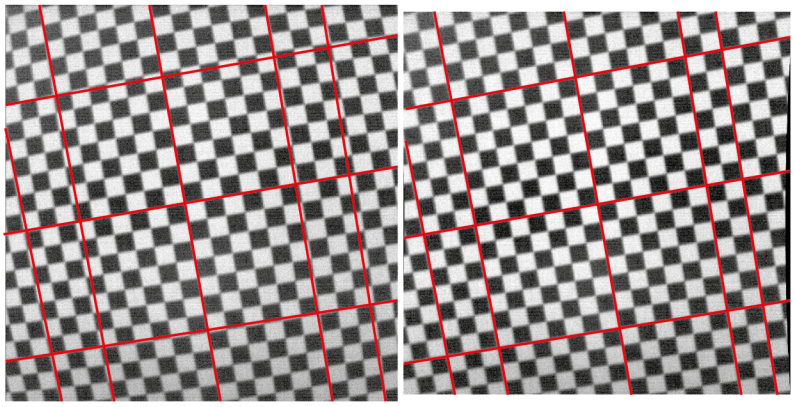

Figure 2-3. Rikola image of checkerboard pattern before (**left**) and after (**right**) lens distortion correction (Section 2.5.2). Red lines added for clarity.

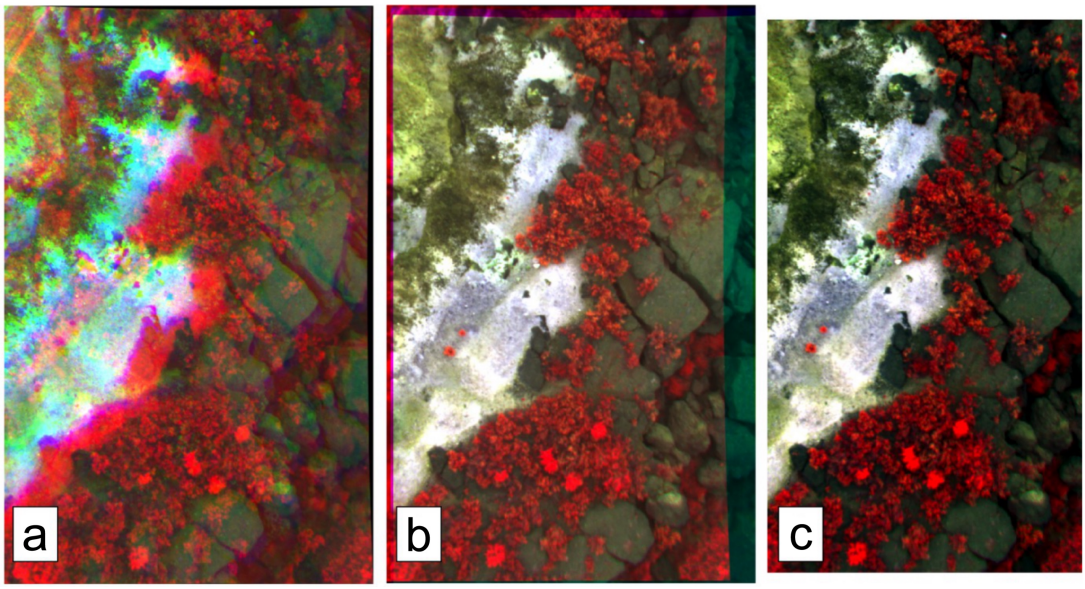

Figure 2-4. Rikola image before (**a**) and after (**b**) band co-registration and after subsequent residual edge cutting (**c**). Displayed bands are: red: Band 42 (832 nm); green: Band 23 (680 nm); blue: Band 1 (504 nm).

Rough terrain surfaces require an appropriate correction for the surface irregular geometry. Thus, all algorithms presented in Section 2.6.5 were tested on the georeferenced images. As the illumination conditions at the Spanish test site were very good with a high Sun angle of 54°, the correction effect is low, and all methods show only slightly different results. Therefore, c-factor, Minnaert, and Minnaert with slope are giving the smoothest results, while cosine tends to over-correct values at edges. The improved cosine shows this effect to a much lower extent, while the percent only has a very low to no correction effect at all. To compare the performance of the distinct algorithms under sub-optimal conditions, they were additionally tested on a drone-borne hyperspectral image with extreme illumination differences. In addition to high relief, the images were acquired in the late afternoon, resulting in a Sun horizon angle of 23°. The resulting corrected image for each tested method at Sylvestr mine is displayed in **Figure 2-5**. The gamma and percent algorithms show only a negligible correction effect. The methods cosine, Minnaert, and Minnaert with slope deliver very good results for illuminated parts of the image. However, they fail to correct for the shadowed

steep cliffs. Moreover, in the case of the latter two, the algorithms are not able to handle incidence angles over 90 degrees. The improved cosine and c-factor are the only algorithms to correct for the shadowed parts in the image. Nevertheless, improved cosine struggles with immense artifacts especially in the highly illuminated parts, where the incidence angle is around 90 degrees. The only method to correct for both highly illuminated, as well as highly shadowed parts in the image is the c-factor algorithm. Thus, it was therefore used to correct the test site mosaic.

After the successful completion of the previous correction steps, the images can be easily merged to a mosaic. If necessary, a feathering can be applied for a smoother image overlap. The additionally implemented automatic mosaicking algorithm can be used for the stitching of un-georeferenced images without the need for further orientation or geolocation information. It returned precisely-merged mosaics and was able to stitch even images with high topographic influences. Still, the accuracy lies behind the stitching of already orthorectified images.

After mosaicking, the image spectra are converted to reflectance. Within most surveys, the white calibration panel was neglected due to over-saturation. However, the empirical line calibration using only the black and the grey calibration panel delivers excellent results, as the image spectra show a very high resemblance to the validation field spectra (see **Figure 2-6**) regarding both shape and intensity. For a subsequent spectral smoothing, we applied a Savitzky–Golay filter with a window size of five and a polynomial degree of two.

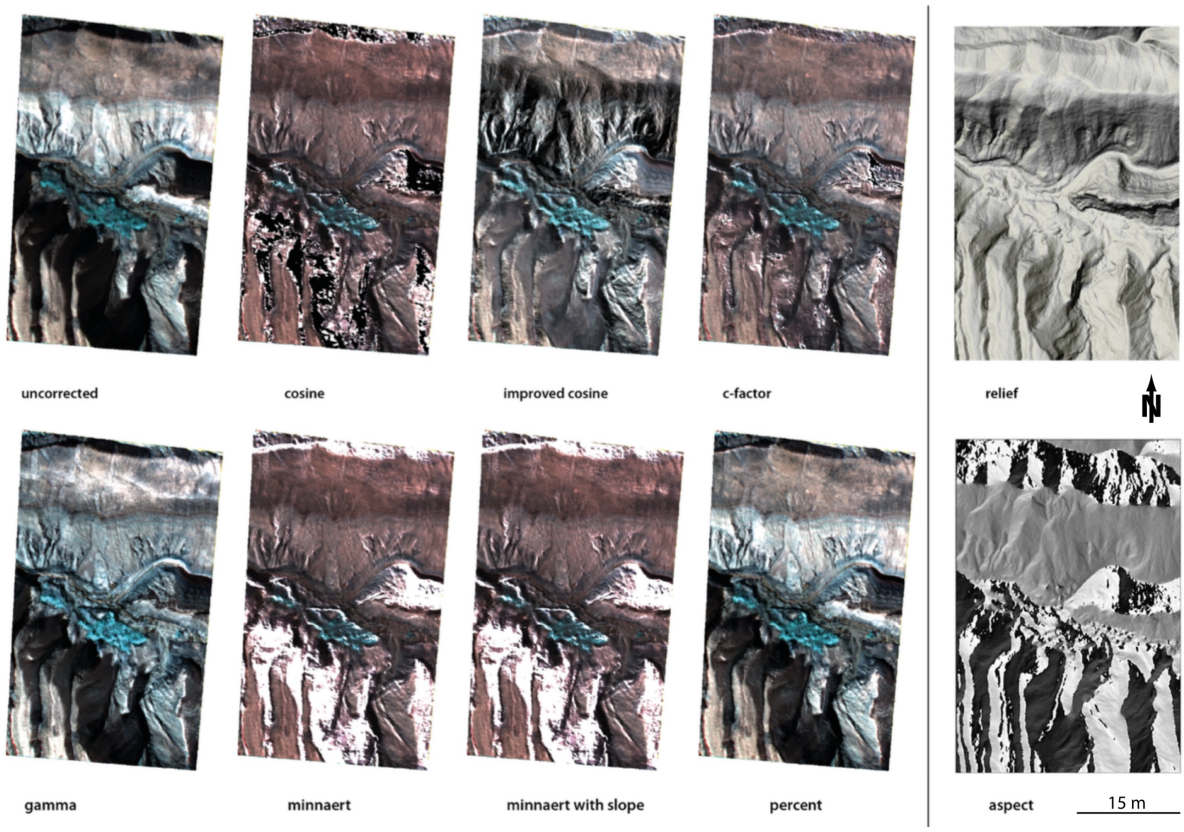

Figure 2-5. Comparison of topographic correction algorithms for drone-borne data under extreme illumination conditions (Sylvester mine test site, solar elevation angle: 23°).

Vegetation can be easily distinguished in the spectral data by the so-called red edge around 700 nm. Therefore, it can be easily masked out using the Normalized Difference Vegetation Index (NDVI). In contrast, the main lithological components of the test site show only very low differences and nearly no highly distinctive absorption features in the VNIR spectral range. This accounts both for the field validation spectra,

as well as the image spectra. Nevertheless, small differences in intensity, convexity, and slope of the spectral curve are present. They can be used to distinguish several lithological endmembers. Therefore, gossan, nearby occurring massive sulfide and altered shale, as well as artificial concrete structures and river sediments can be clearly distinguished from each other (see **Figure 2-6**) using the principal components of the hyperspectral image. This differentiation is impossible from the RGB orthophoto.

2.8 Discussion

The presented processing chain for drone-borne HSI data works robustly and is able to correct raw data to reflectance with the least loss of spectral information. Lens correction, band registration, and residual edge cutting are eligible to remove distortions caused by both the camera system and movement of the aerial platform.

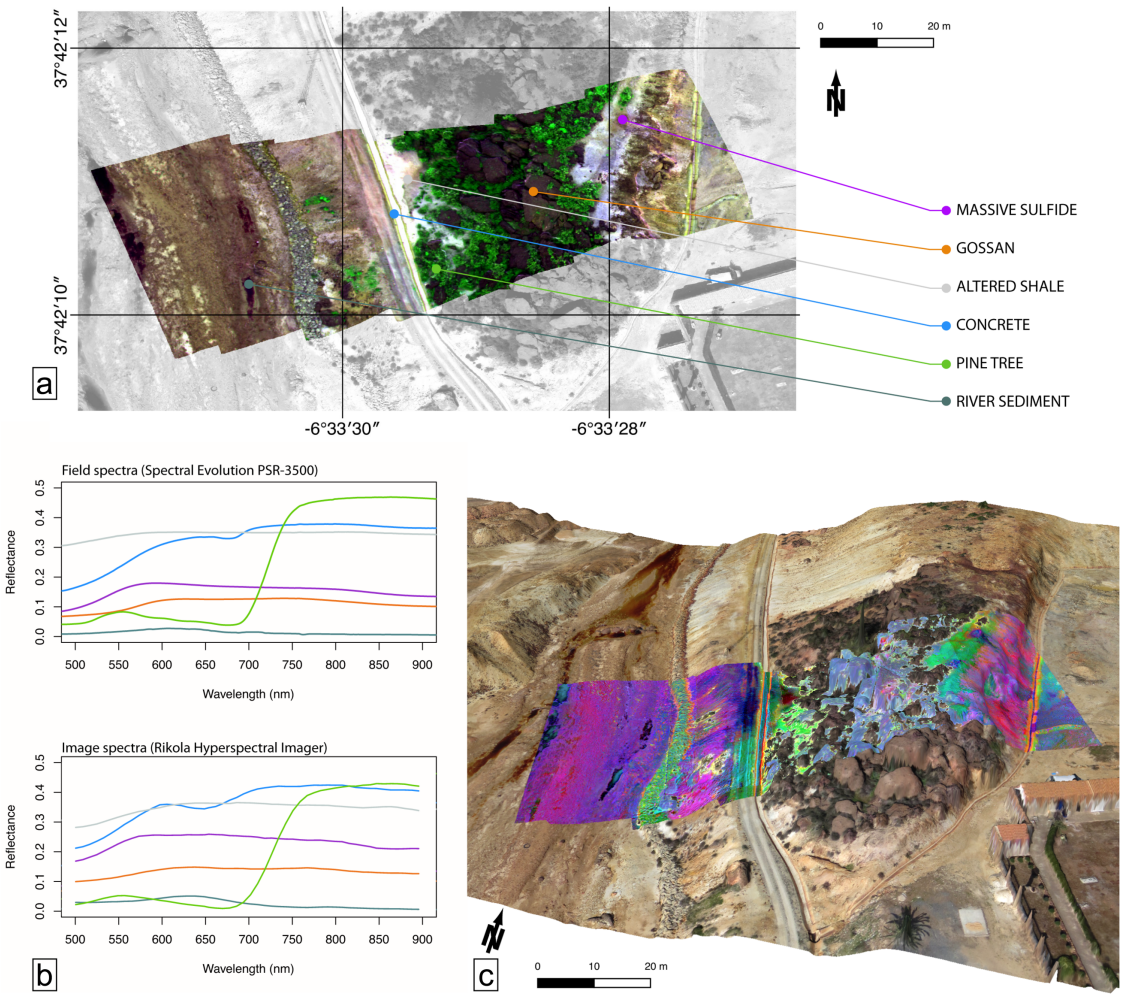

Figure 2-6. (a) Corrected and geolocated hyperspectral mosaic with the location of spectral validation sampling points. Displayed bands are: red: Band 19 (651 nm); green: Band 45 (856 nm); blue: Band 7 (552 nm). **(b)** Comparison of field and image spectra taken from the points of interest displayed in (a). **(c)** Vegetation masked Principal Components 2, 3, and 5, draped on a 3D orthophoto model of the test site (view from south-southeast).

Automatic georeferencing, orthorectification, and mosaicking are time saving compared to the manual approach or using GCPs. The implemented algorithms work reliable even for complex geometries and with

high accuracy. Slightly distorted data, such as images over a low-relief landscape, can be treated quickly using homographic or polynomial transformations. Even data with high local distortions caused by the underlying topography, typical for drone-borne geological imagery, can be processed. A subsequent topographic correction is highly recommended for sites with high relief or sub-optimal illumination conditions during data acquisition. The best results were derived from c-factor, Minnaert, and Minnaert with slope. However, only c-factor can be applied to images with highly shadowed parts and is therefore recommended for the topographic correction of drone-borne HSI data.

Figure 2-7 shows the progress of data pre-processing at two exemplary pixel spectra. The correction of the lens parameters and the band registration achieve a distinct improvement of the spectral shape, which is mainly explainable by the now aligned corresponding pixel values along the spectral dimension axis. Orthorectification and topographic correction do not influence the shape of the spectral curve. While orthorectification only influences the spatial pixel positioning, topographic correction corrects for the relative spectral intensity between pixels without changing the spectral shape itself. The conversion to reflectance finally achieves a reliable and completely corrected spectrum. An optional spectral smoothing reduces remaining noise. After correction, the absorption features of ferrous and ferric iron (around 650 and 900 nm) within the spectrum of the iron-rich gossanous sample become clearly visible, as well as the characteristic vegetation spectrum with the red edge around 700 nm for the pine tree sample pixel. The comparison of the different correction steps distinctly reveals the importance of all correction steps. Further, it highly recommends their use to achieve reliable and highly accurate image spectra, which are crucial for the discrimination of geological targets.

The calculation of reflectance by empirical line conversion yields smooth spectra with a high resemblance to measured validation spectra (see **Figure 2-6**). Interestingly, the white calibration panel turned out to be unsuitable for the conversion to reflectance due to over-saturation in most of the surveys. This originates from the integration time used during the image acquisition. Integration time is always adjusted for an optimal exposure of the complete survey area having a much lower reflectance than the white panel. Adding additional panels in different shades of grey would be a possible straight-forward solution. Resulting reflectance spectra of the corrected image data feature low noise and show a high resemblance to the validation field spectra. **Figure 2-8** shows a comparison of the spectral reflectance of field and drone-borne spectra for six sample materials. Results stress a linear correlation between both sensors. The spectral responses are similar for most of the targets.

However, differences in overall reflectance intensity occur due to non-identical measurement conditions and the spatial coverages of the sensors. Another issue to be considered is that, although the position error of the measurement spots seems negligible, it can highly affect the spectral response in heterogeneous materials. The detected VNIR range of the spectrum features only a low amount of characteristic mineral-related absorption features, such as for iron oxides. However, different iron-bearing facies occurring at the test site could be distinguished. Therefore, massive sulfides and gossan show a slight absorption feature around 650 nm (**Figure 2-6**), which is not abundant in the spectrum of sediment from Riotinto River. This feature is characteristic for the charge transfer of Fe^{3+} and Fe^{2+} and can be related to Fe^{3+}-bearing minerals, such as goethite (Hunt et al. 1971). In addition, most materials in the scene feature a Fe^{2+} absorption indicated by a broad and shallow absorption around 900 nm. Depending on the actual mineralogical composition, the position of the absorption can be shifted or show differing intensities. This can be used to differentiate between the different lithologies. These small spectral differences enable one to distinguish even between spectrally quite similar iron-bearing materials.

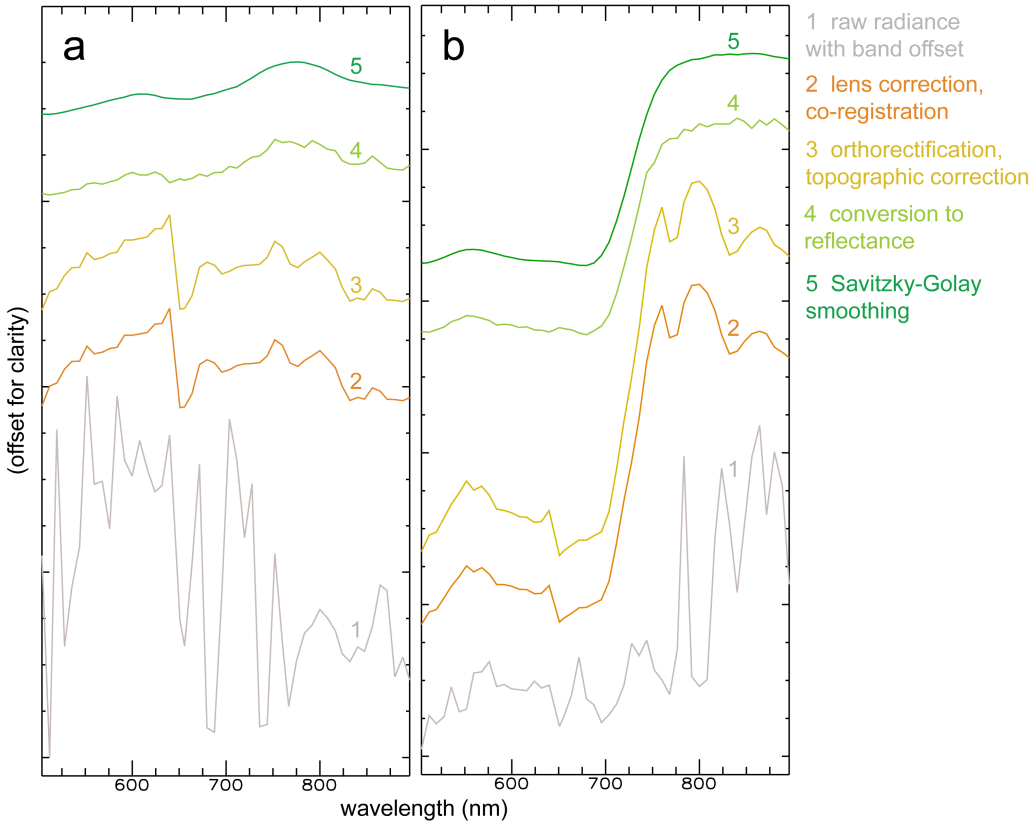

Figure 2-7. Comparison of spectra of image pixel after several correction steps: (**a**) iron-rich gossanous rock; (**b**) pine tree.

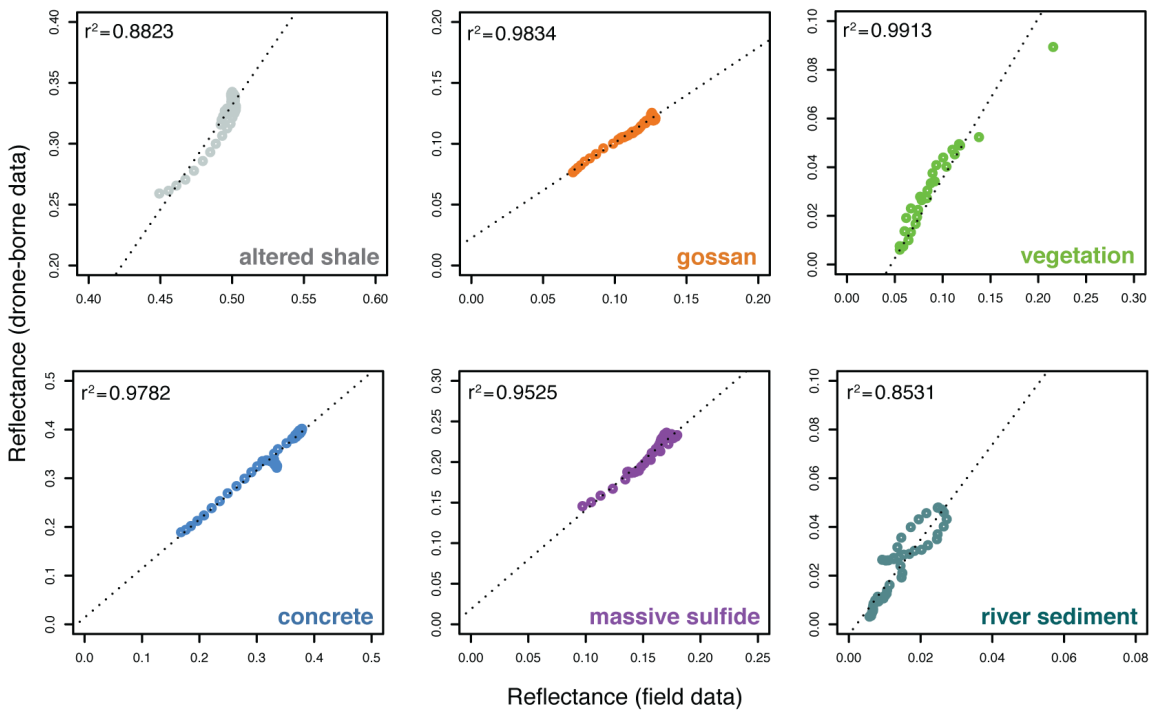

Figure 2-8. Correlation of the reflectance values of field spectra and drone-borne HSI data for six sample target materials.

The results stress the use of drone-borne HSI data as valuable support for mapping alteration and enrichment zones. It further indicates the abilities to map different iron minerals, e.g., for acid mine drainage. The automated workflow enables an easy processing of large flight surveys and a much faster provision of hyperspectral imagery compared to a manual approach. Due to the precise orthorectification and georeferencing, as well as the high spatial resolution of HSI data, orthophoto, and DSM, hyperspectral 3D models can be created to visualize the mapping results. Hereby, the HSI results can be set into spatial relation with topographical and structural features.

The presented toolbox is not especially designed for Rikola hyperspectral data, but can be easily adapted for any frame-based hyper- or multi-spectral sensor on the market. Additionally, the application of the corrected drone-borne hyperspectral mosaics is not limited to lithological or mineral mapping.

2.9 Conclusions

For the first time, we proved that drone-borne HSI data can be used in geological studies. We further presented a toolbox including all crucial steps for the pre-processing of drone-borne HSI data for geological applications. Results have the advantage of both high spectral similarity to validation field spectrometer measurements and high spatial resolution. The presented workflow ensures a proper and careful pre-processing, which is important to obtain reliable hyperspectral reflectance data. It shows excellent performance for frame-based hyperspectral images and was tested on data acquired with a common Rikola hyperspectral drone-borne sensor. In addition to sensor- and platform-specific geometric distortion corrections, a topographic correction step is implemented for rough terrain surfaces. We recommend the use of the c-factor-algorithm here. Further, panels in different shades of grey should be preferred over using a white panel to convert radiance to reflectance due to the generally low reflectance of geologic materials.

Despite the low number of mineralogy-related characteristic absorption features in the VNIR spectral range, a differentiation of lithological endmembers is possible due to small differences in the slope, convexity, and intensity of reflectance. We proved, e.g., that the corrected HSI data are sensitive enough to distinguish different iron-bearing facies. Thus, we highly recommend the use of the presented correction steps for drone-borne HSI data to ensure an image result highly accurate in geometry, location, and spectral information.

Additionally, we highly endorse the increased use of drone-borne HSI data for geological aims, as they show a high potential for fast and accurate mapping of small-scale alteration and enrichment zones. However, their applicability is not limited to mineral exploration, but can comprise and support any other geological and environmental studies.

Acknowledgments: The authors thank the entire group of “Exploration Technology” at Helmholtz-Institute Freiberg for their constructive feedback and extensive testing of the toolbox. We grateful acknowledge the long discussions with Louis Andreani and Eric Pohl on Python. We further thank Atalaya Mining for showing the site and for supporting extensive fieldwork in the Riotinto area. Sokolovska Uhelna AG and the Czech Geological Survey are also thanked for collaboration at the Sylvestr site.

Author Contributions: All authors contributed in a substantial way to the manuscript. S.J. developed the processing toolbox and performed the analysis and interpretation of the hyperspectral data. R.Z. was responsible for the UAS surveys and processed orthomosaics and DSM. R.G. outlined the research topic and supervised the study at all stages. All authors contributed by writing and editing parts of the manuscript and conducting field work for data acquisition and validation.

Conflicts of Interest: The authors declare no conflict of interest.

Chapter Discussion

The presented paper constitutes an important step towards the way hyperspectral UAS-borne data is utilized today. At the point of its publication, drones were emerging rapidly as novel remote sensing platform in research and industry, filling the gap between ground-based and airborne surveys in a cheap and easily deployable manner. Due to the restrictions in weight, deployed sensors were usually either RGB, multi- or hyperspectral cameras bount to the VNIR range of the electromagnetic spectrum. The most common applications were, and still are, high-resolution photogrammetric surveying of natural and anthropogenic targets and spectral analysis of vegetation for agriculture, forestry, and environmental studies. Numerous studies and reviews on suitable sensors and applicational approaches were published, however, most of them remained at an immature stage or underutilized the data's potential. UAS-based data require specific steps of pre-processing and correction which differ from aircraft and satellite platforms. The novelty of the approach, but also the diversity and customizability of UAS platforms and deployable sensors impeded the establishment of correction workflows available for any user. As a result, most published UAS-borne datasets were only partly or not corrected for platform-specific radiometric and geometric effects. First promising correction workflows comprised sensor calibration, image-to-image illumination correction and reflectance calculation using reference targets. The influence of topography-induced variation of illumination angles on spectral intensity and shape was, however, neglected. In particular for targets with highly variably morphology this can cause distinct distortions within the dataset. While it is still possible to retrieve meaningful information from poorly corrected data using simple two-band-ratios, detailed spectral analysis of usually narrow aborption features is not possible. Geological applications in particular rely on reliable spectral information, as the spectral differences between mineralogical domains are usually subtle. This was probably the main reason that before the publishing of the presented manuscript no successful application of UAS-borne hyperspectral data for geological applications was known. This motivated us to carefully analyze the steps required to retrieve a meaningful, spatially and spectrally sufficiently corrected dataset even under non-ideal conditions as they are common in geological campaigns. The presented workflow represents a selection of methods that proved successful under comparable circumstances and were now adapted to the current demands. Due to the vast amount of datacubes created during an average UAS-based survey, I attempted largly automized approaches, able to process large amounts of data on a reliable and routinized basis. Such, the utilization of automatic keypoint extraction and matching is a central part of the presented workflow. The selection of features invariant to scale, orientation, perspective, and wavelength range is of paramount importance for both band-to-band alignment as well as image-to-image co-registration (HSI-to-HSI as well as HSI-to-RGB). This accurate spatial alignment is as crucial prerequisite for the success of other pre-processing steps such as the correction of topography-induced illumination differences.

To meet the diversity of sensors and platforms in UAS-HSI, the proposed workflow is designed to be versatile and straight-forward. It emphasizes the key role of a careful pre-processing of UAS-HSI, and suggests a possible solution. The used methodologies for each processing steps are state-of-the-art, however, are also meant to be developed further or can also be easily substituted by alterantive algorithms. In particular, further work is required to optimize the current methodology for better performance, e.g. to enhance speed and reliability of the matching process. Current in-house improvements comprise the substitution of the keypoint detection algorithm, SIFT, by a distinctly faster alternative, ORB (Rublee et al. 2011), and the inclusion of drone- or sensor-tracked GPS information for a more targeted automatic geolocation, crucially increasing speed and reliability of the orthorectification process. Recent developments in the research

community propose promising approaches that could be included in the workflow in the future, e.g. radiometric block adjustment for an automated radiometric correction of overlapping HSI data (Honkavaara et al. 2018). A comprehensive review of current measurement procedures and data correction workflows has been given recently by Aasen et al. (2018) and indicates a strong development trend towards more adapted algorithms.

Application-wise, the presented work showed the successful usage of UAS-HSI for the characterization of a geological target for the first time and is still one of few. Dering et al. (2019) gave a comprehensive review on the usage of drone-technology for the mapping of dykes and veins, indicating a current focus of the research community on photogrammetric methods and an underrepresentation of UAS-based spectral sensors in geological research. Most available light-weight HSI sensors operate in the VNIR part of the electromagnetic spectrum, make them useful for the detection of iron-bearing minerals and Rare Earth Elements. Current publications focus on these materials and show the applicability of UAS-HSI for the mapping of gossans and other alteration zones (presented paper, Kirsch et al. 2018), the discrimination of different acid-mine-drainage-induced iron minerals occurrences (Jackisch et al. 2018) or the detection of Rare Earth Elements in carbonatite deposits (Booysen et al. 2018). The current rapid positive development of light-weight sensor technology gives hope for the availability of high SNR sensors with an extended spectral range any time soon. Light and easily deployable HS or narrowband multi-spectral sensors with a spectral coverage of the upper SWIR (~1.7–2.5 μm) and LWIR (~7–12 μm) would be particularly beneficial for the detection of many important rock-forming and alteration minerals. Few full-SWIR (up to 2.5 μm) sensors are currently available for UAS-based use, however, both the initial CAPEX (capital expenditures) and take-off weight are rather high, setting barriers for a broad use in the remote sensing community.

References

Aasen H, Burkart A, Bolten A, Bareth G. Generating 3D hyperspectral information with lightweight UAV snapshot cameras for vegetation monitoring: From camera calibration to quality assurance. *ISPRS Journal of Photogrammetry and Remote Sensing* **2015**, 108, 245–259. DOI: 10.1016/j.isprsjprs.2015.08.002

Aasen H, Honkavaara E, Lucieer A, Zarco-Tejada PJ. Quantitative Remote Sensing at Ultra-High Resolution with UAV Spectroscopy: A Review of Sensor Technology, Measurement Procedures, and Data Correction Workflows. *Remote Sensing* **2018**, 10, 1091. DOI: 10.3390/rs10071091

Amici S, Turci M, Giulietti F, Giammanco S, Buongiorno MF, Spina AL, Spampinato L. Volcanic environments monitoring by drones, Mud Volcano case study. *ISPRS - International Archives of the Photogrammetry, Remote Sensing and Spatial Information Sciences* **2013**, XL-1/W2, 5–10. DOI: 10.5194/isprsarchives-xl-1-w2-5-2013

Bemis SP, Micklethwaite S, Turner D, James MR, Akciz S, Thiele ST, Bangash HA. Ground-based and UAV-Based photogrammetry: A multi-scale, high-resolution mapping tool for structural geology and paleoseismology. *Jouranl of Structural Geology* **2014**, 69, 163–178. DOI: 10.1016/j.jsg.2014.10.007

Berni J, Zarco-Tejada P, Suarez L, Fereres E. Thermal and narrowband multispectral remote sensing for vegetation monitoring from an unmanned aerial vehicle. *IEEE Transactions on Geoscience and Remote Sensing* **2009**, 47 (3), 722–738. DOI: 10.1109/tgrs.2008.2010457

Bradski G. The opencv library. *Dr. Dobb's Journal of Software Tools* **2000**, 25 (11), 122–125.

Civco DL. Topographic normalization of Landsat Thematic Mapper digital imagery. *Photogrammetric Engineering and Remote Sensing* **1989**, 55, 1303–1309.

Colby J. Topographic normalization in rugged terrain. *Photogrammetric Engineering and Remote Sensing* **1991**, 57, 531–537.

Cubert GmbH. **2016**. Available online: http://cubert-gmbh.com/product/uhd-185-firefly/ (accessed on 17.01.2017).

Dering GM, Micklethwaite S, Thiele S, Vollgger S, Cruden A. Review of drones, photogrammetry and emerging sensor technology for the study of dykes: Best practises and future potential. *Journal of Volcanology and Geothermal Research* **2019**, 373. DOI: 10.1016/j.jvolgeores.2019.01.018

Donaire T, Chaves FA, Garcia E, Gonzalez F, Roldan MG, Mantero E, Monero C, Pascual E, de Almodovar GR, Saez R, et al. Geologia de la zona Surportuguesa (Andevalo). In: *Geologia de Huelva*; Universidad de Huelva: Huelva, Spain, **2008**, 14–20.

Eltner A, Kaiser A, Castillo C, Rock G, Neugirg F, Abellan A. Image-based surface reconstruction in geomorphometry—Merits, limits and developments of a promising tool for geoscientists. *Earth Surface Dynamics* **2016**, 4 (2), 359–389. DOI: 10.5194/esurf-4-359-2016

Honkavaara E, Kaivosoja J, Mäkynen J, Pellikka I, Pesonen L, Saari H, Salo H, Hakala T, Marklelin L, Rosnell T. Hyperspectral reflectance signatures and point clouds for precision agriculture by light weight UAV imaging system. *ISPRS Annals of Photogrammetry, Remote Sensing and Spatial Information Sciences* **2012**, I-7, 353–358. DOI: 10.5194/isprsannals-i-7-353-2012

Honkavaara, E, Saari H, Kaivosoja J, Pölönen I, Hakala T, Litkey P, Mäkynen J, Pesonen L. Processing and assessment of spectrometric, stereoscopic imagery collected using a lightweight UAV spectral camera for precision agriculture. *Remote Sensing* **2013**, 5, 5006–5039. DOI: 10.3390/rs5105006

Honkavaara E, Khoramshahi E. Radiometric Correction of Close-Range Spectral Image Blocks Captured using an Unmanned Aerial Vehicle with a Radiometric Block Adjustment. *Remote Sensing* **2018**, 10 (2), 256. DOI: 10.3390/rs10020256

Hunt E, Hively WD, Fujikawa SJ, Linden D, Daughtry C, McCarty G. Acquisition of NIR-Green-Blue digital photographs from unmanned aircraft for crop monitoring. *Remote Sensing* **2010**, 2 (1), 290–305. DOI: 10.3390/rs2010290

Hunt G, Salisbury J, Lenhoff C. Visible to near-infrared spectra of minerals and rocks: III. Oxides and hydroxides. *Modern Geology* **1971**, 2, 195–205.

Jackisch R, Lorenz S, Zimmermann R, Möckel R, Gloaguen R. Drone-Borne Hyperspectral Monitoring of Acid Mine Drainage: An Example from the Sokolov Lignite District *Remote Sens*ing **2018**, 10 (3), 385. DOI: 10.3390/rs10030385

Jakob S, Gloaguen R, Laukamp C. Remote sensing-based exploration of structurally-related mineralizations around Mount Isa, Queensland, Australia. *Remote Sensing* **2016**, 8, 358. DOI: 10.3390/rs8050358

Johnson L, Herwitz S, Dunagan S, Lobitz B, Sullivan D, Slye R. Collection of ultra high spatial and spectral resolution image data over california vineyards with a small UAV. In: *Proceedings of the International Symposium on Remote Sensing of Environment*, Honolulu, US, 10–14 Nov **2003**.

Kirsch M, Lorenz S, Zimmermann R, Tusa L, Möckel R, Hödl P, Booysen R, Khodadadzadeh M, Gloaguen R. Integration of Terrestrial and Drone-Borne Hyperspectral and Photogrammetric Sensing Methods for Exploration Mapping and Mining Monitoring. *Remote Sensing* **2018**, 10, 1366. DOI: 10.3390/rs10091366

Kopackova V. Using multiple spectral feature analysis for quantitative pH mapping in a mining environment. *International Journal of Applied Earth Observation and Geoinformation* **2014**, 28, 28–42. DOI: 10.1016/j.jag.2013.10.008

Laakso K, Rivard B, Peter J, White H, Maloley M, Harris J, Rogge D. Application of airborne, laboratory, and field hyperspectral methods to mineral exploration in the Canadian arctic: Recognition and characterization of volcanogenic massive sulfide-associated hydrothermal alteration in the Izok Lake Deposit area, Nunnavut, Canada. *Economic Geology* **2015**, 110, 925–941. DOI: 10.2113/econgeo.110.4.925

Laliberte AS, Goforth MA, Steele CM, Rango A. Multispectral remote sensing from unmanned aircraft: Image processing workflows and applications for rangeland environments. *Remote Sensing* **2011**, 3, 2529–2551. DOI: 10.3390/rs3112529

Lelong CCD, Burger P, Jubelin G, Roux B, Labbé S, Baret F. Assessment of unmanned aerial vehicles imagery for quantitative monitoring of wheat crop in small plots. *Sensors* **2008**, 8 (5), 3557–3585. DOI: 10.3390/s8053557

Lowe DG. Object recognition from local scale-invariant features. In: *Proceedings of the International Conference on Computer Vision (ICCV)*, Corfu, GR, 20–25 Sept **1999**, 2, 1150–1157. DOI: 10.1109/iccv.1999.790410

Micklethwaite S, Turner D, Vasuki Y, Kovesi P, Lucieer A. Mapping from an Armchair: Rapid, high-resolution mapping using UAV and computer vision technology. In: *Proceedings of Structural Geology and Resources*, Kalgoorlie, AU, 26–28 Sept **2012**, 130–133.

Minnaert M. The reciprocity principle in lunar photometry. *The Astrophysical Journal* **1941**, 93, 403–410. DOI: 10.1086/144279

Muja M, Lowe DG. Fast approximate nearest neighbors with automatic algorithm configuration. In: *Proceedings of the International Conference on Computer Vision Theory and Applications (VISAPP '09)*, Lisboa, PT, 5–8 Febr **2009**, 1–10. DOI: 10.5220/0001787803310340

Niethammer U, James MR, Rothmund S, Travelletti J, Joswig M. UAV-based remote sensing of the Super-Sauze landslide: Evaluation and results. *Engineering Geology* **2012**, 128, 2–11. DOI: 10.1016/j.enggeo.2011.03.012

Riaza A, Buzzi J, Garcia-Melendez E, Vazquez I, Bellido E, Carrere V, Müller A. Pyrite mine waste and water mapping using HyMap and Hyperion hyperspectral data. *Environmental Earth Sciences* **2012**, 66 (7), 1957–1971. DOI: 10.1007/s12665-011-1422-0

Richter R, Kellenberger T, Kaufmann H. Comparison of topographic correction methods. *Remote Sensing* **2009**, 1, 184–196. DOI: 10.3390/rs1030184

Richter R, Schläpfer D. Geo-atmospheric processing of airborne imaging spectrometry data. Part 2: Atmospheric/topographic correction. *International Journal of Remote Sensing* **2002**, 23 (13), 2631–2649. DOI: 10.1080/01431160110115834

Rikola Ltd. **2016**. Available online: http://www.rikola.fi/products/hyperspectral-camera/ (accessed on 17.01.2017).

Rojik P. New stratigraphic subdivision of the Tertiary in the Sokolov Basin in Northwestern Bohemia. *Journal of the Czech Geological Society* **2004**, 49, 173–185.

Rublee E, Rabaud V, Konolige K, Bradski G. ORB: An efficient alternative to SIFT or SURF. In: *Proceedings of the IEEE International Conference Computer Vision*, Barcelona, ES, 6–13 Nov **2011**, 2564–2571. DOI: 10.1109/iccv.2011.6126544

Saez, R, Donaire, T. Corta Atalaya. In: *Geologia de Huelva*; Universidad de Huelva: Huelva, ES, **2008**, 106–111.

Savitzky A, Golay MJE. Smoothing and differentiation of data by simplified least squares procedures. *Analytical Chemistry* **1964**, 36, 1627–1639. DOI: 10.1021/ac60214a047

Schläpfer D, Richter R. Geo-atmospheric processing of airborne imaging spectrometry data. Part 1: Parametric orthorectification. *International Journal of Remote Sensing* **2002**, 23 (13), 2609–2630. DOI: 10.1080/01431160110115825

Snavely N, Seitz S, Szeliski R. Photo tourism: exploring photo collections in 3-D. *ACM Transactions on Graphics* **2006**, 25 (3), 835–846. DOI: 10.1145/1141911.1141964

Soriano C, Casas J. Variscan tectonics in the Iberian Pyrite Belt, South Portuguese Zone. *International Journal of Earth Sciences* **2002**, 91 (5), 882–896. DOI: 10.1007/s00531-001-0253-8

Teillet PM, Guindon B, Goodenough D. On the slope-aspect correction of multispectral scanner data. *Canadian Journal of Remote Sensing* **1982**, 8, 84–106. DOI: 10.1080/07038992.1982.10855028

Tizado EJ. i.topo.corr – Computes Topographic Correction of Reflectance (Computer Software), Technical Report of the Open Source Geospatial Foundation: Chicago, US, **2011**. Available online: https://grass.osgeo.org/grass70/manuals/ i.topo.corr.html (accessed on 17.01.2017)

Turner D, Lucieer A, Watson C. An automated technique for generating georectified mosaics from ultra-high resolution Unmanned Aerial Vehicle (UAV) imagery, based on Structure from Motion (SfM) point clouds. *Remote Sensing* **2012**, 4, 1392–1410. DOI: 10.3390/rs4051392

Van der Meer FD, van der Werff H, van Ruitenbeek F, Hecker C, Bakker W, Noomen M, van der Meijde M, Carranza E, de Smeth J, Woldai T. Multi- and hyperspectral geologic remote sensing: A review. *International Journal of Applied Earth Observation and Geoinformation* **2012**, 14, 112–128. DOI: 10.1016/j.jag.2011.08.002

Watts A, Ambrosia V, Hinkley E. Unmanned aircraft systems in remote sensing and scientific research: Classification and considerations of use. *Remote Sensing* **2012**, 4, 1671–1692. DOI: 10.3390/rs4061671

Westoby M, Brasington J, Glasser N, Hambrey M, Reynolds J. "Structure-from-motion" photogrammetry: A low-cost, effective tool for geoscience applications. *Geomorphology* **2012**, 179, 300–314. DOI: 10.1016/j.geomorph.2012.08.021

Wu T, Zhang L, Cen Y, Wang J, Tong Q. Light weight airborne imaging spectrometer remote sensing system for mineral exploration in China. In: *Proceedings of SPIE 9104: Spectral Imaging Sensor Technologies: Innovation Driving Advanced Application Capabilities*, Baltimore, US, 28 May **2014**, 910406. DOI: 10.1117/12.2053098.

Zimmermann R, Brandmeier M, Andreani L, Mhopjeni K, Gloaguen R. Remote sensing exploration of Nb-Ta-LREE-enriched carbonatite (Epembe/Namibia). *Remote Sensing* **2016**, 8, 620. DOI: 10.3390/rs8080620

CHAPTER 3 RADIOMETRIC CORRECTION AND 3D INTEGRATION OF LONG-RANGE GROUND-BASED HYPERSPECTRAL IMAGERY FOR MINERAL EXPLORATION OF VERTICAL OUTCROPS

Preface

At the time of the study, terrestrial HSI has been nearly exclusively used for close-range applications, which comprise sensor-target distances of up to a few hundred meters. The imaging of more distant targets as well as a correction for the influence of atmospheric effects and topography-induced illumination differences remained an unmet challenge. In addition, the unusual and diverse viewing angles of terrestrial data complicate the georeferencing of the datasets and by that, their integrability with data from other viewing angles, acquisition times, locations, and sensors.

The following chapter presents a new processing workflow that was developed to meet these challenges. It successfully attempts to overcome the mentioned effects and offers reliable spectral mapping results of vertical and completely inaccessible outcrops. The achieved spectral mapping products are integrated with 3D photogrammetric data to create large-scale now-called "hyperclouds", i.e. geometrically correct representations of the hyperspectral datacube. The approach enables the integration of hyperspectral scenes from different acquisition locations and dates as well as the integration with other data-sources. The presented workflow can be of benefit for any geological or environmental study using comparable datasets, as it is capable to provide image data highly accurate in geometry, location, and spectral information.

The contents of this chapter were published as research paper in *Remote Sensing*[6] and additionally presented at the *2018 Workshop on Hyperspectral Images and Signal Processing: Evolution in Remote Sensing (WHISPERS)*[7]. The presented workflow was added to MEPHySTo (see Chapter 2), established as in-house pre-processing routine and has been in constant development since its publication. It was used in two parallel, co-authored publications. The first showed the applicability of the corrected data for HSI geological mapping of steep cliffs in the artic from a boat[8], the second the successful 2.5D-integration of several VNIR-SWIR datasets with terrestrial LWIR and drone-borne VNIR imagery for lithological mapping in a quarry[9].

---

[6] Lorenz S, Salehi S, Kirsch M, Zimmermann R, Unger G, Sørensen E-V, Gloaguen R. *Remote Sensing* **2018**, 10, 176. DOI: 10.3390/rs10020176

[7] Lorenz S, Salehi S, Kirsch M, Zimmermann R, Unger G, Sørensen E-V, Gloaguen R. *9th Workshop on Hyperspectral Images and Signal Processing: Evolution in Remote Sensing (WHISPERS),* 23-26 Sept **2018**, Amsterdam, The Netherlands.

[8] Salehi S, Lorenz S, Sørensen E-V, Zimmermann R, Fensholt R, Heincke BH, Kirsch M, Gloaguen R. *Remote Sensing* **2018**, 10, 175. DOI: 10.3390/rs10020175

[9] Kirsch M, Lorenz S, Zimmermann R, Tusa L, Möckel R, Hödl P, Booysen R, Khodadadzadeh M, Gloaguen R. *Remote Sensing* **2018**, 10, 1366. DOI: 10.3390/rs10091366

Radiometric Correction and 3D Integration of Long-Range Ground-Based Hyperspectral Imagery for Mineral Exploration of Vertical Outcrops[10]

Sandra Lorenz [1], Sara Salehi [2,3], Moritz Kirsch [1], Robert Zimmermann [1], Gabriel Unger [1], Erik Vest Sørensen [2], and Richard Gloaguen [1]

[1]Helmholtz-Zentrum Dresden-Rossendorf, Helmholtz Institute Freiberg for Resource Technology, Division "Exploration Technology", Chemnitzer Straße 40, 09599 Freiberg, Germany;
m.kirsch@hzdr.de (M.K.); r.zimmermann@hzdr.de (R.Z.); g.unger@hzdr.de (G.U.); r.gloaguen@hzdr.de (R.G.)
[2]Department of Petrology and Economic Geology, Geological Survey of Denmark and Greenland, 1350 Copenhagen K, Denmark; ssal@geus.dk (S.S.); evs@geus.dk (E.V.S.)
[3]Department of Geosciences and Natural Resource Management, University of Copenhagen, 1165 Copenhagen K, Denmark

3.1 Abstract

Recently, ground-based hyperspectral imaging has come to the fore, supporting the arduous task of mapping near-vertical, difficult-to-access geological outcrops. The application of outcrop sensing within a range of one to several hundred meters, including geometric corrections and integration with accurate terrestrial laser scanning models, is already developing rapidly. However, there are few studies dealing with ground-based imaging of distant targets (i.e., in the range of several kilometers) such as mountain ridges, cliffs, and pit walls. In particular, the extreme influence of atmospheric effects and topography-induced illumination differences have remained an unmet challenge on the spectral data. These effects cannot be corrected by means of common correction tools for nadir satellite or airborne data. Thus, this article presents an adapted workflow to overcome the challenges of long-range outcrop sensing, including straightforward atmospheric and topographic corrections. Using two datasets with different characteristics, we demonstrate the application of the workflow and highlight the importance of the presented corrections for a reliable geological interpretation. The achieved spectral mapping products are integrated with 3D photogrammetric data to create large-scale now-called "hyperclouds", i.e., geometrically correct representations of the hyperspectral data cube. The presented workflow opens up a new range of application possibilities of hyperspectral imagery by significantly enlarging the scale of ground-based measurements.

Keywords: hyperspectral; topographic correction; atmospheric correction; radiometric correction; long-range; long-distance; Structure from Motion (SfM); photogrammetry; mineral mapping; minimum wavelength mapping; Maarmorilik; Riotinto

3.2 Introduction

Hyperspectral imaging has been increasingly used to support mineral exploration and geological mapping campaigns. The obtained spectral signatures provide detailed information about the composition of rocks and the occurrence of economic minerals. The hyperspectral instruments are conventionally operated with a nadir viewing angle, comprising different scales of area coverage and spatial resolution by operation on satellite (Hubbard et al. 2003, Kruse 2003), airplane (Bedini 2009, Laukamp et al. 2011, Zimmermann et al. 2016, Jakob et al. 2016) or drone (Jakob et al. 2017). Depending on the acquisition altitude, a varying influence of the atmosphere between sensor and target, as well as illumination differences due to topography, can be observed in the acquired spectral imagery. Numerous approaches have been introduced

---

[10] Published: Lorenz S., Salehi S., Kirsch M., Zimmermann R., Unger G., Sørensen E.-V., Gloaguen R. *Remote Sensing* **2018**, 10, 176. DOI: 10.3390/rs10020176 (Author's post-print version)

in an attempt to overcome these effects: Atmospheric influences are either corrected by atmospheric modelling using radiative transfer models (e.g., Gao et al. 1993, Adler-Golden et al. 1999, Richter & Schläpfer 2002), the use of ground targets with known or assumed spectra (empirical line calibration, Smith & Milton 1999, flat field correction, Roberts et al. 1986, dark object subtraction, Chavez 1988), or a combination of both (Clark et al. 2002). Whereas radiative transfer models rely on the correct input of a set of external parameters and are mainly used for satellite and airborne data, the use of ground targets, dark objects, or flat fields provides a much more straightforward approach. However, these methods require a spatial resolution high enough to resolve spectrally uniform reference target(s) and/or a reasonable knowledge on the spectra of those materials present, and are therefore mainly used for drone- or airborne data with low acquisition altitudes (e.g., Jakob et al. 2017, Laliberte et al. 2011).

In the last few years, a ground-based approach of using hyperspectral sensors for geological applications has emerged. A tripod-mounted device can be used to rapidly acquire spectrally and spatially highly resolved data of near-vertical geological outcrops, i.e., spatial orientations that are not (or hardly) observable by nadir-faced instruments. Near-vertical outcrops may comprise steep mountain slopes, water-faced cliffs, open pit mine walls, and road cuts. Particularly in arctic or humid regions, where snow and ice, lichens, or dense vegetation cover the Earth's surface, the investigation of such natural or artificial cuts through the strata might be the only possibility to obtain spectral information of the local geology. Currently, ground-based hyperspectral sensors for geological applications are nearly exclusively used for targets at distances between one to several hundred meters (e.g., Kurz et al. 2013, Kurz & Buckley 2016, Murphy et al. 2015). Within this range, the spatial resolution varies between centimeter and decimeter scale, enough to resolve even small-scale mineral compounds and fault systems. Another significant benefit of close-distance measurements is the negligible influence of the atmosphere, which potentially voids the need for an elaborate radiometric correction. Instead, an empirical line approach using reference targets with the same orientation, distance, and illumination conditions as the geological target is sufficient for the conversion to reflectance. However, observing a geological target at close range is not always feasible or reasonable. In particular, larger and vertically oriented targets such as steep mountain slopes, sea- or lake-faced cliffs, and walls of large open pit mines are often only fully visible from an opposing location such as a neighboring mountain (Rosa et al. 2017), pit level, shore, or even a boat (Salehi et al. 2018). The distance between the sensor and the target of interest can then easily exceed the close-range and extend to several kilometers. These distances not only lead to major atmospheric distortions, but also prevent the logistical setup of visible reference targets for radiometric correction as well as ground control points for image georeferencing. Additionally, owing to the much larger scale of the observed surface and the ground-based viewing perspective, pixels within one scene can represent a range of different distances and orientations, leading to highly variable radiometric distortions. For those reasons, correction methods established for nadir acquisitions are not applicable or need to be intensely modified to account for the special conditions of long-range ground-based sensing.

In this paper, we meet these additional challenges and present a novel workflow that allows the creation of fully corrected long-range ground-based hyperspectral image data for geological applications. In addition to sensor-induced geometric distortion corrections, the workflow now includes a new approach for the radiometric correction of long-range ground-based data as well as a topographic correction algorithm based on integration with 3D surface data using automatic matching algorithms. We also describe a detailed methodology for producing 3D hyperclouds, i.e., geometrically correct representations of the hyperspectral datacube, for the display of generated spectral mapping products. The methods presented will be included in the open source Mineral Exploration Python Hyperspectral Toolbox MEPHySTo (Jakob et al. 2017). We

demonstrate the methodology in two areas that differ in geology, climate, and scientific objectives. The first area is located in an arctic environment, where two hyperspectral scans acquired from different points of view are used to detect and map mineralogical variations in the composition of the Mârmorilik Formation marbles in West Greenland. The single result map is integrated with photogrammetry data to provide spatial context and a 3D view that can be integrated into 3D modelling. The second dataset was acquired at the now-abandoned open pit mine Corta Atalaya near Minas de Riotinto, Spain. The Spanish dataset demonstrates the applicability of the corrected dataset for alteration zone mapping of a massive sulfide deposit under hot and dusty conditions as well as the integrability of datasets acquired at different times.

3.3 Areas of Investigation

3.3.1 Nunngarut Peninsula, Maarmorilik, Greenland

The first study area is located in central West Greenland, within the regions of Uummannaq Fjord and Karrat Isfjord (**Figure 3-1**). The investigated area covers large parts of the Nunngarut Peninsula at the Qaamarujuk fjord, where the former mining town of Maarmorilik is located. The nearby Black Angle Pb–Zn deposit is separated from the Nunngarut Peninsula by the smaller Affarlikassaa fjord. The study area belongs to the Mârmorilik Formation, a 1600 m thick carbonate-dominated rock sequence representing the southernmost stratigraphy of the Paleoproterozoic Karrat Group (Kolb et al. 2016). It was deposited between 2.1 and 1.9 Ga in an epicontinental marginal basin as platform carbonates (Kolb et al. 2016), nonconformably overlies a suite of strong deformed Archean orthogneisses, and is overlain by flysch-type metasedimentary rocks of the Nûkavsak Formation (Sørensen et al. 2013).

The Mârmorilik Formation is dominated by dolomite-rich marbles in the lower part and calcite-rich marbles in the upper part. Locally, interbedded horizons of quartzites, tremolite-rich marbles, and possible metamorphosed evaporites in the form of anhydrite occur (Kolb et al. 2016, Grocott & McCaffrey 2017). The Black Angel Mississippi Valley-Type (MVT) Pb–Zn deposit is emplaced within the Mârmorilik Formation (Pedersen 1980, Sørensen et al. 2013), causing an overprint of the marbles by basal brines. The whole succession of Archean basement and the Karrat Group was strongly folded and thrusted by the Nagssugtoqidian–Rinkian orogenesis. During this orogenesis, the Mârmorilik Formation underwent at least three phases of deformation (Rosa et al. 2017), leading to recrystallisation and metamorphism under high greenschist to amphibolite facies conditions (Henderson & Pulvertaft 1987). The Mârmorilik Formation is interpreted to be the lateral equivalent to the Qaarsukassak Formation (Guarnieri et al. 2016), and together they form a several hundred square kilometer large prospective region for zinc mineralization (Rosa et al. 2016, Rosa et al. 2017).

3.3.2 Corta Atalaya, Riotinto, Spain

Corta Atalaya, near Minas de Riotinto in the province of Huelva (southern Spain), is, with a size of 1200x900 m and a maximal depth of 365 m, one of the most famous open pits of the Riotinto mining district (**Figure 3-1**). The Volcanogenic Massive Sulfide (VMS) mineralization of Riotinto is associated with the Iberian Pyrite Belt (IPB), which is considered to host the largest concentration of massive sulfides in the Earth's crust (Sáez & Donaire 2008). The IPB is located in a north-vergent fold and thrust belt of late Variscan age (Soriano & Casas 2002) extending from east of Setubal, Portugal, to north of Seville, Spain, and has been extensively mined for copper, manganese, iron, and gold since the Bronze Age. At Riotinto, the lithostratigraphic succession can be divided into three units (from bottom to top): (i) phyllites and quartzites; (ii) slates, basalt sills, felsic volcanics (rhyolites and dacites); and (iii) the so-called Culm series (greywackes

and slates). The stratabound, VMS lenses are located within felsic volcanics of Upper Devonian to Lower Carboniferous ages (Sáez & Donaire 2008). Zones of chloritic and argillitic alteration are associated with the massive sulfide mineralization. Stockwork zones occur underneath the lenses in the vicinity of faults (Sáez & Donaire 2008). A gossan usually forms in the cap-rock above. The deposit of Riotinto itself is situated in the hinge of an E–W-trending anticline with an east-plunging fold axis. Corta Atalaya is located on the southern flank of this so-called Riotinto anticline.

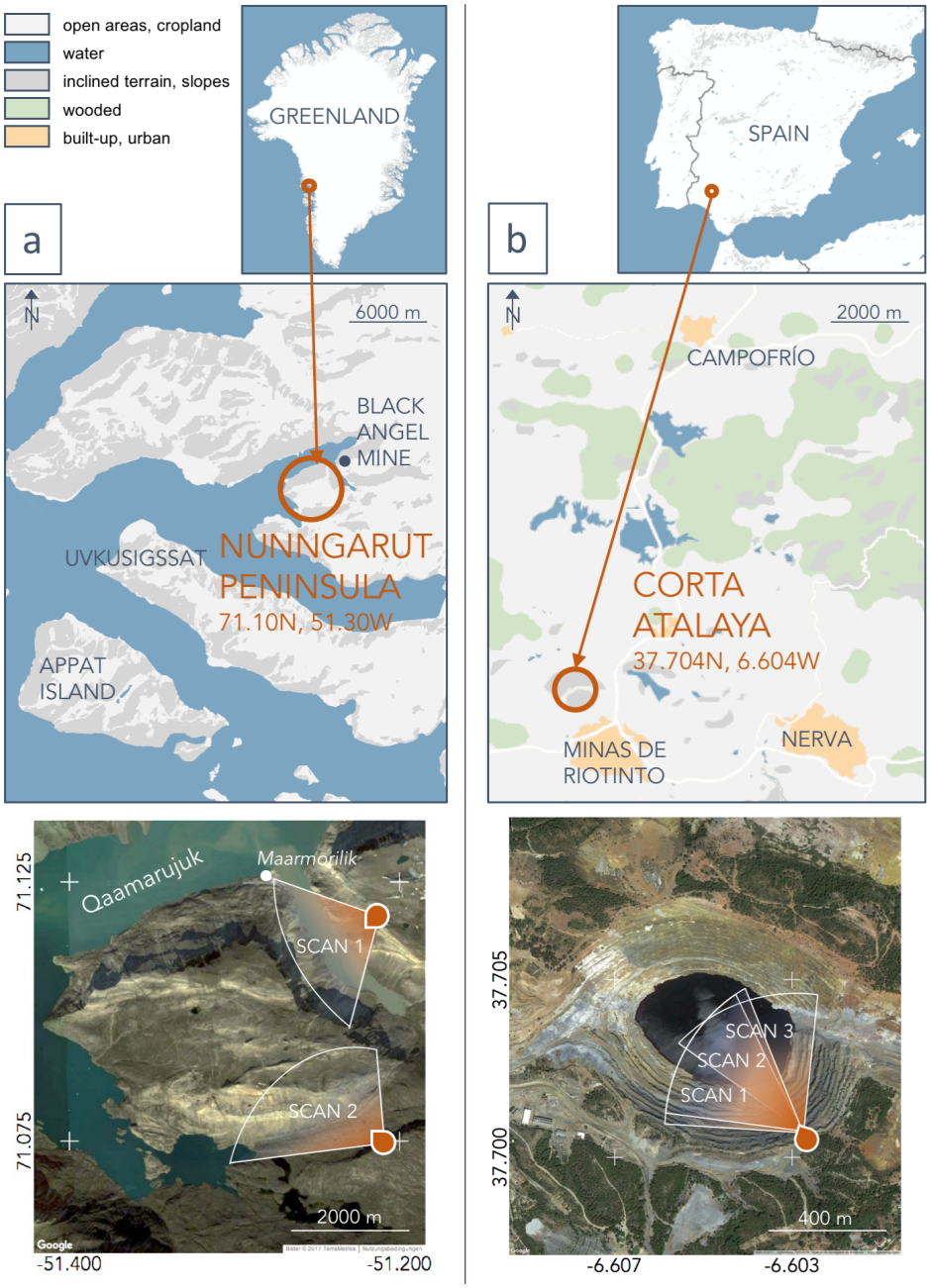

Figure 3-1. Location of the two investigated sites and schematic coverage of the acquired AisaFENIX hyperspectral imagery at: (**a**) Nunngarut Peninsula, Maarmorilik, Greenland; and (**b**) Corta Atalaya open pit, Minas de Rio Tinto, Spain.

Stockwork and massive ore bodies are associated with E–W-striking thrusts. A set of later NW–SE-oriented transverse faults offsets the Riotinto anticline. The most prominent of these faults, the Falla Eduardo, displaces the massive sulfide body San Dionisio about 150 m to the south and finds its continuation in the

Filón Sur ore body east of Corta Atalaya (Sáez & Donaire 2008). The massive sulfide body San Dionisio, which was exploited in Corta Atalaya, originally had reserves of 100 million tons. Originally, the mine was dedicated to the extraction of iron and copper sulfides (mainly pyrite with smaller amounts of chalcopyrite). The initial objective was to extract copper from copper sulfides, but, subsequently, the sulfur contained in pyrite was used for the manufacturing of sulfuric acid until final closure of the open pit in 1991 (Sáez & Donaire 2008).

3.4 Data Acquisition

3.4.1 Hyperspectral Imagery

The hyperspectral image (HSI) data was acquired using a SPECIM AisaFENIX push-broom scanner. The scanner has 384 swath pixels with 624 spectral bands each, covering the visible and near-infrared (VNIR) to short-wave infrared (SWIR) range between 380 and 2500 nm. The spectral resolution (Full Width at Half Maximum–FWHM) varies between 3.5 nm for the VNIR and 12 nm in the SWIR at a spectral sampling distance of about 1.5 nm (VNIR) and 5 nm (SWIR), respectively. By mounting the instrument on a rotary stage, a continuous hyperspectral image with a vertical field of view (FOV) of 32.3° and a maximum scanning angle of 130° could be acquired in one measurement. During the measurements, the GPS position of the camera, acquisition time, and general viewing direction (from here on referred to as 'camera angle') of the scan were recorded. A Spectralon SRS-99 white panel was set up near the camera within the FOV and with a similar general orientation as the imaged outcrop.

3.4.2 Photogrammetry Data/3D Data

Images for reconstruction of surface geometry were recorded using precalibrated RGB and hyperspectral cameras. In the case of Maarmorilik, a Nikon D800E with a 35 mm 1.4 Zeiss lens was used from a helicopter. The 3D pointcloud of Corta Atalaya was based on fusion of drone-borne images from a Rikola Hyperspectral Imager (red band) and a Canon EOS M with EF-M 22 mm f/2 STM lens (as grey-scale image). Camera positions were obtained from an attached GPS device, whereas the imaging geometry was reconstructed using a Structure from Motion (SfM) and MultiView Stereo (MVS) workflow. Prior to the photogrammetry workflow, image distortions were removed.

3.4.3 Validation Sampling

Samples of the main lithologies were taken for a validation of the correction workflow and of the mineral mapping results. Sample locations were recorded using a handheld GPS device. Spectra of representative fresh and altered rock surfaces were acquired in situ using a portable Spectral Evolution PSR-3500 spectroradiometer using a contact probe (8 mm spot size) with an internal, artificial light source. Its spectral resolution is 3.5 nm (1.5 nm sampling interval) in VNIR and 7 nm (2.5 nm sampling interval) in the SWIR, resulting in 1024 channels in the spectral range from 350 to 2500 nm. Radiance values were converted to reflectance using a calibrated PTFE panel with >99% reflectance in VNIR and >95% in SWIR (either Spectralon SRS-99 or Zenith Polymer). Each spectral record consisted of 10 individual measurements, which were taken consecutively and then averaged.

3.5 Processing Workflow

3.5.1 Preprocessing of Hyperspectral Raw Data

The acquired raw hyperspectral datasets are first converted to At-Sensor-Radiance using dark-current subtraction followed by image normalization and multiplication of sensor- and band-specific radiometric calibration data (**Figure 3-2**).

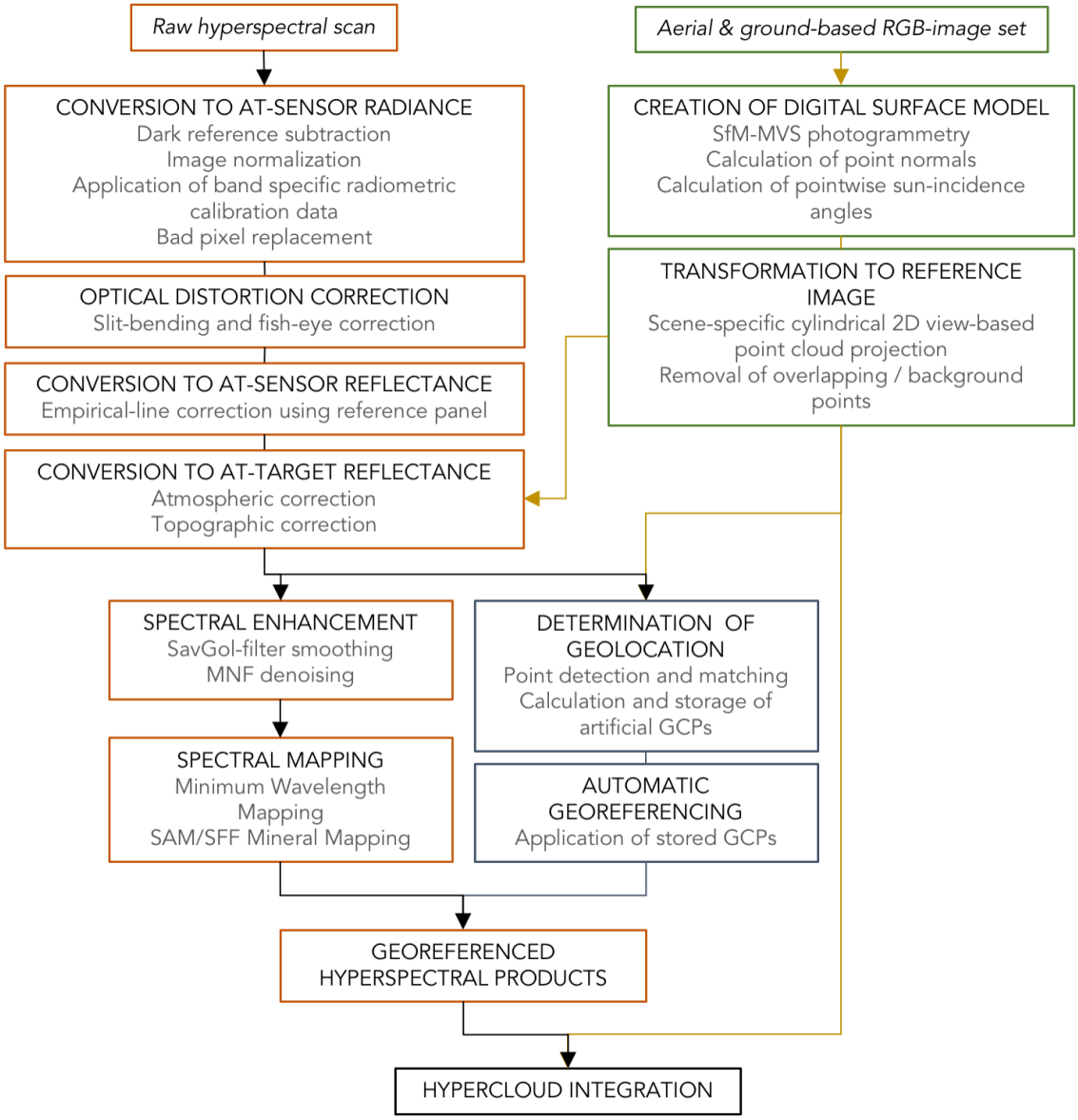

Figure 3-2. Schematic workflow for the correction, processing, and 3D integration of long-range ground-based hyperspectral imagery.

In a second step, two geometric corrections of sensor-specific optical distortions need to be applied. The first effect is a distortion along the FOV comparable to the distortion of fish-eye lenses. This leads to an increasing shortening of the image from the center to the upper and lower image boundaries. The second effect can be described as slit bending and refers to a curved recording of the currently scanned (straight) line. Both effects can be removed by applying correction values for each pixel in the FOV. The required parameters are included in a lookup table provided by the manufacturer of the sensor. In the case that several scans of

the same scene have been acquired with the same settings, a stacking and averaging of those scenes can be performed at this point. By image stacking, the signal-to-noise ratio can be increased, reducing possible temporal illumination variations due to changing cloud cover.

3.5.2 Radiometric Correction of Hyperspectral Radiance Data

Subsequent to the transformation of the raw hyperspectral data into radiance, a conversion to at-sensor reflectance needs to be applied, which can be achieved using a white reference panel placed near the sensor. This Spectralon (SRS-99) reference target is close to an ideal Lambertian reflector with >99% reflectance in the VNIR and >95% in the SWIR. Its exact reflectance spectrum is known and can be used for an empirical line correction of the radiance data. Hereby, a linear regression between the image radiance values and the reference reflectance values is calculated and applied for each band.

Depending on the imaging distance and the climatic conditions, the resulting at-sensor reflectance image may still feature atmospheric distortions (see **Figure 3-3**). In contrast to air- or spaceborne data, the scene-specific intermediate atmospheric layer can be assumed to have a uniform composition with only negligible variations. Nevertheless, the amount of atmospheric influence varies for each pixel and depends mainly on the distance between sensor and target, but can be also influenced by local variations, e.g., differing intensities of upwelling water vapor. Given these circumstances, we attempt to perform a radiometric correction to remove atmospheric distortions using a single atmospheric correction spectrum for each scene. The intensity of correction needs to be varied according to the amount of atmospheric distortion. For the correction approach to be robust and independent from additional parameters or knowledge about the composition of the influencing atmospheric layer, the atmospheric correction spectrum is derived directly and automatically from the hyperspectral image itself. Hereby, the correction spectrum is a comprehensive representation of all scene-abundant spectrally influencing atmospheric components, which may encompass atmospheric dust, water vapor, and other atmospheric gases. The correction spectrum is neither selective nor restricted to defined components and is thus applicable for any atmospheric setting. Owing to the assumed constant composition of the atmosphere over the scene, the depths of all atmosphere-related features should change equally if the atmospheric influence is altered. This approach allows us to evaluate the amount of atmospheric influence for each pixel by the depth of only one atmospheric absorption feature and eliminates the need for atmospheric models, additional calibration targets, and distance measurements. The now-called control feature must necessarily be both common in all possibly occurring atmospheric compositions and strong enough to be detectable even for low atmospheric influence. Additionally, it should not overlap with any characteristic mineralogy-related features to avoid interference and miscorrections. The absorption band we found to fulfill these conditions best is situated at 1126 nm (**Figure 3-3d**) and is related to atmospheric water vapor (Clark et al. 2002).

The atmospheric correction workflow consists of several steps, which can also be retraced in **Figure 3-3**:

1. Masking of sky-related pixels: All image pixels representing sky and sky reflected by mirroring surfaces such as water are masked out automatically from the reflectance image using a ratio between the image bands located at 410 and 890 nm. These wavelength positions are set to encompass two ends of the extreme decline in VNIR reflectance that is specific for sky-related spectra. This characteristic shape leads to a usually very distinct ratio difference between sky and non-sky pixels. In our examples, the masking threshold was most successful in a ratio range between 1.0 and 2.0.

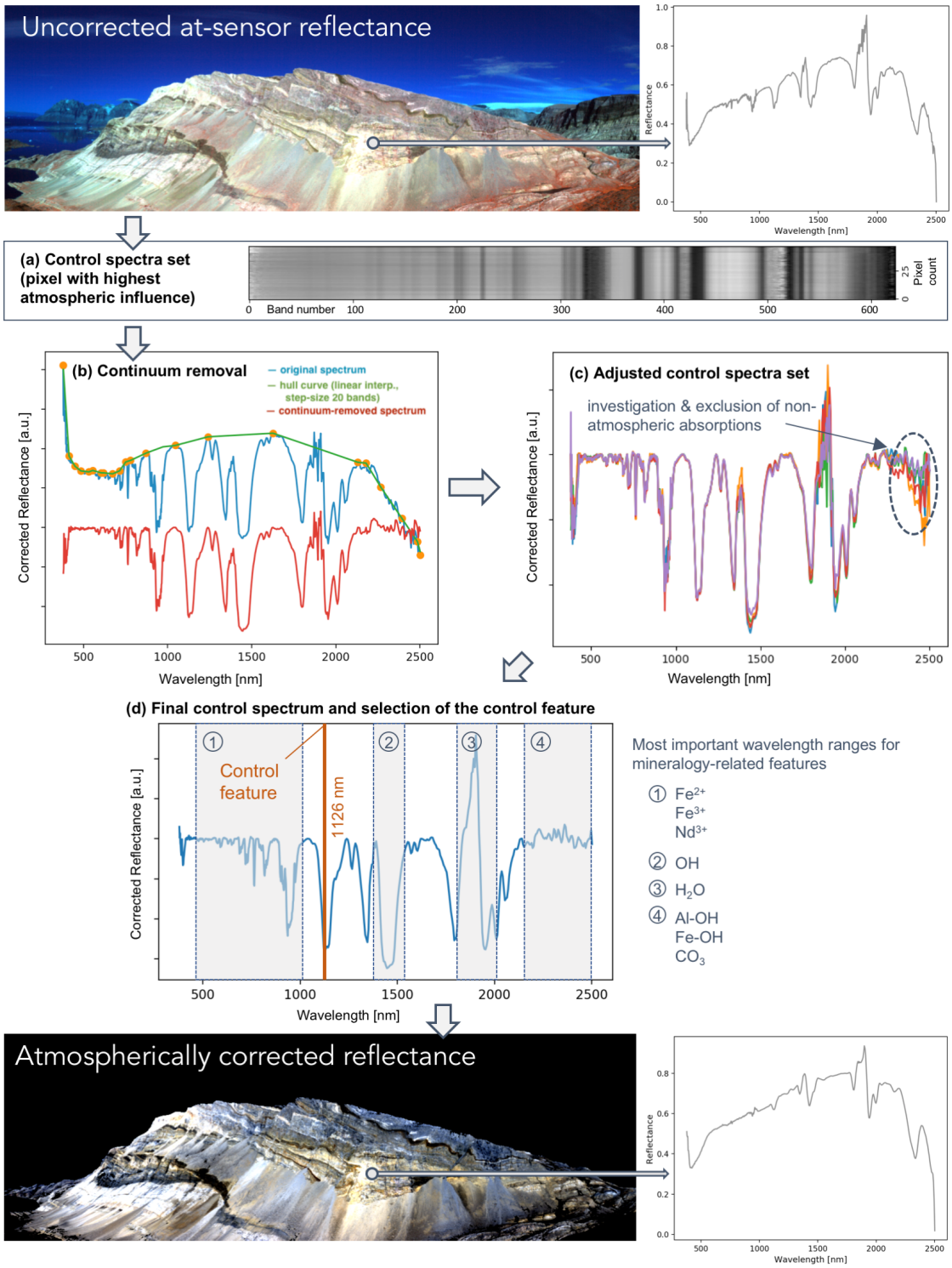

Figure 3-3. Atmospheric correction workflow on the example of the Maarmorilik marble cliffs (Nunngarut, Scan 2). Hyperspectral images are displayed using spectral true color representative bands (R: 640 nm G: 550 nm B: 470 nm). See text for a detailed description. **(a)** Control spectra set; **(b)** continuum removal; **(c)** adjusted control spectra set; **(d)** final control spectrum and selection of the control feature.

2. Determination and processing of possible correction spectra: The depth of the control feature at 1126 nm is calculated for all remaining pixels. All pixel spectra with a control feature depth within 80–100% of the maximum are extracted as a control spectrum set (**Figure 3-3a**), which will be used to determine the final atmospheric correction spectrum. A continuum removal and an equalization of the control

feature depth are applied on each spectrum of the control set separately. The respective continuum hull is calculated using a linear interpolation of stepwise acquired maxima all over the respective spectrum (**Figure 3-3b**). The moving window for the continuum hull calculation can either be set to a fixed step size or restricted to specific stored wavelength ranges that are located outside or at the edge of known atmospheric absorption windows.

3. Exclusion of non-atmospheric features: Some spectra of the resulting equalized control spectra set may still contain additional non-atmospheric absorptions. These features should be excluded from the correction spectrum to avoid a weakening or deletion of important mineralogical features during the atmospheric correction process. In contrast to atmospheric features, non-atmospheric absorptions occur with differing intensities and only in a spectral subset of the control spectra (**Figure 3-3c** and **d**). They can be excluded from the control spectrum set by maintaining only the highest of all spectral values for each wavelength. The used threshold can be varied manually if needed.
4. Calculation and application of the final control spectrum: The remaining spectral information is averaged for each wavelength to reduce possible noise. The outcome of the whole procedure provides a single continuum-removed correction spectrum containing solely the characteristic atmospheric contribution of the analyzed hyperspectral image (**Figure 3-3d**). The atmospheric correction itself is performed pixelwise. For each pixel, the intensity of the correction spectrum needs to be adjusted to both depth and reflectance value of the control feature in the pixel spectrum. The correction itself is then achieved by a simple division of the pixel spectrum by the adjusted correction spectrum. The original reflectance intensities are maintained in the corrected image spectra during that process.

The processing time for the automatic correction of a hyperspectral scan with the spatial and spectral dimensions as in our examples is less than one minute. Thus, the method is extremely time- and effort-saving and can be easily integrated into a batch-processing workflow.
Depending on the Signal-to-Noise ratio (SNR) of the processed dataset, a subsequent Minimum Noise Fraction (MNF) smoothing can be advantageous. MNF smoothing entails a transformation of the image into MNF space, a rejection of bands with low SNR, and a subsequent back-transformation into the original image space (Green et al. 1988). The number of MNF bands to be rejected can be determined by looking at the eigenvalue function of the calculated MNF bands, which reaches a plateau after a sharp increase and suggests a rejection if the asymptotic eigenvalue function approaches a linear function (Phillips et al. 2009).

3.5.3 SfM-MVS Photogrammetry

The Digital Surface Model is derived from aerial and ground-based images using the Structure-from-Motion MultiView Stereo (SfM-MVS) algorithms in Agisoft Photoscan Professional 1.2.5. SfM-MVS is a low-cost, user-friendly workflow combining photogrammetric techniques, 3D computer vision, and conventional surveying techniques. It solves the equations for camera pose and scene geometry automatically using a highly redundant bundle adjustment (Westoby et al. 2012, Eltner et al. 2016). A typical SfM-MVS workflow towards a final surface model consists of the following eight steps (Eltner et al. 2016, Carrivick et al. 2016):

1. Detection of characteristic image points;
2. Automatic point matching using a homologous transformation;
3. Keypoint filtering—this step is crucial for model accuracy and validation of later results (James et al. 2017);

4. Iterative bundle adjustment to reconstruct the image acquisition geometry and internal camera parameters;
5. Scaling and georeferencing of the intrinsic coordinate system to available reference points (GCPs) or camera coordinates and optimization of the resulting sparse cloud;
6. Applying MultiView Stereo algorithms (dense matching) to compute the dense cloud—the resulting dense cloud is the basis for the geometric correction of the hyperspectral data;
7. Interpolation of the dense cloud by, e.g., Meshing or Inverse Distance Weighting (IDW), to retrieve a Digital Surface Model (DSM);
8. Texturizing of the 3D model.

3.5.4 Calculation of Sun Incidence Angles for Topographic Correction

Knowledge of the sun incidence angle for each pixel of the hyperspectral image is crucial for its topographic correction. In contrast to nadir data, vertical outcrop scans can have multiple pixels located at any given latitude/longitude coordinate position, which can be only spatially differentiated by their elevation values. Therefore, common tools for the calculation of slope, aspect, and sun incidence angle of Digital Elevation Models (DEM) cannot be applied here. Instead, we calculate the sun incidence angle for each individual point of the point cloud generated in Section 3.5.3 as the angle between the point normal and the sun vector (**Figure 3-4a**). The point normals were either calculated during the point cloud construction or can be computed retroactively using a triangulation of neighboring points. The sun vector is characterized by

$$sunvec = \begin{pmatrix} \sin(SZ) * \sin(AZ) \\ \sin(SZ) * \cos(AZ) \\ \cos(SZ) \end{pmatrix} \tag{3-1}$$

with SZ being the sun zenith angle and AZ the sun azimuth at the given date, time, and position of the acquisition. The calculated sun incidence angles are stored as additional point properties in the point cloud file and retained in all following processing steps.

3.5.5 Projection of Pointcloud and HSI Matching

An integration of 2D hyperspectral data and 3D point cloud data is needed for topographic correction and final creation of the 3D hypercloud. In order to facilitate automatic matching and reduce distortion in the subsequent wrapping process, the point cloud is projected onto a 2D surface in a way that resembles the view of the hyperspectral camera during image acquisition. It is crucial here that through the entire process of ensuing transformations the original coordinates of each point of the cloud are stored as additional parameters. Due to the push-broom character of the sensor, a simple orthographic projection of the point cloud onto a plane is not suitable.

Instead, the point cloud is first transformed so that the camera position is set as the new origin and the camera viewing angle is set along the *y*-axis of the coordinate system by

$$Transformed\ points = Original\ points - Camera\ Position\ * (-Camera\ Angle). \tag{3-2}$$

The spatial relation between point cloud, camera angle, and camera position in the transformed coordinate system is displayed in **Figure 3-5**.

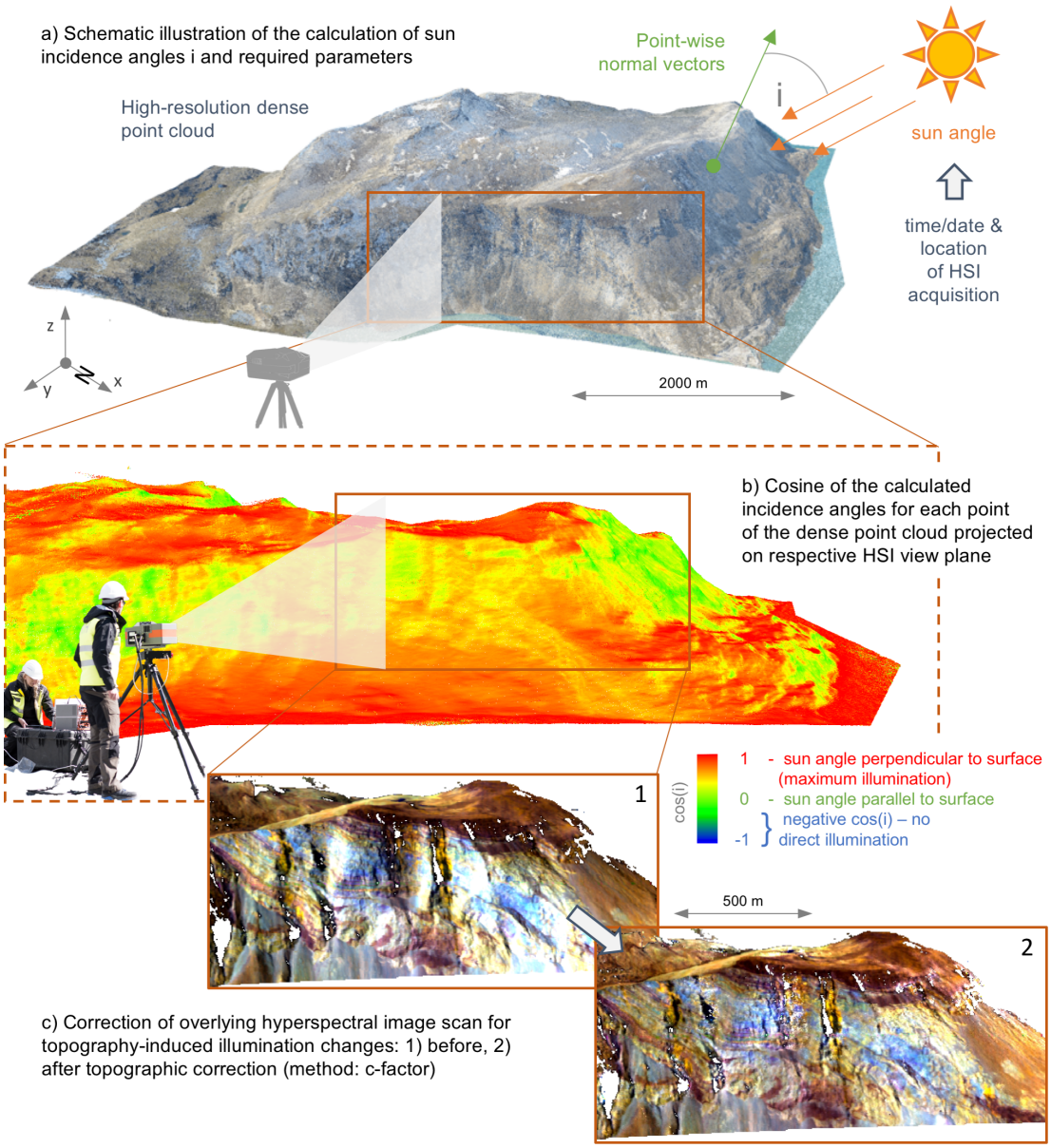

Figure 3-4. Topographic correction of vertical HSI (Nunngarut, Scan 1). **(a)** Schematic illustration of the calculation of sun incidence angles *i* and required parameters; **(b)** cosine of the calculated incidence angles for each point of the dense point cloud projected on respective HSI view plane; **(c)** correction of overlying hyperspectral image scan for topography-induced illumination changes: 1) before, 2) after topographic correction (method: c-factor).

Each point coordinate of the transformed point cloud now corresponds to the vector $\vec{v}$ between the transformed camera position at (0,0,0) and the point at (x_{3D}, y_{3D}, z_{3D}). If we assume that the camera FOV is a subset of a virtual surrounding view sphere with the center at the camera position, the point cloud can be projected onto that sphere by normalizing each point vector by

$$(x_n, y_n, z_n) = \frac{\vec{v}}{|\vec{v}|}$$
$$\text{with } \vec{v} = \begin{pmatrix} x_{3D} \\ y_{3D} \\ z_{3D} \end{pmatrix}; \qquad (3\text{-}3)$$

see also **Figure 3-5b**.

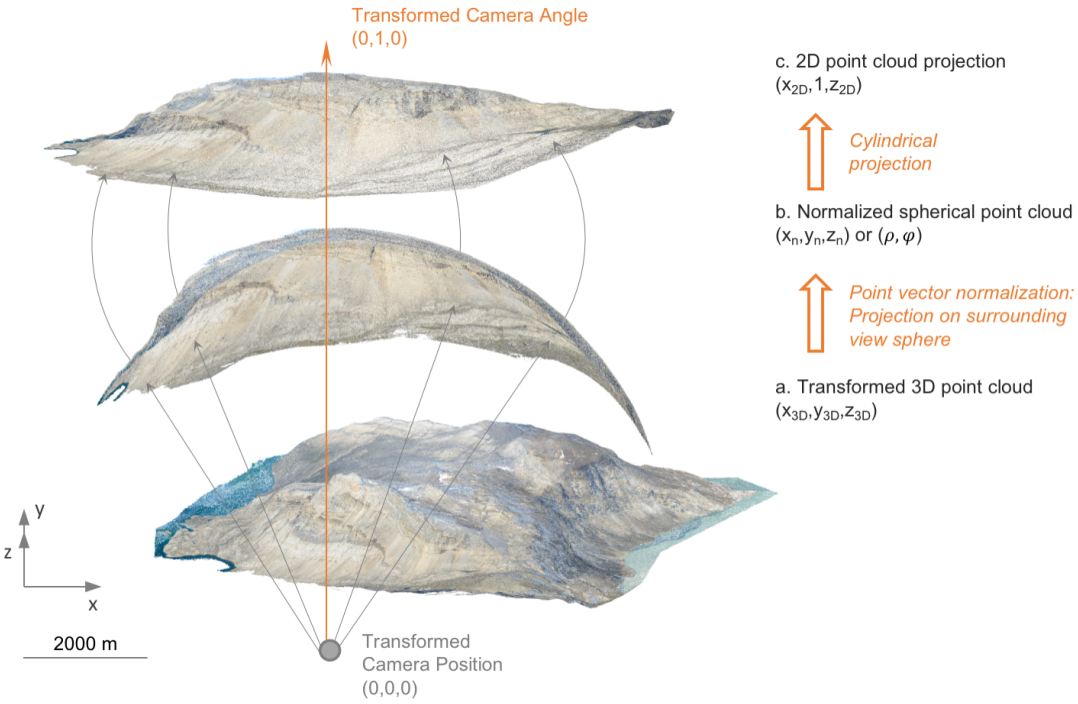

Figure 3-5. Schematic workflow of the point cloud transformation and projection to create a 2D image resembling the panoramic view of a push-broom hyperspectral imager (Nunngarut, Scan 2).

The projected point cloud is now unfolded onto a 2D plane using a cylindrical projection with

$$x_{2D} = \rho \text{ with } \rho = \tan^{-1}(y_n/x_n)\,,$$
$$y_{2D} = 1, \tag{3-4}$$
$$z_{2D} = \tan\varphi \text{ with } \varphi = \pi/2 - \tan^{-1}\left(\sqrt{{x_n}^2 + {y_n}^2}/z_n\right),$$

with x_{2D} and y_{2D} being the Cartesian coordinates of the created 2D image, and with x_n, y_n, and z_n or ρ and φ being the Cartesian or spherical coordinates of the normalised 3D point cloud, respectively (**Figure 3-5c**). The angle at which the cylinder is cut for the projection can be set by an additional parameter.

The projection into 2D space considers all of the points in the true line of sight of the hyperspectral camera, which includes points hidden behind points in the foreground (front points), such as the backside of a mountain (back points). This leads to artefacts within the created 2D image (see **Figure 3-6a**) and would adversely affect subsequent processing steps. Using a maximum threshold for the original spatial distance between neighboring points, the adverse back points can be removed. To ensure a fast processing even for huge point clouds, a moving window is used to process several points at once. For each applied window, the contained point with the closest distance to the camera position is found. This distance can be calculated from the original coordination of the point cloud, which is still saved as additional point parameters. Hereby, it is advantageous to use only the original coordination axis that was closest to the original camera angle. While neighboring front points show a similar location with generally from decimeters to a few meters difference (depending on the spatial accuracy of the data), back points mostly feature locations far off, with distances of several tens to hundreds of meters from the camera-closest front point. According to this, the threshold is set and all resulting back points are deleted (**Figure 3-6b**). Due to the nature of this workflow, a smaller window size guarantees a higher accuracy, but also a higher computation time.

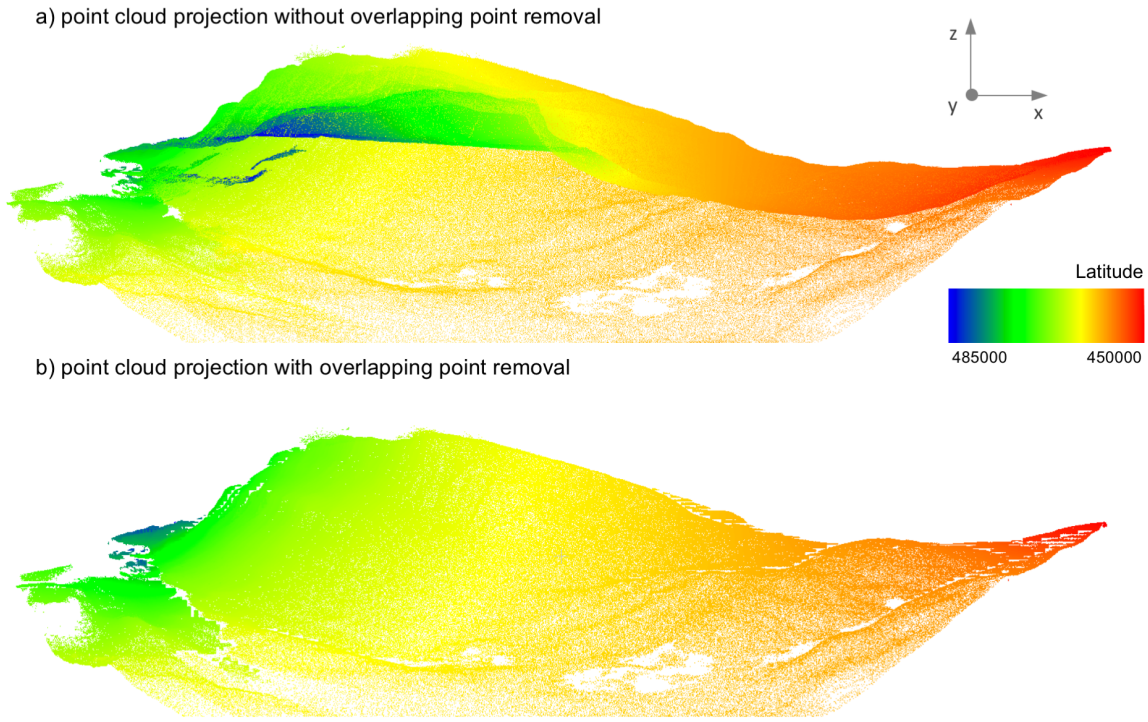

Figure 3-6. Effect of the overlapping point removal on the quality of the 2D point cloud projection image on the example of Nunngarut, Scan 2. The original x-coordination of the points is illustrated by a color gradient. **(a)** Point cloud projection without overlapping point removal; **(b)** point cloud projection with overlapping point removal.

After the deletion of the interfering back points, the remaining front points are interpolated into a raster with a spatial resolution similar to or slightly higher than the spatial resolution of the hyperspectral data. Apart from RGB color information, this ortho-image has four additional bands containing the original point cloud coordinates and the calculated sun incidence angles. The created RGB raster can now be used for an automatic co-registration of the hyperspectral image. The matching workflow used for the co-registration will be part of the MEPHySTo toolbox presented in Jakob et al. (2017) and is also successfully adapted and used for the integration of vessel-based hyperspectral data and 3D point clouds in an accompanying paper (Salehi et al. 2018). The workflow is based on the SIFT (Scale-invariant feature transform) algorithm (Lowe 1999), which, from both images, extracts local features or keypoints that are invariant to translation, rotation, and scale and partly invariant to affine or 3D projection and illumination changes. Using the FLANN (Fast Library for Approximate Nearest Neighbors) matching algorithm library (Muja & Lowe 2009), correlating point pairs between both keypoint sets are found. The best-matching point pairs are used as control points for a polynomial warping of the hyperspectral image to fit on the RGB raster. After the co-registration, each overlapping point of both datasets features high-resolution spectral data, geographic position, and elevation, as well as the sun incidence angle at the time of the acquisition.

3.5.6 Topographic Correction of Referenced HSI

The topographic correction is similar to the approach described in Jakob et al. (2017). The main difference is the calculation of pixel-specific sun incidence angles, which is described above in Section 3.5.4. The calculated angles can now be used to apply a topographic correction algorithm. The c-factor method returned the best correction results of all the methods implemented in the toolbox and achieved a very smooth and

accurate correction even for high illumination differences (see **Figure 3-4c**). The topographically corrected image is calculated by

$$R_c = R_o * \frac{\cos(SZ) + c}{IL + c} \tag{3-5}$$

where c is a/m from the linear regression of $R_o = a + m * IL$ and $IL = cos(i)$ (Teillet et al. 1982, compare Section 2.6.5). The *c-factor* approach is applied separately for each spectral band. The correction of a common hyperspectral scan usually takes less than a minute. For very dark and deeply shaded regions of the image, pixels can be heavily overcorrected. These pixels are characterized by extreme, up to infinite values, which exceed the common value range of reflectance data distinctly. The affected pixels are detected and masked using appropriate thresholds, which are set according to the spectral reflectance minimum and maximum of the topographically uncorrected image (e.g., 0 and 1).

3.5.7 Minimum Wavelength Mapping

The finally corrected HSI can now be used for subsequent mapping and interpretation. In the present paper, a Minimum Wavelength (MWL) mapping approach is exemplarily used to test the quality and applicability of the data for mineral mapping. MWL mapping using the Wavelength Mapper (Bakker et al. 2011, van der Meer et al. 2018) aims to estimate the position of the deepest absorption feature in a given wavelength range. The position of the absorption minimum is a key to link surface mineralogy to subtle variations in mineral composition (e.g., shift of the Al–OH feature depending on the coordination of the Al). First, a hull curve is calculated and divided from the spectra. Second, position and depth of the most prominent absorption are computed using a second-order polynomial function. These two parameters can be used to create MWL position maps, where the position of the investigated feature is displayed by a color change, while the color intensity is controlled by the absorption depth. The success of the MWL mapping approach depends crucially on the analysis of subtle changes of position and depth of mostly small mineralogical absorption features. Therefore, it is an excellent possibility to evaluate image correction methods, which affect both the intensity ratio between single pixels of the image (topographic correction) and the shape of the spectrum itself (radiometric and atmospheric correction). In this context, the successful removal of distortions is as important as maintaining existing and real intensity relations and spectral features.

3.5.8 Generation of Hyperclouds

At the end of the workflow described above, each pixel of the HSI (and any HSI mapping product) has an assigned geographic position and elevation through the corresponding pixel in the projected and rasterized 2D point cloud. By deriving this information for each pixel of the spectral raster, we can create a so-called “hypercloud”, which visualizes the spectral data as a 3D point cloud. The displayed data can comprise any spectral data or result, such as simple reflectance data, results from decorrelation, and endmember mapping methods, or MWL mapping results as presented here. The hypercloud can be displayed and processed further with respective 3D software such as CloudCompare (open-source software under General Public License, retrievable from http://www.cloudcompare.org/) or SKUA-GOCAD (Emerson/Paradigm, Houston, United States). If the hyperspectral survey consisted of several scans covering different parts of the observed area, the creation of hyperclouds can be an excellent option to set the single mapping results into a spatial context by simultaneously displaying or merging multiple hyperclouds. The 3D hypercloud also allows for integration with other spatial datasets such as boreholes or structural observations.

3.6 Results

3.6.1 Nunngarut Peninsula, Maarmorilik, Greenland

Two hyperspectral scans were acquired from two different scanning locations, covering the largest part of the south and east coast of the Nunngarut Peninsula (**Figure 3-1a**). The approximate distance between sensor and observed target ranged between 2 and 5 km for the majority of all outcrop-related image pixels. Despite overall dry and sunny conditions during acquisition, numerous sharp atmospheric absorption features within the spectral data (see **Figure 3-3** and **Figure 3-7**) suggested a high influence of the atmospheric layer between the sensor and the target. **Figure 3-7** displays the known major atmospheric contributions (in this case water vapor, CO_2, O_2, and O_3) to the overall observed atmospheric perturbances and the resulting calculated spectrum used for the corrections. We showcase that the radiometric correction approach presented here allows us to remove the influence of the atmosphere almost completely, whereas typical mineral-related spectral features of the Mârmorilik Formation remain. In the resulting atmospherically corrected target spectrum, the remaining absorption features are indubitably attributable to characteristic mineral features. Besides the distinct carbonate feature of the Mârmorilik marbles, the characteristic AlOH and OH/H_2O features are clearly represented. These characteristic absorptions are related either to abundant evaporitic gypsum and/or clay minerals originating from inclusions or nearby pelite horizons known to be present in this lithological unit.

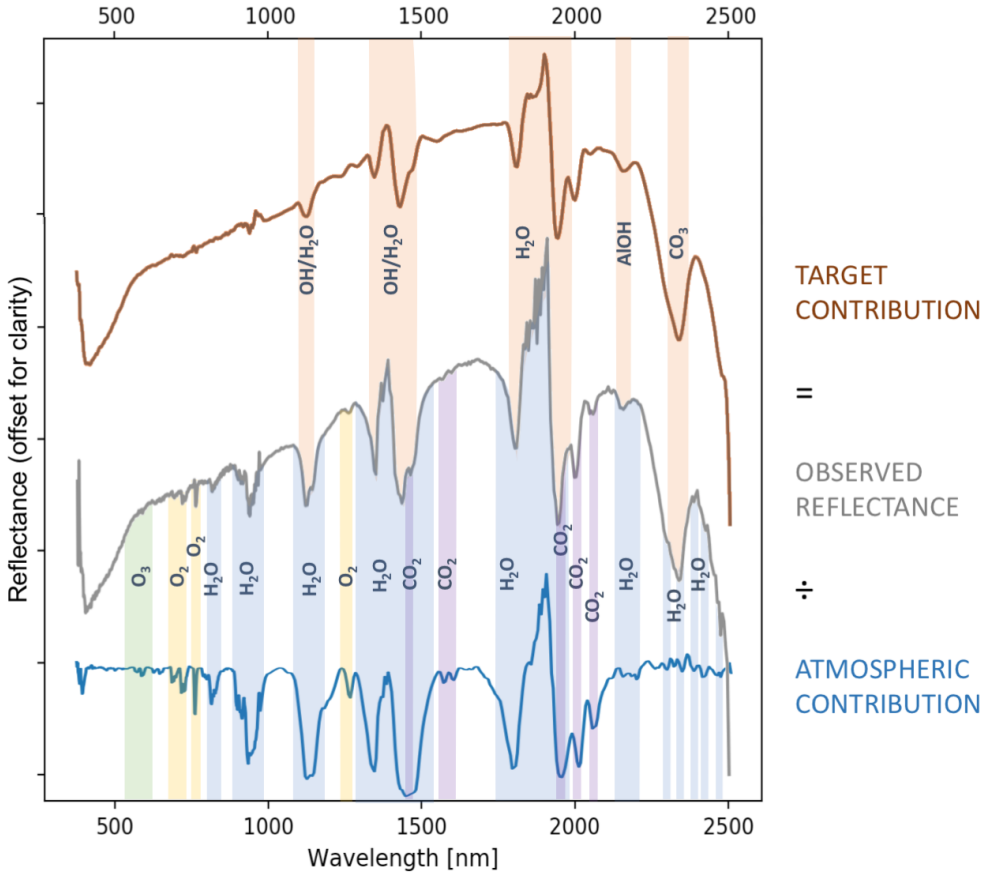

Figure 3-7. Contribution of geological target and atmosphere to an exemplaric observed reflectance spectrum (Nunngarut study area, Mârmorilik Formation). At this, the target contribution equals the reflectance spectrum after atmospheric correction.

Scan 1, imaging the south facing cliff of the Nunngarut Peninsula, was directly opposed to the sun during the measurements and is therefore evenly illuminated. In contrast, Scan 2, acquired in the morning and facing the eastern coast of the peninsula, featured high illumination differences, which made a topographic correction crucial for the subsequent mapping process (**Figure 3-4c**).

With atmospheric and topographic corrections successfully applied to the hyperspectral datacubes, the datacubes provide the basis for a characterization of the mineralogical composition of the Mârmorilik Formation carbonates, with relevance for exploration mapping. The identification of different carbonates from hyperspectral data is possible using the position and depth of the carbonate-related vibrational overtone absorption band between 2310 and 2340 nm (Gaffey 1985). Whereas pure calcite features an absorption around 2340 nm, the absorption band of pure dolomite occurs at 2320 nm.

Carbonate-related absorptions at even shorter wavelengths can indicate an occurrence of tremolite together with dolomite. This relationship is confirmed by spectroscopic analysis of representative rock samples from the Mârmorilik Formation (**Figure 3-8a**). Elemental and mineralogical composition of the samples are further validated by pXRF (portable X-ray fluorescence) and thin section analysis, respectively (see Rosa et al. 2017; pers. commun. C.A. Partin). From the pXRF results, the respective Ca/Mg ratios of four to six measurement spots on each sample were calculated and compared to the classification of limestones and dolomites of Chilingar (1957). Sample #SLA15 featured high Ca/Mg ratios between 31.2 ± 0.7 and 619.3 ± 13.7 and would be therefore classified as calcitic limestone. The ratio of sample #562032 ranged between 2.0 ± 0.5 and 5.9 ± 0.9, indicating a highly dolomitic limestone or calcareous dolomite. Sample #562048 ranges between a dolomite and magnesian dolomite with a low Ca/Mg ratio between 1.0 ± 0.1 and 2.0 ± 0.1 (Chilingar 1957).

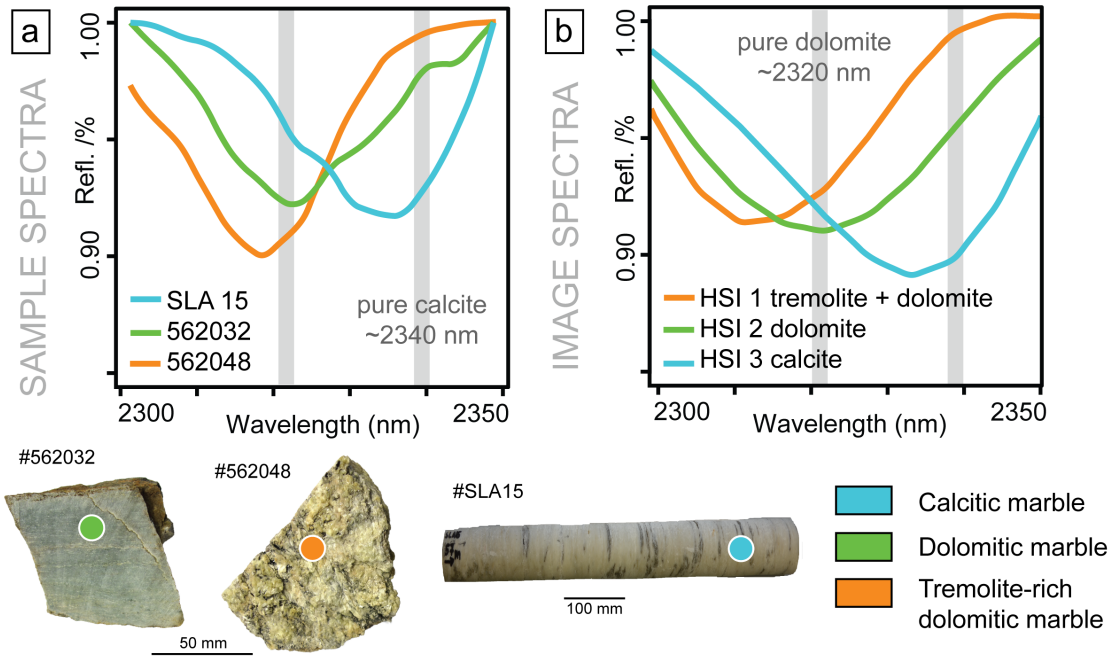

Figure 3-8. Spectral validation of the Minimum-Wavelength-Position-based mapping of the carbonate composition at Nunngarut test site. (**a**) Lab point spectra of three carbonate samples of the Maarmorilik formation, representing typical calcitic, dolomitic, and tremolite-rich dolomitic end members; (**b**) HSI spectral plot of the sampling positions marked in Figure 3-9, representing calcite-, dolomite-, and tremolite-rich dolomitic end members of the scene. A continuum removal was applied on all spectra. Elemental and mineralogical composition is further validated by portable XRF (pXRF) and thin section analysis, respectively (see Rosa et al. 2017).

A simple MWL mapping approach hence provides a good means of distinguishing these different carbonate phases in the outcrop (**Figure 3-9**). Pelite horizons and noncarbonatitic rocks, which are spectrally characterized by a very weak or nonexistent carbonate feature, were masked out using a threshold based on the MWL depth of the mapped carbonate feature. The contact between the upper and lower Mârmorilik Formation is clearly visible on the east-facing slope of Nunngarut, as the lower Mârmorilik Formation is dominated by dolomite interbedded with tremolite-rich horizons (Garde 1978), whereas the upper Mârmorilik Formation is calcite-dominated. Also, a dolomitization along faults can be traced.

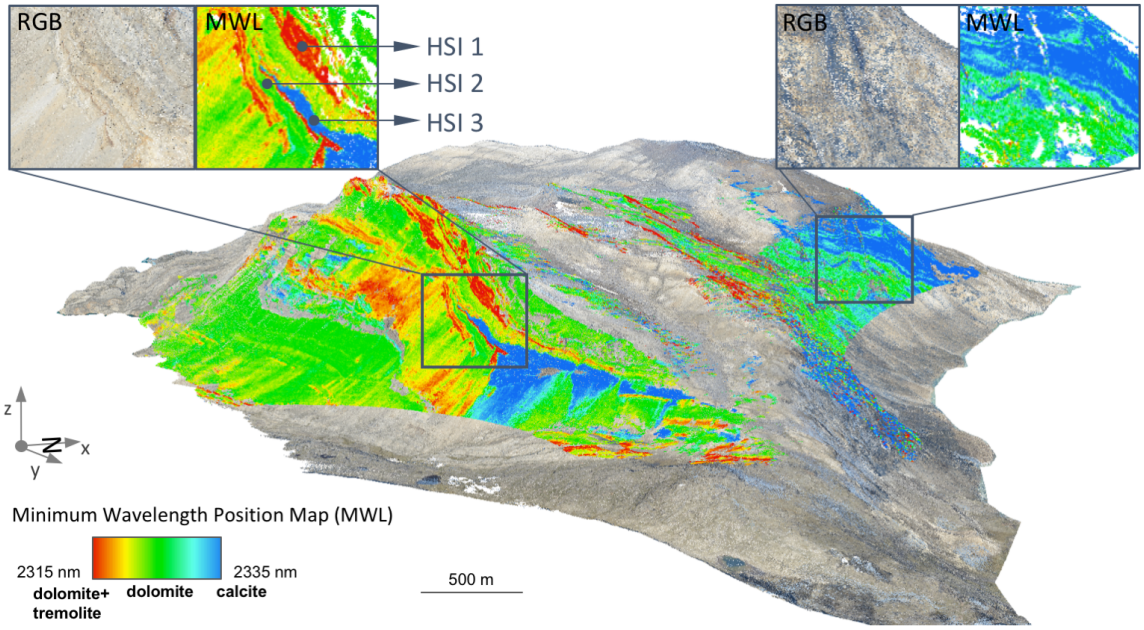

Figure 3-9. 3D hypercloud of two individual HSI image scenes overlain on photogrammetric RGB point cloud of the Maarmorilik marble cliffs. Minimum Wavelength Position Mapping was applied to both HSI datacubes to highlight variations in carbonate composition. HSI 1, 2 and 3 mark the sampling points of Figure 3-8.

3.6.2 Corta Atalaya, Riotinto, Spain

For the Corta Atalaya, three overlapping hyperspectral scans are used to demonstrate the described workflow (**Figure 3-1b**). The scans were acquired from the same panorama viewpoint of Corta Atalaya, but at different times: Scan 1 was acquired in March 2016, and Scans 2 and 3 were acquired in October 2016. The distance between sensor and target ranges broadly between 400 and 1100 m. The conditions on both acquisition days were dry and sunny, with a very good and constant illumination of the imaged pit wall. Despite the shorter distance to the target compared with that at Nunngarut test site and the Mediterranean climate conditions, i.e., with hot and dry summers, distinct atmospheric absorption features were observed in the image data. All scans were atmospherically corrected and geometrically rectified using the photogrammetric pointcloud. A topographic correction was attempted but deemed unnecessary in the end, because the geologically most interesting northern and eastern part of the outcrop are evenly illuminated, and the shaded southern wall of the pit does not contain sufficient spectral information. After preprocessing and correction of the scenes, a Minimum Wavelength Position Mapping of the AlOH feature between 2190 and 2215 nm was conducted on all three scenes, to exemplarily show the capability of the corrected datasets for alteration mapping. The subsequently created hyperclouds show a great coincidence in the mapped alteration zones and could be easily merged into one final Hypercloud AlOH map (**Figure 3-10**).

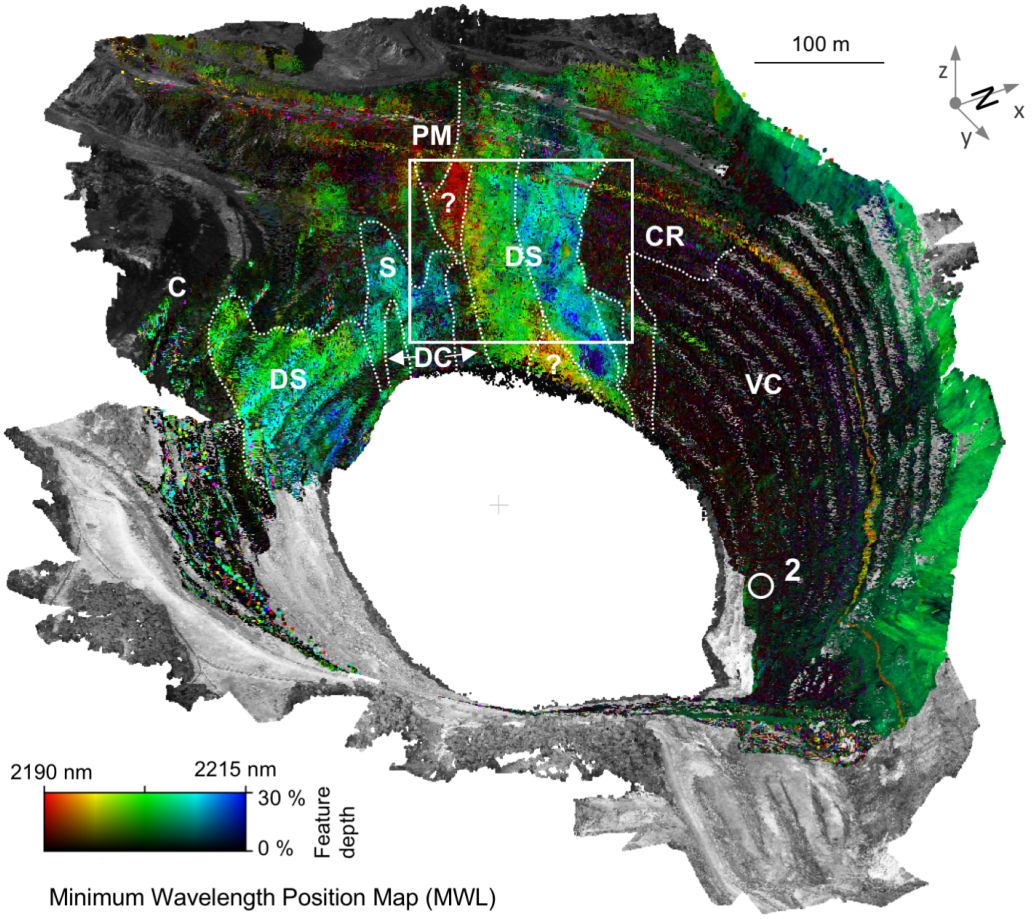

Main lithologies and alteration zones after Sáez & Donaire 2008:

DC	Dacites with chloritic alteration	CR	Conglomerates	C	Culm
DS	Dacites with sericitic alteration	S	Massive sulfides		
VC	(Sub-)volcanics with chloritic alteration	PM	Pink shales/ Pizarras Moradas		

Figure 3-10. 3D hypercloud display of three individual HSI image scenes overlain on photogrammetric RGB point cloud of the Corta Atalaya open pit. All three scenes were used for MWL position mapping to highlight lithological variations associated with differences in the abundance of AlOH-bearing minerals. The white rectangle marks the area shown in Figure 3-11. The color differences in the MWL hypercloud show excellent correlation with the known main lithologies and alteration zones (Sáez & Donaire 2008). Zones not described in Sáez & Donaire 2008 are indicated with question marks. Sample locations for Figure 3-11b are marked with white circles and numbers.

The spectral validation of the mapping result was conducted using a set of field spectrometer data acquired in situ. Due to the restricted accessibility of the mine pit, the spectral readings are limited to a few pit levels. However, a wide range of lithologies could be covered and compared to the respective HSI pixel spectrum. A selection is shown in **Figure 3-11a** and proves the similarity of spectral shape and the occurrence of spectral features between image and field spectra. The given field sample density allows also us to validate the AlOH MWL position distribution. In **Figure 3-11b** the AlOH feature position of each field spectrometer measurement within the main region of interest is displayed as colored squares using the same color scale as the underlying HSI mapping result.

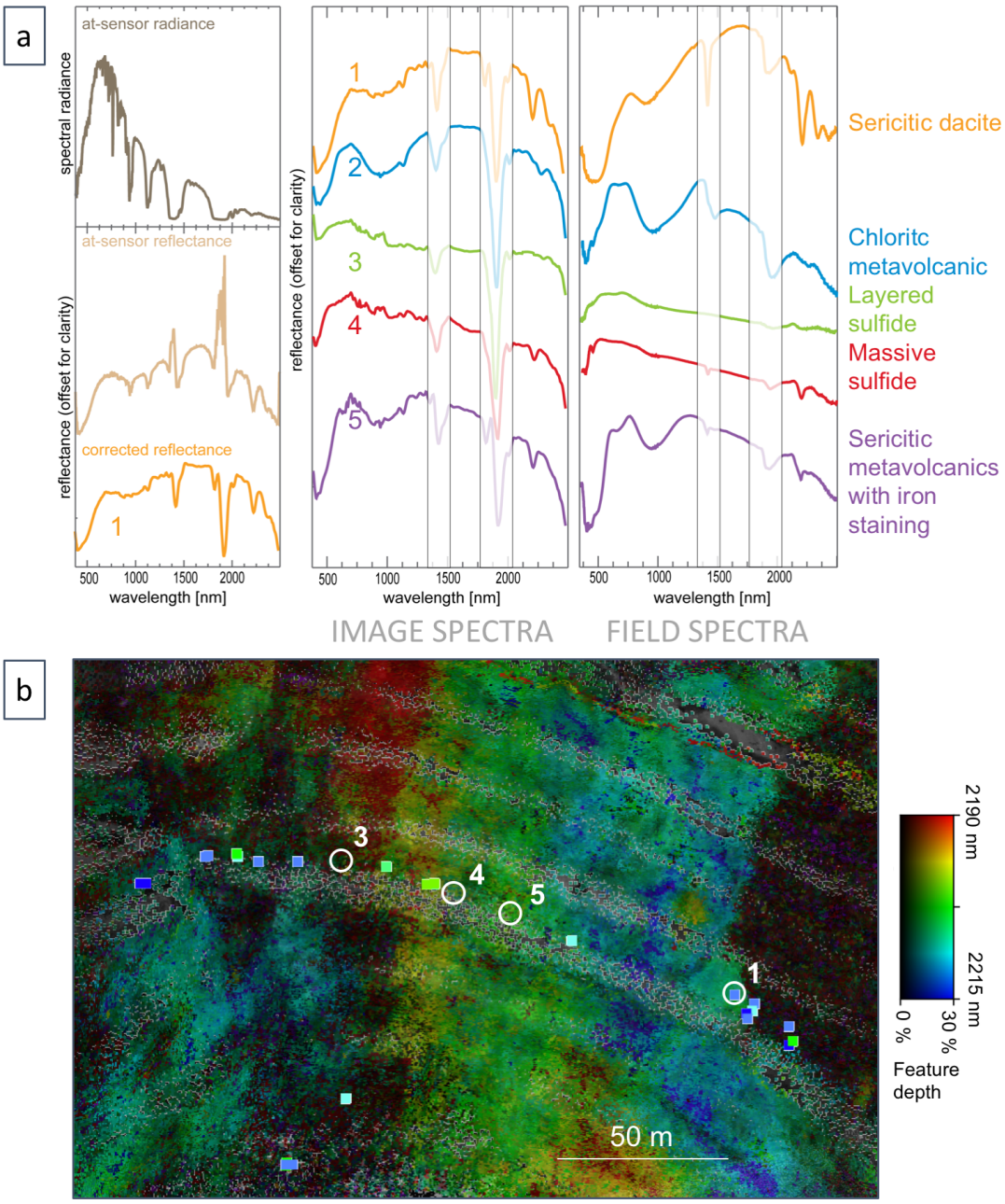

Figure 3-11. Validation of HSI data of the Corta Atalaya open pit. (**a**) Left: Spectral signature improvement of Sample Point 1 within different processing stages. Right: Comparison of spectral shape between field spectra and image spectra of the approximate same location. Sample locations are marked with white circles and numbers in Figure 3-10 and Figure 3-11b; (**b**) Comparison of feature position: minimum wavelength map for AlOH (see map extent in Figure 3-10) and feature position of field spectra (colored squares; same coloring scheme).

3.7 Discussion

3.7.1 Radiometric and Atmospheric Correction

Both test scenarios contain spectral distortions due to atmospheric absorption features. At Corta Atalaya/Spain, most of the observed atmospheric absorption features could originate both from upwelling water vapor of the pit lake and from dust and particles caused by the nearby mining activities in the adjacent

Cerro Colorado open pit. This assumption is supported by the distribution of the atmospherically disturbed image pixels, which are not directly related to the distance of target and sensor, but mainly occur in areas where the signal needed to pass over the water surface in the mining pit. In contrast, for the Greenland site, the intensity of the atmospheric absorptions was roughly proportional to the distance between sensor and target. Here, contributions both from general air humidity and from upwelling water vapor from the fjords separating Nunngarut Peninsula and the respective observation positions on adjacent cliffs can be assumed. The overall atmospheric influence on the signal was much higher than that at Corta Atalaya, which may be related to both the distinctly increased distance to the target and the generally higher air humidity of the arctic climate. The described novel atmospheric correction workflow considers this variability in the composition of the atmospheric layer between sensor and target by extracting the shape of the correction curve directly from the scene and determining the correction intensity according to the pixel-specific atmospheric absorption depth and not the distance to the target.

For all five processed datasets, the atmospheric correction approach was fast and robust. Atmospheric absorptions were removed, whereas the general spectral shape and smaller mineral-related features were maintained. It was shown that the correction approach respects all abundant atmospheric components that contribute to the extracted pervasive signal and which we attribute to atmospheric perturbations. Besides water vapor, this may comprise any abundant atmospheric gases (such as CO_2 or O_3) and minor or pervasive amounts of atmospheric dust that show significant spectral absorption features in the VNIR and SWIR. Only in the rare case of an extreme amount of locally concentrated atmospheric dust or gas, e.g., due to blasting or the exhaust of waste gases within a mine, may the atmospheric correction fail for the affected image region. In this case, the local atmospheric perturbations will deviate distinctly from the used correction spectrum and cause an unsatisfactory spectral result. However, such scenarios can be avoided easily by the respective timing of the image acquisition, e.g., ahead of scheduled blasting operations.

It should be noted that for highly distorted pixels, spectral noise can remain at the former atmospheric absorption positions. The affected pixels mostly originate from extremely distant targets. Here, the proportion of the target signal on the spectral signal received at the sensor is so low that a removal of the atmospheric influence leads to an extremely low signal-to-noise ratio of the returned spectrum, which therefore appears noisy and featureless. This may suggest an upper distance limit for long-range HSI. However, this limit would be at an up to ten or more kilometer distance, depending on the atmospheric conditions of the scene. At this distance, the resulting pixel footprint on the ground would be in the range of several hundred square meters, questioning the informative value of the measurement. In conclusion, we were able to prove the successful application of the introduced atmospheric correction approach within a reasonable imaging distance.

3.7.2 Topographic Correction

As shown in the example of Nunngarut Peninsula in **Figure 3-4**, topographic correction is necessary under certain circumstances, as it ensures the comparability of absorption intensities between differently illuminated parts of the image. However, whereas the correction is effective for the adjustment of intensity changes, it cannot reconstruct spectral features in poorly illuminated areas of the image with associated low signal intensity, SNR, and feature detail. Therefore, we recommend a masking or at least careful interpretation of extremely poorly illuminated or deeply shadowed image parts. We further suggest evaluating the usefulness of a topographic correction for each imaged scene. From our general experience and the specific performance of the shown examples, natural targets such as mountain slopes or cliffs often have a smoother topography and therefore more consistent illumination than manmade outcrops like

quarries and open pit mines. In natural targets, with the resulting smoother transitions between image parts with maximum and minimum illumination, respectively, the topographic correction usually performs well. Artificial targets often feature a terraced geometry and/or rough edges due to blasting and excavation, which generates large illumination differences. A topographic correction will not necessarily give an improvement of the image, as the applied corrections in the well-illuminated parts are minor, while the correction of the dark parts may be futile due to the mentioned reasons.

The c-factor method, despite its good performance for topographic correction, needs to be applied carefully. Due to the band-wise calculation of the correction factor using a linear regression, extreme or infinite values in one or several bands can cause an exaggeration of the correction factor for those bands and, finally, a change in the spectral shape. These peak values can be caused by bad pixels in the HSI sensor, which, due to the push-broom character of the camera, form bad pixel lines that are restricted to few adjacent bands. If a topographic correction needs to be applied, a correction or masking of those bad lines is inevitably required for a reliable image result.

3.7.3 Validation

The spectral validation using field spectrometer data demonstrated a great accuracy of both spectral shape and feature position of the corrected image spectra. In general, the difference between the interpolated minimum wavelength of field spectra and the corresponding library spectra for a certain absorption feature was below 5 nm in both areas of investigation. This value represents the band sampling distance of the SWIR data and lies below the achievable spectral resolution of 12 nm (FWHM). Locally, higher errors between some image and validation spectra points were observed, but these may be related to the large difference in spatial footprints of the different instruments. The field spectrometer data were retrieved from one or several 8 mm spots of a single lithologically representative sample, whereas the respective HSI pixel can easily represent a mixture of an area of some square meters of outcrop, depending on the distance to the sensor. Local variability in alteration can affect the representability of the spectrometer reading and lead to deviations from the recorded image spectrum at the same location. Additional to the spectral variations, slight mislocation of the spectrometer readings, which can be caused by the limited accuracy of the sample GPS position that can reach up to 5 m, needs to be taken into account.

3.7.4 3D Integration

The potential, the spatial accuracy, and a possible application of the HSI integration with photogrammetric point clouds is discussed in more detail in Salehi et al. (2018). The current paper confirms not only the successful 3D integration for two additional examples, but further proves the capability of the workflow to integrate and merge hyperspectral datasets from different camera locations and viewing angles as well as different acquisition dates and times by eliminating the effects of topography, different illumination conditions, and atmospheric absorptions. This allows the use of hyperspectral data in a new way, as it facilitates the evaluation of spatial relationships between hyperspectral results that are not visible from one observation point or displayable in one dataset, such as opposing faces of a mountain or a mining pit.

3.8 Conclusions

With this paper, we present a novel approach for the atmospheric and topographic correction of long-range ground-based hyperspectral imagery. Such corrections are essential for obtaining reliable information on mineral composition in geological applications. The general workflow is partly based on the algorithms developed for drone-borne and vessel-based HSI data, which were presented and used in our previous papers

(Jakob et al. 2017, Salehi et al. 2018), but is adapted and extended by adding radiometric and topographic correction approaches to meet the particular challenges of long-range, ground-based HSI.

The most important outcomes of this paper are the following:

1. The correction spectrum for the atmospheric correction is derived directly from the scene, and the correction intensity is determined according to the pixel-specific atmospheric absorption depth. As a result, the workflow is independent from knowledge about the composition of the atmospheric layer or the distance to the target.
2. The incidence angles for the topographic corrections are calculated using the point normals of the photogrammetric 3D outcrop model. This allows us, for the first time, to utilize common topographic correction algorithms, such as the used c-factor method, for vertical outcrops.
3. The generation of a hypercloud, i.e., a geometrically and spectrally accurate combination of a photogrammetric point cloud and the HSI datacube, is achieved through the projective transformations of a photogrammetric 3D outcrop model. The removal of the effects of atmosphere and topography allows the integration of hyperspectral mapping results originating from different camera positions, dates, and, therefore, varying illumination conditions.
4. Two study areas with five HSI datasets in total proved the applicability and robustness of the workflow in differently challenging measuring conditions regarding climate, distance, atmospheric composition, geological diversity, and mapping objectives. A successful MWL mapping demonstrated both the geological applicability and the accuracy of spectral absorption positions and depths.
5. The accuracy and reliability of the created data and mapping results is validated by field spectra and the mineralogical analysis of geological samples.
6. The presented workflow is fast and simple and requires only a minimum of input parameters. Most of the processing steps are automatized and need no or extremely few manual actions.
7. The workflow enables (i) reliable spectral mapping of vertical and completely inaccessible outcrops; (ii) three-dimensional integration of multiple scans and other data sources; and (iii) a higher spectral resolution, range, and SNR than most drone- or air-borne HSI data.

On account of the promising quality of the presented datasets, we highly encourage the use of carefully processed and corrected long-range ground-based HSI data for geological applications and suggest a further development of highly adapted topographic and atmospheric correction algorithms. In several upcoming application-based papers, we will further present and discuss the geological interpretation of data corrected with the presented workflow and their integration with other data types such as structural data and long-wave infrared (LWIR) hyperspectral data.

Acknowledgments: The Helmholtz Institute Freiberg for Resource Technology is gratefully thanked for supporting and funding this project. The authors thank the entire group of “Exploration Technology” for their constructive feedback and extensive testing of the scripts. Further, we thank Atalaya Mining for access to Riotinto mine and IPH Ingeniería y proyectos for performing the UAS flight in Corta Atalaya. The Ministry for Mineral Resources, Government of Greenland, and the Geological Survey of Denmark and Greenland are gratefully acknowledged for funding and supporting fieldwork and data acquisition within the project “Karrat Zinc”.

Author Contributions: S.L. developed the processing workflow with substantial contributions from S.S., M.K., and R.G. and implemented the workflow in Python. R.Z. and E.V.S. delivered logistic support in the field and were responsible for data acquisition and photogrammetric processing. S.L., R.Z., and G.U. processed the hyperspectral datasets and performed the geological interpretation and validation. S.L. wrote the manuscript with input from all authors. R.G. supervised the study at all stages.

Conflicts of Interest: The authors declare no conflict of interest.

Chapter Discussion

In the last couple of years, a number of studies deploying terrestrial HSI for geological outcrop sensing have been published by different research groups (e.g., Denk et al. 2015, Murphy et al. 2015, Greenberger et al. 2016). A large motivation is the high number of targets of interest, which no other approach could map sufficiently yet. The usually large and vertical oriented targets, such as cliffs, river incisions, or coast lines, are often barely accessible for geological field mapping and sampling, while the vertical orientation inhibits air- or spaceborne surveys. Photogeology, i.e. the geological interpretation according to high-resolution RGB imagery, is a common mapping approach for such outcrops, however, the informative value is often limited and depending on the subjective interpretation of the geologist. Hyperspectral measurements represent a promising alternative, allowing a remote and objective analysis according to the spectral characteristics of the material, extended beyond the visible range of the electromagnetic spectrum. The sensors are easily deployable, fast in acquisition, and require minimum logistics and running costs, in particular, when compared to helicopter or extensive field mapping surveys. As the sensor platform is a stable tripod, there are basically no limits in sensor weight, enabling the use of high-quality sensors with high SNR and wide spectral ranges. First results such as mineral abundance maps or the location of the main spectral domains can be provided quickly after the acquisition to support the geologist in the field. Interesting geological structures can be identified for further investigation and a much faster, more targeted and meaningful sampling is possible.

Despite the potential of terrestrial HSI data in geoscience and exploration, major challenges in regard to the geometric and radiometric correction of the data remain. Illumination variations and shadows are usually higher than for (near-)nadir data, as the angles between a (near-)vertical surface and the sun irradiance are rather small and the morphology variation of the target high. Correction algorithms for similar effects occurring in air- or spaceborne data exist, but require accurate information on the spatial orientation of each pixel compared to the illumination source. The required spatial registration of the HS data is, however, difficult. Most utilized sensors are designed as push broom scanners, which are commonly orthorectified using the current position and angle of the sensor during the acquisition of the specific line. While providing sufficient results in air-borne imaging, this approach partially can cause high location errors in terrestrial data. Due to the combination of high sensor-target-distance and strong morphology, smallest deviations in angle and position can lead to a crucial mis-location of the pixel. A promising registration approach featured the concurrent acquisition of HSI and terrestrial laser-scanning (TLS) on the same platform. Using common GCPs within both datasets, the external camera parameters of both sensors are calculated and used for an accurate registration of spectral and spatial information (Kurz et al. 2011, Buckley et al. 2013). In the presented study I use a different approach that utilizes the projection of an available 3D pointcloud into the HSI space while maintaining the original coordinates for each projected point in the resulting pseudo-orthophoto. After automated keypoint-extraction-based registration of HSI and pseudo-orthophoto, each HS pixel is assigned to its respective 3D position and can be visualized in a geolocated 3D environment. This common space allows the integration of terrestrial HSI with any other available data, e.g., UAS- or airborne data, georeferenced lithological maps, geochemical measurements, point spectra, drill-core data, geophysical data or extracted structures and veins. It allows to set large datasets with different acquisition times and locations into a spatial context, to add spectral information for 3D modelling or to use morphological information for the interpretation of spectral images. If a target is covered by HS scans from different sides, one can attempt to interpolate the composition of material in-between the measured surfaces, which is either hidden under the surface (mountain) or already lost (open-pit mine).

The link between surface morphology and spectral characteristics is not only beneficial in the later interpretation, but is also prerequisite for the geometrical restoration as well as topographic correction of the HSI. The latter is particularly important for any spectral analysis in the SWIR. As the BRDF effect is wavelength-dependent, position, and depth of absorption features might appear shifted relative to other image regions with different surface orientation. If no correction is applied, this effect can lead to substantial errors in calculated mineral abundance and composition maps. Despite the importance of the topographic correction, it is usually not considered and makes the accuracy of results questionable. Validation data is often not presented or not available due to the inaccessibility of the targets. Within the presented paper I emphasize on the importance of such a correction and offer a straight-forward approach that allows the application of established topographic correction algorithms such as *c-factor* or *minnaert*. A restoration of core shadows is not implemented in the workflow and remains a future challenge. I commonly observed a drop of the reflectance information down to the noise level within core shadow areas, which questions the possibility of a spectral restoration in these regions.

Longer range terrestrial measurements or acquisition over water bodies pose a specific challenge as the water vapor and general atmospheric thickness lead to spectral disturbances that can affect the spectral position and depth of important mineral-related features. Model-based atmospheric correction approaches are not applicable due to the variable and usually small viewing angle. Largely varying sensor-target-distances and local water vapor cause varying intensities in atmospheric contribution over the image. The proposed atmospheric correction workflow is able to retrieve the spectral shape and intensity of the atmospheric contribution directly from the image, and, by that, is able to handle different scenarios without requiring user's knowledge on atmospheric composition or pixel-wise sensor-target-distances.

The presented study focuses on VNIR and SWIR HSI, however, an extension of the wavelength range to the LWIR would be an asset as it enhances the range of detectable minerals. While the geometric correction steps of the workflow do also apply for LWIR data, radiometric correction need to be adjusted. A careful temperature-emissivity-separation (TES) is required, utilizing different calibration targets and processing algorithms. Successful applications of LWIR data for outcrop sensing has been illustrated in several studies, such as Boubanga-Tombet et al. (2018), Kirsch et al. (2018) and Lorenz et al. (2018).

References

Adler-Golden SM, Matthew WM, Bernstein LS, Levine RY, Berk A, Richtsmeier SC, Acharya PK, Anderson GP, Felde JW, Gardner JA, et al. Atmospheric correction for shortwave spectral imagery based on MODTRAN4. In Green RO (ed.): *Summaries of the 8th JPL Airborne Earth Science Workshop*, Jet Propulsion Laboratory: Pasadena, US, **1999**; 99–17, 21–29.

Bakker WH, van Ruitenbeek FJA, van der Werff HMA. Hyperspectral image mapping by automatic color coding of absorption features. In: *Proceedings of the 7th EARSEL Workshop of the Special Interest Group in Imaging Spectroscopy*, Edinburgh, UK, 11–13 Apr **2011**, 56–57.

Bedini E. Mapping lithology of the Sarfartoq carbonatite complex, southern West Greenland, using HyMap imaging spectrometer data. *Remote Sensing of the Environment* **2009**, 113, 1208–1219. DOI: 10.1016/j.rse.2009.02.007

Boubanga-Tombet S, Huot A, Vitins I, Heuberger S, Veuve C, Eisele A, Hewson R, Guyot E, Marcotte F, Chamberland M. Thermal Infrared Hyperspectral Imaging for Mineralogy Mapping of a Mine Face. *Remote Sensing* **2018**, 10, 1518. DOI: 10.3390/rs10101518

Carrivick JL, Smith MW, Quincey DJ. Structure from Motion in the Geosciences, John Wiley & Sons, Ltd.: Chichester, UK, **2016**.

Chavez PS. An improved dark-object subtraction technique for atmospheric scattering correction of multispectral data. *Remote Sensing of the Environment* **1988**, 24, 459–479. DOI: 10.1016/0034-425790019-3

Chilingar GV. Classification of Limestones and Dolomites on Basis of Ca/Mg Ratio. *SEPM Journal of Sedimentary Research* **1957**, 27, 187–189. DOI: 10.1306/74D7069B-2B21-11D7-8648000102C1865D

Clark RN, Swayze GA, Livo KE, Kokaly RF, King TVV, Dalton JB, Vance JS, Rockwell BW, Hoefen T, McDougal RR. Surface Reflectance Calibration of Terrestrial Imaging Spectroscopy Data: A Tutorial Using AVIRIS. In: *Proceedings of the 10th Airborne Earth Science Workshop*, Jet Propulsion Laboratory: Pasadena, US, **2002**, 02-1.

Denk M, Gläßer C, Kurz TH, Buckley SJ, Drissen P. Mapping of iron and steelwork by-products using close range hyperspectral imaging: A case study in Thuringia, Germany. *European Journal of Remote Sensing* **2015**, 48 (1), 489–509. DOI: 10.5721/EuJRS20154828

Eltner A, Kaiser A, Castillo C, Rock G, Neugirg F, Abellán A. Image-based surface reconstruction in geomorphometry - Merits, limits and developments. *Earth Surface Dynamics* **2016**, 4, 359–389. DOI: 10.5194/esurf-4-359-2016

Gaffey SJ. Reflectance spectroscopy in the visible and near-infrared (0.35–2.55 μm): Applications in carbonate petrology. *Geology* **1985**, 13, 270–273. DOI: 10.1130/0091-761313<270:RSITVA>2.0.CO;2

Gao B-C, Heidebrecht KB, Goetz AFH. Derivation of scaled surface reflectances from AVIRIS data. *Remote Sensing of the Environment* **1993**, 44, 165–178. DOI: 10.1016/0034-4257(93)90014-o

Garde AA. The Lower Proterozoic Marmorilik Formation, East of Mârmorilik, West Greenland. Nyt Nordisk Forlag Arnold Busck: Copenhagen, Denmark, **1978**, 200.

Green AA, Berman M, Switzer P, Craig MD. A transformation for ordering multispectral data in terms of image quality with implications for noise removal. *IEEE Transactions on Geoscience and Remote Sensing* **1988**, 26, 65–74. DOI: 10.1109/36.3001

Greenberger RN, Ehlmann BL, Jewell PW, Birgenheier LP, Green RO. Detection of organic-rich oil shales of the green river formation, Utah, with ground-based imaging spectroscopy. In: *8th Workshop on Hyperspectral Image and Signal Processing: Evolution in Remote Sensing (WHISPERS)*, Los Angeles, CA, 21–24 Aug **2016**, 1–5. DOI: 10.1109/WHISPERS.2016.8071807

Grocott J, McCaffrey KJW. Basin evolution and destruction in an Early Proterozoic continental margin: The Rinkian fold–thrust belt of central West Greenland. *Journal of the Geological Society* **2017**, 174, 453–467. DOI: 10.1144/jgs2016-109

Guarnieri P, Partin C, Rosa D. Palaeovalleys at the Basal Unconformity of the Palaeoproterozoic Karrat Group, West Greenland. *Geological Survey of Denmark and Greenland Bulletin*, Geological Survey of Denmark and Greenland: Copenhagen, DK, **2016**, 63–66.

Henderson G, Pulvertaft TCR. Geological Map of Greenland, 1:100 000. Mârmorilik 71 V.2 Syd, Nûgâtsiaq 71 V.2 Nord, Pangnertôq 72 V.2 Syd. Lithostratigraphy and Structure of a Lower Proterozoic Dome and Nappe Complex; Geological Survey of Greenland: Copenhagen, DK, **1987**, 72.

Hubbard BE, Crowley CK, Zimbelman DR. Comparative alteration mineral mapping using visible to shortwave infrared (0.4–2.4 mm) Hyperion, ALI, and ASTER imagery. *IEEE Transactions on Geoscience and Remote Sensing* **2003**, 41, 1401–1410. DOI: 10.1109/tgrs.2003.812906

Jakob S, Gloaguen R, Laukamp C. Remote Sensing-Based Exploration of Structurally-Related Mineralizations around Mount Isa, Queensland, Australia. *Remote Sensing* **2016**, 8, 358. DOI: 10.3390/rs8050358

Jakob S, Zimmermann R, Gloaguen R. The Need for Accurate Geometric and Radiometric Corrections of Drone-Borne Hyperspectral Data for Mineral Exploration: MEPHySTo—A Toolbox for Pre-Processing Drone-Borne Hyperspectral Data. *Remote Sensing* **2017**, 9, 88. DOI: 10.3390/rs9010088

James MR, Robson S, d'Oleire-Oltmanns S, Niethammer U. Optimising UAV topographic surveys processed with structure-from-motion: Ground control quality, quantity and bundle adjustment. *Geomorphology* **2017**, 280, 51–66. DOI: 10.1016/j.geomorph.2016.11.021

Kirsch M, Lorenz S, Zimmermann R, Tusa L, Möckel R, Hödl P, Booysen R, Khodadadzadeh M, Gloaguen R. Integration of Terrestrial and Drone-Borne Hyperspectral and Photogrammetric Sensing Methods for Exploration Mapping and Mining Monitoring. *Remote Sens* **2018**, 10, 1366. DOI: 10.3390/rs10091366

Kolb J, Keiding JK, Steenfeld A, Secher K, Keulen N, Rosa D, Stensgaard BM. Metallogeny of Greenland. *Ore Geology Reviews* **2016**, 78, 493–555. DOI: 10.1016/j.oregeorev.2016.03.006

Kruse FA. Mineral mapping with AVIRIS and EO-1 Hyperion. In: *Proceedings of the 12th JPL Airborne Geoscience Workshop*, Jet Propulsion Laboratory: Pasadena, US, 24–28 Jan **2003**, 41, 149–156.

Kurz TH, Buckley SJ. A review of hyperspectral imaging in close range applications. *International Archives of Photogrammetry, Remote Sensing and Spatial Information Sciences* **2016**, 41, 865–870. DOI: 10.5194/isprsarchives-XLI-B5-865-2016

Kurz TH, Buckley SJ, Howell JA. Close-range hyperspectral imaging for geological field studies: Workflow and methods. *International Journal of Remote Sensing* **2013**, 34, 1798–1822. DOI: 10.1080/01431161.2012.727039

Laliberte AS, Goforth MA, Steele CM, Rango A. Multispectral remote sensing from unmanned aircraft: Image processing workflows and applications for rangeland environments. *Remote Sensing* **2011**, 3, 2529–2551. DOI: 10.3390/rs3112529

Laukamp C, Cudahy T, Thomas M, Jones M, Cleverley JS, Oliver NH. Hydrothermal mineral alteration patterns in the Mount Isa Inlier revealed by airborne hyperspectral data. *Australian Journal of Earth Scences.* **2011**, 58, 917–936. DOI: 10.1080/08120099.2011.571287

Lorenz S, Kirsch M, Zimmermann R, Tusa L, Möckel R, Chamberland M, Gloaguen R. Long-Wave Hyperspectral Imaging for Lithological Mapping: A Case Study. In: *IEEE International Geoscience and Remote Sensing Symposium (IGARSS)*, Valencia, Spain, 22–27 July **2018**, 1620–3.

Lowe DG. Object recognition from local scale-invariant features. In: *Proceedings of the International Conference on Computer Vision*, Kerkyra, GR, 20–27 Sept **1999**, 2, 1150–1157. DOI: 10.1109/iccv.1999.790410

Muja M, Lowe D. Fast approximate nearest neighbors with automatic algorithm configuration. In: *Proceedings of the 4th International Conference on Computer Vision Theory and Applications*, Lisboa, PT, 5–8 Feb **2009**, 1, 1–10. DOI: 10.5220/0001787803310340

Murphy RJ, Taylor Z, Schneider S, Nieto J. Mapping clay minerals in an open-pit mine using hyperspectral and LiDAR data. *European Journal of Remote Sensing* **2015**, 48, 511–526. DOI: 10.5721/eujrs20154829

Pedersen FD. Remobilization of the massive sulfide ore of the Black Angel Mine, central West Greenland. *Economic Geology* **1980**, 75, 1022–1041. DOI: 10.2113/gsecongeo.75.7.1022

Phillips RD, Blinn CE, Watson LT, Wynne RH. An Adaptive Noise-Filtering Algorithm for AVIRIS Data with Implications for Classification Accuracy. *IEEE Transactions on Geoscience and Remote Sensing* **2009**, 47, 3168–3179. DOI: 10.1109/TGRS.2009.2020156

Richter R, Schläpfer D. Geo-atmospheric processing of airborne imaging spectrometry data, Part 2: Atmospheric/topographic correction. *International Journal of Remote Sensing* **2002**, 23, 2631–2649. DOI: 10.1080/01431160110115834

Roberts DA, Yamaguchi Y, Lyon R. Comparison of various techniques for calibration of AIS data. In: *Proceedings of the 2nd Airborne Imaging Spectrometer Data Analysis Workshop*, Jet Propulsion Laboratory: Pasadena, US, 6–8 May **1986**, 86–35, 21–30.

Rosa D, Dewolfe M, Guarnieri P, Kolb J, Laflamme C, Partin CA, Salehi S, Sørensen EV, Thaarup S, Thrane K, Zimmermann R. Architecture and Mineral Potential of the Paleoproterozoic Karrat Group, West Greenland: Results of the 2016 Season. *GEUS Rapport 2017/5*, Geological Survey of Denmark and Greenland: Copenhagen, DK, **2017**, 112.

Rosa D, Guarnieri P, Hollis J, Kolb J, Partin CA, Petersen J, Sørensen EV, Thomassen B, Thomsen L, Thrane K. Architecture and Mineral Potential of the Paleoproterozoic Karrat Group, West Greenland: Results of the 2015 Season. Geological Survey of Denmark and Greenland: Copenhagen, Denmark, **2016**, 98.

Sáez R, Donaire T. Corta Atalaya. In: *Geología de Huelva: Lugares de Interés Geológico*; Universidad de Huelva, Facultad de Ciencias Experimentales: Huelva, ES, **2008**, 106–111.

Salehi S, Lorenz S, Sørensen EV, Zimmermann R, Fensholt R, Heincke BH, Kirsch M, Gloaguen R. Integration of Vessel-Based Hyperspectral Scanning and 3D-Photogrammetry for Mobile Mapping of Steep Coastal Cliffs in the Arctic. *Remote Sensing* **2018**, 10 (2), 175. DOI: 10.3390/rs10020175

Smith GM, Milton EJ. The use of the empirical line method to calibrate remotely sensed data to reflectance. *International Journal of Remote Sensing* **1999**, 20, 2653–2662. DOI: 10.1080/014311699211994

Sørensen LL, Stensgaard BM, Thrane K, Rosa D, Kalvig P. Sediment-Hosted Zinc Potential in Greenland. *GEUS Rapport 2013/56*, Geological Survey of Denmark and Greenland: Copenhagen, DK, **2013**, 184.

Soriano C, Casas J. Variscan tectonics in the Iberian Pyrite Belt, South Portuguese Zone. *International Journal of Earth Sciences* **2002**, 91, 882–896. DOI:10.1007/s00531-001-0253-8

Teillet PM, Guindon B, Goodenough DG. On the Slope-Aspect Correction of Multispectral Scanner Data. *Canadian Journal of Remote Sensing* **1982**, 8, 84–106. DOI: 10.1080/07038992.1982.10855028.

van der Meer F, Kopačková V, Koucká L, van der Werff HMA, van Ruitenbeek FJA, Bakker WH. Wavelength feature mapping as a proxy to mineral chemistry for investigating geologic systems: An example from the Rodalquilar epithermal system. *International Journal of Applied Earth Observation and Geoinformation* **2018**, *64*, 237–248. DOI: 10.1016/j.jag.2017.09.008

Westoby MJ, Brasington J, Glasser NF, Hambrey MJ, Reynolds JM. 'Structure-from-Motion' photogrammetry: A low-cost, effective tool for geoscience applications. *Geomorphology* **2012**, 179, 300–314. DOI: 10.1016/j.geomorph.2012.08.021

Zimmermann R, Brandmeier M, Andreani L, Mhopjeni K, Gloaguen R. Remote Sensing Exploration of Nb-Ta-LREE-Enriched Carbonatite (Epembe/Namibia). *Remote Sensing* **2016**, 8, 620. DOI: 10.3390/rs8080620

CHAPTER 4 INTEGRATION OF MULTI-SENSOR HYPERSPECTRAL IMAGING FOR NEAR-FIELD SENSING IN MINERAL EXPLORATION

Preface

The following chapter represents a yet unpublished manuscript that will be submitted shortly. It is dedicated to near-field/lab-scale hyperspectral imaging in mineral exploration, a topic that has evolved rapidly in the recent decade and underwent rapid development. In particular, the boom of available low-cost computing power and memory enabled the possibility to acquire and process large hyperspectral datasets for batch sample mapping in a controlled environment. A wide range of deployable sensors is available nowadays, providing high flexibility in spectral as well as spatial resolution and coverage. In reality, however, the data is usually acquired and interpreted in a fixed setup or by a single sensor only, which reduces the customizability of the setup to the current application. Fusion of data from different customized setups is challenging and usually not conducted. In the following study, the spatial integration of such multi-sensor datasets is demonstrated on data acquired from five commercially available HS sensors and a pair of stereo RGB cameras. A workflow for the integrated image analyses using advanced machine learning methods is presented. The suggested workflow is able to overcome differences in sensor and setup parameters as well spectroscopic characteristics, which allows e.g., a straight-forward integration of VNIR/SWIR and LWIR data or of sensors with highly different spatial and spectral resolution for a more accurate classification result.

Integration of Multi-Sensor Hyperspectral Imaging for Near-Field Sensing in Mineral Exploration

Sandra Lorenz, Peter Seidel, Robert Zimmermann, Laura Tusa, Mahdi Khodadadzadeh, Pedram Ghamisi, and Richard Gloaguen

Helmholtz-Zentrum Dresden-Rossendorf, Helmholtz Institute Freiberg for Resource Technology, Division "Exploration Technology", Chemnitzer Straße 40, 09599 Freiberg, Germany;
s.lorenz@hzdr.de (S.L.), p.seidel@hzdr.de (P.S.); r.zimmermann@hzdr.de (R.Z.); p.ghamisi@hzdr.de (P.G.); r.gloaguen@hzdr.de (R.G.)

4.1 Abstract

Hyperspectral mapping in the near-field or lab-scale (sensor–target distance below two meters) has emerged as a fast and non-invasive characterization method for larger amounts of complex sample material. Geological samples in particular pose a challenge due to their compositional and textural complexity. We use a multi-sensor setup to allow a comprehensive identification of minerals important from a lithological and resource perspective. Such a setup ideally covers (1) high spatial resolution RGB stereo cameras, which can be utilized to retrieve surface elevation information such as objects or textures, (2) VNIR and SWIR hyperspectral-based mapping for the localization of alteration minerals, and (3) LWIR hyperspectral-based mapping for the detection of most rock forming minerals such as silicates and carbonates. To allow the spatial integration of all datasets, current multi-sensor solutions are usually fixed to sensors with similar FOV and spatial resolution. In such setups, a customized sensor integration is not possible, preventing the target-specific setting of the desired amount of detail and acquisition speed. This paper describes a workflow for the acquisition and processing of a multi-sensor dataset using a range of hyperspectral sensors selected to optimize specific instrumental parameters crucial for geological sample characterization, i.e. wavelength range, spatial and spectral resolution, signal-to-noise ratio, sensitivity, acquisition speed, and data handling. We evaluate the data on a set of geological samples with detailed mineralogical and spectral validation data that is used to confirm the outcomes of the study. We show that the spatial and spectral integration of the resulting multi-sensor dataset is feasible and advisable. We propose a workflow for the fusion of the multi-sensor data for image classification, using sophisticated Orthogonal Total Variation Component Analysis (OTVCA) and Support Vector Machine (SVM) classification with cross-validation. On the outcome, we analyze the potential application fields of the different sensors in mineral mapping and show the value of a multi-sensor approach. Beyond the field of mineral mapping, the combination of sensors has many potential application fields, e.g. in the mineral processing, recycling or food industry.

Keywords: hyperspectral; multi-sensor data; data fusion; feature extraction; Support Vector Machine (SVM); Orthogonal Total Variation Component Analysis (OTVCA); near-field mineral exploration

4.2 Introduction

The usage of spectroscopic information for the evaluation, classification, and sorting of large amounts of material is an established approach in industry and mining. As speed, cost-efficiency, and reliability are crucial, the measurement setups are usually simple and highly adapted to a specific sorting problem. The algorithms rely often on binary decisions (e.g., ore – waste) based on experience-based threshold values allowing the separation into predefined object classes according to shape, size or a specific spectral property (Wotruba and Harbeck 2010). In these cases, a high spectral resolution is not needed such that the acquired dataset can be limited to a few spectral bands. Hyperspectral solutions exist, but are usually focused on the UV/VNIR or lower SWIR range of the electromagnetic spectrum. Commercial sensor systems are available

by several companies, such as LLA Instruments GmbH & Co.KG, Perception Park GmbH, Spectral Imaging Ltd. (Specim), and BK Instruments Inc.

Whereas these approaches are sufficient for a wide range of applications, the analysis of spectrally and spatially complex samples such as drill cores and other geological samples requires higher spectral resolution and a wider spectral range. To enable full spectrum analysis at a sufficient speed, a common approach is the integration of spectral information over a larger spatial area. This is especially advantageous if the spectral composition of the analyzed samples is locally homogenous and only large-scale compositional changes should be recorded. The most prominent spectral point sampling sensor is the HyLogger (Mason & Huntington 2012, Schodlok et al. 2016), which integrates a point spectrum over several measurements and can cover VNIR, SWIR and LWIR. It is widely used for drill-core logging in mineral exploration (Tappert et al. 2011, Arne et al. 2016, Ayling et al. 2016, Gordon et al. 2016). The spectral point measurements are often combined with other parameters such as pXRF (Burley et al. 2017), magnetic susceptibility or gamma ray attenuation (Ross et al. 2013). However, these methods are usually slow and pose a security issue in radiation safety. There have also been approaches to integrate spectral point sampling with RGB imaging for a 2D extrapolation (Wang et al. 2016).

The spectral logging approach is often not sufficient when a more detailed analysis of mineralogical composition is required as well as for the mapping of textures, structures, veins or local mineral associations in complex deposits. To add this local spatial component, higher resolution spectral mapping at a sufficient ratio between coverage, speed, and cost is needed. One of the first HS mapping approaches of drill cores was performed by Kruse (1996) using a PIMA II spectrometer for spectral sampling in a grid to create a dataset similar to an HS datacube. Since then, the usage of push broom HS scanners for drill core analysis came to the forth. With these, the HSI can be created by moving samples and sensor relative to each other at constant speed. This allows the acquisition of data from different subsequent sensors at the same time, resulting in a high throughput of material. Most commonly, single or integrated sensors covering VNIR (Bolin & Moon 2003) and/or SWIR (Kruse et al. 2010, Baissa et al 2011, Turner et al. 2014, Mathieu et al. 2017, Dalm et al. 2018) are used, often in combination with RGB image data. Recent studies aim at automatic vein extraction directly from the HSI to allow an interpretation of veins and structural features based on their spectral and spatial characteristics (Tusa et al. 2019). To handle the large amount of data, machine learning approaches have recently been applied to drill core HS data. Using machine learning techniques, Mineral Liberation Analysis (MLA) of a small representative sample can be fused with HSI and extrapolated to a larger scale by defining mineralogically meaningful classes, which themselves can be used as training data for the automatic interpretation of a much larger sample batch (Contreras et al. 2018).

The mineral mapping capabilities of VNIR and SWIR are mainly limited to alteration minerals such as iron oxides and hydroxides, or clays (Hunt 1977). Mapping of important rock-forming minerals, such as quartz and feldspars, requires an extension of the spectral range to the LWIR. However, the combined interpretation of VNIR/SWIR and LWIR data is challenging due to the different nature of occurring spectroscopic features. Spectral absorptions in the VNIR and SWIR are usually caused by electron transfer processes and overtones of vibrational bonds (Hunt 1977, see section 1.1). The resulting features appear as rather discrete, narrow, and wavelength-specific minima. In contrast, absorption related features in the LWIR appear usually as wide, smooth and highly overlapping reflectance maxima (Clark et al. 1999). Commonly, VNIR/SWIR and LWIR data are interpreted separately, only few studies have attempted an integrated analysis. Two general approaches have been published, (1) the independent analysis of each dataset and subsequent integration of abundances by geologically directed logical operators or clustering (Kruse 2015, McDowell and Kruse 2016); and (2) the concurrent analysis of both datasets after wavelength-

range specific absorption feature analysis (Kopačková and Koucká 2017) or continuous wavelet analysis (Feng et al. 2018). At the moment only two HS LWIR sensors are available for lab-scale imaging, the Specim AisaOWL and the Telops Hyper-Cam. The push broom OWL is integrated as part of the Specim SisuROCK drill-core scanner setup (e.g. Kuosmanen et al. 2015). The FOV of the OWL is identical to other available SisuRock sensors, which allows a straight-forward co-registration of RGB, VNIR, SWIR, and LWIR data (Reginiussen 2014, Armengol 2015, Kendro 2015, Tappert et al. 2015). However, this sensor provides only a rather coarse spatial resolution (1.6 mm in the SisuRock setup). The Telops Hyper-Cam is designed as FTIR (Fourier-Transform Infrared Spectrometry) frame imager and allows a distinctly finer spatial and spectral resolution at a comparable spectral sensitivity. No publications on its usage for lab-scale mineralogical sample analysis or drill-core scanning exist.

Those apparent gaps in lab-scale multi-sensor HSI integration motivated us to investigate (1) the integrability and value of multi-sensor datasets acquired in different experimental setups to achieve optimal conditions for the desired application, (2) the fusion of multi-sensor data for a more reliable mineral detection using sophisticated machine learning algorithms, and (3) the evaluation of the used commercial sensors for application fields in mineral exploration. We acquire image data of a set of geological samples divers in mineralogy, using stereo RGB imagery as well as five HS sensors with differing specifications in terms of sensor design, acquisition speed, spatial resolution, and spectral range. For validation, we obtained mineralogical information in form of MLA (Mineral Liberation Analysis) maps and point measurements covering the complete electromagnetic spectrum in the wavelength range between 0.35 and 15.39 μm. We co-register the datasets preferably using automatically extracted keypoints. We calculate a surface model from stereo RGB data and extract both elevation and contour information to separate sample pixels and background in all datasets. We use Orthogonal Total Variation Component Analysis (OTVCA) feature extraction to extract about five to seven most variant features on each dataset, reducing overall data dimensionality and size. This step is not only required to reduce the overall processing time and data redundancy, but also to tackle the Hughes Phenomenon (Hughes 1968). This effect is also known as “curse of dimensionality” and refers to the drop of classification accuracy that potentially is caused when the number of spectral bands is increased while the number of training samples stays limited. We use the extracted features as input for SVM with Radial Basis Function kernel (SVM-RBF) to map mineralogical classes. We demonstrate this workflow on two sample subsets, (1) with spectrally pure and well-defined, but spatially highly unbalanced classes; and (2) with spatially balanced, but spectrally mixed, variable and sparse class definitions. We compare the classification accuracies of several single- and multi-sensor inputs and discuss the influence of the sensor specifications on the classification outcome. For an overview on the proposed workflow, refer to **Figure 4-1**.

4.3 Data Acquisition and Processing

4.3.1 Experimental Setup & Sensor Parameters

The used hyperspectral sensors are selected to cover the mineralogically most important wavelength ranges in the VNIR, SWIR, and LWIR. Additional important parameters for the applicability in scanning of geological samples, such as spatial and spectral resolution, acquisition speed and data handling, are evaluated by comparing different sensors operating at similar wavelength ranges. The important specification and experiment parameters of the used sensors are shown in **Table 4-1** and **Table 4-2**.

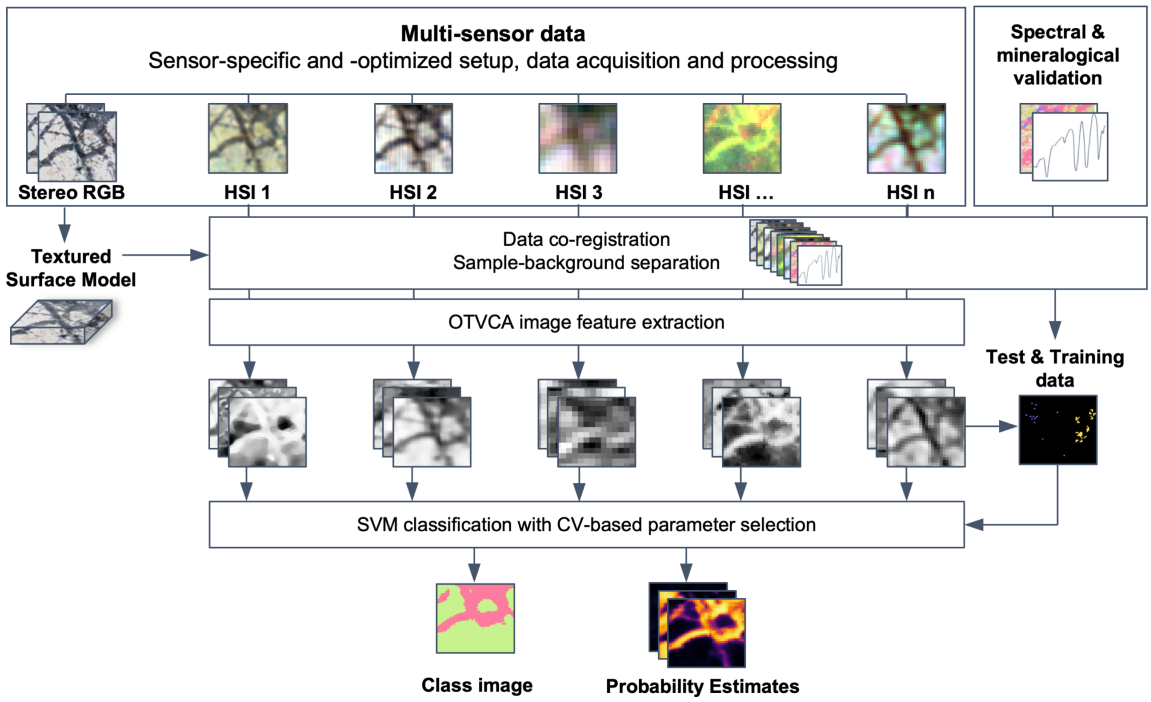

Figure 4-1. Proposed workflow for the fusion of multi-sensor HSI data using OTVCA feature extraction and SVM classification.

In particular note the differences in spatial resolution and field of view (FOV), which do not allow a co-registration by simple overlaying. The sensors are used in specific setups that ensure optimal conditions for each acquisition (see **Figure 4-2** for all system setups) and demonstrate the integration of data regardless of changing external conditions. Such, the Specim AisaFENIX (from here on **FENIX**) and the Specim sCMOS (from here on **sCMOS**) are operated in a Specim SisuRock frame.

Table 4-1. Specifications of the used sensors in their current setup.

Sensor	Spectral range	Spectral res. (FWHM)	Approx. Peak-SNR	Image size (px)	FOV	Spatial res.[1]
Teledyne Dalsa C4020 (2x)	RGB (Bayer)	-	-	4000x2000 px frame	54.6°x 27.3°	0.15 mm
Specim sCMOS	VNIR: 0.40–1.00 µm	2.9 nm	170:1	2185 px line	15°	0.08 mm
Specim FX10	VNIR: 0.40–1.00 µm	5.5 nm	600:1	1024 px line	54°	0.58 mm
Specim FX17	SWIR: 0.90–1.70 µm	8 nm	1000:1	640 px line	75°	0.96 mm
Specim AisaFENIX	VNIR: 0.38–0.97 µm SWIR: 0.97–2.50 µm	3.5 nm 12 nm	600–1000:1 1050:1	384 px line	32.3°	1.54 mm
Telops Hyper-Cam	LWIR: 1300–881 cm^{-1} / 7.70–11.80 µm	6 cm^{-1} / 36–76 nm	250:1	320x256 px frame	6.4°x 5.1°	0.62 mm
Spectral Evolution PSR-3500	VNIR: 0.35–1.00 µm SWIR: 1.00–2.50 µm	3.5 nm 7–10 nm	600:1	Point measurement	-	~5.00 mm
Agilent 4300 FTIR	SWIR-LWIR: 4500–650 cm^{-1} / 2.22–15.39 µm	2 cm^{-1}/ 1–47 nm		Point measurement	-	~2.00 mm

[1] length of quadratic pixel

Table 4-2. Setup parameters for each sensor used for the experiments performed in the present study.

Sensor	Sensor-Target-Distance	Exposure time	Frame rate	Conveyor speed[1]	Binning (spat/spec)[1]	Data size (150x240 mm)
Teledyne Dalsa C4020 (stereo)	60 cm	1 ms	8 Hz (frame)	13 cm/s	-	75 MB
Specim sCMOS	65 cm	10 ms	60 Hz	0.8 cm/s	2/1	5600 MB
Specim FX10	58 cm	4 ms	240 Hz	13 cm/s	1/2	133 MB
Specim FX17	40 cm	4 ms	140 Hz	13 cm/s	1/1	50 MB
Specim AisaFENIX	102 cm	VNIR: 14 ms SWIR: 4 ms	30 Hz	5 cm/s	VNIR: 2/2 SWIR: 1/1	37 MB
Telops Hyper-Cam	177 cm	0.25 ms	0.08 Hz (frame)	-	-	31 MB

[1] if applicable

Due to its smaller FOV in the current setup, two separate scans are needed to cover the sample set with the sCMOS. The Specim FX10, FX17, and two Teledyne Dalsa RGB cameras (from here on **FX10**, **FX17**, and **RGB**) are used in a custom setup above a moving conveyor belt, but could also be mounted in the SisuRock frame. In both setups, even illumination of the respective imaged area is achieved by two (SisuRock) or four (conveyor belt setup) broad-band quartz-tungsten halogen units (without protective glass cover) covering the VNIR and SWIR. For all line scanners, the images are created over time by constant linear movement of the sample table. The RGB cameras are mounted in opposing angles of approximately 3–5° to allow later stereo matching and surface reconstruction. The Telops Hyper-Cam (from here on **HC**) is operated in a separate test stand allowing an easy adjustment of the sensor-target distance (see **Figure 4-2**).

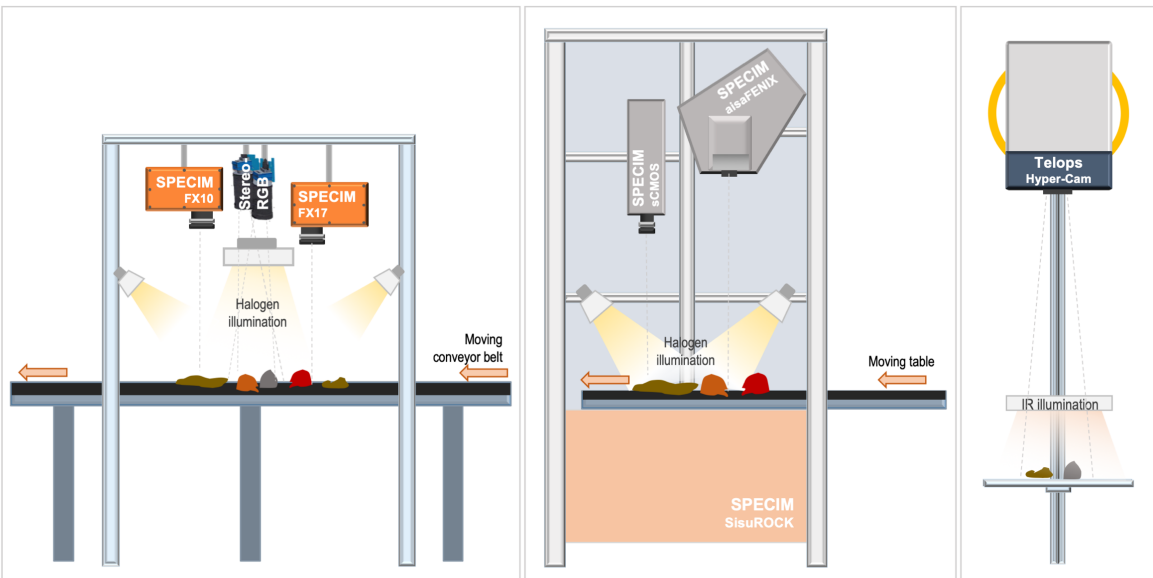

Figure 4-2. Schematic illustration of the experimental setup (not to scale). Detailed setup parameters can be found in Table 4-2.

The scene is illuminated by two STIR® infrared quartz radiators such that they provide the highest possible irradiance without a signal saturation at diffuse reflectors. Due to a short, but noticeable pre-heating phase the units are left switched on during the whole experiment; the samples are only moved into the scene right before image acquisition. In this way, heating of the sample is neglectable, i.e. the sample emissivity does not increase over the time of the measurement. For the subtraction of ambient radiation and temperature-

related sample emissivity, a dark scene without IR illumination is acquired in addition to each illuminated image. A sand-blasted aluminum panel of high reflectivity (~83%) is used as diffuse reflector to obtain the pure irradiance signal. The small FOV of the used lens and the sample-detector-distance of 1.77 m results in a high spatial resolution, but distinctly limits the image footprint. For this reason, four single images are needed to cover the presented sample set.

All sensors are used at no or low binning to take advantage of the maximum deliverable spatial and spectral resolution. Exposure time and frame rate are balanced to achieve sufficient signal response at a reasonable conveyor speed. The entire measurement series is conducted under directed artificial irradiance. Undirected irradiance from ambient light was reduced to avoid noise by unstable or flickering irradiance from ceiling lamps or daylight (especially at VNIR and SWIR). The sensor-target-distances are primarily defined by the minimal focus distance, but also adjusted to deliver a good compromise between spatial resolution and coverage.

4.3.2 Samples Analyzed

A batch of samples with different spectral, textural, and spatial features is investigated. This comprises several cut rocks and thick-sections (~2mm thickness) from different mineral deposits, two drill-core halves (cut face, one up and one down), one hand specimen, as well as three epoxy resin disks with Rare Earth Element (REE)-bearing minerals from important deposits around the world (**Figure 4-3**).

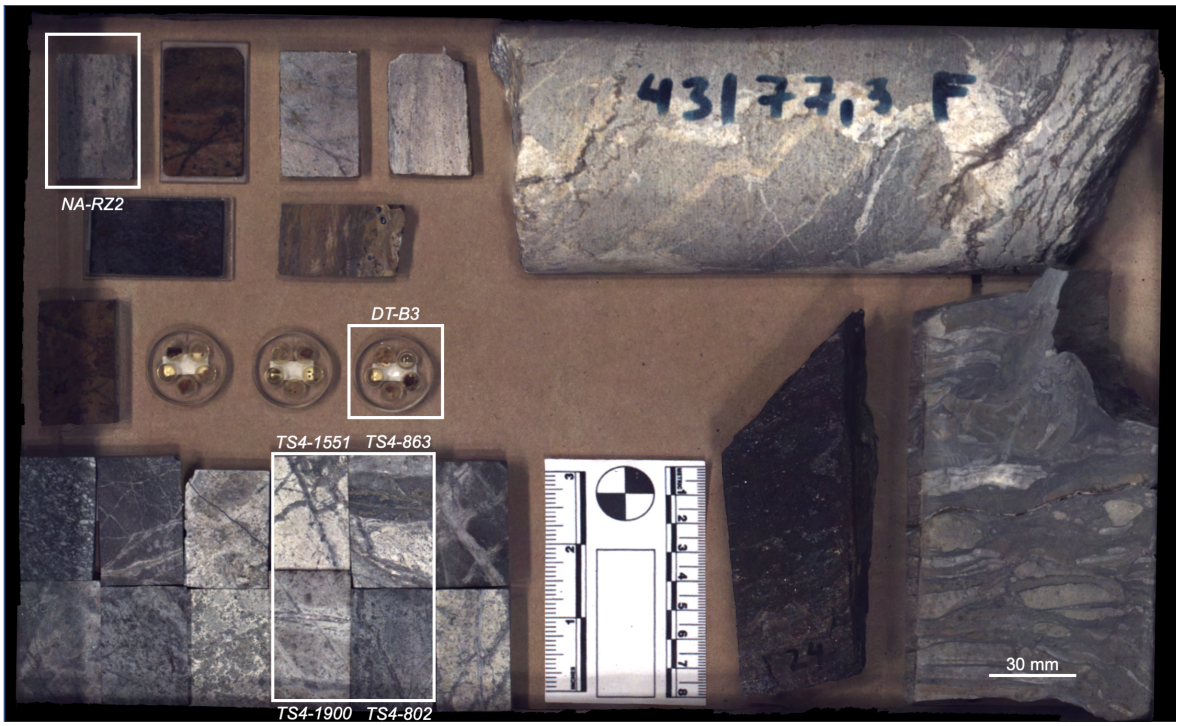

Figure 4-3. RGB photo of the analyzed sample setup, including thick- and thin-sections, drill-cores, hand specimen, and epoxy-resin embedded REE minerals. Sample analyzed in detail in current study are marked and labeled in white.

The samples are arranged and fixed on a tray to avoid any positioning changes between the single measurements. For clarity, only a subset of all samples will be depicted in the current study (marked with white frames in **Figure 4-3**). A detailed overview on those sample's respective type, origin, and mineralogy is given in **Table 4-3**.

Table 4-3. Overview on the analyzed samples regarding origin, surface treatment, and mineralogy. Sample positions are marked in Figure 4-3.

Sample Number	Origin	Sample treatment	Main mineralogy[1] / main REE (if applicable)[2]
NA-RZ2	Carbonatite, Namibia	Rock, clean cut	Cal, Ms, Ab, Ap, Fl / La, Ce, Nd
TS04-802	Copper-Gold-Porphyry, Romania	Rock, clean cut	Ms, Ab, Qz, Gp, Or, Fe-Oxide, An_{70}, Chm, Chl, Hbl, Ilt
TS04-863		Rock, clean cut	Qz, Ms, Py, Or, Gp
TS04-1551		Rock, clean cut	Qz, Ms, Ank, Or, Gp, Hbl
TS04-1900		Rock, clean cut	Qz, Ab, Ms, An_{70}, Gp, Or, Chm, Hbl, Py, Ilt
DT-B3	Miscellaneous	Embedded mineral grains, polished	Parisite / La, Ce, Pr, Nd, Sm, Y Bastnaesite / La, Ce, Pr, Nd, Sm

[1] MLA map > 1 area%, descending order, minerals abbreviated after IMA (International Mineralogical Association); [2] Rare Earth Elements > 0.1 wt.%, determined with Electron Micro Probe Analysis (EMPA, DT sample)

For spectral validation, all samples are analyzed at single reference points using the Spectral Evolution PSR-3500 (from here on **PSR**) and Agilent 4300 FTIR handheld spectrometer (from here on **FTIR**). Each PSR spectrum is the result ten consecutive, averaged measurements. A PTFE panel with over 99% reflectance in the VNIR and over 95% reflectance in the SWIR is used for reflectance conversion. Each FTIR scan is created by 32 consecutive, averaged measurements and converted to reflectance using a diffuse gold standard. Using this approach, each reference point is characterized by a continuous, high-resolution reflectance spectrum ranging from 0.35 µm (Near-UV) up to 15.4 µm (LWIR). From all rock cuts and thick-sections, high-resolution MLA maps exist.

4.3.3 Data Pre-processing

Teledyne Dalsa RGB:

The raw images are saved as bayer 8-bit frame, where the individual information for the red, green, and blue channel is saved side by side within a single channel in a grid-like pattern (**Figure 4-4**, left/middle). With knowledge of the color sequence, an RGB image can be calculated by respective interpolation of all red, green, and blue pixels as new separate image channels (**Figure 4-4**, right).

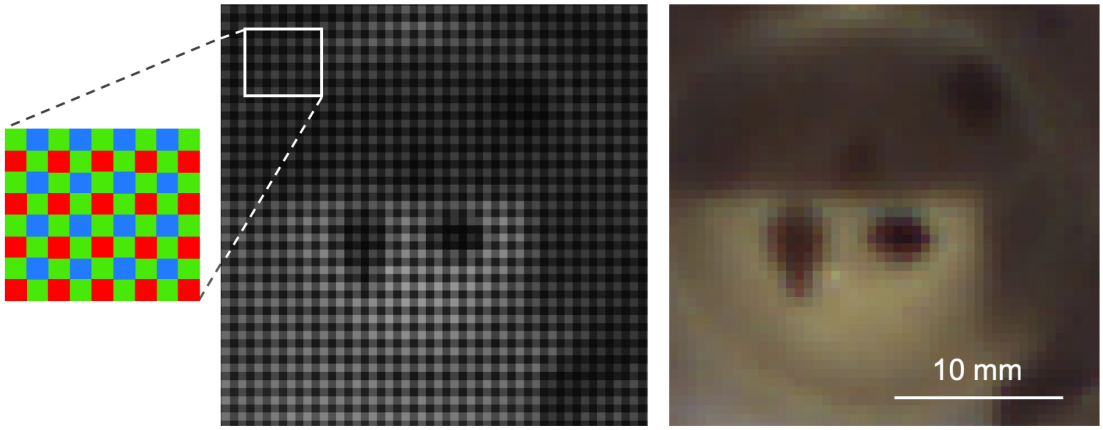

Figure 4-4. Schematic layout of a bayered RGB matrix (**left**), exemplary bayered RGB image (**middle**) and corresponding RGB image after de-bayering conversion (**right**).

The retrieved RGB image needs to undergo subsequent white-balancing, which is achieved with a white or grey PTFE reference target. The high frame rate and the off-nadir mounting of the two cameras returns images from the observed samples from different viewing angles. This dataset can be used to retrieve a

surface model of the covered samples. We use the SfM-MVS (Structure from Motion–Multiview Stereo, Westoby et al. 2012, Eltner et al. 2016) workflow implemented in Agisoft PhotoScan Professional 1.2.5. All processing parameters are adjusted to achieve the highest matching accuracy and model quality. The resulting model is cropped to the extent of the sample set. True-color orthophoto and digital surface model (DSM) are exported with a resolution of 0.05 mm per pixel. Scene-intern markers with known spatial relations are used to reference the exported data to a true scale. For position localization, we use an artificial Cartesian reference system.

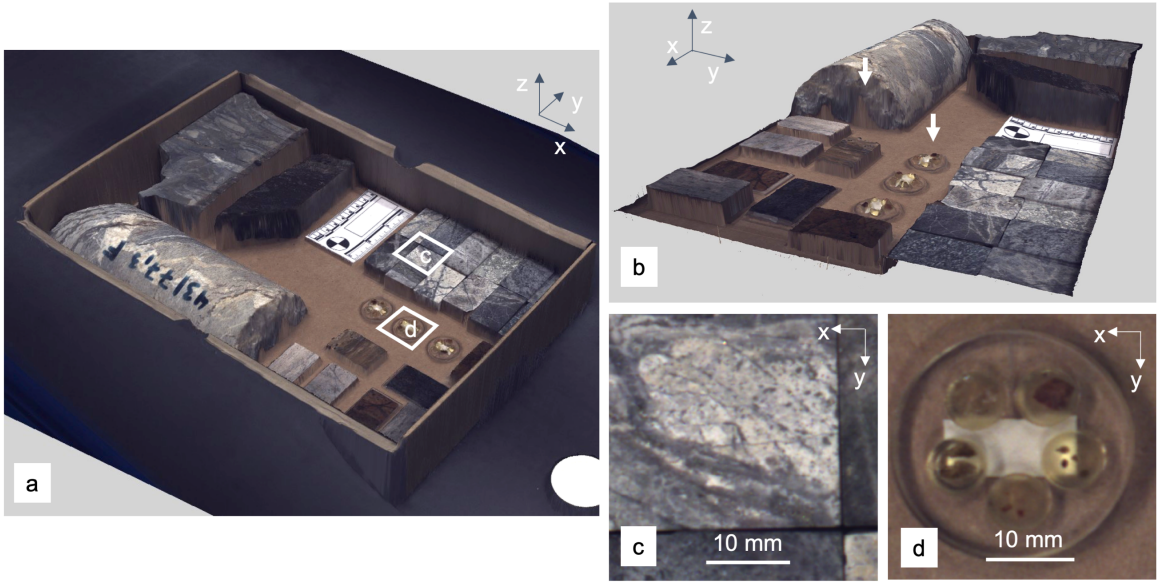

Figure 4-5. Results of the SfM-MVS 2.5D reconstruction. (**a**) Texturized model of the sample set, (**b**) side view to showcase artefacts at concealed regions and transparent objects (markers), (**c**, **d**) zoom to details marked in (a).

Specim HSI sensors:

The preprocessing of all push broom data is mutually similar. Before each measurement, several lines are acquired with closed shutter for dark current subtraction and with open shutter over three calibration targets. The targets consist of a white, grey, and black reference with known reflectance spectra averaging at >99%, 50%, and 6% reflectance in the VNIR, respectively. All calibration datasets are averaged over time (along scan direction) and used to convert raw digital number (DN) over radiance to reflectance. Radiance is retrieved by wavelength- and row-specific subtraction of the dark current from the raw image and subsequent multiplication with a sensor-specific calibration matrix. After this step, bad and hot pixel appear as single NaN or infinite values on the sensor. They can be automatically detected and subsequently corrected by interpolation. White, grey and black calibration target data are converted to radiance in the same manner, averaged separately, and used in an empirical line approach to convert the image to reflectance. In the resulting reflectance image, remaining lateral illumination differences can be detected in the reflectance distribution across the calibration targets. We use these differences for a row-specific correction to achieve a uniform illumination.

For the FENIX additional geometric corrections are required to remove the effect of signal diffraction at the sensor slit and a barrel distortion across the scanning direction. The respective correction factors are provided by the manufacturer.

Telops Hyper-Cam:

If the illumination on the sample is strong, but sample emissivity low to neglectable, reflectance, R, in LWIR data can be directly assumed from the dataset by

$$R = \frac{L_{ill} - L_{dark}}{DR_{ill} - DR_{dark}} \tag{4-1}$$

with L_{ill} and L_{dark} being radiance measurements with and without illumination, respectively, and DR_{ill} and DR_{dark} being the spectra of a diffuse reflector under the same conditions. This requires the acquisition of at least two datasets per analysis (dark and illuminated), where a diffuse reflector needs to be within the scene for each dataset. The image sets for each illumination condition are stitched to two separate image mosaics that are subsequently co-registered and subtracted from each other. The spectra DR_{ill} and DR_{dark} are calculated as mean over the imaged diffuse reflector.

Co-registration:

The consistent nadir orientation of all hyperspectral sensors allows a similar view on the sample set despite differing acquisition principles, spatial resolution, and FOV. This enables automatic image registration and orthorectification to the georeferenced RGB orthophoto by point detection and matching algorithms. We use Scale Invariant Feature Transform (SIFT, Lowe 1999) for the extraction of robust keypoints and the Fast Library for Approximate Nearest Neighbors (FLANN, Muja and Lowe 2009) for point matching. The calculated reference points are then used to apply a polynomial transformation on the respective image.

We experienced that in experiments with very dark or spectrally featureless samples sets matching failures occur and additional parameter adjustments are needed, which will prolonger the overall processing time. To increase matching accuracy, reliability, and speed, the usage of additional artificial keypoints within the scene is recommended. Especially in a combined sensor setup, high-contrast markers on the conveyor ease the registration of datasets by providing stable and easily detectable reference points.

Illumination effects:

The off-nadir mounting of the illumination units in all measurement setups provides a uniform illumination of the investigated samples and prevents core shadows (compare section 1.3.2). Remaining reflectance deviations due to illumination are mostly related to cast shadows near sharp object borders, whenever one of the irradiance sources is blocked. Where two illumination sources used, e.g., in the FENIX setup, this results in shadows along the scanning direction, whereas with four lamp units, e.g., RGB, FX10, FX17, shadows both along and across scanning direction can be observed (compare **Figure 4-6**). The manifestation of the shadows within the datasets is additionally dependent on the relative position of sensor and illumination units, which results in different shadow patterns in each dataset. Corrections with methods used for topography induced illumination in remote sensing data, such as *minnaert* or *c-factor*, are not applicable due to the large variety of illumination angles. Accurate modelling of the irradiance is theoretically possible, but extremely complicated, and would need to be done for each sensor and sample set separately. As the shadows are affecting mostly the sample tray and not the samples themselves, the influence of illumination differences can be neglected for this study.

Sample-background separation and masking:

The separation of samples and background is a required task to both reduce data size and enhance feature extraction performance. Especially for larger amounts of irregularly shaped samples, manual masking is not possible within a reasonable time. Automatized classification based on spectral features or reflectance intensity usually fails whenever the spectral response of the background is similar to that of the sample.

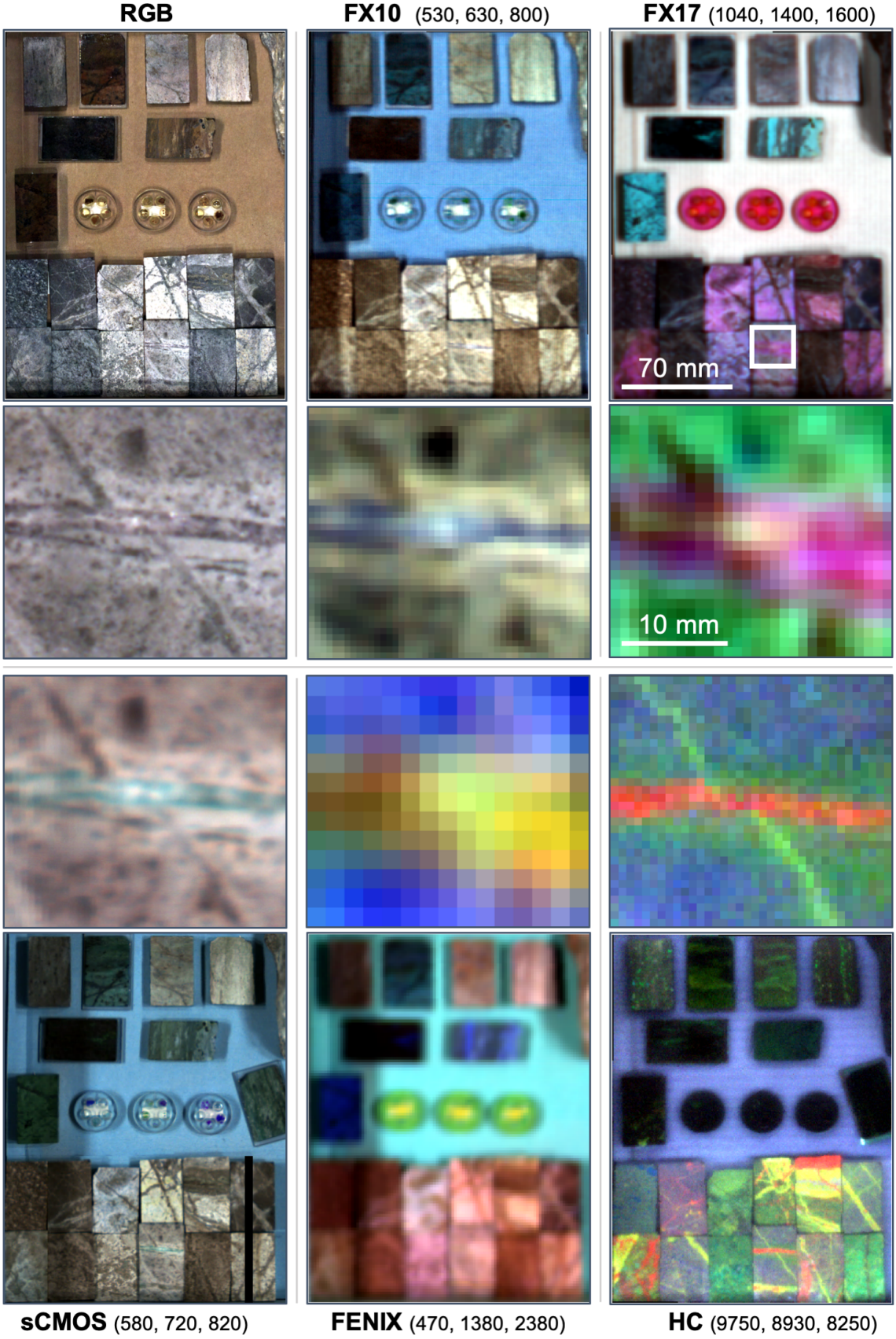

Figure 4-6. Spatial overview on the acquired datasets, shown in false color RGB (displayed wavelengths in parenthesis). For each dataset, an overview image and a zoom on the top half of sample TS04-1900 is shown.

This happens for example when the sample tray is dusty or with dark and featureless samples. An extraction based on elevation information only is also not reliable as the borders of very flat samples such as thin sections can be easily mistaken for background and, vice-versa, slopes or artefacts in the background as samples (**Figure 4-7**, left). We suggest a sample-background separation based on both contours and elevation data. Both can be retrieved from the high-resolution stereo RGB data. In the current case, first a slope map is calculated from the previously provided photogrammetric DEM, indicating abrupt changes in elevation due to evident samples by increased values (**Figure 4-7**, middle). These changes can be extracted as contours, e.g. by using the approach of Suzuki and Abe (1985), which is implemented in the OpenCV toolbox (Bradski 2000). Subsequently, the average elevation values within each contour are compared to the expected background elevation. Whenever this value exceeds a certain threshold height, the specific contour is identified as sample. With this approach, even transparent, flat or neighboring samples are detected, while elevation artefacts or markers in the non-sample areas are ignored (**Figure 4-7**, right). The final mask is then resampled and applied to any co-registered dataset.

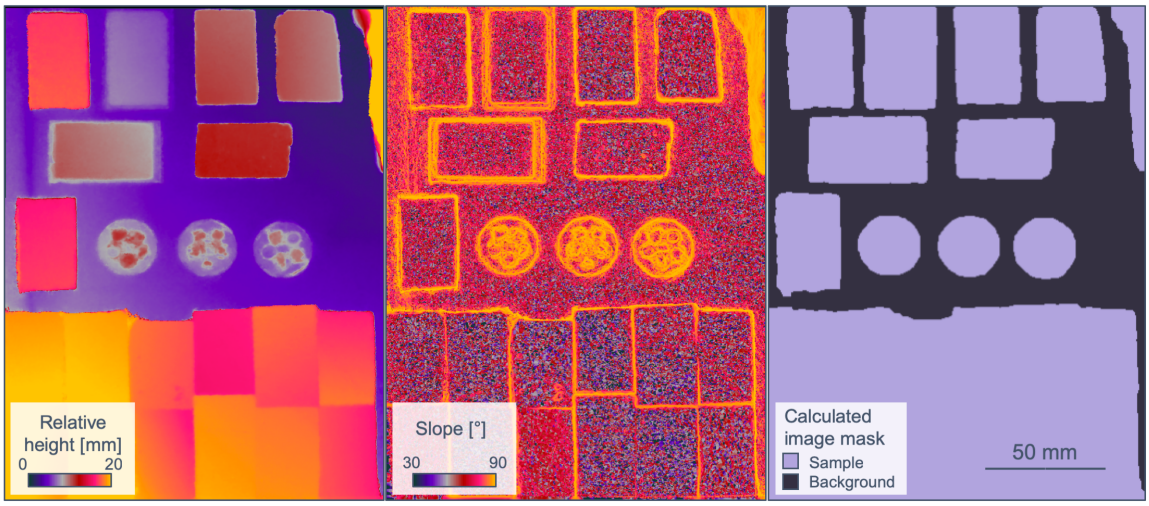

Figure 4-7. Left: elevation (relative height from sample tray); **middle:** first derivative (slope) of the elevation image; **right:** binary mask based on both slope contours and elevation.

Validation:

Spectral validation data from different point sensors are acquired at the same locations. The spectra of each point are stacked to create a continuous validation spectrum ranging from 0.35 up to 15.39 µm for each validation point. Available MLA data are resampled to a pixel size of 0.15 mm to match the pixel size of the Teledyne RGB sensors. During the resampling, the area proportion of each mineral phase within one output pixel is determined and stored as pixel value in a separate channel of the output image. In this way, a datacube of separate mineral maps is created, maintaining the information of all mineral phases and allowing the visualization of the relative abundances of specific mineral phases. Subsequently, all MLA maps are geometrically referenced on the dataset to provide a 2D mineral map validation for the HSI results. The referencing is done manually. On some samples, MLA has been conducted on the counterparts of the imaged samples. Due to sample material that has been lost during the cutting and polishing process, the MLA data of these samples show slight deviations to the surface of the samples in the dataset. Especially in very heterogeneous samples this can lead to large visual differences, complicating the comparison to image-derived maps and causing false negatives during the validation.

4.3.4 Feature Extraction and Classification

Feature extraction is conducted using the orthogonal total variation component analysis (OTVCA, Rasti et al. 2016) method. The algorithm aims to find the best representation of a high dimensional HS input in a low dimensional feature space by optimizing of a non-convex cost function. To preserve the spatial structure of the features, OTVCA solves a total variation (TV) penalized least square cost function subjected to an orthogonality constraint. This constraint achieves the consideration of spatial neighborhood information during feature extraction, leading to spatially smoother features and the inclusion of spatial relationships in subsequent classification. From each single-sensor dataset, around five to seven spectrally and spatially meaningful image features are extracted to achieve a dimensionality near to the number of expected classes. The exact number of features is decided upon a visual check. The resulting image features of all sensors are stacked and resampled to the input file with the finest spatial resolution (here: sCMOS). This creates a spatially highly resolved image containing the most important spectral information of each input dataset, while at the same time featuring a highly reduced data size.

Classification is conducted by Support Vector Machine (SVM, using LibSVM by Chang & Lin 2011) with Radial Basis Function Kernel on single- and selected multi-sensor subsets of the OTVCA image feature stack. Compared to most supervised classification techniques such as maximum likelihood or multi-layer perceptron neural networks, SVM features a low sensitivity to the number of training samples and the homogeneity of classes (Melgani and Bruzzone 2004). With SVM, good classification accuracies can be achieved even at a high dimensionality discrepancy between input data and training samples. This mainly reasons in its concept, which is based on margin maximization rather than statistical criteria. This makes SVM advantageous for our dataset, which is characterized by a high dimensionality of the input data due to the multi-sensor approach, a limited amount of reliable training data and mineralogically mixed (heterogeneous) classes. The optimal hyperplane parameters C (parameter that controls the amount of penalty during the SVM optimization) and γ (spread of the RBF kernel) have been traced in the range of $\gamma = 2^x$ and $C = 10^y$, with x in [-3, -2, -1, 0, 1, 2, 3, 4] and y in [-2, -1, 0, 1, 2, 3, 4], respectively, using five-fold cross-validation (compare also Ghamisi et al. 2017a and 2017b). Both the classification image as well as the probability estimates for each class are exported. The classification accuracies are returned as Overall Accuracy (OA) and Average Accuracy (AA). While OA returns the percentage of all true positives on the total number of reference points, AA averages the separate true positive percentages of all classes. A comparison of both values allows statements on the homogeneity of class accuracies. A large difference between OA and AA indicates a lack in accuracy of only one or a few classes, while similar values of OA and AA report comparable classification accuracies between all classes.

4.4 Results

4.4.1 Spatial and Spectral Integration of the Multi-sensor Dataset

An overview on the processed and registered multi-sensor dataset is shown in **Figure 4-6**, illustrating the large differences in spatial resolution. The co-registration of all datasets allows the comparison of spectra retrieved with different sensors at the exact same spot. The best co-registration results are achieved if spectral range or spatial resolution of base and dataset to register are comparable, which can be used to retrieve faster and more reliable matching results. For example, due to their more comparable spatial resolution, the number of good matches between FX17 and FX10 data is much higher than between FX17 and the RGB orthophoto. In contrast, FX10 data can be matched well to the RGB base due to their overlapping

wavelength ranges, and after registration serve itself as new base for the matching of FX17 data. Such, we are able to register all datasets fast and automatically to a common and meaningful reference space.

A respective spectral overview is displayed in **Figure 4-8**, showcasing the covered spectral ranges of each sensor compared to the spectral point measurements and MLA information for one sample spot. All displayed spectra have been retrieved from the same spatial position. Differences in spectral shape are mainly caused by the different spatial pixel size of each sensor and slight spatial deviations of the acquisition position during the spectrometer point measurements. By extracting the MLA information for each position and spot size, the mineral interpretation of observed spectral features can be supported and validated.

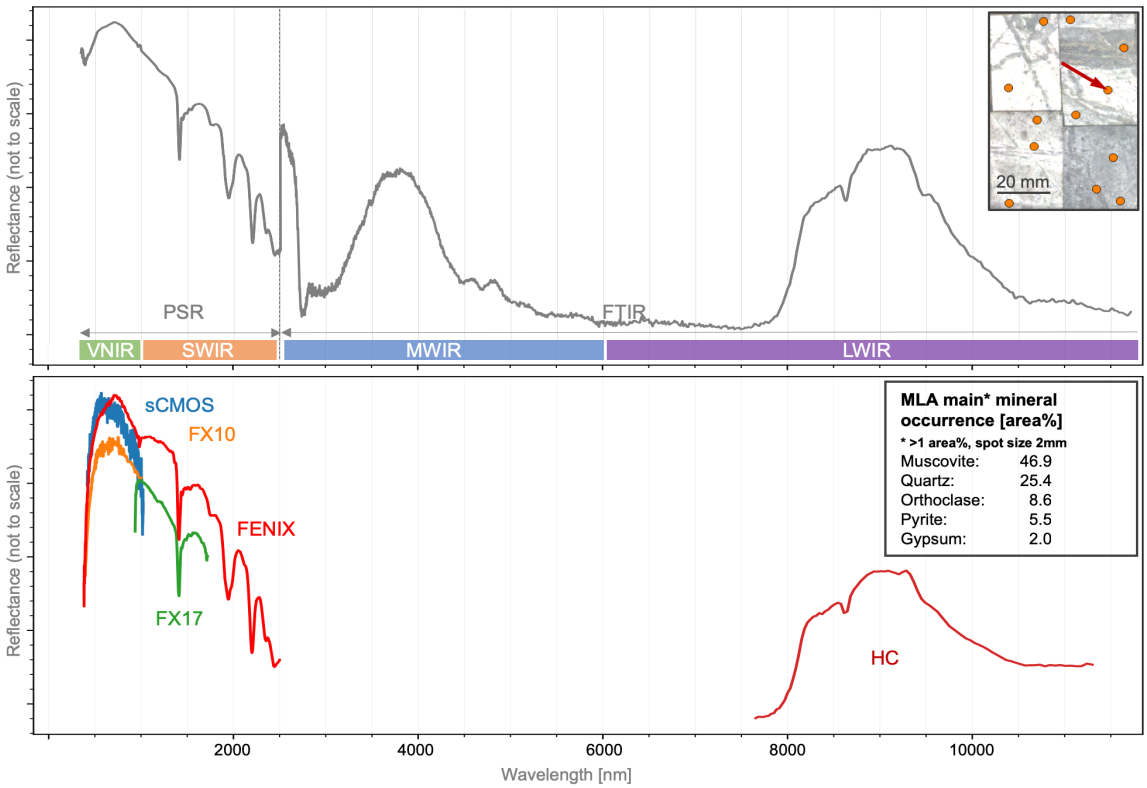

Figure 4-8. Overview on the spectra from different sensors at one validation point on sample TS4-863. **Top**: Merged validation point spectra and position of the measured spot; **bottom**: image spectra and MLA information for the same spot.

To showcase the influence of the sensors' spatial and spectral resolution as well as sensitivity, a set of small-grained REE-bearing minerals is analyzed using all sensors covering the VNIR. The high REE content is spectrally expressed by a range of Nd^{3+}-characteristic absorption features (**Figure 4-9**, lower left, absorption positions validated by Turner 2015). The depth of the most prominent absorptions at 741 and 800 nm can be used to create REE abundance maps for each sensor (**Figure 4-9**, top row). The influence of the spatial resolution is apparent, with highly detailed maps derived from the sCMOS, resolving even smallest grains, down to highly mixed pixels of the FENIX, where several small grains are fused into one larger object. The spectra of the largest mineral grain were extracted for each sensor at the same position and compared to a validation spectrum acquired with the PSR (**Figure 4-9**, bottom row). The sCMOS, with the highest spectral sensitivity and resolution (compare **Table 4-1**), delivers an accurate spectrum resolving even small details. Besides a decreased SNR, the spectrum is free from artefacts. The lower spectral resolution of the FX10 causes a loss in spectral detail, however, the intensity of the visible spectral features is maintained. Spectral

artefacts, such as near 680 nm, complicate the reliable analysis of smaller features. Due to the large spatial pixel size and resulting increased spectral mixing, the FENIX spectrum shows a lowered depth of the visible REE features at similar overall reflectance intensity. However, the SNR and spectral resolution are sufficiently high to provide a clear spectrum depicting even smaller features.

4.4.2 Multi-sensor Data Fusion for Image Classification

For feature extraction and classification, two representative sample subsets with different mineralogy and spatial class distribution are selected from the sample set imaged (compare also **Figure 4-3**): sample NA-RZ2 (from hereon named **RZ2**); and samples TS04-802, TS04-863, TS04-1551, and TS04-1900 (from hereon named **TS4**). All single-sensor datasets are cropped to the extents of RZ2 and TS4.

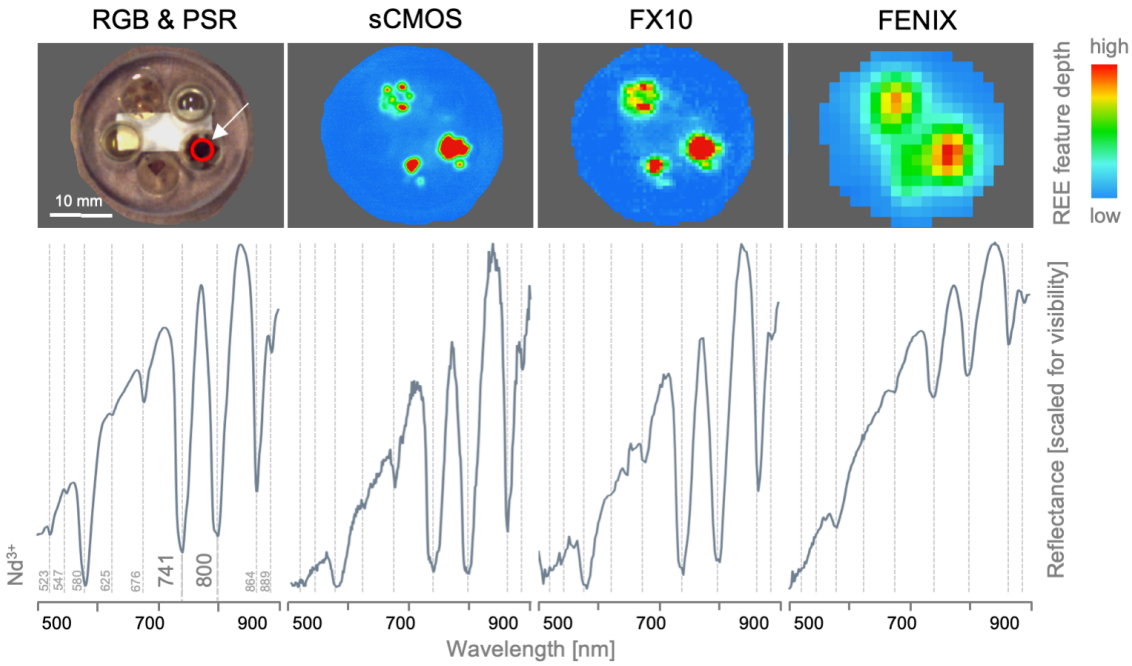

Figure 4-9. Influence of spectral and spatial resolution and sensitivity of the used VNIR sensors on the mapping of small-scale absorptions on the example of single REE grains. **Top row**: RGB image and sensor-specific REE maps (mean of the depths of the Nd^{3+}-characteristic absorptions at 741 and 800 nm). **Bottom row**: Single-pixel reflectance spectra of the same spot (marked with red circle) of portable spectroradiometer (PSR, outer left) and HS sensors.

For RZ2, five mineralogically meaningful classes are defined, i.e. albite, apatite, muscovite, a goethite-dominant phase (with small amounts of calcite) and a calcite-dominated matrix (with small amounts of Fe and Si). For the last two classes, the grain size of the individual minerals lies below the resolution of the MLA, thus, they need to be considered as mineralogically mixed. The spatial coverages of the classes are highly unbalanced, the matrix alone accounts for 75% of the sample area, while the other classes are around 5% each. As the MLA map was taken from the exact sample surface, a direct validation is possible. Such, the MLA information is used to select the mineralogically most pure pixels (about 50% of all pixel) as test data, of which only 100 pixels for each class are excluded and used as training data (0.3% of all pixel). A substantially higher amount of training data cannot be achieved for this sample due to its highly unbalanced spatial distribution of classes.

For TS4, six mineralogically meaningful classes are defined, i.e. quartz, gypsum, anhydrite, muscovite, the feldspars (Or, Ab, An_{70}), and the sulfides (Py, Cp). Due to the material offset between the available MLA validation maps and the imaged surface, only a visual validation is possible. Additionally, MLA is not able

to distinguish gypsum and anhydrite, as the mineralogical difference is matter of the water content. Thus, the training data of TS4 is selected manually. Besides the MLA maps, the selection is guided by characteristic features apparent in the image spectra; and the analysis of validation spectra in regions uniform within the extracted OTVCA features. For each class, around 50 pixels are selected and split randomly into a test and training dataset of around 25 pixels per class each. Compared to RZ2, all classes are approximately balanced, however, subpixel mixtures of some classes occur, especially between muscovite, quartz, and feldspars.

The achieved SVM classification accuracies for sample subsets RZ2 and TS4 are plotted in **Figure 4-10**.

Figure 4-10. Achieved classification accuracies in sample subsets RZ2 (**left**) and TS4 (**right**) using single-sensor data, selected multi-sensor combinations as well as the complete multi-sensor dataset (labeled "All" for SVM on the complete dataset and "All-mean" for an averaging of all single-sensor SVM results).

Shown are OA and AA for several classification attempts, using OTVCA features of single sensors only as well as specific multi-sensor combinations. The complete multi-sensor dataset is classified in two different ways: (1) using SVM on all input bands as in the proposed workflow (labeled "All") and (2) by majority voting of all single-sensor SVM results (labeled "All-mean"). For different sensor combinations, the respective class images and probability estimates of each class are displayed in **Figure 4-11** for RZ2 and in **Figure 4-12** for TS4 next to the available MLA mineral maps. Classification accuracy assessment of RZ2 shows a high difference between OA and AA for most single-sensor and some multi-sensor input. The main reason lies in the fine-grained texture and unbalanced distribution of classes in the sample. Four out of five classes occur finely distributed with grain sizes below the spatial sampling distance of most sensors used. Despite mineralogically well-defined training and test data, the related pixel spectra often contain a mixture of classes. The classified extents of the spatially inferior classes are, thus, often strongly exaggerated. This negatively affects the classification accuracy of the calcite-dominated class, which covers the largest part of the sample. The resulting unbalanced accuracies between the single classes become visible as increased offset between OA and AA. The fusion of the spectrally most expressive sensors (FENIX, HC) with spatially

well resolved input (sCMOS, FX sensors) retrieves the best classification accuracy, visual coherence and class separation. It even allows the true positive classification of objects borders lying in the subpixel space of some datasets.

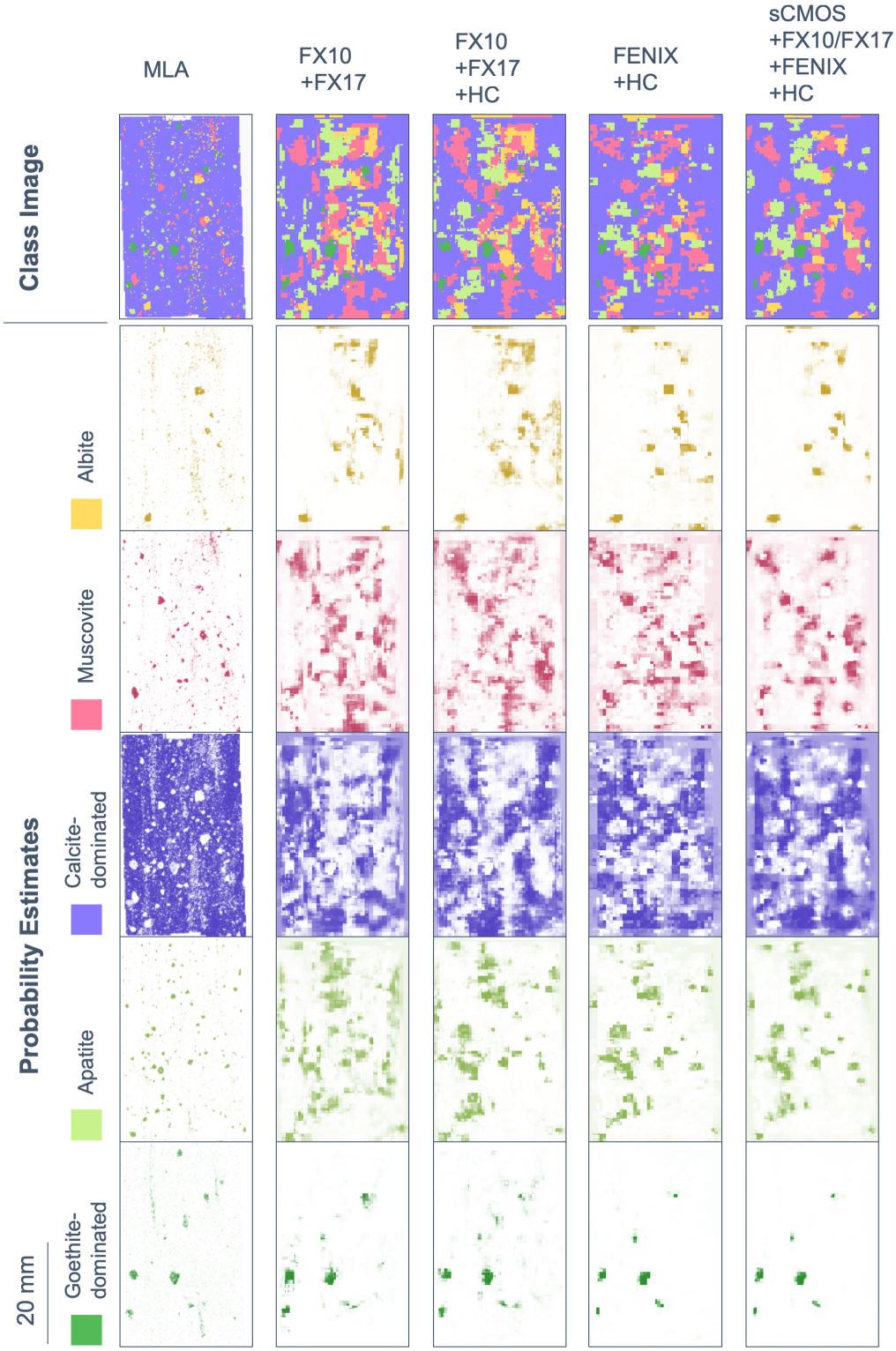

Figure 4-11. Results of SVM mapping of the five most abundant minerals and mineral groups in sample subset RZ2 using selected multi-sensor combinations, compared to the available MLA information.

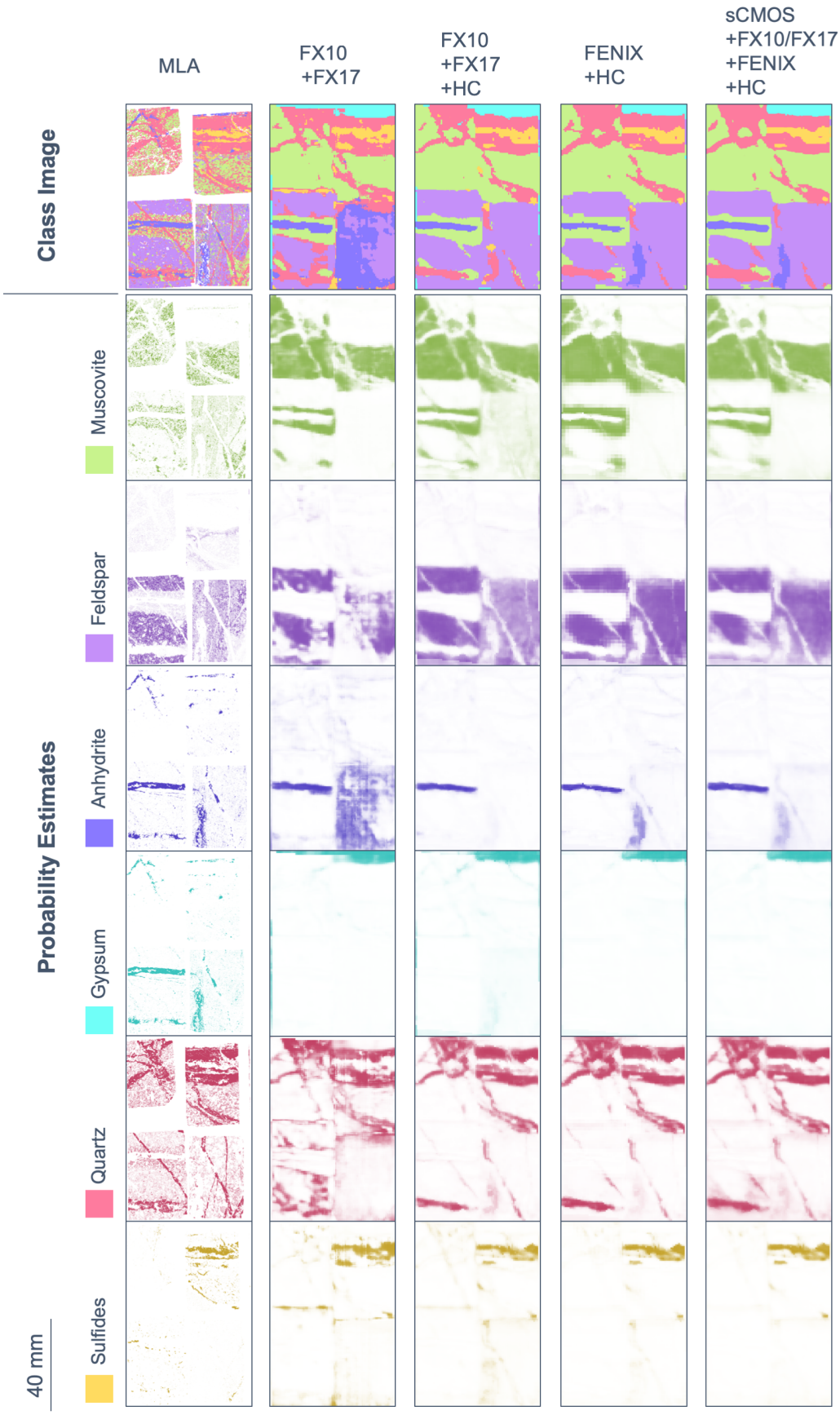

Figure 4-12. Results of SVM mapping of the six most minerals classes (labeled with dominant mineral) in sample subset TS4 using selected multi-sensor combinations, visualized next to the MLA information of the sample counterpieces. Mind that gypsum and anhydrite are not separated by MLA.

Sample subset TS4 features a better balancing between classes, however the training data is much sparser and the classes less distinct. For example, the abundances of quartz, muscovite, and feldspar are often correlated, which generates fluent transitions between the classes labeled as quartz-, muscovite- and feldspar-dominated, respectively. However, the prior extraction of image features and corresponding assignment of training pixels allows a proper discrimination in the classification. The classes gypsum and anhydrite, which cannot be separated in MLA analysis, are clearly distinguished in the spectral data. In general, the classification accuracies and visual validation show that the use of multi-sensor data in general achieves better a classification than the use of single-sensor data. Comparing FX10/FX17 and FX10/FX17/HC, the added value of LWIR data for the accurate discrimination of silicates becomes striking, especially when comparing the probability estimate maps of quartz and feldspar. However, the FX sensors can already give a fair estimation of the distribution of these classes, in particular with respect to the lack of O-Si-O stretching bonds in their spectral range. Here, the advantage of prior image feature extraction accounts, as it does not limit the classification to discrete absorption features, but allows general spectral and spatial patterns to be recognized.

Similar to sample RZ2, the fusion of spectrally meaningful data with spatially highly resolved images enabled the mapping of objects and structures lying in the subpixel scale of the coarser resolved input. Such, the fusion of FENIX data with finer resolved HC data allows the clear separation of veins, which have a width of only half the size of a FENIX pixel. Expectedly, the further inclusion of spatially highly resolved VNIR and lower SWIR data (FX and sCMOS), achieved the highest classification accuracy of all tests. Visual validation confirms its classification outcome as overall best result, too.

Both datasets show that SVM on multi-sensor data ("All") achieves higher accuracy than averaging/majority voting of previously calculated single-sensor-SVM ("All-mean"). With multi-sensory input, a concurrent evaluation of features in several input data is possible, while unrelated information can be suppressed. In contrast, the combination of single SVM-results may give weight to data inconclusive for the evaluated class and, by that, decrease the classification accuracy.

Cross-validation at every performed SVM has been observed a crucial step, for example, the cross-validation accuracy for the multi-sensor dataset at TS4 can vary between eight and 99.3% depending on the chosen parameters.

4.5 Discussion

The proposed workflow has proven to fuse multi-sensor data regardless of their initial spatial and spectral characteristics. It allows the simultaneous analysis of spectral and spatial features of one mineral class in different wavelength ranges. Such, spatially highly resolved data can be fused with spectrally sensitive and diverse sensor information to accurately map even small-scale complex mineral structures. The precedent extraction of image features using OTVCA reduces dimensionality and data size, and by that eases the handling of multi-sensor data. Highly advantageous is the possibility to fuse information from data with very different spectroscopic properties, such as VNIR/SWIR and LWIR data. Future studies could extend the data input beyond reflectance data and include for example information from photoluminescence or Raman scattering experiments.

Secondly, the results show that data integration based on machine learning allows the selection of a smaller number of sensors required to solve a specific classification problem. The mineralogical composition of most samples justifies the definition of mixed classes, distinguishing rather spectral domains that resemble characteristic mineral mixtures than single minerals. The used workflow allows to base the classification of these domains not only on distinct absorption features, but on any spectral and spatial variations. Such, we

are able to discriminate minerals that do not show specific spectral features in the currently used spectral range. For example, the FX sensors were able to discriminate the quartz, feldspar, and sulfide classes, that actually have no distinct spectral features in the covered VNIR and SWIR range. Even if the inclusion of the LWIR further increased the classification accuracies for these mineral domains, the result of the FX data is promising. It shows that using advanced image processing, sensors with reduced spectral range can still provide a meaningful classification of main mineral domains, suggesting the use of rather low-cost and fast sensors for a first sample classification. If a more detailed analysis on selected samples is required, sensors with optimized specifications for the current mineralogy can be applied. For a successful implementation of this approach, an accurate validation is crucial. It is required to define and interpret mineralogical classes, as well as for setting training and test data for the classification itself. The validation can be provided by detailed mineralogical analysis of selected samples, and by the spectral characterization of possible domains using accurate point spectrometer data.

According to the outcomes of the study, the applicability of the used HS sensors for specific tasks in lab-scale mineral mapping can be evaluated:

The FENIX achieved the coarsest spectral resolution; however, it offers the widest spectral range and an overall sufficient spectral quality with high SNR. It is the only tested HSI sensor covering the wavelength range between 2000 and 2500 nm, which is essential for the detection of minerals containing AlOH, MgOH, FeOH or CO_3^{2-} groups by their vibrational overtones. The FENIX is mostly not able to spatially resolve narrow veins or single mineral grains. Such, finely disseminated minerals of interest might be not detected when the intensities of their spectral features do not exceed the noise level of the encompassing mixed pixel spectrum. In contrast, the FENIX can provide an overview on the overall composition of the sample, distinguish lithological zones or larger veins. The data acquisition and pre-processing are quick and straight-forward and able to cover large sample batches in a reasonable time, making it an ideal tool for drill-core scanning. The combination with a sensor with higher spatial resolution has shown to overcome partly its spatial limitations and provide accurate classification of objects at subpixel size.

The FX10 and FX17 provide a less cost-intensive alternative to the FENIX camera. Of all tested sensors, they are able to acquire data at the highest speed, such being able to characterize large amounts material in a short time, such as ore moving on a conveyor belt. The pixel sampling in the current setup was about 1.7 (FX17) to 2.7 (FX10) times higher than those of the FENIX sensor, providing a distinctly higher amount of detail. With an adjusted measurement setup, even lower spatial sampling rates could be achieved, but at the cost of a lower area coverage. The observed SNR of the FX10 is lower than the FENIX', manifesting itself in stripy bands and noisier spectra. With a combined wavelength range of both FX sensors of 400 to 1700 nm the amount of detectable mineral features is, additionally, fairly limited, including mostly Fe^{3+}-, Fe^{2+}-, OH^-- and REE^{3+}-bearing minerals. While in a single-sensor setup this constrains the classification accuracy, a combined interpretation of both FX datasets is able to reach reasonable classification results even for mineral classes showing no distinct absorption features within the used spectral range. Overall the FX sensors are best suited for high-speed scanning and categorizing of samples with high spatial detail and limited spectral complexity, such as the analysis of mixed ore-waste streams.

Similar to the FX10, the covered wavelength range of the sCMOS sensor is limited to the VNIR, however, with the fore-optics used it offered the highest spatial and spectral sampling and sensor sensitivity of all HS sensors in the current setup. Operated at full resolution, this combination of specifications results in low scanning speeds and extreme data sizes. We recommend the use in this mode for the detailed analysis of selected samples only, for which it provides an ideal tool for the accurate mapping of REE even at low concentrations and host mineral sizes. By image feature extraction the data size can be substantially

decreased with only a small loss in spectral information; e.g., the extraction of five OTVCA features from sample set TS4 reduced the data size by the factor 45, for 15 extracted features by factor 16. The extracted components can be used as additional input for the classification of fine-grained samples. Despite the low added value for spectral interpretation sCMOS data has shown that its spatial information crucially increases the classification accuracy of such samples. In such cases, we recommend the acquisition of sCMOS data with full spatial but highly reduced spectral resolution. By this, acquisition speed and initial data size can be fundamentally decreased.

The HC is the only tested HSI sensor covering the LWIR, by that enabling the mapping of many important rock-forming minerals such as quartz, feldspars or carbonates. Its high spectral and spatial resolution allows for a detailed mapping of small veins and mineral grains. The SNR is sufficient to retrieve clear spectra at short illumination times. Despite being designed as frame imager, the Hyper-Cam can be also operated as quasi-line-scanner. By reducing the simultaneously acquired rows to a minimum (two to eight), frame rates of up to 30 Hz can be achieved. The respective scanning speed is reasonable for a future integration of the sensor in a joint setup with VNIR/SWIR push broom imagers. However, the high initial CAPEX (capital expenditure) of the sensor limits its application possibilities. Due to the wide and smooth nature of mineral features in the LWIR, a narrow-band multi-spectral sensor with a similar spatial resolution might be an asset.

4.6 Conclusion

We have shown that the integration of multi-sensor data with different spatial resolution and spectral range is feasible and highly advisable in near-field mineral mapping. Separate acquisition and subsequent data fusion allow for sensor-specific adjustments of experimental parameters and, thus, an optimal result and high flexibility in used sensors. Image feature extraction using OTVCA enables a strong reduction in dimensionality and memory size of each input dataset while maintaining the majority of its spatial and spectral information. This is in particular advantageous for sensors with very high spatial and/or spectral resolution, which are otherwise difficult to handle due to their large data memory requirements. The extracted features are not bound to the occurrence of specific absorption features, but recognize any spatial or spectral patterns. Such we are able to overcome differences in spectral range specific characteristics, e.g. for the fusion of VNIR/SWIR and LWIR data in combined classification approach using SVM. In parallel, the feature extraction approach enables the differentiation of classes with indistinct or mixed spectral features. These mineral domains can be discriminated even if the most characteristic spectral features of the single minerals are outside the analyzed spectral range, reducing the number of sensors required for an overview mapping.

For a more detailed spectral analysis, different multi-sensor combinations can be advantageous. A combination of sensors in the VNIR, SWIR, and LWIR allows a simultaneous detection of both alteration and rock-forming minerals and increases the detection reliability of certain minerals with features in different wavelength regions. The integration of very high spatial resolution data can be used to map mineralogically complex samples at a higher resolution than provided by the spectral dataset.

Within the workflow, stereo RGB cameras revealed a cost-efficient possibility to create high-resolution spatial imagery and surface elevation models, usable for detailed sample overview, data co-registration and sample/object detection. Due to their high spatial resolution, RGB stereo data can be a potential source for surface roughness analysis, texture classification and domain extraction in the future. Similar domains might be extracted from any other spatially expressive data sources and could be included in the image classification for a clearer delineation of classes. Further promising information to integrate could originate

from other surface mapping approaches beyond reflectance data, such as photoluminescence or Raman Scattering.

Acknowledgments: The Helmholtz Institute Freiberg for Resource Technology is gratefully thanked for supporting and funding this project. The authors thank the entire group of "Exploration Technology" for their constructive feedback. Special thanks go out to Benjamin Melzer for his profound support in sensor setup and data acquisition; David Turner[11] for the provision and discussion of appropriate and validated test samples; Isabel Cecilia Contreras Acosta for her expert advice on image classification; and finally, Moritz Kirsch and Erik Herrmann for manuscript review.

Author Contributions: Conceptualization, S.L., R.G. and P.G.; Formal analysis, S.L.; Investigation, S.L., P.S., R.Z.; Resources, P.S., L.T. and R.Z.; Software, S.L., P.S., M.K. and P.G.; Supervision, R.G.; Validation, S.L., L.T. and P.S.; Visualization, S.L.; Writing – original draft, S.L.; Writing – review & editing, P.S., R.Z., P.G. and R.G.

Conflicts of Interest: The authors declare no conflict of interest.

[11] Department of Earth, Ocean and Atmospheric Sciences, University of British Columbia, Vancouver, British Columbia V6T 1Z4, Canada

Chapter Discussion

The fusion of different datasets for a combined interpretation or as input for classification is a common task in remote sensing and becomes increasingly important as the sensor development proceeds. In the controlled environment of near-field or lab-scale measurements, the number of deployed sensors is not limited and can lead to high amounts of data that need to be processed in an automated and time-efficient manner. The usage of high-sensitive sensors is possible as the acquisition parameters can be optimized for any available sensor and environmental influences can be either neglected or controlled. This allows the acquisition of spectrally and spatially very detailed and accurate datasets in the required spectral ranges, but also implies high requirements on data quality. The most important sensor parameters for HS mineral analysis are usually speed/throughput, spectral range, high spatial resolution at a reasonable FOV as well as high spectral resolution at a reasonable SNR. The enhancement of one or several parameters inevitably increases the created data amount per time. Data processing, fusion and interpretation, however, need to happen within short time and at reasonable computing power, while still providing the best possible mapping results. Current approaches introduce the usage of spectral domains or mineral assemblage classes instead of application-wise often meaningless pure mineral endmembers. The domain approach allows the definition of application-important classes such as alteration zones, ore zones or mineralized veins. Due to the characteristic mixed composition, the classes are not characterized by one or several distinct spectral features or ratios only, but the overall spectral characteristics and shapes. This allows the discrimination of classes, which show no sharp and distinct absorption features within the observed spectral range, but a unique overall spectral tendency, shape or feature combination making them discriminable from other classes. Based on this approach, the sensor selection for the current task can be based on overall class discriminability instead of absorption occurrence. Training data required for the classification can be defined according to user knowledge, MLA maps, spectral point measurements, or a detailed mineralogical analysis of a smaller sample subset. An optimized workflow for training data selection and classification needs to be determined, such, first successful approaches were proposed by Tusa et al. (2018) and Contreras et al. (2018).

The core point of the workflow used in the current study is the dimensionality reduction of the acquired HS datasets using feature extraction. In HS remote sensing it is a common approach to tackle the otherwise high executable processing time as well as an issue known as “curse of dimensionality”, i.e. that a growing discrepancy between training and image dimensionality decreases the classification accuracy. Besides these reasons, feature extraction allows the integration of data that relies on different spectroscopic processes and is therefore not directly analyzable using the same methodology, such as SWIR and LWIR data or reflectance and photoluminescence data. Important pre-requisite for a successful integration is the prior co-registration of the data. The utilized automated keypoint detection and matching workflow was already successful implemented in the previous chapters and now provides an accurate and fast possibility to align multi-sensor datasets of different spatial sampling distances for a combined processing.

The choice of the applied feature extraction method crucially influences the outcome of the classification result, as it defines the information extracted from the data and passed to the classifier. A feature extraction method that considers both spatial and spectral aspects such as the used OTVCA algorithm is recommended, as it enhances the discrimination of classes with low spectral differentiability based on spatial patterns. The used classifier influences the accuracy of the classification result to a similar extend and should be chosen carefully. The SVM classifier used in the current study was chosen due its robustness against the low number of training samples and heterogeneity of classes of the used datasets. The determination of optimal

classification parameters by cross-validation is crucial to ensure the best possible classification result with the given data. While being an established step in image processing, it is, however, mostly ignored in the applicational field.

Besides the satisfying classification results achieved in the presented chapter, the used feature extraction and classifier algorithms might still be optimizable. A review of available methods and their added value for mineralogical domain mapping is a future task that could raise the awareness in the applicational community for innovative, but currently underrepresented feature extraction and classification algorithms. The extended usage of spatial information might be an additional future asset for a fast, unsupervised mineralogical analysis. Textural and linear features extracted from high-spatial-resolution image features of different spectral range could be used to extract mineralogical clusters, which are subsequently labeled according to their average spectral characteristics or point-wise geochemical analysis.

References

Armengol AA. Towards automated logging of ore: Positive Identification of Sulphides in the Ores of Agnico Eagle Kittilä and New Boliden Mines. MSc. Thesis, Luleå University of Technology, Sweden, **2015.**

Arne D, House E, Pontual S, Huntington J. Hyperspectral interpretation of selected drill cores from orogenic gold deposits in central Victoria, Australia. *Australian Journal of Earth Sciences* **2016**, 63 (8), 1003–1025. DOI: 10.1080/08120099.2016.1223171

Ayling B, Huntington J, Smith B, Edwards D. Hyperspectral logging of middle Cambrian marine sediments with hydrocarbon prospectivity: a case study from the southern Georgina Basin, northern Australia. *Australian Journal of Earth Sciences* **2016**, 63 (8), 1069–1085. DOI: 10.1080/08120099.2016.1204625

Baissa R, Labbassi K, Launeau P, Gaudin A, Ouajhain B. Using HySpex SWIR-320m hyperspectral data for the identification and mapping of minerals in hand specimens of carbonate rocks from the Ankloute Formation (Agadir Basin, Western Morocco). *Journal of African Earth Sciences* **2011**, 61 (1), 1–9. DOI: 10.1016/j.jafrearsci.2011.04.003

Bolin BJ, Moon TS. Sulfide detection in drill core from the Stillwater Complex using visible/near-infrared imaging spectroscopy. *Geophysics* **2003**, 68 (5), 1561–1568. DOI: 10.1190/1.1620630.

Bradski G. The opencv library. *Dr. Dobb's Journal of Software Tools* **2000**, 25 (11), 120, 122–125.

Broicher HF. Dilution control - online and real-time recognition of ore and waste by LIF. In: *Proceedings of the SME Annual Meeting*, Salt Lake City, US, **2005**, 05–66, 1–5.

Burley LL, Barnes SJ, Laukamp C, Mole DR, Le Vaillant M, Fiorentini ML. Rapid mineralogical and geochemical characterisation of the Fisher East nickel sulphide prospects, Western Australia, using hyperspectral and pXRF data. *Ore Geology Reviews* **2017**, 90, 371–387. DOI: 10.1016/j.oregeorev.2017.04.032

Chang CC, Lin CJ. LIBSVM : a library for support vector machines. *ACM Transactions on Intelligent Systems and Technology* **2011**, 2 (27). Software available at http://www.csie.ntu.edu.tw/~cjlin/libsvm

Clark RN. Chapter 1: Spectroscopy of Rocks and Minerals, and Principles of Spectroscopy. In: *Manual of Remote Sensing, 3, Remote Sensing for the Earth Sciences*, (A.N. Rencz, ed.) John Wiley and Sons, New York, 1999, 3–58.

Contreras IC, Khodadadzadeh M, Tusa L, Gloaguen R. A machine learning technique for drill core hyperspectral data analysis. In: *9th Workshop on Hyperspectral Image and Signal Processing: Evolution in Remote Sensing (WHISPERS)*, 23-26 Sep **2018**, Amsterdam, The Netherlands**.**

Dalm M, Buxton MWN, van Ruitenbeek FJA. Ore–waste discrimination in epithermal deposits using near-infrared to short-wavelength infrared (NIR-SWIR) hyperspectral imagery. *Mathematical Geosciences* **2018**, 1–27. DOI: 10.1007/s11004-018-9758-6

Eltner A, Kaiser A, Castillo C, Rock G, Neugirg F, Abellan A. Image-based surface reconstruction in geomorphometry—Merits, limits and developments of a promising tool for geoscientists. *Earth Surface Dynamics* **2016**, 4, 359–389. DOI: 10.5194/esurf-4-359-2016

Feng J, Rogge D, Rivard B. Comparison of lithological mapping results from airborne hyperspectral VNIR-SWIR, LWIR and combined data. *International Journal of Applied Earth Observation and Geoinformation* **2018**, 64, 340–353. DOI: 10.1016/j.jag.2017.03.003

Ghamisi P, Plaza J, Chen Y, Li J, Plaza AJ. Advanced Spectral Classifiers for Hyperspectral Images: A review. *IEEE Geoscience and Remote Sensing Magazine* **2017**, 5, 8–32. DOI: 10.1109/mgrs.2016.2616418

Ghamisi P, Yokoya N, Li J, Liao W, Liu S, Plaza J, Rasti B, Plaza AJ. Advances in hyperspectral image and signal processing: a comprehensive overview of the state of the art. *IEEE Geoscience and Remote Sensing Magazine* **2017**, 5 (4), 37–78. DOI: 10.1109/mgrs.2017.2762087

Gordon G, McAvaney S, Wade C. Spectral characteristics of the Gawler Range Volcanics in drill core Myall Creek RC1. *Australian Journal of Earth Sciences* **2016**, 63 (8), 973–986. DOI: 10.1080/08120099.2016.1264475

Hughes G. On the mean accuracy of statistical pattern recognizers. *IEEE Transactions on Information Theory* **1968**, 14 (1), 55–63. DOI: 10.1109/tit.1968.1054102

Hunt GR. Spectral signatures of particulate minerals in the visible and near infrared. *Geophysics* **1977**, 42, 501–513. DOI: 10.1190/1.1440721

Kendro K. Towards automated logging of ore: Positive Identification of Iron Oxide Minerals at Malmberget Iron Ore. MSc. Thesis, Luleå University of Technology, Sweden, **2015.**

Kopačková V, Koucká L. Integration of Absorption Feature Information from Visible to Longwave Infrared Spectral Ranges for Mineral Mapping. *Remote Sensing* **2017**, 9, 1006. DOI: 10.3390/rs9101006

Kruse FA. Identification and mapping of minerals in drill core using hyperspectral image analysis of infrared reflectance spectra. *International Journal of Remote Sensing* **1996**, 17 (9), 1623–1632. DOI: 10.1080/01431169608948728

Kruse FA, Weatherbee O, Peppin W, Bedell R, Calvin W, Taranik JV. HSI Mineral Mapping From Airborne, Outcrop, and Drill-Core Perspectives. In: *Proceedings of SPIE 7687: Active and Passive Signatures,* Orlando, US, **2010**, 76870K-1. DOI: 10.1117/12.855445

Kruse FA. Integrated visible and near-infrared, shortwave infrared, and longwave infrared full-range hyperspectral data analysis for geologic mapping. *Journal of Applied Remote Sensing* **2015**, 9, 096005. DOI: 10.1117/1.jrs.9.096005

Kuosmanen V, Arkimaa H, Tiainen M, Bärs R. Hyperspectral close-range LWIR imaging spectrometry – 3 case studies. In Airo M-L (Ed.): Geophysical signatures of mineral deposit types in Finland, Geological Survey of Finland, Special Paper 58, 117-144, **2015**.

Lowe DG. Object recognition from local scale-invariant features. In: *Proceedings of the International Conference on Computer Vision (ICCV),* Corfu, GR, 20–25 Sept **1999**, 2, 1150–1157. DOI: 10.1109/iccv.1999.790410

Mason P, Huntington J. HyLogger 3 components and pre-processing: An overview. Northern Territory Geological Survey, Technical Note 2012-002, **2012**.

Mathieu M, Roy R, Launeau P, Cathelineau M, Quirt D. Alteration mapping on drill cores using a HySpex SWIR-320m hyperspectral camera: Application to the exploration of an unconformity-related uranium deposit (Saskatchewan, Canada). *Journal of Geochemical Exploration* **2017,** 172, 71–88. DOI: 10.1016/j.gexplo.2016.09.008

Melgani F, Bruzzone L. Classification of Hyperspectral Remote Sensing Images With Support Vector Machines. *IEEE Transaction on Geoscience and Remote Sensing* **2004**, 42, 8, 1778–1790. DOI: 10.1109/TGRS.2004.831865

McDowell ML, Kruse FA. Enhanced Compositional Mapping through Integrated Full-Range Spectral Analysis. *Remote Sensing* **2016**, 8, 757. DOI: 10.3390/rs8090757

Muja M, Lowe D. Fast approximate nearest neighbors with automatic algorithm configuration. In: *Proceedings of the Fourth International Conference on Computer Vision Theory and Applications*, Lisboa, Portugal, 5–8 Feb **2009**, 1, 1–10. DOI: 10.5220/0001787803310340

Rasti B, Ulfarsson MO, Sveinsson JR. Hyperspectral Feature Extraction Using Total Variation Component Analysis. *IEEE Transactions on Geoscience and Remote Sensing* **2016**, 54 (12), 6976 – 6985. DOI: 10.1109/TGRS.2016.2593463

Reginiussen H. Borrkärneskanning vid SGU (in Swedish). Borrkärneskanning Workshop, Geological Survey of Sweden, Malå, Sweden, 26–27 Nov **2014**.

Ross P-S, Bourke A, Fresia B. A multi-sensor logger for rock cores: Methodology and preliminary results from the Matagami mining camp, Canada. *Ore Geology Reviews* **2013,** 53, 93–111. DOI: 10.1016/j.oregeorev.2013.01.002

Rost E, Hecker C, Schodlock MC, van der Meer FD. Rock sample surrface preparation influences thermal infrared spectra. *Minerals* **2018,** 8, 475**.** DOI: 10.3390/min8110475

Schodlok MC, Whitbourn L, Huntington J, Mason P, Green A, Berman M, Coward D, Connor P, Wright W, Jolivet M, Martinez R. HyLogger-3, a visible to shortwave and thermal infrared reflectance spectrometer system for drill core logging: functional description. *Australian Journal of Earth Sciences* **2016**, 63 (8), 929–940. DOI: 10.1080/08120099.2016.1231133

Suzuki S, Abe K. Topological Structural Analysis of Digitized Binary Images by Border Following. *Computer Vision, Graphics, and Image Processing* **1985,** 30 (1), 32–46. DOI: 10.1016/0734-189X(85)90016-7

Tappert M, Rivard B, Giles D, Tappert R, Mauger A. Automated Drill Core Logging Using Visible And Near-Infrared Reflectance Spectroscopy: A Case Study From The Olympic Dam IOCG Deposit, South Australia. *Economic Geology* **2011**, 106, 289–296. DOI: 10.2113/econgeo.106.2.289

Tappert MC, Rivard B, Fulop A, Rogge D, Feng J, Tappert R, Stalder R. Characterizing Kimberlite Dilution by Crustal Rocks at the Snap Lake Diamond Mine (Northwest Territories, Canada) using SWIR (1.90–2.36 μm) and LWIR (8.1–11.1 μm) Hyperspectral Imagery Collected from Drill Core. *Economic Geology* **2015**, 110, 1375–1387. DOI: 10.2113/econgeo.110.6.1375

Turner D, Rivard B, Groat L. Rare earth element ore grade estimation of mineralized drill core from hyperspectral imaging spectroscopy. In: *IEEE Geoscience and Remote Sensing Symposium*, Quebec City, QC, 13-18 July **2014**, 4612–4615. DOI: 10.1109/IGARSS.2014.6947520

Turner D. Reflectance spectroscopy and imaging spectroscopy of rare earth element-bearing mineral and rock samples. PhD Thesis, University of British Columbia: Vancouver, **2015**.

Tusa L, Andreani L, Khodadadzadeh M, Contreras C, Ivascanu P, Gloaguen R, Gutzmer J. Mineral Mapping and Vein Detection in Hyperspectral Drill-Core Scans: Application to Porphyry-Type Mineralization. *Minerals* **2019**, 9, 122. DOI: 10.3390/min9020122

Wang D, Lagerstrom R, Sun C, Laukamp C, Quigley M, Whitbourn L, Mason P, Connor P, Fisher L. Automated vein detection for drill core analysis by fusion of hyperspectral and visible image data. In: *23rd International Conference on Mechatronics and Machine Vision in Practice (M2VIP)*, 28–30 Nov **2016**, Nanjing, China. DOI: 10.1109/M2VIP.2016.7827317

Westoby M, Brasington J, Glasser N, Hambrey M, Reynolds J. "Structure-from-motion" photogrammetry: A low-cost, effective tool for geoscience applications. *Geomorphology* **2012**, 179, 300–314. DOI: 10.1016/j.geomorph.2012.08.021

Wotruba H, Harbeck H. Sensor-Based Sorting. *Ullmann's Encyclopedia of Industrial Chemistry* **2010**, Wiley-VCH Verlag GmbH & Co. KGaA, Weinheim. DOI: 10.1002/14356007.b02_18.pub2

Yuan J, Wang D, Cheriyadat AM. Factorization-Based Texture Segmentation. *IEEE Transactions on Image Processing* **2015**, 24 (11), 3488–3497. DOI: 10.1109/TIP.2015.2446948

CHAPTER 5 THE POTENTIAL OF REFLECTANCE AND LASER INDUCED LUMINESCENCE SPECTROSCOPY FOR NEAR-FIELD RARE EARTH ELEMENT DETECTION IN MINERAL EXPLORATION

Preface

The following chapter presents a novel, spectroscopy-based strategy for the detection of Rare Earth Elements (REE) in natural minerals.

For the first time, it combines advanced reflectance imaging spectroscopy with extremely sensitive laser-induced luminescence spectroscopy, which is not yet commonly used for mineral analysis in geosciences, and applies both to natural mineral samples from main REE-deposits around the world. The successful cross-validation of the results proves the method presented an innovative approach for non-invasive REE identification in raw material exploration with increased robustness and a widened range of detectable REE. The combined spectroscopic approach has a high potential to contribute to improvements in a wide range of REE-related research such as the understanding of mineralogy and evolution of deposits as well as REE detection at any step of the raw material value chain, such as in exploration, mining, processing, or recycling. Furthermore, it lays the basis for the development of an integrated imaging spectroscopic sensor system, which would have high potential for many other geoscience and materials science applications, where information of a sample's composition is required (e.g., provenience analysis, impurity analysis).

First results of this study were presented at the *10th EARSeL SIG Imaging Spectroscopy Workshop*[12] in Zurich in 2017. The full paper comprising the contents of this chapter was published as research paper in *Remote Sensing*[13] in 2018.

[12] Jakob S, Fuchs M, Gloaguen R. *10th EARSeL SIG Imaging Spectroscopy Workshop,* 19-21 Apr **2017**, Zurich, CH.

[13] Lorenz S, Beyer J, Fuchs M, Seidel P, Turner D, Heitmann J, Gloaguen R. *Remote Sensing* **2019**, 11, 21. DOI: 10.3390/rs11010021

The Potential of Reflectance and Laser Induced Luminescence Spectroscopy for Near-Field Rare Earth Element Detection in Mineral Exploration[14]

Sandra Lorenz [1], Jan Beyer [2], Margret Fuchs [1], Peter Seidel [1], David Turner [3], Johannes Heitmann [2], and Richard Gloaguen [1]

[1]Helmholtz-Zentrum Dresden-Rossendorf, Helmholtz Institute Freiberg for Resource Technology, Division "Exploration Technology", Chemnitzer Straße 40, 09599 Freiberg, Germany;
m.fuchs@hzdr.de (M.F.); p.seidel@hzdr.de (P.S.); r.gloaguen@hzdr.de (R.G.)

[2] Institute of Applied Physics, Faculty of Chemistry and Physics, Technische Universität Bergakademie Freiberg, Leipziger Straße 23, 09599 Freiberg, Germany;
jan.beyer@physik.tu-freiberg.de (J.B.), johannes.heitmann@physik.tu-freiberg.de (J.H.)

[3] Department of Earth, Ocean and Atmospheric Sciences, University of British Columbia, Vancouver, British Columbia V6T 1Z4, Canada, dturner@eoas.ubc.ca (D.T.)

5.1 Abstract

New energy, transport, computer, and telecommunication technologies require an increasing supply of rare earth elements (REEs). As a consequence, adequate and robust detection methods become essential for the exploration and discovery of new deposits, the improved characterization of existing deposits and the future recycling of today's high-tech products. Within this paper, we investigate the potential of combining passive reflectance (imaging and point sampling) with laser stimulated luminescence (point sampling) spectroscopic measurements across the visible, near, and shortwave infrared for REE detection in non-invasive near-field mineral exploration. We analyze natural REE-bearing mineral samples from main REE-deposits around the world and focus on challenges such as the discrimination of overlapping spectroscopic features and the influence of the mineral type on detectability, feature position, and mineral matrix luminescence. We demonstrate that the cross-validation of results from both methods increases the robustness and sensitivity, provides the potential for semi-quantification and enables the time- and cost-efficient detection of economically important REE, including Ce, Pr, Nd, Sm, Eu, Dy, Er, Yb, and potentially also Ho and Tm.

Keywords: laser induced luminescence spectroscopy, reflectance spectroscopy, hyperspectral imaging, laser-induced fluorescence, photoluminescence, rare earth elements

5.2 Introduction

Rare earth elements (REE) are a group of 17 metallic elements, comprising the lanthanoid group, yttrium and scandium. With their valuable physical and chemical characteristics such as unique magnetic, phosphorescent, and catalytic properties, they represent crucial components of many nowadays high-tech consumer products and green technologies. Due to their unique characteristics and both globally and element-wise inhomogeneous occurrence, REE were included in the European Commission's Critical Raw Materials list published in 2014 and updated in 2017, which set the safeguarding of a sustainable supply of raw materials within the European Union as key priority. Especially Neodymium (Nd), Europium (Eu), Terbium (Tb), Dysprosium (Dy), and Yttrium (Y), as well as Praseodymium (Pr) as a substituent for Neodymium in high-intensity permanent magnets, are commonly indicated as the most critical rare earths for both short and long term, based on their role in clean energy as well as supply risk (Bauer et al. 2010, Moss et al. 2013, Guyonnet et al. 2015, Nassar et al. 2015). The increasing importance of these critical raw

[14] Published: Lorenz S., Beyer J., Fuchs M., Seidel P., Turner D., Heitmann J., Gloaguen R. *Remote Sensing* **2019**, *11*, 21. DOI: 10.3390/rs11010021 (Author's post-print version)

materials for modern civilization and the associated striving for sustainability and efficiency has equally increased the need for non-invasive and fast detection methods in exploration and mining.

Common approaches for the detection of REE deposits in remote sensing rely on indirect mapping of the host lithology or associated structural features from air- or space-borne data (Rajendran et al. 2013, Zimmermann et al. 2016, Shavers et al. 2018). For direct REE detection in the near field (sample-detector distance from centimeter up to meter scale) such as for field validation and the logging of bulk samples or drill cores, two spectroscopic approaches have independently shown their potential as alternative to time-consuming geochemical analysis, that is, reflectance and laser-induced photoluminescence (PL) spectroscopy (e.g., Friis 2009, Turner et al. 2015). Reflectance spectroscopy refers to the analysis of the characteristic reflectance signal of a material illuminated with a spectrally broad-band light source. PL spectroscopy refers to the measurement of the luminescence of a material excited with a spectrally narrow-band light source such as a laser or high-power LED. Several studies have been published on REE characterization by one or the other method (see following chapter). Nevertheless, none prevailed as standard for reliable REE detection yet. Important reasons are the detection limitations of reflectance spectroscopy and the complicated interpretation of PL in natural minerals. A complementary approach to combine fast and straight-forward reflectance with highly sensitive PL spectroscopy could be a promising solution, however, the methods have, to our knowledge, never been compared or integrated in a combined REE detection approach.

This motivated us to investigate the detectability of REE in natural minerals using both reflectance and PL spectroscopy. As we strive to assess the benefits and obstacles of an integrated result analysis for the new task of REE mapping, we use sample-detector distances from centimeter up to meter scale. We focus on the analysis of the potential gain in interpretation reliability as well as additional constraints of the combined approach. We decided to use a preferably simple and robust methodology, as the goal is to use this technology in mining operations, such as for ore grade assessments along conveyor-belts. We separately acquire continuous-wave laser-induced luminescence measurements under three different excitation wavelengths and reflectance imagery using two recent light weight hyperspectral (HS) sensors. To evaluate detection limits and determine the influence of different sample composition, we use a geochemically well-characterized collection of natural REE-bearing samples of a wide range of mineral hosts and origins. We first analyze each acquired dataset separately to evaluate their specific characteristics. We then use the results for combined interpretation and cross-validation.

The outcomes of this study are, besides the added value in REE detectability and robustness, a required basis for the future development of an integrated sensor which allows the operational application of the combined spectroscopic approach for routine REE mapping in complex natural rock samples and drill-cores.

5.3 Previous Studies of REE Spectroscopy

5.3.1 NIR-SWIR Reflectance Spectroscopy

In contrast to transition elements, trivalent REE ions are characterized by very pronounced and sharp absorptions features. They are based on particularly confined electronic 4f levels, localized close to the nuclei, from which electrons can be excited by incident radiation and which are comparably unaffected by different chemical environments (Adams 1965).

Early fundamental work on the reflectance spectroscopy of free REE^{2+} and REE^{3+} ions was provided by Dieke and Crosswhite (1963), followed by a range of studies on the detection of single REE in synthetic compounds and the effects of grain size and crystal orientation, such as in Jassie (1964, $REECl_3 \cdot 6H_2O$ and $REEWO_4$

powders), White (1967, REE_2O_3), Ropp (1969, $REEPO_4$), and Weidner et al. (1986, REE_2O_3). In parallel, foundation work on natural minerals was started such as by Adams (1965), who recognized differences between the absorption patterns of light (LREE) and heavy REE (HREE)-dominated as well as mixed samples. Later, Rowan et al. (1986) started to analyze specific REE in natural carbonatite samples of different origin, focusing on the investigation of the absorption wavelength position and depth of Nd and Sm. In 2014, 2015, and 2018, Turner et al. published a series of studies on visible/near infrared (VNIR) and shortwave infrared (SWIR) reflectance spectroscopy of important natural REE bearing mineral classes such as fluorocarbonates, phosphates, and silicates from various deposits all over the world. Scanning Electron Microscopy (SEM) and Electron Micro Probe Analysis (EMPA) enabled the validation of the HS measurements. By that, Turner et al. provided detailed insights into the factors influencing the occurrence and position of REE absorption features.

Parallel to the fundamental research, several papers were published that focus on the applicability of HS imaging for the detection and mapping of REE, ranging from drill core logging systems (Huntington et al. 2015, Turner et al. 2014) to outcrop mapping (Bösche et al. 2014) to regional geological surveys using airborne and space-borne systems (Rowan & Mars 2003, Neave et al. 2016). The general consensus is that the detection success relies on a sufficient ratio between REE absorption feature depth and spectral noise. This ratio is dependent on sensor sensitivity, image processing, pixel size (as a result of target distance) and REE grade within the observed pixel. As the latter is usually low, high-quality sensors need to be operated with a sufficient spatial resolution and undergo a subsequent careful radiometric correction to enable REE detection. This has been achieved at airborne (McDowell & Kruse 2015) and drone-borne level (Booysen et al. 2018), but not yet for spaceborne data (Neave et al. 2016). The detected REE are usually limited to a few, such as Nd or Sm, which occur in comparably high concentrations and feature both strong and characteristic features.

5.3.2 Laser Induced NIR Luminescence Spectroscopy

The luminescence of rare earth elements exhibits unique features which are related to the special electronic configuration of REE ions. The *4f-4f* transitions show narrow emission lines while having a long lifetime (Lüthi 1980). In contrast to transition metals, such as Fe^{3+} or Mn^{4+}, the crystal field splitting (also known as *Stark level splitting*), induced by the presence of different electrostatic environments for the rare earth ion, is less pronounced, mainly in the order of 100–200 cm^{-1}. For example, the crystal field splitting of Nd^{3+} leads to various emission lines from 880 nm to 910 nm (Lenz et al. 2013). A result of this effect are the variable relative intensities of the split emission lines, if the rare earth ion is hosted in different matrices.

Fundamental investigations of the luminescence properties of REE by PL were conducted by Gaft et al. in 1996, 1998, 1999, and 2005. The focus was set on the detection of REE in natural minerals using laser-induced time-resolved luminescence (TRLS) with several laser excitation wavelengths and resulted in an extensive library of PL spectra and characteristic peak positions. Further studies cover not only REE luminescence, but also a broad range of mineral- and transition metal luminescence and other effects such as molecular or radiation-induced centers. In 2016, Fuchs et al. built up a feature library for the detection of REE in synthetic standards, focusing especially on REE phosphates and fluorides. A comprehensive study on REE luminescence in natural minerals and doped crystals was conducted by Friis (2009). Besides the detection and interpretation of REE related emissions in natural minerals and doped crystals, the study elaborated thoroughly on the high complexity of the application of luminescence for REE analysis and questions the possibility of a quantitative REE characterization using PL. A similar conclusion was reached by Lenz et al. (2013), who investigated the influencing factors on the luminescence of Nd^{3+} in minerals, as

they observed a strong relation between the intensity of certain REE sublevel peaks with both the crystal orientation of the sample as well as the polarization of incoming laser light and received emission. In 2015, Lenz et al. discussed the characteristics and advantages of laser-induced REE photoluminescence artifacts in Raman spectroscopy. Beside the PL analysis of single REE-salts and mixed-REE natural mineral samples, they provided a detailed 2D PL map to illustrate the distribution of specific REE emission intensities within mineral grains.

There have been different approaches to extend the application of PL beyond the lab scale. Airborne Laser-induced Fluorescence (ALF) sensors or Fluorescence LiDAR systems have been used widely to detect and monitor organic compounds from long distances. Applications are widespread, such as the detection, mapping or monitoring of hydrocarbons, chlorophyll, and dissolved organic matter in surface water (Keizer & Gordon 1973, Kim 1973, Rogers et al. 2012), pollen in the atmosphere (Saito et al. 2018), green terrestrial vegetation (Günther et al. 1994, Hoge et al. 1983), and photoautotrophic biodeteriogens on stone monuments (Raimondi et al. 2009).

The observation of inorganic compounds such as REE from larger distances or/and under ambient light is more difficult, as their cross-section with UV and NIR light is usually much lower compared to organics due to the different binding situation (Forget & Chénais 2013). To receive a sufficient signal to noise ratio, high laser densities and long exposure times are needed, which usually collide with security standards and reasonable acquisition times. Therefore, most PL applications on inorganics focus on near-field measurements in a maximum range of few meters, a dark environment, or a reduced spectral resolution. A prominent application is the online separation of ore and waste material, and its use for mining machine control and bulk sorting (Nienhaus & Bayer 2003, Broicher 2005, Pollmanns 2008). Other application studies on inorganics comprise the characterization of mineral coatings on depleted uranium (Baumann et al. 2008) and the integration of PL true color imaging and Raman spectroscopy for the use within a rapid drill core scanner system (Kauppinen et al. 2014). None of these approaches were yet used for the reliable detection of REE in routine sample analytics, as their low intensity and uniquely narrow emission lines require both high spectral resolution and signal to noise ratio.

5.4 Materials and Methods

5.4.1 Analyzed Samples & Mineral Chemistry

We analyzed a collection of 24 naturally REE-bearing samples of different mineral species and origin. This includes samples of eleven different economically important minerals of fluorocarbonates, oxides, phosphates, and silicates with varying REE content and composition (see **Table 5-1**). All samples had been embedded in epoxy-resin discs and analyzed using electron microprobe (EMPA) with average REE_2O_3-detection limits of approximately 0.03 wt.% (Turner 2015). The samples were found to be compositionally unzoned through SEM-BSE (Scanning Electron Microscope Backscattered-Electron Imaging) investigations (Turner 2015). As the spatial coverage of the conducted spectral measurements was always set with respect to the EMPA measurement spots, a high accordance in composition and concentration between the spectral and EMPA data can be assumed. This allowed a validated interpretation of the observed spectral features as well as a correlation of feature intensities and REE concentrations. By that, approximate detection limits for both methods could be estimated. A reference spectral library was built from both literature derived values as well as by analysis of a suite of synthetic single-REE phosphate ($REE\text{-}PO_4$) and fluoride ($REE\text{-}F_3$) salts, available as partly epoxy-resin embedded single crystals. For PL data, this library was described by Fuchs et al. (2016).

Table 5-1. Overview of the investigated mineral samples with formulae, origin, and electron micro probe analysis (EMPA) average total rare earth element (REE) content (Turner 2015). Dominance of LREE (La to Gd) versus HREE (Tb to Lu+Y) is indicated.

Mineral Group	Mineral Species	General Formula	Sample Origin	Total $[REE+Y]_2O_3$ [%]
Fluoro-carbonates	Bastnaesite	$CeCO_3F$	Diao Lou Shan (Sichuan, CN)	69.35 (LREE)
	Parisite	$CaCe_2(CO_3)_3F_2$	Muzo (Boyacá, CO)	58.61 (LREE)
			Snowbird (Montana, US)	58.99 (LREE)
			Mexico	48.44 (LREE)
	Synchysite	$CaCe(CO_3)_2F$	Mt. St. Hilaire (Quebec, CA)	48.54 (LREE)
Oxides	Fergusonite	$(Y,REE)NbO_4$	Lyndoch Township (Ontario, CA)	14.49 (HREE)
Phosphates	Monazite	$(Ce,La,Nd,Th)PO_4$	Elk Mountain (Nebraska, US)	59.00 (LREE)
			Serra Verde (Para, BR)	63.71 (LREE)
			Unknown	65.28 (LREE)
	Xenotime	$(Y,Yb)PO_4$	Novo Horizonte (Bahia, BR)	69.63 (HREE)
			Novo Horizonte (Bahia, BR)	68.26 (HREE)
			Serra Verde (Para, BR)	66.55 (HREE)
	Britholite	$(Ce,Ca)_5(SiO_4,PO_4)_3(OH)$	Oka (Quebec, CA)	44.09 (LREE)
			Kipawa (Ontario, CA)	53.58 (LREE)
Silicates	Cerite	$(Ce,La,Ca)_9(Mg,Fe)(SiO_4)_6(SiO_3OH)(OH)_3$	Bastnas (Västmanland, SE)	69.21 (LREE)
	Eudialyte	$Na_{15}Ca_6(Fe,Mn)_3Zr_3SiO(O,OH,H_2O)_3(Si_3O_9)_2(Si_9O_{27})_2(OH,Cl)_2$	Kipawa (Ontario, CA)	5.25 (HREE)
			Kipawa (Ontario, CA)	4.82 (HREE)
			Kipawa (Ontario, CA)	5.63 (HREE)
	Kainosite	$Ca_2Y_2(SiO_3)_4(CO_3)\cdot H_2O$	Long Lake (New York, US)	36.93 (HREE)
	Zircon	$ZrSiO_4$	Green River (Wyoming, US)	0.32 (HREE)
			Mt. Malosa (Zomba, MW)	4.83 (HREE)
			Mudtank (Harts Range, AU)	0.04 (HREE)
			North Burgess (Ontario, CA)	0.04 (HREE)
			St. Peters Dome (Colorado, US)	0.10 (HREE)

5.4.2 Reflectance Spectroscopy – Technical Setup and Implementation

Reflectance spectroscopy data was acquired using both point measurements and HS imagery (**Figure 5-1**). The point measurements were acquired with a Spectral Evolution PSR-3500 spectrometer (see **Table 5-2** for detailed specifications). An internal white light source and intermediate white target calibrations (Spectralon SRS-99) ensured stable measurement conditions and resulted in accurate and highly resolved spectra. The signal was integrated over ten single measurements at a target spot of around 3 mm^2. Due to the very small size of some of the investigated mineral grains, which can fall far below the measurement spot diameter, a light blocking foil was used as background to reduce the influence of ambient light. An influence of the surrounding resin is still possible and needs to be considered for the respective samples. In contrast to point measurements, HS imagery adds a spatial component to the reflectance data by providing a spectrum for each pixel of a measured scene. Thus, spectral information can be set into a spatial context and used to provide mineral or element abundance maps. However, a high spatial resolution often goes along with a loss in spectral sampling and/or wavelength detection range, as the imager must be able to acquire and process a large batch of spectra simultaneously.

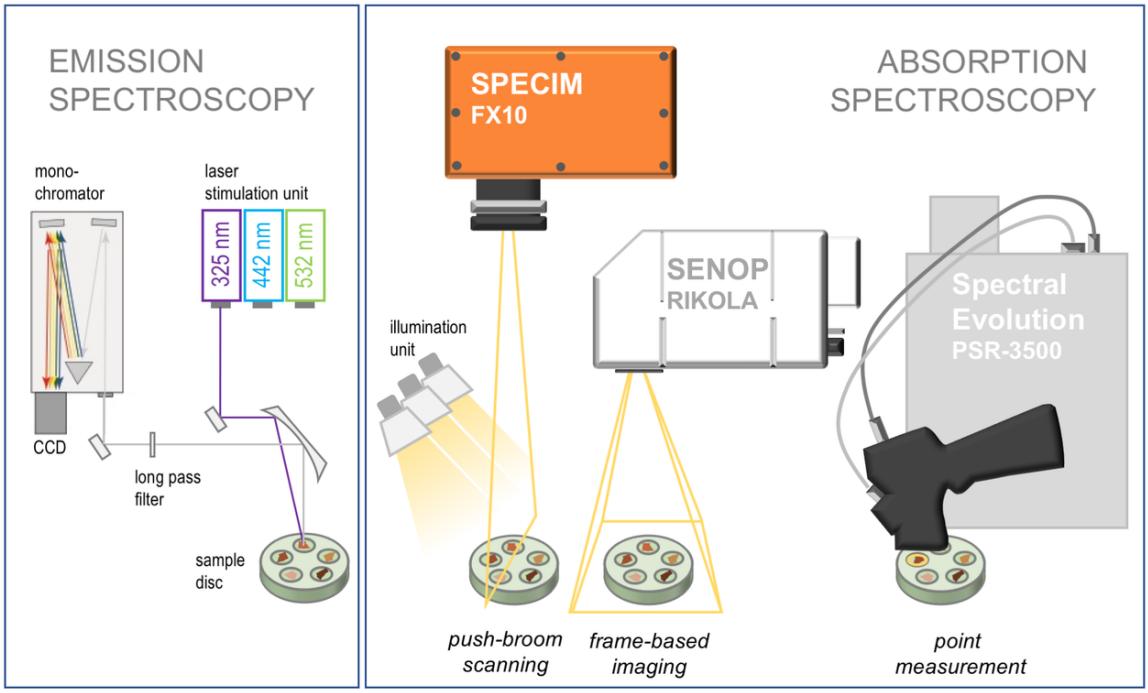

Figure 5-1. Schematic illustration of the technical setup (not to scale).

In order to test the applicability of common commercial low-to-medium priced HS imagers for the mapping of REEs in natural minerals, the data was acquired using both the frame-based *Senop Rikola HS Camera* as well as the push-broom *Specim FX10* (see **Table 5-2** for detailed specifications). The spatial resolution of both sensors is sufficient to separate smaller mineral grains, while the covered wavelength ranges include most of the relevant REE absorption features. The spectral resolution in VNIR is coarser compared to spectrometer point measurements but is usable to detect the most prominent absorption features. During the image acquisition, a uniform illumination over the whole sample batch was needed to ensure the comparability of REE absorption depths in different samples. Therefore, the imaging was conducted using the sample illumination unit of the *Specim SisuRock* drill-core scanner, which features two rows of full-spectrum halogen spotlights, uniformly illuminating an area of ~640x200 mm.

Table 5-2. Visible/near infrared (VNIR) HS sensor characteristics. *FWHM = full width at half maximum, **SNR values estimated for each spectral channel as ratio of mean and standard deviation of 20–40 spectra acquired under uniform conditions.

	Spectral Evolution PSR-3500	**Senop Rikola**	**Specim FX 10**
sensor type	portable field spectrometer	frame-based imager	push broom scanner
data dimension	1 px	1010x1010 px frame	1024 px line
wavelength range	350–2500 nm	500–900 nm	400–1000 nm
spectral resolution (FWHM*)	3.5 nm (VNIR), 7-10 nm (SWIR)	10 nm	5.5 nm
estimated peak signal-to-noise ratio (SNR)**	600:1	150:1	600:1
spatial resolution (length of quadratic pixel)	2 mm	distance dependent (here: 0.14 mm, slightly defocused)	distance dependent (here: 0.41 mm, focused)
spectral bands	1024	up to 380	224

Although the Rikola sensor theoretically features a similar spatial resolution to the FX10 at the same working distance, its significantly lower SNR results in a noisier image. To still deliver a sufficient image

quality even for very small samples, it was required to operate the sensor at reduced distance. This resulted in optimal imaging distances of about 430 mm for the Rikola and 600 mm for the FX10. However, as the optics of the Rikola are fixed with an optimal focusing distance of approximately 600 mm to infinity, a minor but acceptable blur was noticeable within the data.

5.4.3 PL Spectroscopy – Technical setup and Implementation

The PL spectroscopy measurements were conducted in a darkroom lab to avoid the influence of ambient light on the measurement result. The samples were investigated under three different continuous wave laser excitation wavelengths to analyze potential REE detection variabilities (**Figure 5-1**). The used laser excitation wavelengths, respective spot sizes, and resulting power densities are given in **Table 5-3**.

Table 5-3. Laser specifications. Beam diameter is given as $1/e^2$ of a gaussian fit. The power density is calculated assuming a constant power distribution over the given beam diameter.

Laser wavelength (laser type)	Beam diameter	Power density
325 nm (Kimmon He-Cd-laser)	185 µm	14.58 W/cm^2
442 nm (Kimmon He-Cd-laser)	170 µm	16.73 W/cm^2
532 nm (diode-pumped frequency-doubled Nd:YAG)	143 µm	26.93 W/cm^2

The power of the respective laser beams has been tuned to 4 mW for all lasers. The luminescence signal of the excited sample is dispersed by an Acton SP2560 Triple-Grating Monochromator (300 gr/mm grating, blazed at 750 nm) and recorded by a Princeton Instruments SPEC-10:100BR_eXcelon CCD-Camera (**Figure 5-1**). The data are recorded in up to 5743 channels for a full spectrum from 340 to 1080 nm. The measurements with 325 and 442 nm laser excitation were conducted in two single measurements, differing in the employed long-pass filters to suppress excitation laser light on the one hand and spectral second order effects from the monochromator gratings on the other hand. The two measurements are later merged in the post-processing of the spectral data (Fuchs et al. 2016). Due to limited sensitivity at extreme wavelengths, data under 400 and over 1050 nm is excluded from the analysis.

5.5 Results

5.5.1 Reflectance Spectroscopy

Reference reflectance spectra and positions of characteristic absorption features for each REE were determined from the single-REE salt suites using both lightweight HS imagers (see example in **Figure 5-2**) and were validated by point spectrometer data. This measurement redundancy was important to consider possible sensor specific disturbances such as feature shifts and ensure valid feature positions. The resulting feature tables were complemented with additional feature positions reported in the literature (White 1967, Ropp 1969, Rowan et al. 1986, Turner 2015). The resulting library shows a potential detectability of Pr^{3+}, Nd^{3+}, Dy^{3+}, Ho^{3+}, Er^{3+}, and Tm^{3+} for both Rikola and FX10. An overview on the most characteristic and best observable REE features in the VNIR is shown in **Figure 5-3a**. The most characteristic absorption features of Sm^{3+}, Eu^{3+}, Tb^{3+}, and Yb^{3+} are located outside the wavelength coverage of both VNIR imaging spectrometers, but Sm^{3+} and Yb^{3+} can be reliably detected at the extended wavelength coverage of the hand spectrometer. A detection of these elements using a SWIR HS camera should therefore be possible, as documented in Turner (2015). However, the absorption features of Eu^{3+} and Tb^{3+} expected in the VNIR are weak and often hardly visible, which questions their potential detectability with reflectance spectroscopy. The same accounts for Sc^{3+}, Y^{3+}, La^{3+}, Ce^{3+}, Gd^{3+}, and Lu^{3+}, which are not detectable with any

of the used devices, as they do not absorb at all in the VNIR and SWIR wavelength region due to their respective electronic configuration (White 1967).

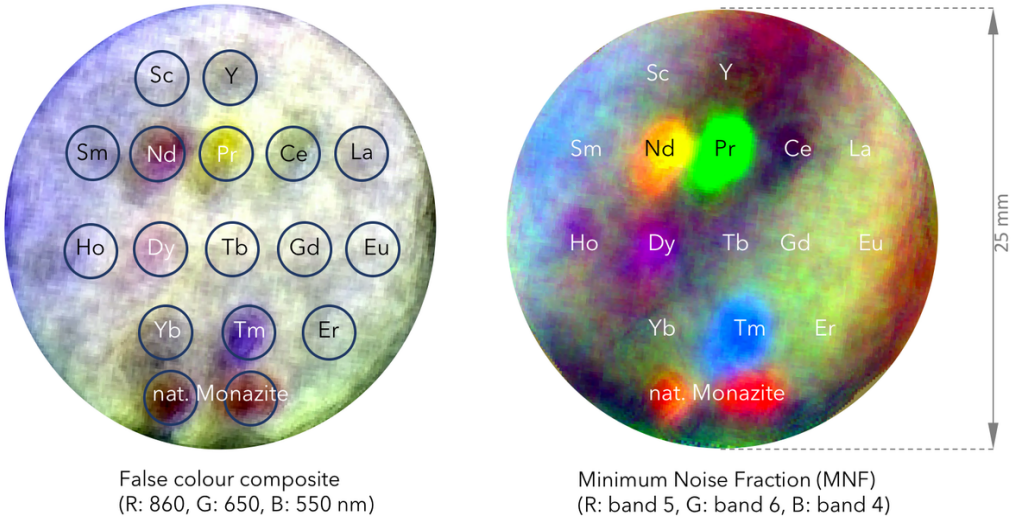

Figure 5-2. HS imaging of an REE-PO4 standard sample disc using a lightweight Senop Rikola sensor. The data are displayed as false color and minimum noise fraction (MNF, Green et al. 1988) composite.

After the compilation of the absorption feature catalogue, the mixed-REE natural sample batches were analyzed and imaged with the same procedure. In **Figure 5-3b**, two example image spectra for both LREE- and HREE-dominated samples are shown. The given EMPA-derived REE-concentrations represent a mean of five single EMPA measurements of the respective sample (Turner 2015). Low standard deviations suggest relatively uniform values for chemical composition and REE^{3+}-concentrations within the analyzed mineral grain. A comparison of the spectral datasets of the Rikola and FX10 sensor with known REE absorption feature positions pictures a distinct, but constant spectral shift of the Rikola data to higher wavelengths by about 10 nm (**Figure 5-3b**), which might originate from an internal sensor misalignment and must be considered for data interpretation. The spectral gap between the two built-in sensors in the Rikola generates an additional spectral disturbance observed as a sharp artifact around 636–650 nm (**Figure 5-3b**). Despite the mentioned spectral perturbations, the shapes of the received spectra for both sensors match well, however, the spectral quality of the FX10 data exceeds the Rikola data due to higher spectral resolution (FWHM) and Signal-to-Noise-Ratio (SNR) (**Table 5-2**). The depicted spectra of LREE-enriched monazite and britholite are clearly dominated by the absorption features of Nd^{3+} and Pr^{3+}. Especially the prominent absorptions around 580, 750, 800, and 880 nm are very characteristic and easily detectable. The exact positions of the absorption minima vary slightly according to the present quantities of the main absorbents, such as Pr^{3+}, Nd^{3+}, Er^{3+} and Dy^{3+}, which each contribute to the respective observed absorption feature. A good example is the shift of the feature around 810 nm, which is influenced by absorptions of Nd^{3+} (800 nm), Er^{3+} (805 nm), and Dy^{3+} (810 and 830 nm). Both HS sensors are not able to separate these features, so they result in a single deep minimum and its exact position is dependent on the abundance of the three REE. For example, the spectrum of the monazite sample with low Er^{3+} and Dy^{3+} content features a mixed, but clearly Nd-dominated absorption at 802 nm (**Figure 5-3b**). In contrast, the spectrum of the HREE-enriched xenotime sample is characterized mainly by Er^{3+} and Dy^{3+} related features. Here, a distinct shift of the feature to longer wavelengths and towards the pure Dy^{3+} absorption can be seen (812 nm). Features solely related to LREE, such as the mixed 590 nm absorption of Nd^{3+} and Pr^{3+}, are weak or not observable in this sample.

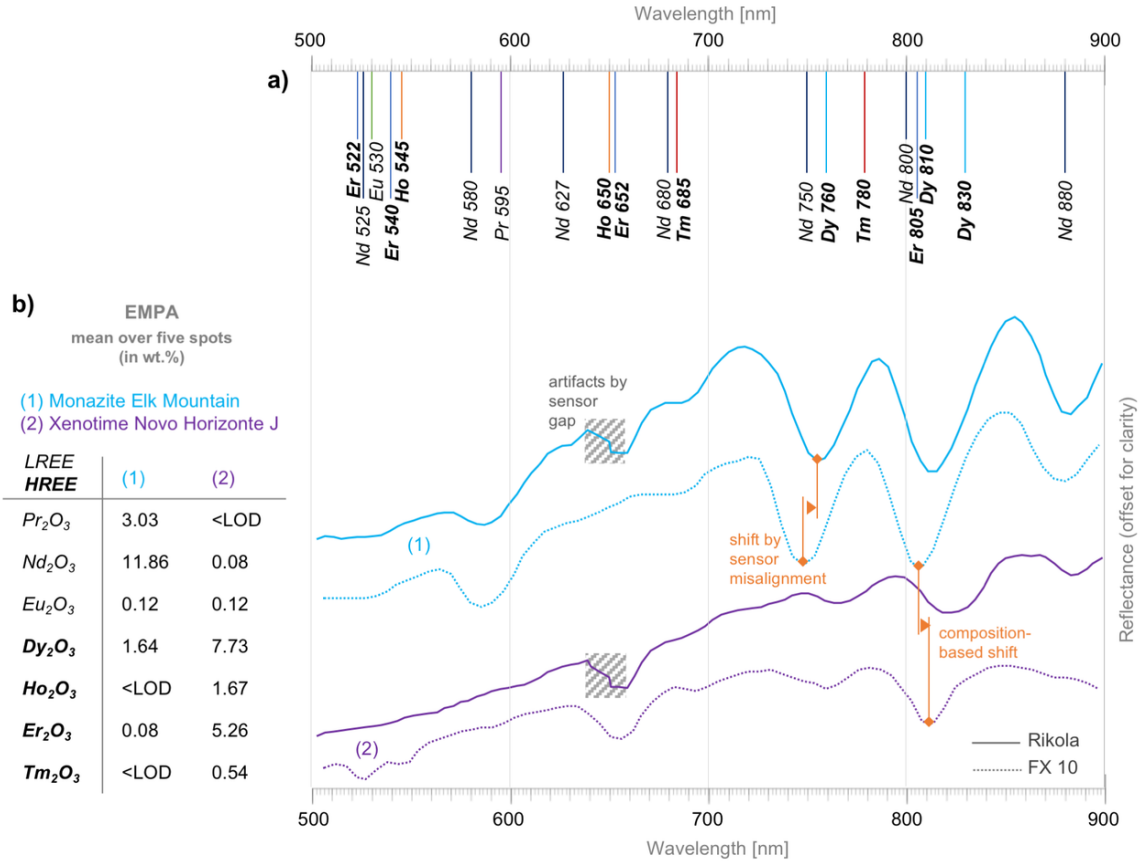

LREE / HREE	(1)	(2)
Pr_2O_3	3.03	<LOD
Nd_2O_3	11.86	0.08
Eu_2O_3	0.12	0.12
Dy_2O_3	1.64	7.73
Ho_2O_3	<LOD	1.67
Er_2O_3	0.08	5.26
Tm_2O_3	<LOD	0.54

Figure 5-3. a) Position of the most characteristic REE absorption features in the VNIR range according to the analysis of single-REE salts and literature review, **b)** extracted spectra from HS imaging of natural mixed REE mineral samples using two different HS sensors. Sample (1) represents LREE-enriched grains, while (2) is HREE-dominated. EMPA analysis results are given as mean of a series of five measurements (<LOD: below Limit of Detection).

To illustrate the correlation between absorption shift and the relative quantity of the respective absorbing REE, a Minimum Wavelength Map (Bakker et al. 2011) of the REE related absorption around 810 nm was conducted. With this approach, the wavelength position and depth of the deepest signal minimum within a defined wavelength window (here: 790–860 nm) is determined for each pixel and plotted after as wavelength position map (see **Figure 5-4a**). The wavelength position of the reflectance minimum is determined using a 5th order polynomial fit of the investigated spectral range. Even if such high-order polynomial may feature possible instability in the presence of spectral distortions, Murphy et al. (2014) shows that this method delivers a good accuracy and reliability of the result, as it excludes artificial position shifts due to spectral noise. In **Figure 5-4b** the shifts of the absorption minimum wavelength of the respective samples are plotted against the ratio of Nd_2O_3 (LREE) and Dy_2O_3 (HREE). For most of the samples, a very good correlation between composition and shift can be observed. Highly LREE-rich samples (numbers 5 and 6, in red) can be easily distinguished from HREE-rich samples (numbers 2 and 3, in blue). Furthermore, LREE-HREE-mixed samples can be characterized and compositionally arranged in between (numbers 4 and 7, ranging from orange to green according to LREE-HREE-ratio). Only one sample seems to be off the trend and features a strong shift to larger wavelengths despite its comparably low Dy concentration (**Figure 5-4**, sample number 1). This aspect can be explained as the hosting sample is britholite, which is known for high systematic shifts of occurring Nd^{3+} features to longer wavelengths by

about 5–7 nm (Turner 2015). Taking this into account, the remaining shift indicates an LREE-HREE-ratio in the range of sample number 7, which correlates to the EMPA results.

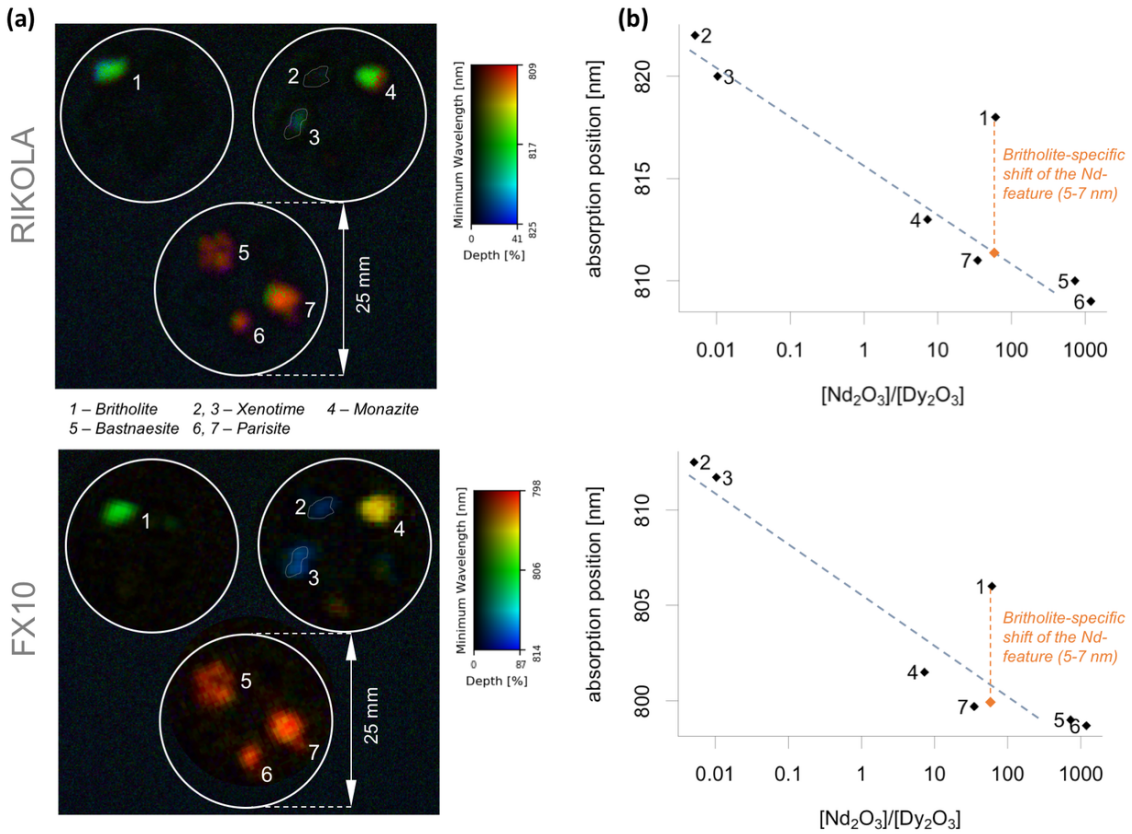

Figure 5-4. Relation between relative abundances of different REE and observed absorption feature positions for both used HS imagers: (**a**) Reflectance minimum wavelength mapping in the range of 790 and 860 nm for three natural mineral sample batches and (**b**) scatter plot between observed minimum wavelength and the respective ratio of EMPA derived Nd^{3+} and Dy^{3+} concentrations for seven sample grains marked in (a).

The resulting graph proves a clear correlation between the observed minimum position and the Nd_2O_3-Dy_2O_3-ratio. However, this relation is not assumed to be linear, especially as the individual ratio between concentration and resulting absorption depth is not identical for different REE. Still, it opens up the possibility for both an indirect detection of REE with features hidden by neighboring absorptions and the semi-quantitative estimation of the involved REE. A few REE remain indiscernible in natural minerals despite being detectable in single-REE salts. For example, Eu^{3+} showed weak features in all analyzed single-REE salts, which are situated mainly in the lower VNIR (380–600 nm) and the upper SWIR (especially 1900–2200 nm) (Jassie 1964, White 1967, Ropp 1969). However, within natural samples, the detection of Eu^{3+} becomes nearly impossible due to a strong overlap of the weak VNIR features with other highly visible REE such as Nd^{3+}, Er^{3+}, and Ho^{3+}. The characteristic SWIR features around 1900–2100 nm (not shown here) may in mixed pixels additionally overlap and be confused with nearby characteristic broad features of OH/H_2O (center wavelength around 1900 nm). Similar to Eu^{3+}, the features of Tb^{3+} were hardly visible and highly ambiguous, which excludes both elements from the list of REE potentially detectable with reflectance spectroscopy.

5.5.2 PL Spectroscopy

Reference PL spectra and positions of characteristic emission features for each REE were previously determined using a series of single-REE salts (Fuchs et al. 2016). The resulting feature library was merged and extended with similar and additional feature positions reported in the literature (Gaft et al. 2005, Reisfeld et al. 1996). Results showed a potential robust detectability of Nd^{3+}, Sm^{3+}, Eu^{3+}, Yb^{3+}, Dy^{3+}, Er^{3+}, and Tb^{3+} when using continuous-wave laser-induced fluorescence with excitation wavelengths of 325, 442, and 532 nm on single-REE salts. The same experimental setup was used in the current study to analyze the described natural REE-bearing mineral sample suite. Several factors and effects were observed accompanying mixed samples, which may support or hinder a robust detection of specific REE. These effects need to be considered during data interpretation and are described in more detail in the following.

Influence of the Excitation Wavelength:

Due to the discrete nature of the REE 4f-4f intra-configurational transitions, direct optical excitation of the typical REE luminescence lines is possible only for excitation wavelengths in the visible range which are specific to each REE (Kim et al. 1998). Broad-band, more unspecific, excitation is only possible for high excitation energies, reaching the charge transfer bands or the host's conduction band, which may be far in the UV range. Thus, by stimulating using an appropriate wavelength, specific REE luminescence may be enhanced or suppressed, which opens up the possibility for (1) the discrimination of overlapping REE features and (2) the suppression of broad emissions originating from non-REE impurities and crystal structure defects. The influence of the employed excitation wavelength on the detectable REE is displayed for an analyzed xenotime sample in **Figure 5-5**. For some REE, such as Yb^{3+}, Er^{3+} or Ho^{3+}, the excitation wavelength influences mainly the feature intensity or the occurrence and position of sub-level peaks. Others, such as Dy^{3+} and Sm^{3+} show a clearer dependency on the chosen excitation wavelength and are suppressed or not visible at other excitation wavelengths. For those elements featuring a variety of strong peaks that often superpose other REE, this excitation wavelength dependency demonstrates a possibility to reveal hidden REE peaks or discriminate and interpret overlapping features.

The excitation wavelength dependency of broad matrix emissions is shown on spectra of eudialyte and zircon (**Figure 5-6**). In all analyzed eudialyte samples, several broadband luminescence features occur, whose visibilities are dependent on the respective excitation wavelength. At this, a strong Ce^{3+}-luminescence at 380–400 nm can be observed only at 325 nm excitation wavelength (**Figure 5-6a**). However, at longer excitation wavelengths a previously not visible broadband feature appears at 600 nm (**Figure 5-6c**) and most probably originates from the substitution of Ca^{2+} with Mn^{2+} within the crystal (Rastsvetaeva 2007). A respective MnO content of ~1.4 wt.% is validated by EMPA data for this sample. A third broadband luminescence at 505 nm, possibly related to the sample embedding epoxy resin, occurs only with blue excitation. It overlaps with the slightly weaker 600 nm luminescence, which appears as shoulder (**Figure 5-6b**). The observed broad emissions in zircon are many and often of uncertain origin, but commonly dependent on specific excitation wavelengths, such as:

(I) A strong and broad emission with a center wavelength of 580 to 590 nm visible mainly at 325 nm excitation (**Figure 5-6d**, I) and substantially decreased at longer excitation wavelengths (**Figure 5-6e** and **f**, I). It originates probably in radiation damage centers that cause the characteristic red-brown color of many zircons and is decreased in intensity for longer excitation wavelengths (Gaft 1992, Gaft et al. 2005).

(II) A broadband near-infrared luminescence (center-wavelength around 780 nm) was observed in some zircon samples under 325 nm (**Figure 5-6d**, II) and 442 nm excitation (**Figure 5-6e**, II) and might be related to Fe^{3+} or Ti^{3+} (Gaft 1992, Gaft et al. 2005). It nearly disappears under 532 nm excitation (**Figure 5-6f**, II).

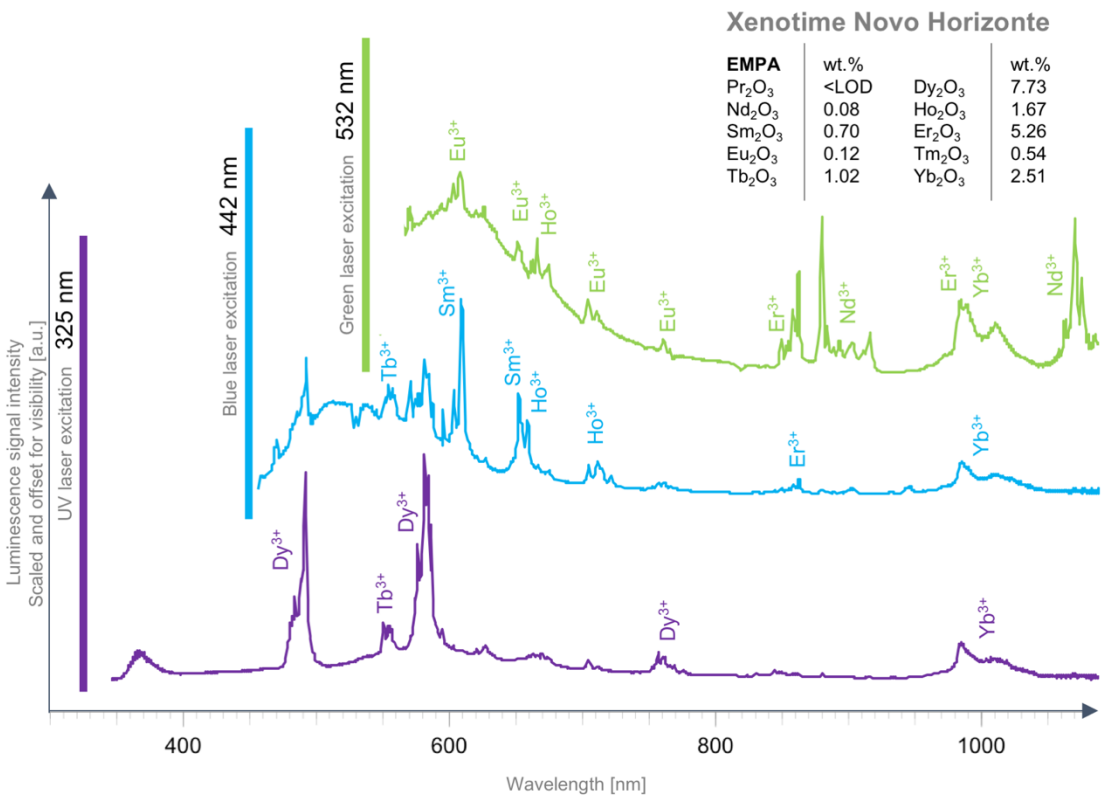

Figure 5-5. REE and matrix emission variability in a xenotime sample are displayed as a function of three different laser excitation wavelengths. Selected REE emissions have been labeled according to reference feature positions (see text, Section 4.2).

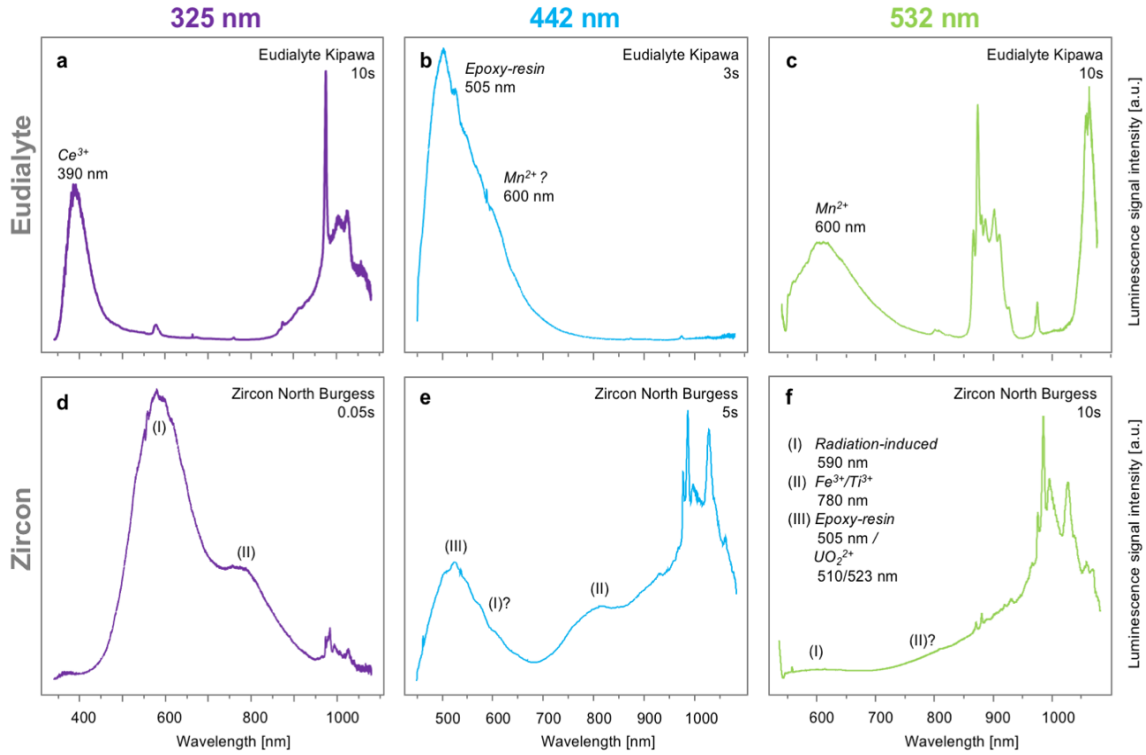

Figure 5-6. Interpretation of variable broad emission features as a function of excitation wavelength in (**a-c**) eudialyte and (**d-f**) zircon samples. Excitation wavelengths are indicated on top of each plot group.

(**III**) A strong green luminescence appears around 510 nm under 442 nm excitation (**Figure 5-6e**, III), which in zircon is usually connected to the luminescence centers of UO_2^{2+} (Gaft 2002). It may also originate from the sample embedding epoxy resin, which shows a very similar feature. At 325 nm excitation, this center is weak and hardly observable, as it is nearly covered by the stronger orange broadband luminescence (**Figure 5-6d**, I).

Influence of the Mineral Type:

The spectral position of specific REE emission lines were found to be constant within a few nanometers, which reasons in the REE 4f-4f transitions that are generally not affected by their chemical environment. However, the specific Stark-level peak positions and relative intensities varied heavily between host minerals and slightly between samples of the same host mineral from different geological localities (**Figure 5-7**).

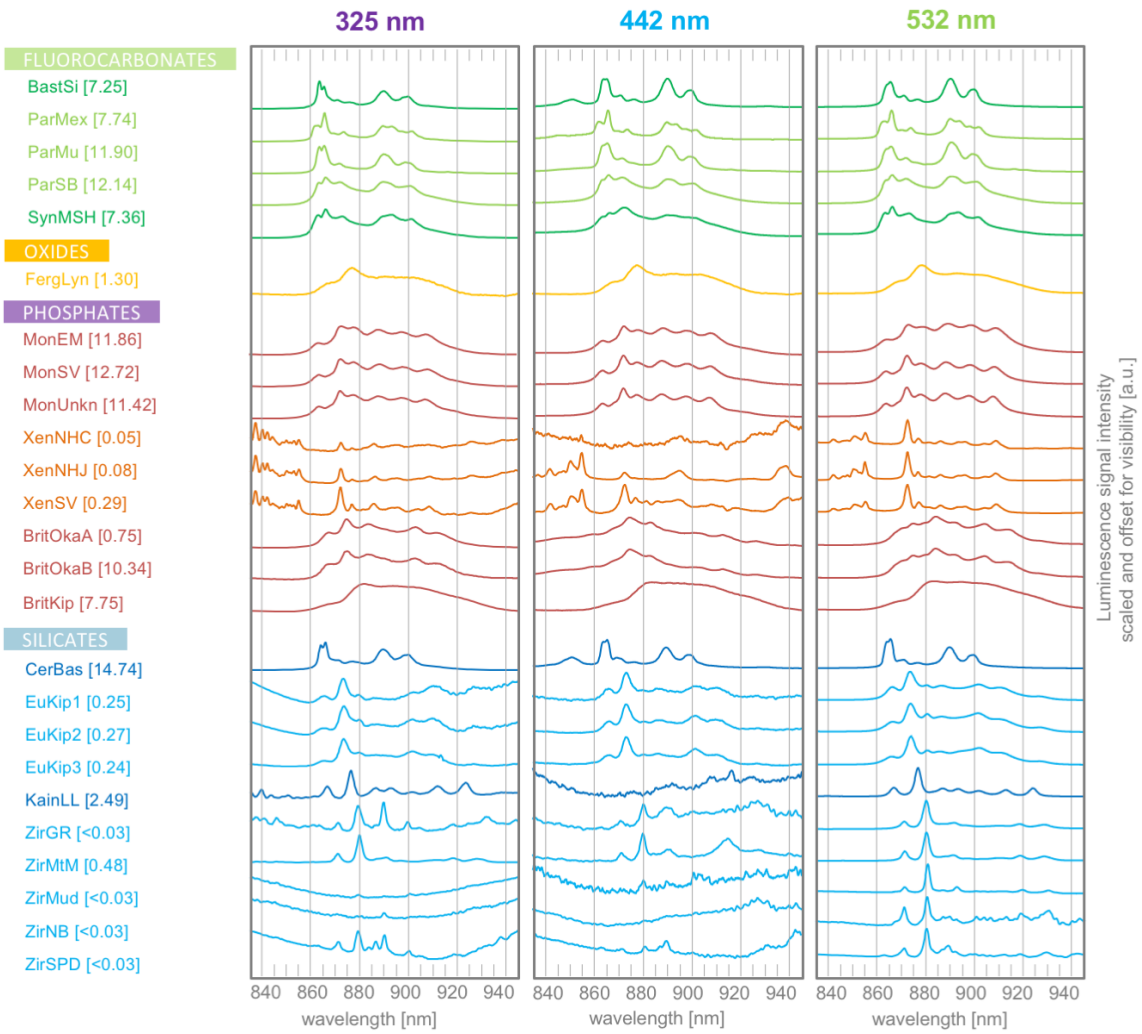

Figure 5-7. Variability of Stark-level emission peaks for the literature reported Nd^{3+} feature center wavelength of 890 nm (Reisfeld et al. 1996, Gaft et al. 2005) for different samples and excitation wavelengths. EMPA derived Nd_2O_3-concentrations are given in squared brackets in wt.%. Excitation wavelengths are indicated on top of each plot group.

This observation coincides with statements in the literature, such as in Burns (1993) and Lenz et al. (2015). Accordingly, the local structural environment of the REE^{3+}-ion decides on the splitting of the recorded emission peaks, which is also known as crystal-field dependent Stark's splitting. A respective REE^{3+} sub-

level peak database would open up the possibility to a fingerprint-like detection of the host mineral (Lenz et al. 2015). **Figure 5-7** displays the variability of the observed sub-level peaks at the characteristic Nd^{3+} feature center wavelength of 890 nm (Reisfeld et al. 1996, Gaft et al. 2005) for the investigated samples in dependency of the excitation wavelength and gives an example on such a potential database. Remarkable are the bandwidth of occurring sub peak positions and the overall similarity of spectral shape and sub peak positions within one mineral type or even group. Similar patterns were observed for many mineral types such as for monazite or eudialyte. Few minerals such as britholite showed a higher variability, which in the current case might be related to abundant REE-bearing apatite in the britholite samples from Oka.

In some samples such as xenotime or kainosite, characteristic Er^{3+} features around 855 nm become apparent, which interfere with the investigated Nd^{3+} sub-level peaks. A high variability in response to different excitation wavelengths is given, ranging from no change (monazite) over differing spectral shape (britholite) up to a suppression of detectability (zircon).

REE Absorption Effects in PL Spectra:

For samples and excitation wavelengths where intense and broad emissions occur around 500 to 800 nm, specific absorptions effects were likely to be observed within the PL signal. For each case, they could be certainly assigned to occurring REE (**Figure 5-8**).

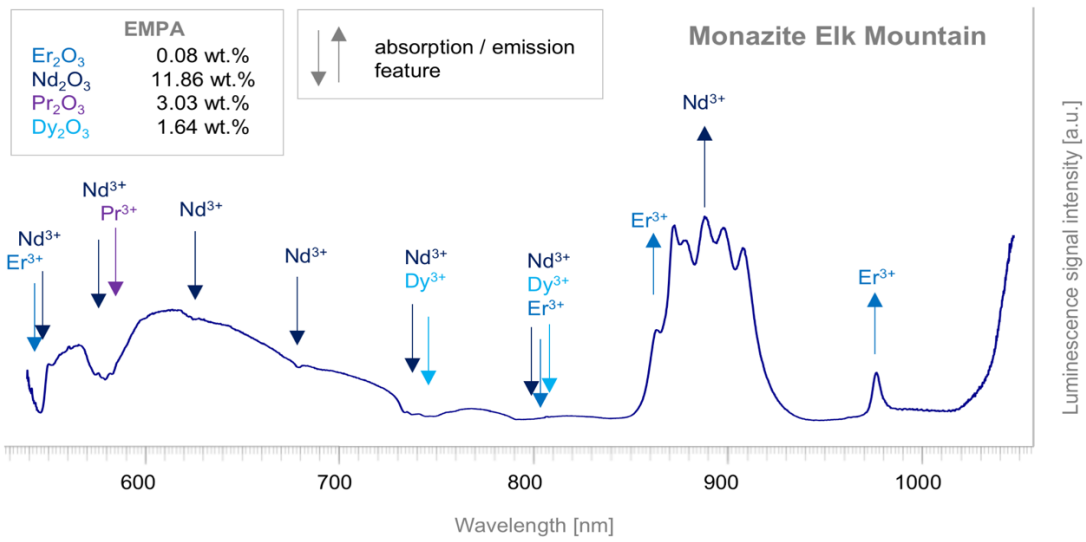

Figure 5-8. Occurrence of REE absorption features within PL spectra on the example of Monazite Elk Mountain sample. Significant features are labeled with the most probably related REE (also compare Figure 5-3a). Laser excitation: 532 nm.

The features originate mainly from Nd^{3+}, which is known to show extremely distinct absorption features in this wavelength region, and to a lesser degree Pr^{3+}, Dy^{3+}, and Er^{3+}, which strongly overlap with the Nd^{3+} features. While providing additional information on these four elements, this phenomenon also holds a crucial disadvantage. Weak, but characteristic emission features of other REE in this wavelength range can be either annihilated completely or masked to an extent, where they are not discriminable anymore from, for example, artificial peaks originating from two adjacent absorptions. For example, the two most characteristic Pr^{3+} emission features are located at 480 and 599 nm and are often completely masked by strong Nd^{3+}-related absorptions around 475 and 580 nm, Dy^{3+}-related absorptions at 476 nm, and the Pr^{3+}-related absorption around 593 nm (see also **Figure 5-3a**). This crucially affects the general detectability with PL spectroscopy of all REE that are solely detectable by peaks in the respective wavelength ranges,

such as Tm^{3+}, and weakens the detectability robustness of REE with characteristic peaks in the respective wavelength ranges, such as Pr^{3+}, Sm^{3+} and Ho^{3+}. Variation of the excitation wavelength can be used to avoid broad-band emission of the mineral host and by that to reduce the influence of absorption on the PL signal (see also Section 5.5.2).

5.6 Discussion and Cross-Method Considerations

A concise overview on the features, advantages and weaknesses of both reflectance and PL spectroscopy is given in **Table 5-4** and discussed further in detail in following sections.

Table 5-4. Concluding overview on the capabilities of reflectance and PL spectroscopy for near-field REE detection.

	Reflectance spectroscopy	**PL spectroscopy (325/442/532 nm excitation)**
Detectable REE in single-REE salts	Robust: Pr^{3+}, Nd^{3+}, Sm^{3+}, Dy^{3+}, Ho^{3+}, Er^{3+}, Tm^{3+}, Yb^{3+} Weak: Eu^{3+}	Robust: Ce^{3+}, Pr^{3+}, Nd^{3+}, Sm^{3+}, Eu^{3+}, Tb^{3+}, Dy^{3+}, Er^{3+}, Yb^{3+} Weak: Ho^{3+}, Tm^{3+}
Detectable REE in mixed-REE natural samples	Robust: Nd^{3+}, Sm^{3+}, Dy^{3+}, Yb^{3+} Ambiguous (detectable by feature shift): Pr^{3+}, Ho^{3+}, Er^{3+}, Tm^{3+}	Robust: Ce^{3+}, Nd^{3+}, Eu^{3+}, Dy^{3+}, Er^{3+}, Yb^{3+} Ambiguous: Pr^{3+}, Sm^{3+}, Ho^{3+},
REE detection limit	down to ~0.10 wt.%	less than 0.03 wt.%
Acquisition time: Point measurements	ms–s	ms–s
Acquisition time: Mapping of 100x100px	ms–s (commercial push broom and frame-based sensors available)	hours (x-y rastering of point measurements)
Quantitative analysis	semi-quantitative by correlation of absorption depth and position with REE grade	not yet applicable

5.6.1 Qualitative REE Detection

REE can be classified into four groups according to their qualitative detectability by the used PL and reflectance spectroscopy methods in natural samples with mixed REE content (see also **Figure 5-9**):

(I) No detectable features for both methods: Sc^{3+}, Y^{3+}, La^{3+}, Gd^{3+}, Lu^{3+}

(II) Weak, masked, or otherwise inconsistently detectable features for both methods: Tb^{3+}, Ho^{3+}, Tm^{3+}

(III) Well detectable features for one spectroscopic method: Ce^{3+}, Pr^{3+}, Sm^{3+}, Eu^{3+}, Er^{3+}

(IV) Well detectable features for both spectroscopic methods: Nd^{3+}, Dy^{3+}, Yb^{3+}

The classification shows that few REE, which were well detectable in single-REE standards (Fuchs et al. 2016), feature a decreased or inconsistent detectability in mixed natural samples for either one or both methods. This applies especially for Pr^{3+}, Sm^{3+}, Tb^{3+}, Ho^{3+}, and Tm^{3+}. Two main explanations can be found: (1) hindered detection through overlapping REE- or mineral-matrix-related features (especially in PL data), and (2) non-comparability of single-REE salt concentrations versus fundamentally lower concentrations of certain REE in natural samples that may fall near or below the detection limit of the used method (especially for reflectance spectroscopy). For example, the concentration of $TbPO_4$ samples used as reference amounts for roughly 60 wt.% Tb^{3+}, while in the analyzed natural minerals Tb^{3+} rarely exceeds 1 wt.% (Turner 2015). Thus, REE features showing only weak spectral representations in high-grade single-REE salts might be expected to vanish in natural mixed-REE sample spectra. For the affected elements, a direct detection using one method is often not possible, thus, a combination of both methods and/or a variation in the acquisition parameters such as laser excitation wavelength is needed. For example, Pr^{3+}, as one of the critical REE, is

hardly detectable in natural minerals by continuous-wave PL, as its features can be easily confused with the characteristic peaks of Dy^{3+} at 470–490 nm, Sm^{3+} at 600–650 nm, and Nd^{3+} at 870–900 nm, respectively. By variation of the excitation wavelength, Dy^{3+} and Pr^{3+} can be distinguished, as Dy^{3+} is well observable under 325 nm, but not 442 nm excitation, which is vice versa for Pr^{3+}. Similar dependencies exist for Nd^{3+} and Sm^{3+}. With a parallel sample analysis using reflectance spectroscopy, the occurrence and relative content of Dy^{3+}, Sm^{3+}, and Nd^{3+} can be cross-validated, as those elements show very specific features in reflectance spectroscopy data. By that, the results of reflectance spectroscopy can support the interpretation of PL spectroscopy data.

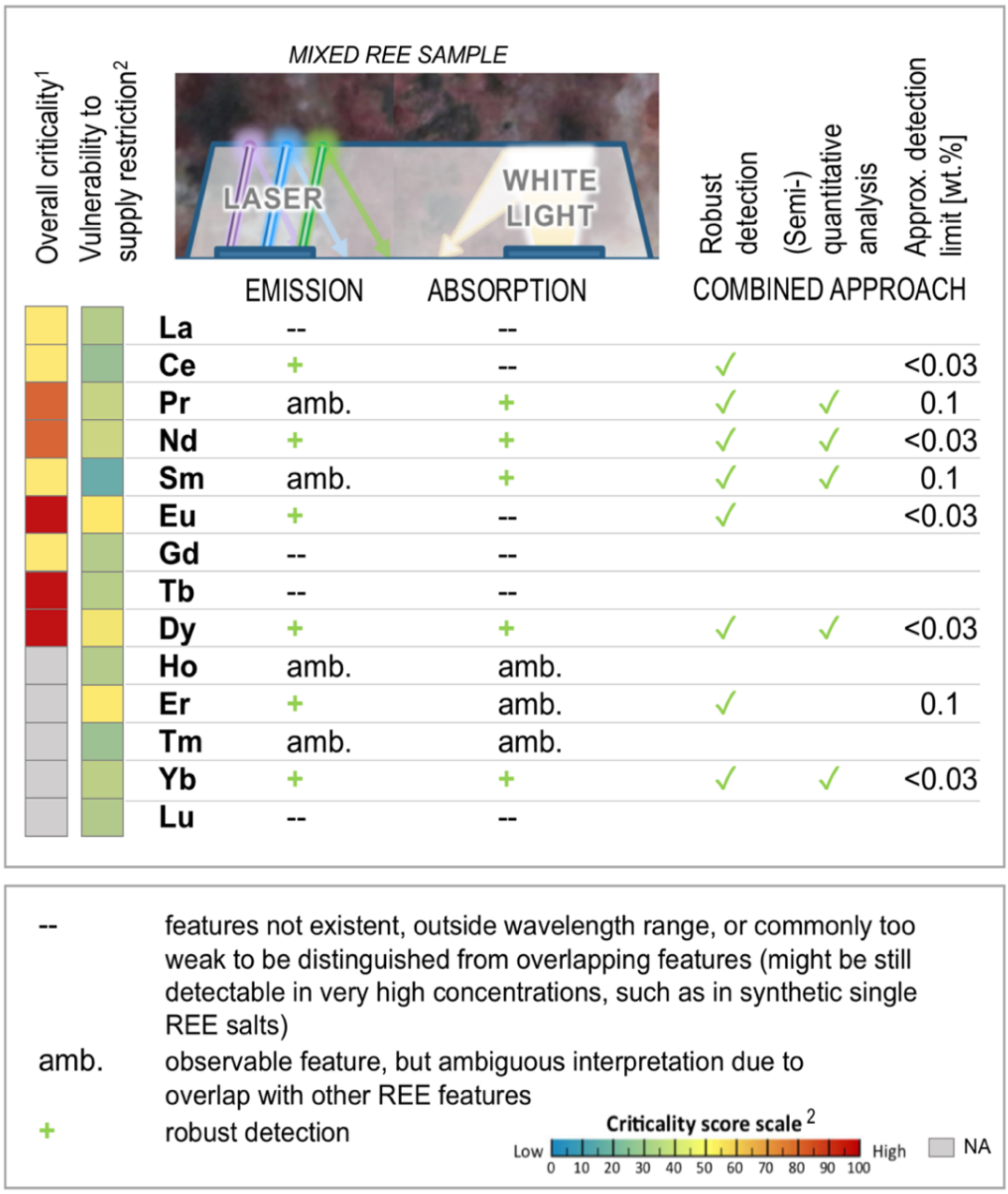

Figure 5-9. Overview on the performance of the employed reflectance and PL approaches for the detection of REE and the possibilities of a combined approach. A comparison of detectability with criticality and vulnerability to supply restrictions of the individual REE shows the economic value of the presented approach (NA: no data available).

5.6.2 Quantitative REE Detection and Detection Limits

In the current study, moderate detection limits of about 0.1 wt.% REE_2O_3 for each spectrally active REE were estimated for reflectance spectroscopy. As shown in Turner (2015), the absorption feature depth analysis of similar absorptions at different samples allows for a semi-quantification of the REE content. A relationship between absorption depth and concentration exists and can be used for single defined absorption features. Within this study, we could add on to this by providing a semi-quantification approach for overlapping REE features using the minimum wavelength position. The respective analysis of the best observable REE absorption feature at 800–810 nm enables a straight-forward sample categorization into HREE (low Nd^{3+}/Dy^{3+}-ratio, feature shifted to longer wavelengths) or LREE (high Nd^{3+}/Dy^{3+}-ratio, feature shifted to shorter wavelengths) enriched mineralization. Equivalent analyses could be used to evaluate the Nd^{3+}/Pr^{3+}- (580–595 nm), Er^{3+}/Ho^{3+}- (540–545 nm), and Tm^{3+}/Dy^{3+}-ratios (760–780 nm) of different samples.
In contrast, PL spectroscopy provides significantly lower detection limits, but currently without the possibility of robust quantification. In many samples, distinct emissions could be unequivocally attributed to REE that were not or only in very low amounts detected by EMPA. As the EMPA detection limit for each REE was in average given with 0.03 wt.% REE_2O_3, a similar or even lower detection limit for PL spectroscopy can be assumed. However, the relation between emission intensity and REE content was inconsistent, up to the point of no or extremely weak detection despite EMPA proven REE occurrence. This confirms the findings of Friis (2009) and Lenz (2013), stating the complexity of REE emission and the resulting difficulty of REE quantification using PL analysis.

5.6.3 Considerations on the Measurement Setup

Spatial Data Integration:

A successful integration of PL and reflectance spectroscopy results is dependent on the subsequent observation of the exact same spot of the sample. This applies not only between reflectance and PL spectroscopy results, but also between PL measurements with different excitation wavelengths. Hereby, not only the lateral extent and position correspondence of the measurement spot needs to be considered. At constant excitation wavelength, the penetration depth of a certain light source is also dependent on the optical and chemical characteristics of the investigated sample type (Friis 2009). In addition to that, a relation between the wavelength of the illumination source and penetration depth exists. Such, a 532 nm laser reaches a slightly deeper penetration than a 325 nm laser with the same power at the same surface spot, and therefore also stimulates deeper zones of the mineral crystal or, in case of very small grains or heterogeneous samples, can also excite emissions of surrounding minerals or embedding resin. These usually broad emissions can interfere with the target emission by both signal mixture as well as by providing a broad signal in which absorption effects can occur. These can mask or interfere smaller emission peaks nearby and complicate the overall spectral interpretation (see also section 5.5.2).

Excitation Wavelength:

A variation of the laser excitation wavelength can be used to highlight or suppress specific REE emissions, and also to minimize the influence of possible mineral matrix background emissions. However, the use of a laser with a longer excitation wavelength also leads generally to a loss in spectral coverage, as only features in a wavelength range longer than the laser excitation wavelength are recorded. Up-conversion measurements that enable the detection of emission features at shorter wavelengths than the laser wavelength could be a work-around and subject of a subsequent study.

Sample Size and Spatial Resolution:

For both single-REE salts as well as mixed-REE natural mineral grains, the detectability by reflectance spectroscopy was highly influenced by the sample size. Some of the analyzed single grains samples featured diameters of less than a millimeter and even lower thicknesses. This made them hard to investigate with the portable spectroradiometer, whose measurement spot size exceeds the sample size. Thus, for very small or thin and transparent samples spectral mixing with the embedding resin or the surface below the analyzed sample can occur. Additionally, scattering of the emitted and reflected light within the transparent embedding resin can lead to additional disturbances within the observed spectral signal. Such spectral influences from neighboring or surrounding materials must also be expected for future measurements on rock samples. For this reason, it makes sense to consider the grain size of the examined sample when selecting the sensor parameters for both PL and reflectance measurements.

Sensor Calibration:

During the measurements, a constant and distinct calibration offset of about 10 nm between the measured spectral signal and the expected wavelength labelling was observed for the Rikola sensor. As this might be expected also for other sensors, routine calibration checks are highly recommended. By that, instrumental deviations can be distinguished from natural variability in absorption features, which occur due to changes in chemical concentration, spectral mixtures or environmental effects. This is especially important for the analysis of overlapping REE absorption features, which relies on the evaluation of the exact absorption position. The calibration could be easily done by a reference measurement of a standard material with a known absorption feature position.

5.7 Conclusion

Our study outlines the strengths of combining hyperspectral reflectance and PL spectroscopy for the detection of REE in natural minerals. Challenges accompanying the analysis of natural samples using only one of the two methods, such as masking of characteristic features by broad mineral matrix emissions and overlapping REE features, can be addressed by this combined approach. The integration of HS reflectance spectra and luminescence induced by continuous-wave lasers with different excitation wavelengths offers a possibility to cross-validate the observed results and robustly assign otherwise ambiguous features to specific REE. This increases the certainty of correct feature interpretation and enables more robust detection of economically important REE, including Ce, Pr, Nd, Sm, Eu, Dy, Er, Yb, and potentially also Ho and Tm. PL spectroscopy provides an extremely high sensitivity such that it partly outruns the detection limit of the conducted EMPA measurements (here: ~0.03 wt.% per individual REE_2O_3). Reflectance spectroscopy in general delivers a higher detection limit (>0.10 wt.% for selected REE_2O_3), but in contrast offers the possibility for semi-quantification through the analysis of absorption depth or, in case of highly overlapping features, absorption position.

The integrated reflectance and PL spectroscopy offers already at the present laboratory stage an innovative, robust tool for non-invasive REE detection in near-field (in the range of 0.5 to 2.0 m) raw material exploration. It delivers especially advances in small-scale, high-precision sample mapping, and can directly be applied to REE detection in ore samples, drill cores, and as fast validation approach in large-scale REE exploration.

As the integrated reflectance and PL analysis has now been proven to be successful for natural and complex samples, the next steps will need to focus on the technical implementation and the optimization of sensor parameters such as spatial and spectral resolution to produce integrable mineral maps. Co-registration of

the resulting PL data cubes with the presented HS reflectance imagery will allow a pixel-wise integration and by that, a combined mapping approach uniting the strengths of both methods. Further technical optimization may include the implementation of time-resolved PL as it is known to increase the discriminability of specific REE, but this will be at the cost of increasing the complexity of the setup, while already great benefit could be achieved with the integration of the here presented simple PL instrumentation.

The relevance of integrating reflectance and PL spectroscopy for mineral mapping lies at present in a wide range of near field sensing applications with focus on any REE detection, may it be in geology, exploration, mining, processing or recycling. Expanding especially the PL spectral library beyond the focus on REE has significant potential to enable the robust detection and cross-validation of other critical raw materials.

Applications beyond the current near-field scale need to tackle especially the challenge of ambient light for PL spectroscopy. Similar questions apply for the simultaneous acquisition of reflectance and PL signals using narrow and broad-band illumination at the same time. Both applications are generally possible, but require specific solutions, because PL signals are orders of magnitude less intense and rely on sufficient discrimination from much brighter reflectance signals and ambient light, respectively. Yet, a technical solution is available in form of, for example, a Fluorescence LiDAR system (Raimondi et al. 2009) for biogenic materials. To transfer the approach to the essentially weaker REE signal is possible, but requires advanced camera systems of high sensitivity and distinctly increased power of the laser excitation source. Besides security issues and possible sample altering, interferences between REE emission and absorption features occurring in close spectral proximity will cause a loss in informative value. For these reasons, the detailed and sensitive REE characterization is the strength of our combined spectroscopic approach. A separate acquisition guarantees to record the full range of information from both methods and is suitable especially for small sample-sensor distances (cm to m) under separate acquisition of reflectance and PL spectra.

Author Contributions: Conceptualization, S.L., M.F. and R.G.; Formal analysis, S.L., M.F. and P.S.; Investigation, S.L. and J.B.; Resources, J.B. and D.T.; Software, S.L. and M.F.; Supervision, J.H. and R.G.; Validation, S.L.; Visualization, S.L.; Writing – original draft, S.L.; Writing – review & editing, J.B., M.F., P.S., D.T., J.H. and R.G.

Funding: This research received no external funding.

Acknowledgments: We like to thank Robert Zimmermann (HZDR-HIF) for his engineering support during the HSI recordings.

Conflicts of Interest: The authors declare no conflict of interest.

Chapter Discussion

Spectral characterization of valuable elements in mineral exploration such as REE with only one spectroscopic method is often not sufficient or only provides insufficient information, either regarding the nature of discriminable elements or their concentrations. Alternative methods that allow a much more sensitive characterization may exist and could extend the number of discriminable elements or reduce the ambiguousness of overlapping features. However, as it is the case for PL spectroscopy, the higher sensitivity is usually accompanied by the integration of several measurements over a given area or a longer integration time. The combination of several spectroscopic methods is therefore recommended for better material characterization. However, prior knowledge and dedicated feature libraries are needed to reliably link the observation of a specific spectral feature to the occurrence of a specific ion, molecule or mineral. A large number of fundamental studies on the spectroscopic features of REE and other ions exist, however, they are usually focused on synthetic materials and do not apply to relevant natural rocks in mineral exploration. Alternatively, the applied methodology is complex or highly specialized to the current sample or ion, e.g., using specific excitation wavelengths and decay-time windows in PL spectroscopy. Reflectance spectroscopy is an established technique in geosciences and has repeatedly been used to detect REE in rock samples, however, due to the higher detection limit and usually lower sensor-SNR in remote sensing, the detectable REE are limited to a few elements (Nd, Dy, Sm).

The characterization of REE using both reflectance and PL spectroscopy as described in the presented chapter allowed a much more detailed analysis of REE than it would be possible with only one spectroscopic method. A resulting workflow for the routine REE characterization in rock samples could include the location and semi-quantification of REE-relevant regions in sample batches using HS reflectance imaging, followed by a detailed analysis and characterization with PL on selected samples with specific excitation wavelengths to determine the occurring REE. Observed Stark-level emission peaks could be cataloged and used for the characterization of the REEs' host lattice. Future 2D mapping of PL and other spectroscopic data types and their integration with HSI could help to discriminate even more substances or to further increase the reliability of the detection.

For example, Raman spectroscopy could be utilized to gain more information on the host minerals and by that, help to interpret the spectral features observed in HSI and PL. In particular, the results could support addressing observed broad-band emissions, which are usually attributed to the host lattice.

References

Adams JW. The visible region absorption spectra of rare earth minerals. *American Mineralogist* **1965**, 50, 356–366.

Bakker WH, van Ruitenbeek FJA, van der Werff HMA. Hyperspectral image mapping by automatic color coding of absorption features. In: *7th EARSEL Workshop of the Special Interest Group in Imaging Spectroscopy*, Edinburgh, UK, 11–13 Apr **2011**, 56–57.

Bauer D, Diamond D, Li J, Sandalow D, Telleen P, Wanner B. Critical Materials Strategy; U.S. Department of Energy, **2010**, 166.

Baumann N, Arnold T, Foerstendorf H, Read D. Spectroscopic Verification of the Mineralogy of an Ultrathin Mineral Film on Depleted Uranium. *Environmental Science & Technology* **2008**, 42, 8266–8269. DOI: 10.1021/es800801h

Booysen R, Zimmermann R, Lorenz S, Gloaguen R, Nex PAM. Multi-source hyperspectral imaging of carbonatite-hosted REE-Nb- Ta mineralization at Marinkas Quellen, Namibia. In: *9th Workshop on Hyperspectral Image and Signal Processing: Evolution in Remote Sensing (WHISPERS),* 23–26 Sep **2018**, Amsterdam, The Netherlands**.**

Bösche NK, Rogaß C, Mielke C, Kaufmann H. Hyperspectral digital image analysis and geochemical analysis of a rare earth elements mineralized intrusive complex (fen carbonatite complex in Telemarkregion, Norway). In: *Proceedings of the EARSeL 34th Symposium*, Warsaw, PL, 16–20 June **2014**, 13, 1–6. DOI: 10.12760/03-2014-07

Broicher HF. Dilution control - online and real-time recognition of ore and waste by LIF. In: *Proceedings of the SME Annual Meeting*, Salt Lake City, USA, 28 Feb–02 Mar **2005**, 05–66, 1–5.

Burns RG. Mineralogical Applications of Crystal Field Theory. *Cambridge Topics in Mineral Physics and Chemistry*, Cambridge University Press, **1993**. DOI: 10.1017/CBO9780511524899

Dieke GH, Crosswhite HM. The Spectra of the Doubly and Triply Ionized Rare Earths. *Applied Optics* **1963**, 2, 675–686. DOI: 10.1364/AO.2.000675.

European Commission. Communication from the commission to the European parliament, the council, the European economic and social committee and the committee of the regions. On the review of the list of critical raw materials for the EU and the implementation of the Raw Materials Initiative, Brussels, **2014**.

European Commission. Communication from the commission to the European parliament, the council, the European economic and social committee and the committee of the regions on the 2017 list of Critical Raw Materials for the EU, Brussels, **2017**.

Forget S, Chénais S. Organic Solid-State Lasers. *Springer Series in Optical Sciences*, Springer: Berlin-Heidelberg, **2013**.

Friis H. Luminescence Spectroscopy of Natural and Synthetic REE-bearing Minerals. PhD Thesis, University of St. Andrews, UK, **2009**.

Fuchs MC, Gloaguen R, Beyer J, Jakob S, Heitman J. Emission spectroscopy for the identification of rare earth elements using laser-induced photoluminescence. In: *8th Workshop on Hyperspectral Image and Signal Processing: Evolution in Remote Sensing (WHISPERS),* Los Angeles, US, 21–24 Aug **2016**, 1–5. DOI: 10.1109/whispers.2016.8071681

Gaft M. Application of thermal treatment of zircon for the interpretation of luminescence centers. *Journal of Thermal Analysis* **1992**, 38, 2281–2290. DOI: 10.1007/BF02123981

Gaft M. Laser-Induced Time-Resolved Luminescence And Laser-Induced Breakdown Spectroscopy For Evaluation Of Phosphates With High Dolomite Content. In: *Benefication of phosphates, fundamentals and technology*, SME: Littleton, US, **2002**, 145–152.

Gaft M, Reisfeld R, Panczer G. Modern luminescence spectroscopy of minerals and materials. Springer: Berlin, New York, **2005**. DOI: 10.1007/b137490

Gaft M, Reisfeld R, Panczer G, Blank P, Boulon G. Laser-induced time-resolved luminescence of minerals. *Spectrochimica Acta Part A: Molecular and Biomolecular Spectroscopy* **1998**, 54, 2163–2175. DOI: 10.1016/S1386-1425(98)00134-6

Gaft M, Reisfeld R, Panczer G, Uspensky E, Varrel B, Boulon G. Luminescence of Pr^{3+} in minerals. *Optical Materials* **1999**, 13, 71–79, DOI: 10.1016/S0925-3467(99)00014-2

Gaft M, Shoval S, Panczer G, Nathan Y, Champagnon B, Garapon C. Luminescence of uranium and rare-earth elements in apatite of fossil fish teeth. *Palaeogeography, Palaeoclimatology, Palaeoecology* **1996**, 126, 187–193. DOI: 10.1016/S0031-0182(96)00079-X

Green AA, Berman M, Switzer P, Craig MD. A transformation for ordering multispectral data in terms of image quality with implications for noise removal. *IEEE Transactions on Geoscience and Remote Sensing* **1988**, 26, 65–74. DOI: 10.1109/36.3001

Günther KP, Dahn H-G, Lüdeker W. Remote sensing vegetation status by laser-induced fluorescence. *Remote Sensing of the Environment* **1994**, 47, 10–17. DOI: 10.1016/0034-4257(94)90122-8

Guyonnet D, Planchon M, Rollat A, Escalon V, Tuduri J, Charles N, Vaxelaire S, Dubois D, Fargier H. Material flow analysis applied to rare earth elements in Europe. *Journal of Cleaner Production* **2015**, 107, 215–228. DOI: 10.1016/j.jclepro.2015.04.123

Hoge FE, Swift RN, Yungel JK. Feasibility of airborne detection of laser-induced fluorescence emissions from green terrestrial plants. *Applied Optics* **1983**, 22, 2991. DOI: 10.1364/ao.22.002991

Huntington J, Laukamp C. Drill Core Reflectance Spectroscopy applied to the Carbonatite hosted REE deposit at Cummins Range (Australia). In: *Proceedings of the 13th SGA Biennal Meeting*, Nancy, FR, 24–27 Aug **2015**, 3, 1017–1020.

Jassie LB. Diffuse reflectance spectra of ten rare earths. *Spectrochimica Acta* **1964**, 20, 169–177. DOI: 10.1016/0371-1951(64)80006-0

Kauppinen T, Khajehzadeh N, Haavisto O. Laser-induced fluorescence images and Raman spectroscopy studies on rapid scanning of rock drillcore samples. *International Journal of Mineral Processing* **2014**, 132, 26–33. DOI: 10.1016/j.minpro.2014.09.003

Keizer PD, Gordon Jr. DC. Detection of Trace Amounts of Oil in Sea Water by Fluorescence Spectroscopy. *Journal of the Fisheries Research Board of Canada* **1973**, 30, 1039–1046. DOI: 10.1139/f73-175

Kim HH. New Algae Mapping Technique by the Use of an Airborne Laser Fluorosensor. *Applied Optics* **1973**, 12, 1454–1459. DOI: 10.1364/AO.12.001454

Kim S, Rhee SJ, Li X, Coleman JJ, Bishop SG. Photoluminescence and photoluminescence excitation spectroscopy of multiple Nd^{3+} sites in Nd-implanted GaN. *Physical Review B* **1998**, 57, 14588–14591. DOI: 10.1103/PhysRevB.57.14588

Lenz C, Nasdala L, Talla D, Hauzenberger C, Seitz R, Kolitsch U. Laser-induced REE^{3+} photoluminescence of selected accessory minerals — An "advantageous artefact" in Raman spectroscopy. *Chemical Geology* **2015**, 415, 1–16. DOI: 10.1016/j.chemgeo.2015.09.001

Lenz C, Talla D, Ruschel K, Škoda R, Götze J, Nasdala L. Factors affecting the Nd^{3+} (REE^{3+}) luminescence of minerals. *Mineralogy and Petrology* **2013**, 107, 415–428. DOI: 10.1007/s00710-013-0286-2

Lüthi B. Crystal field effects in rare earth systems. *Journal of Magnetism and Magnetic Materials* **1980**, 15–18, 1–8. DOI: 10.1016/0304-8853(80)90922-1

McDowell ML, Kruse FA. Integrated visible to near infrared, short wave infrared, and long wave infrared spectral analysis for surface composition mapping near Mountain Pass, California. In: *Algorithms and technologies for multispectral and ultraspectral imagery XXI* (Velez-Reyes M, Kruse FA, Eds.), Baltimore, Maryland, United States, **2015**, 94721C.

Moss R, Tzimas E, Willis P, Arendorf J, Thompson P, Chapman A, Morley N, Sims E, Bryson R, Peason J, et al. Critical metals in the path towards the decarbonisation of the EU energy sector: Assessing rare metals as supply-chain bottlenecks in low-carbon energy technologies. European Commission, **2013**, 242.

Murphy RJ, Schneider S, Monteiro ST. Consistency of measurements of wavelength position from hyperspectral imagery: use of the ferric iron crystal field absorption at ~900 nm as an indicator of mineralogy. *IEEE Transactions on Geoscience and Remote Sensing* **2014**, 52. DOI: 10.1109/tgrs.2013.2266672

Nassar NT, Du X, Graedel TE. Criticality of the Rare Earth Elements. *Journal of Industrial Ecology* **2015**, 19, 1044–1054. DOI: 10.1111/jiec.12237

Neave DA, Black M, Riley TR, Gibson SA, Ferrier G, Wall F, Broom-Fendley S. On the Feasibility of Imaging Carbonatite-Hosted Rare Earth Element Deposits Using Remote Sensing. *Economic Geology* **2016**, 111, 641–665. DOI: 10.2113/econgeo.111.3.641

Nienhaus K, Bayer AK. Innovative Systems for Horizon Control of Mining Machines by Means of Laser Induced Fluorescence (LIF). In: *Mine Planning and Equipment Selection*, Kalgoorlie, WA, 23–25 Apr **2003**, 1–7.

Pollmanns J. Identifikation von Mineralien und Schüttgütern mit Hilfe der laserinduzierten Fluoreszenz. *Bergbau* **2008**, 7, 322–325.

Raimondi V, Cecchi G, Lognoli D, Palombi L, Grönlund R, Johansson A, Svanberg S, Barup K, Hällström J. The fluorescence lidar technique for the remote sensing of photoautotrophic biodeteriogens in the outdoor cultural heritage: A decade of in situ experiments. *International Biodeterioration & Biodegradation* **2009**, 63, 823–835. DOI: 10.1016/j.ibiod.2009.03.006

Rajendran S, Nasir S, Kusky TM, Ghulam A, Gabr S, El-Ghali MAK. Detection of hydrothermal mineralized zones associated with listwaenites in Central Oman using ASTER data. *Ore Geology Reviews* **2013**, 53, 470–488. DOI: 10.1016/j.oregeorev.2013.02.008

Rastsvetaeva RK. Structural mineralogy of the eudialyte group: A review. *Crystallography Reports* **2007**, 52, 47–64. DOI: 10.1134/S1063774507010063.

Reisfeld R, Gaft M, Boulon G, Panczer C, Jørgensen CK. Laser-induced luminescence of rare-earth elements in natural fluor-apatites. *Journal of Luminescence* **1996**, 69, 343–353. DOI: 10.1016/S0022-2313(96)00114-7

Rogers SR, Webster T, Livingstone W, O'Driscoll NJ. Airborne Laser-Induced Fluorescence (LIF) Light Detection and Ranging (LiDAR) for the Quantification of Dissolved Organic Matter Concentration in Natural Waters. *Estuaries Coasts* **2012**, 35, 959–975. DOI: 10.1007/s12237-012-9509-8

Ropp RC. Phosphors Based on Rare Earth Phosphates: II. Reflection Spectra of Rare Earth Phosphates. *Journal of The Electrochemical Society* **1969**, 116, 623–629. DOI: 10.1149/1.2411313

Rowan LC, Kingston MJ, Crowley JK. Spectral reflectance of carbonatites and related alkalic igneous rocks; selected samples from four North American localities. *Economic Geology* **1986**, 81, 857–871. DOI: 10.2113/gsecongeo.81.4.857

Rowan LC, Mars JC. Lithologic mapping in the Mountain Pass, California area using Advanced Spaceborne Thermal Emission and Reflection Radiometer (ASTER) data. *Remote Sensing of the Environment* **2003**, 84, 350–366. DOI: 10.1016/S0034-4257(02)00127-X

Saito Y, Ichihara K, Morishita K, Uchiyama K, Kobayashi F, Tomida,T. Remote Detection of the Fluorescence Spectrum of Natural Pollens Floating in the Atmosphere Using a Laser-Induced-Fluorescence Spectrum (LIFS) Lidar. *Remote Sensing* **2018**, 10, 1533. DOI: 10.3390/rs10101533

Shavers EJ, Ghulam A, Encarnacion J. Surface alteration of a melilitite-clan carbonatite and the potential for remote carbonatite detection. *Ore Geology Reviews* **2018**, 92, 19–28. DOI: 10.1016/j.oregeorev.2017.11.002

Turner D. Reflectance spectroscopy and imaging spectroscopy of rare earth element-bearing mineral and rock samples. PhD Thesis, University of British Columbia: Vancouver, **2015**.

Turner D, Rivard B, Groat L. Rare earth element ore grade estimation of mineralized drill core from hyperspectral imaging spectroscopy. In: *2014 IEEE Geoscience and Remote Sensing Symposium*, Quebec City, QC, 13–18 July **2014**, 4612–4615. DOI: 10.1109/igarss.2014.6947520

Turner D, Rivard B, Groat LA. Visible to shortwave infrared reflectance spectroscopy of rare earth element minerals. In: Simandl GJ, Neetz M, Eds., British Columbia Geological Survey Paper, British Columbia Ministry of Energy and Mines: Victoria, British Columbia, **2015**, 3, 219–229.

Turner DJ, Rivard B, Groat LA. Visible and short-wave infrared reflectance spectroscopy of REE fluorocarbonates. *American Mineralogist* **2014**, 99, 1335–1346. DOI: 10.2138/am.2014.4674

Turner DJ, Rivard B, Groat LA. Visible and short-wave infrared reflectance spectroscopy of selected REE-bearing silicate minerals. *American Mineralogist* **2018**, 103, 927–943. DOI: 10.2138/am-2018-6195

Weidner VR, Barnes PY, Eckerle KL. A wavelength standard for the near infrared based on the reflectance of rare-earth oxides. *Journal of Research of the National Bureau of Standards* **1986**, 91, 243. DOI: 10.6028/jres.091.030

White WB. Diffuse-Reflectance Spectra of Rare-Earth Oxides. *Applied Spectroscopy* **1967**, 21, 167–171. DOI: 10.1366/000370267774385173

Zimmermann R, Brandmeier M, Andreani L, Mhopjeni K, Gloaguen R. Remote Sensing Exploration of Nb-Ta-LREE-Enriched Carbonatite (Epembe/Namibia). *Remote Sensing* **2016**, 8, 620. DOI: 10.3390/rs8080620

CHAPTER 6 CONCLUDING REMARKS

6.1 Discussion

The importance of rigorous pre-processing for the retrieval of spectrally and spatially meaningful data is well known in established remote sensing fields such as air- or space-borne imaging. Commonly accepted pre-processing workflows allow users to track the correction level of published data and obtain well-corrected images for their specific needs. I found drone-borne, terrestrial, and lab-scale spectral imaging approaches to have no comparable established routines yet, may it be due to their novelty, the diversity of used sensors or the fact that these data are often acquired by the end users themselves. The awareness of the users for required data corrections is usually low, and readily available software rare. This often ends in the publication of results based on insufficiently corrected data or in the contemporaneous development of customized, usually not publicly available data processing solutions. The presented work showed the potential that lies in well-corrected spectral image data and how such data could be utilized for complex tasks in mineral exploration and geosciences. The proposed workflows may provide a guideline for the applicational community and raise the awareness for the importance of rigorous pre-processing. Further optimized and combined with available open-source algorithms, a set of tools could be delivered for public use, allowing each user to obtain well-corrected data for his specific needs.

In the course of the study, I noticed several important aspects that are particularly relevant to all fields of spectral imaging and require a summarizing discussion to emphasize their importance:

Large datasets are common as a sufficient target area needs to be covered optimally with high spectral and spatial sampling rates. **Automation and speed** are paramount features of a practicable processing, not least as first results are often demanded after short turnaround times. A prominent example is the required (near-)real-time interpretation of data in the field. Ideally, overview scans or high-elevation flights are conducted in the first days of a field campaign. After data correction, feature extraction or clustering approaches can deliver an overview on the spectral (and by that mineralogical) variability of the target and be used to locate the most important regions of interest. These might be subject to further investigation by close-range scans or low-elevation flights with higher resolution. First mineralogical maps created from the resulting data can help to guide geologists in the field for targeted validation sampling and further investigation. Automation in processing is a key pre-requisite for such a workflow.

A paramount but usually tedious task is the **co-registration** of images required for any sensor or data scale. Common application fields are image correction (such as band alignment), mosaicking or georeferencing. A manual selection of the required control points is usually only feasible for a low number of images or simple transformations. For more complex tasks I proposed the use of robust key point detection and matching algorithms that are invariant to size, orientation, spectral range, brightness, and perspective. The SIFT key point detection algorithm features such robustness and performed well for most tasks. However, it is slow compared to other available methods. The ORB algorithm turned out to be a promising alternative for simple matching tasks such as band-to-band registration, but also has a decreased scale-invariance. A use of ORB for HSI-to-RGB or multi-sensor registration could therefore not yet be implemented in the presented workflows. As an alternative, I decided to add supporting parameters to decrease processing time, e.g. the integration of GPS data for the georeferencing of UAS-HSI, logged either by the platform or the sensor itself. The geotag of each image can be used to refine the search radius for the matching process, which decreases processing time and enhances the reliability of the matching in data with high textural similarity. Further

code optimization such as the implementation of parallel processing will be an upcoming task to enhance the performance of the used tools.

The effect of **BRDF** is one aspect that is particularly important to be considered for any spectral imaging survey. The wavelength-dependency of the effect can affect the observed position and depth of absorption features, whereas the illumination-angle-dependency causes these changes to vary between image regions with different surface orientation. If no correction is applied, substantial errors may occur in calculated mineral abundance and composition maps. BRDF is widely considered in the correction of air- and space-borne images, e.g. by application of a topographic correction using a DEM with enhanced spatial resolution. Radiometric block adjustment poses a solution to reduce anisotropy-related differences in reflectance for UAS data with high image overlap and low morphological variation (Honkavaara et al. 2012). However, these pre-requisites are not fulfillable in common geological surveys, where strong changes in surface orientation and texture are common and acquisition conditions may inhibit a sufficient image overlap. I found a transfer of the topographical correction approach used in space- and airborne data to UAS- and terrestrial imaging most beneficial. It is based on an accurate link of the drone-borne spectral imagery to high-resolution morphological information in form of a DEM or pointcloud, which may be provided by photogrammetric or LiDAR surveys. The **integration of morphological and spectral information** is further beneficial as it allows to assign each spectral pixel to its real 3D position. The 3D geolocation removes geometric distortions and delivers a common space where HSI can be visualized and integrated with any other available geolocated data, e.g. other remote sensing data, georeferenced lithological maps, geochemical measurements, point spectra, drill-core data, geophysical data, or extracted structures and veins. Georeferencing spectral imagery is not a new task, however, terrestrial data demand specific treatment due to their characteristic small viewing angle. The basic principle of our georeferencing approach is in line with that of Kurz et al. (2011). However, instead of directly projecting the HSI into the geolocated 3D space, I project the morphological information to the geographically artificial space of the spectral image. From there any spectral results can be exported to a “hypercloud”, i.e. the representation of the HSI or its results as pointcloud in a 3D environment. The reversed workflow causes no distortion or interpolation of the original spectral data and allows to handle and process morphological information together with the HSI in a 2D environment, a concept similar to the visualization of nadir HSI, DEM, and orthophoto in a Lat/Lon Geographic Information System (GIS). Morphological information from photogrammetric and LiDAR data can provide information about geological structures such as dykes and fractures. For example, the work of Thiele et al. (2017) provides a tool to trace lineaments and structural patterns in RGB pointclouds. The benefit of a fusion of topographical and spectral information for geological mapping was discussed by Kirsch et al. (2018) and Dering et al. (2019) and is a required task in the future. The potential of a combined interpretation of multi-sensor datasets in general needs to be emphasized at this point. Besides topographical information this may encompass data acquired at different spectral ranges, experimental scales or settings. Two prominent examples were given in Chapter 4 and 5, which illustrated the enormous potential of multi-sensor datasets at the lab-scale for mineral domain mapping and raw material detection, respectively.

The review of the current state of the art in HS image processing and applications revealed an important issue that is not originating from the data itself but from an apparent **communication gap** between sensor development, image processing community and application field. Despite the overall number of publications in each field, the exchange of knowledge between these communities often seems hampered. Many novel developments in image processing algorithms do not reach the application stage, as the tools do either not tackle the users’ specific challenges or the users are not aware that these tools could be beneficial for their

specific task. Methodology used in the applicational field is more often linked to what is available in commercial software, even if more suited approaches may be already published. A profound review of available advanced algorithms, e.g. for feature extraction and classification, would be beneficial to evaluate their applicability in applicational conditions and promote their establishment in the users' community.

In this context, I additionally promote the importance of **target-oriented spectral analysis** in mineral mapping. The selection of the approach used for data interpretation should be reasonable and tailored to the task or desired outcome. For example, classes may be defined according to mineral mixtures or domains that are important to distinguish for the current aim and not by automatically extracted endmembers, which are usually difficult to interpret and may miss minor, but important spectral variations. Unsupervised clustering can be helpful to present an overview on the spectral variations within the image, however, if information on specific compositional variations is required, a targeted mapping of specific absorption features is more meaningful. This recommendation also affects the selection of the used classifiers or feature extraction algorithms, which should be justifiable on a data or applicational basis.

6.2 Summary

Current remote spectral imaging, benefitting from novel operational principles, allows to overcome the scale, flexibility and cost limitations of traditional space and airborne surveys. These in particular encompass ground- and UAS-based remote sensing as well as near-field multi-sensor solutions. In mineral exploration, these approaches support the detailed mapping of small-scale, otherwise inaccessible or vertical targets as well as the quick mineralogical analysis of samples and drill-cores.

The novel acquisition approaches are accompanied by new challenges, inherent to unique radiometric and geometric effects. However, a proper pre-processing is often neglected in contemporary UAS-borne, terrestrial or near-field sensing studies. For most pre-processing tasks, no applicable software solutions existed and the development of appropriate tools is complex. In contrast, the scientific community recently made tremendous contributions to the development of algorithms for subsequent spectral analysis and mapping. Such processing tools are quasi-independent from the data scale or acquisition approach, as they are usually developed using synthetic or well-corrected data. The quality difference between synthetic and non-controlled datasets is apparent, which is why many promising machine learning algorithms are not yet implemented by the end users. Instead, the raw material sector often sticks to simple, outdated workflows or commercial software that allows a very restricted range of tools. Thus, resulting spectral maps remain subject to strong distortions, are barely validated or have no spatial relation to other datasets. A balance between the complexity of data correction and processing workflows needs to be achieved to allow a meaningful data interpretation based on spectrally and spatially sound datasets.

The outcomes of the thesis contribute substantially to solve this major challenge in current most emerging imaging spectroscopy applications in mineral exploration. The presented Mineral Exploration Hyperspectral Toolbox ("MEPHySTo") reduces the complexity of required pre-processing steps to a set of rather straight-forward workflows that can be composed and adapted for most imaging sensors, scales or platforms (**Figure 6-1**). The results show the overall positive impact of accurate preprocessing on both the amount of feasible application scenarios as well as the scientific soundness of the created material maps. MEPHySTo allows to retrieve accurate spectroscopic information even under challenging acquisition conditions, and to set the corrected data into a spatially meaningful context. This allows the combined interpretation or even fusion of datasets acquired under different acquisition circumstances such as sensor-type, sensor position, viewing angle or illumination.

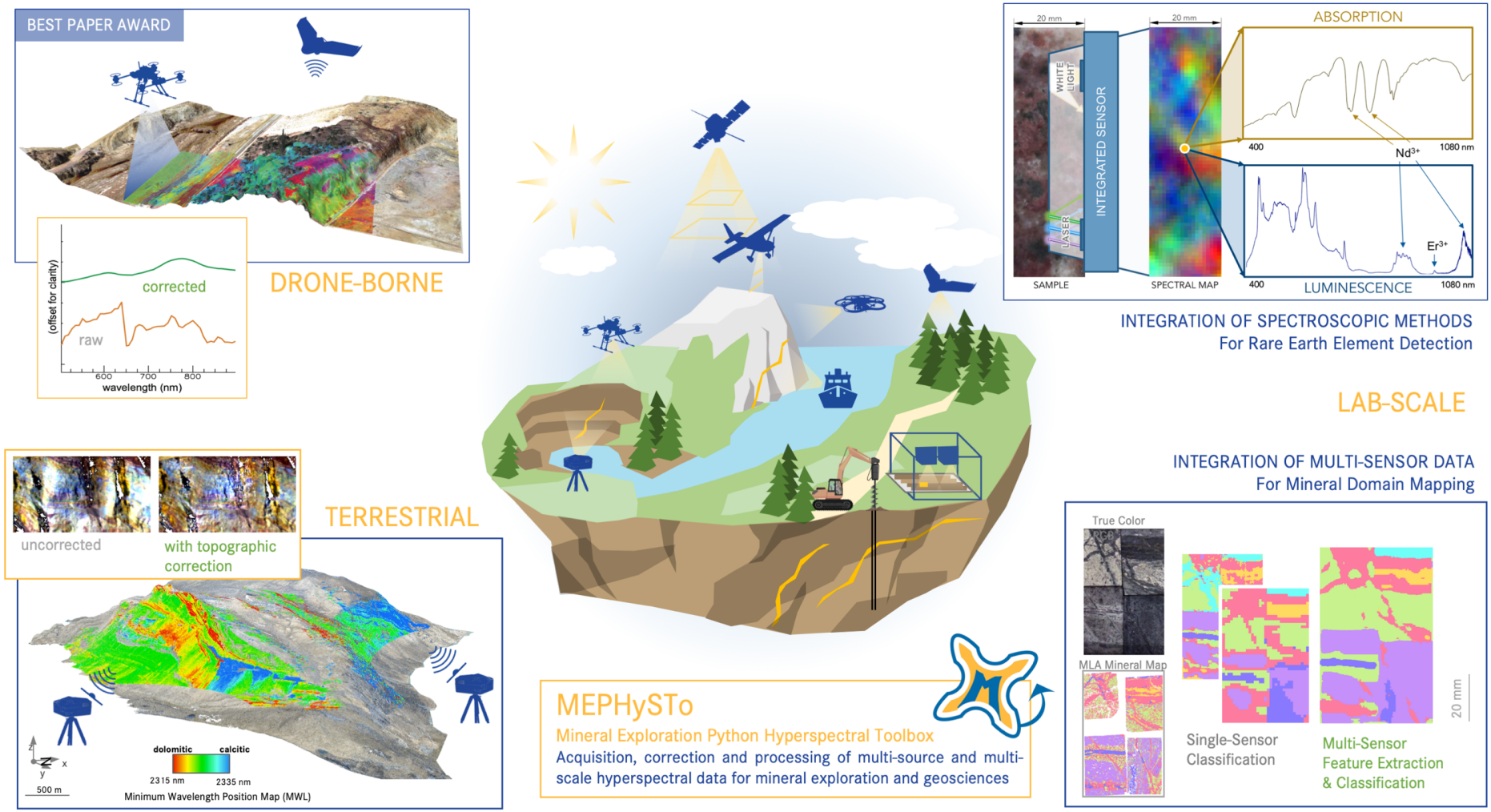

Figure 6-1. Schematic summary of the outcomes of the thesis.

In more detail, the main tools of MEPHySTo are the following:

(1) Correction routines of sensor-specific internal geometric and radiometric disturbances – for both push broom and frame-based HS imagers;

(2) Workflows for automatic co-registration of images – usable for the correction of band-offsets in frame-based HS image data, automatic georeferencing and orthorectification of UAS-, ground-and near-field data, and the stitching of overlapping images;

(3) External radiometric correction solutions – including data-driven atmospheric correction for long-range off-nadir HS images, where common radiometric models do not apply;

(4) Integration of 3D surface and hyperspectral image data – enabling both the correction of topography-/ surface-induced geometric distortions and illumination differences, as well as the addition of geo-spatial reference to each hyperspectral pixel. The resulting "hyperclouds" can be calculated for any hyperspectral scene independent of acquisition time, angle or sensor specification, which allows the combined interpretation of different datasets. This approach is applicable for all acquisition scales and principles and poses the preposition for multi-sensor fusion.

(5) Optimized data acquisition and fusion of multi-sensor data for a better mapping result and flexibility in used sensors – the retrieval of spectrally and spatially meaningful image features allows the integration of highly different HSI and a substantial dimensionality reduction for large datasets;

(6) Fusion of hyperspectral reflectance data with further spectroscopic methods to increase and cross-validate their spectroscopic significance – application to the enhanced characterization of Rare Earth Elements by the integration of photoluminescence data.

Altogether, the MEPHySTo bridges data acquisition and image processing, research fields that are often independent. A comprehensive image processing workflow is provided instead, starting with the acquisition of raw data in the field or lab, to returning fully corrected, validated and spatially registered at-target reflectance datasets. Case studies exemplarily demonstrated their value for subsequent spectral analysis, image classification or fusion in different acquisition scales and environments.

The positive feedback received on our publications and presentations indicated a large field of potential users and application fields, such as

- Mineral exploration: Being in the focus of the thesis, mineral exploration is one of the major application fields of the presented tools. No matter whether outcrop, drill-core or sample scale, the small and often indistinct spectral features of minerals of interest require a careful data correction. Rough acquisition conditions and inaccessible targets cause prominent radiometric and geometric disturbances and often limit the amount of available validation. The presented workflows allow the retrieval of reliable HS data even under challenging circumstances and set them into a common spatial context with other exploration-relevant information such as drill-core logs or geological profiles.
- Mining: Both the acquisition and correction of data under active mining conditions is comparable to exploration surveys, however, the workflows need to be routinized, reliable, and straight-forward. Frequent tasks such as mine-face mapping for grade control after blasting demand flexibility, short turn-around times, and resistance of the equipment for dust, weather, and repeated assembly and disassembly. The proposed correction of topography-induced illumination differences and spectral disturbances due to dust, as well as the accurate geolocation of separate acquisitions are crucial to retrieve meaningful and comparable multi-temporal HS measurements.

- Mineral processing, material sorting, and recycling: While usually conducted under controlled conditions, these application fields place special requirements on speed and reliability. Tailored sensor solutions and accurate processing workflows are required to optimize specific tasks, e.g., the semi-quantitative monitoring of rare earths content during mineral processing. The integration of reflectance data with other material characterization methods was shown to increase the reliability of the analysis as well as the amount of detectable materials.
- Geological research: Similar to mineral exploration, HS workflows can complement and improve efficiency of lithological, mineral, and structural mapping in general, by contributing to the understanding of geological processes and subtle mineralogical differences.
- Agriculture and environmental monitoring: Further applications of interest apart from mineral resources include (not comprehensively) the monitoring of spectrally indicative parameters in agriculture and environmental studies. Despite the differing focus, most challenges in HS image processing are similar, which allows a smooth transfer of the workflows.

While providing solutions for each of the mentioned topics, the further optimization of MEPHySTo for specific applications is a future challenge and might be boosted by already existing approaches in machine learning. Tailoring these algorithms to important applications and raising the awareness in the user communities for already existing methods is a crucial task. They might further improve specific steps such as topographic and atmospheric corrections, image denoising or sharpening, or the overall optimization in regard to time and data memory consumption. The further development of sensors and platforms might bring up new challenges, but also opportunities to acquire data at enhanced resolution and spectral ranges.

References

Dering GM, Micklethwaite S, Thiele S, Vollgger S, Cruden A. Review of drones, photogrammetry and emerging sensor technology for the study of dykes: Best practises and future potential. *Journal of Volcanology and Geothermal Research* **2019**, 373. DOI: 10.1016/j.jvolgeores.2019.01.018

Honkavaara E, Kaivosoja J, Mäkynen J, Pellikka I, Pesonen L, Saari H, Salo H, Hakala T, Marklelin L, Rosnell T. Hyperspectral reflectance signatures and point clouds for precision agriculture by light weight UAV imaging system. *ISPRS Annals of Photogrammetry, Remote Sensing and Spatial Information Sciences* **2012**, I-7, 353–358. DOI: 10.5194/isprsannals-i-7-353-2012

Kirsch M, Lorenz S, Zimmermann R, Tusa L, Möckel R, Hödl P, Booysen R, Khodadadzadeh M, Gloaguen R. Integration of Terrestrial and Drone-Borne Hyperspectral and Photogrammetric Sensing Methods for Exploration Mapping and Mining Monitoring. *Remote Sens* **2018**, 10, 1366. DOI: 10.3390/rs10091366

Kurz TH, Buckley SJ, Howell JA. Integration of Panoramic Hyperspectral Imaging with Terrestrial LIDAR Data. *The Photogrammetric Record* **2011**, 26 (134), 212–228. DOI: 10.1111/j.1477-9730.2011.00632.x

Thiele ST, Grose L, Samsu A, Micklethwaite S, Vollgger SA, Cruden AR. Rapid, semi-automatic fracture and contact mapping for point clouds, images and geophysical data. *Solid Earth* **2017**, 8, 1241–1253. DOI: 10.5194/se-8-1241-2017